ANALYSES OF FLAME RESPONSE TO ACOUSTIC FORCING IN A ROCKET COMBUSTOR

Scott Kenneth Beinke

A thesis submitted in fulfilment of
the requirements for the degree
of
Doctor of Philosophy
April 2017

School of Mechanical Engineering
The University of Adelaide
South Australia 5005
Australia

Abstract

High frequency combustion instabilities in liquid propellant rocket engines are spontaneously occurring pressure fluctuations that are coupled with unsteady combustion processes. Under the right conditions the unsteady fluctuations can grow to a point where they affect the operation of the combustion chamber. The cause of combustion instabilities, including which processes are responsible and under what conditions they arise, are not yet fully understood. The ability to predict and prevent combustion instabilities during the design of new combustion chambers, through better understanding, would dramatically reduce the uncertainty and risk in the development of new engines.

An experimental combustor, designated BKH, is used to conduct high frequency combustion instability experiments. BKH operates with liquid oxygen and gaseous hydrogen propellants at supercritical conditions analogous to real rocket engines. The chamber features an acoustic excitation system that imposes an acoustic disturbance representative of a high frequency instability upon a cluster of five coaxial injection elements in the center of the chamber. The response of the elements to the imposed acoustic disturbance is observed using high speed optical diagnostics.

The main aim of this project is to develop methods for predicting the flame response to high frequency acoustic forcing representative of combustion instability phenomena. BKH is employed as an experimental and numerical test case for investigating the flame response. Modelling and complementary data analysis methods are developed and applied to model the chamber flow field, identify and predict the excited acoustic disturbance, identify the flame response using optical data, and to predict the flame response numerically.

The BKH experiments are first characterised by modelling the chamber numerically and determining the local acoustic disturbance acting upon the flame. A steady state chamber model with supercritical oxygen-hydrogen combustion was computed using a specialised CFD code. The model results indicate the secondary injection in BKH has a strong influence on the resulting flame distribution.

A method for reconstructing the acoustic field from dynamic pressure sensor data was developed to determine the local acoustic disturbance acting upon the combustion zone over a range of excitation frequencies. A low-order acoustic modelling approach is also shown to predict the resonant mode frequencies and the evolution of the acoustic field.

The flame response to the imposed acoustic disturbance is identified by analysing optical data from BKH experiments and unsteady CFD modelling. Multi-variable dynamic mode decomposition (DMD) analysis is used to isolate the flame response to the imposed acoustic disturbance in shadowgraph and OH* imaging data. Wave-like structures propagating along the surface of the liquid oxygen (LOx) jet and a phase difference of 45° between acoustic pressure and observed intensity fluctuations were identified.

An unsteady model of an injection element subjected to representative acoustic forcing is used to predict the flame response for a range of excitation amplitudes. Velocity ratio fluctuations caused by acoustic coupling with the oxidiser post in a pressure antinode are identified. The trend of exponential decay of the length of the LOx core with increasing transverse acoustic amplitude excitation is reproduced numerically and the flattening and flapping motion of the flame was further investigated using the numerical results.

Declaration of Originality

I certify that this work contains no material which has been accepted for the award of any other degree or diploma in any university or other tertiary institution and, to the best of my knowledge and belief, contains no material previously published or written by another person, except where due reference has been made in the text. In addition, I certify that no part of this work will, in the future, be used in a submission for any other degree or diploma in any university or other tertiary institution without the prior approval of the University of Adelaide and where applicable, any partner institution responsible for the joint-award of this degree.

I give consent to this copy of my thesis, when deposited in the University Library, being made available for loan and photocopying, subject to the provisions of the Copyright Act 1968.

I also give permission for the digital version of my thesis to be made available on the web, via the Universitys digital research repository, the Library catalogue and also through web search engines, unless permission has been granted by the University to restrict access for a period of time.

Scott K. Beinke
20^{th} April 2017

Acknowledgements

First and foremost I would like to thank my supervisors, Prof Bassam Dally, Prof Michael Oschwald, and Dr Justin Hardi, for granting me the opportunity to pursue my PhD project through the University of Adelaide and in cooperation with the DLR. I thank you for the guidance, knowledge, and experience you have provided me over the duration of this project. I also cannot express the gratitude I have for your continued support and understanding that allowed me to see this project through to its completion.

I would like to acknowledge the financial support provided by the University of Adelaide School of Mechanical Engineering, and the Sir Ross and Sir Keith Smith fund. This funding allowed me to travel to and work at the DLR facilities in Germany, and I am very grateful for the many opportunities it has granted and the many friends I have made while interacting with the European space and scientific research community.

I would like to thank the DLR Institute of Space Propulsion for the financial support and resources for my project, and Dmitry Suslov and the P8 test facility team for their assistance conducting experimental campaigns. I would also like to acknowledge the invaluable assistance from Joachim Sender, Michaela Hanke, Melanie Schmidt, and Isabell Böhringer that allowed me to navigate the many technical and bureaucratic hurdles during my time at the DLR.

I would also like to acknowledge the CFD expertise and support from the DLR Institute of Aerodynamics and Flow Technology. In particular the guidance and technical support from Sebastian Karl, Daniel Banuti, and Volker Hannemann. I would also like to thank Klaus Hannemann, Bernd Wagner, and the DLR ProTAU project for supporting my PhD research.

Thanks also to Matthew Wierman, for providing instruction on the application of the DMD method, and to Hideto Kawashima, for his initial work on the acoustic field reconstruction.

For the many good times and distractions that allowed me to survive my PhD I must also thank the Wohnheimers: Michael Wohlhüter, Michele and Anna Negri, Cristiano Bombardieri, Michael Börner, Dirk Schneider, Wolfgang Armbruster, Sarah Dommers, and many others. Thank you for the many unique and memorable experiences I will take away from my time in Germany.

I would also like to thank my colleagues from the HF group, Stefan Gröning and Samuel Webster. I truly value your support and friendship and the good fortune that allowed us to conduct our PhD research together.

I must especially thank my supervisor who paved the way for me to follow him to Germany, Dr Justin Hardi. I am still very grateful for the opportunity to work with you and learn from your example. I am even more grateful to you and your family, Katharina and Kai Hardi, for your unending support and for the great times we shared in both Marbach and Möckmühl.

Finally, my deepest thanks go to my parents and Kara Jerman, without whose love and support this would not have been possible.

Disclaimer

Research undertaken for this report has been assisted with a grant from the Sir Ross and Sir Keith Smith Fund (Smith Fund) (www.smithfund.org.au). The support is acknowledged and greatly appreciated. The Smith Fund by providing funding for this project does not verify the accuracy of any findings or any representations contained in it. Any reliance on the findings in any written report or information provided to you should be based solely on your own assessment and conclusions. The Smith fund does not accept any responsibility or liability from any person, company or entity that may have relied on any written report or representations contained in this report if that person, company or entity suffers any loss (financial or otherwise) as a result.

THE SIR ROSS & SIR KEITH SMITH FUND

Contents

List of Figures

List of Tables

Glossary

Nomenclature

α, β	Stoichiometric coefficients	q, Q	Heat release
a	Speed of sound	q_d	Dipole source term
c	Speed of light	Re	Reynolds number
D	Diffusion coefficient	ρ	Density
D_0	Diameter	R	Reflection coefficient
f	Frequency	R_0	Radius
γ	Ratio of specific heats	σ	Surface tension
H	Height	Sc	Schmidt number
h	Planck constant	St	Strouhal number
I	Image intensity	T	Temperature
I_n	Identity matrix	t	Time
J	Momentum ratio	T_s	Period
Kn	Knudsen Number	τ	Time delay factor
κ	Thermal conductivity	v, $\mathbf{V}$	Velocity
k_b	Boltzmann constant	VR	Velocity ratio
λ	Wavelength	μ	Viscosity
L	Length	V	Volume
$\dot{m}$	mass flow rate	We	Aerodynamic Weber number
N	Response factor	We_L	Weber number
n	Amplification factor	ω	Angular frequency
p, P	Pressure	Z	Acoustic impedance
P_v	Viscous stress tensor	z	Specific acoustic impedance

Subscripts

∞	Free stream properties
cr	Critical properties
CC	Combustion chamber properties
f	Fuel
ox	Oxidizer
LOx	Liquid oxygen
$conv$	Convection
G	Gas
L	Liquid
R	Real part
I	Imaginary part
lam	Laminar
T	Turbulent
$BPRMS$	Band-passed RMS result
RMS	Root Mean Squared result

Superscripts

a'	Perturbation or oscillating value
$\hat{a}$	Complex valued property
$\bar{a}$	Mean property
a^f	Forward reaction coefficient
a^b	Backward reaction coefficient

Acronyms

AFRL	Air Force Research Laboratory
AVBP	LES solver jointly developed by Cerfacs, IFPEN, and EM2C
AVSP	Acoustic solver developed by Cerfacs
BKD	Combustion chamber (*German: Brennkammer*) 'D', operated by DLR
BKH	Combustion chamber (*German: Brennkammer*) 'H', operated by DLR
BPRMS	Band-passed Root Mean Squared
CAA	Computational Aero Acoustics
CEA	Chemical Equilibrium Analysis
CFD	Computational Fluid Dynamics
CVRC	Continuously Variable Research Combustor, operated by Purdue University
CRC	Common Research Chamber, operated by DLR
DLR	German Aerospace Center (*Deutsches Zentrum für Luft und Raumfahrt*)
DMD	Dynamic Mode Decomposition
DNS	Direct Numerical Simulation
EM2C	Energetics and combustion lab at CentraleSupélec
FEM	Finite Element Methods
FFT	Fast Fourier Transform
FTF	Flame Transfer Function
HF	High Frequency
IFPEN	French public-sector research, innovation and training center
JAXA	Japanese Aerospace Exploration Agency
LEE	Linearised Euler Equations
LES	Large Eddy Simulation
LE-7A	Mitsubishi LE-7(A) rocket engine
LF	Low Frequency
LOx	Liquid Oxygen
MIC	Multiple-Injector Combustor, operated by ONERA
ONERA	French national aerospace research center
P8	European Test Facility for Cryogenic Rocket Propulsion
PCCDYN	Dynamic pressure sensors installed in BKH
POD	Proper Orthogonal Decomposition
RANS	Reynolds Averaged Navier Stokes
RMS	Root Mean Squared
ROF	Ratio of Oxidizer to Fuel mass flow rate
SSME	Space Shuttle Main Engine
TAU	CFD solver developed by the DLR
TIC	Transverse Instability Combustor, operated by Purdue University
TUM	Technical University of Munich (*Technische Universität München*)
URANS	Unsteady Reynolds Averaged Navier Stokes
VHAM	Very High Amplitude Modulator, operated by ONERA

Chapter 1

Introduction

Combustion instability in rocket engines refers to pressure oscillations that couple with unsteady combustion processes and become self sustaining. The large amount of energy released inside rocket engine combustion chambers means that if even a small percentage of the energy is converted to an acoustic instability it may be significant enough to impact the engine. If left unchecked, the instability may compromise the structural integrity and operation of the combustion chamber, reducing the operational lifetime of the rocket engine or cause a catastrophic failure leading to loss of a rocket mission.

Combustion instabilities are often classified by the observed frequency of the pressure oscillations. Low frequency combustion instability, sometimes known as chugging or buzzing, may cause vibrations strong enough to damage a payload if left un-dampened. Low frequency combustion instability occurs at frequencies typically less than 1 kHz and is often caused by the propellant feed system. Low frequency instabilities and may often be eliminated by redesigning key components of the system. High frequency combustion instability, which occurs at frequencies greater than 1 kHz, is less understood and more damaging.

High frequency instabilities are the result of the propellant injection and combustion processes interacting with the acoustic field within the combustion chamber. Under certain conditions, the acoustic field can oscillate at the resonant frequency of the combustion chamber volume. If the combustion and injection processes act to support and reinforce the acoustic resonance, the pressure oscillations will grow and may exceed the capacity of the structure. The disturbance may also disturb the boundary layer at the wall of the combustion chamber that protects the structure from the high temperature combustion products. How the acoustic and combustion processes support each other at high frequencies is not yet understood. This poses a significant challenge to combustion chamber designers and additional risk when developing a new rocket engine. The stability of a rocket engine remains the greatest unknown before the flight qualification process.

The high cost of rocket systems and their payloads, and the potential for loss of human life on manned space missions, has motivated research into the sources of combustion instabilities and how they may be prevented. Design methodologies have been developed to modify the acoustics of chambers and decrease the likelihood of high frequency combustion instabilities such as incorporating baffles or resonator cavities into combustion chambers. However, no current design method can guarantee an engine will not experience combustion instability over its entire operational envelope. Expensive full scale tests of assembled combustion systems, such as that performed at the DLR site in Lampoldshausen, are still required to ensure safe and reliable operation of each of the manufactured engines. With the advancement in computational technology in recent decades, researchers now aim to develop suitable models and numerical tools to replace the need for ground testing and significantly reduce the cost and duration of rocket engine qualification.

Determining and modelling the mechanisms that cause combustion instability is highly complex due to the number of physical and chemical processes occurring simultaneously within the combustion chamber such as injection, vaporisation, atomisation, mixing, and combustion. To gain insight into each process, specialised lab scale experimental rocket combustors have been developed by independent research institutes in the past. The experimental rocket combustors are used to simulate high frequency combustion instabilities and examine the effects of various configurations and operating conditions on the acoustic field. The results collected from such experiments are used to develop computational models and combustion instability theories. While significant modelling efforts have been made to accurately reproduce the results from experimental combustors, most have modelled experiments conducted at moderate operating pressures which are not representative of real rocket engines.

This thesis focuses on the study of a research combustor, dubbed BKH (German: Brennkammer 'H'), operated by the DLR (German Aerospace Center) at the test facilities in Lampoldshausen, Germany. BKH is used to conduct high frequency combustion instability experiments at supercritical pressures representative of real rocket engines. Windows installed in BKH allow unique high-speed optical data to be recorded from the combustion zone while operating with liquid oxygen and gaseous hydrogen propellants. BKH also features an acoustic excitation system which can produce acoustic fluctuations inside the chamber representative of a high frequency acoustic instability. The BKH experiments are used to observe the flame response to an imposed high frequency acoustic disturbance.

BKH experimental data has been previously collected and analysed by Hardi [49] and Webster [159]. However the experimental data provide limited insight into the flame response and coupling between combustion and acoustic processes. The BKH data, and the optical access and low number of reacting elements compared to full scale engines, provides a unique opportunity for developing and validating numerical models. Validated numerical models would allow the flame response to be investigated in detail and improve our understanding of combustion instability phenomena.

1.1 Aim

The aim of this thesis is to develop modelling approaches that can be used to predict the flame response to an acoustic disturbance and to compare the model results with BKH experimental data. Once validated, the models may be used to investigate and characterise new rocket engine designs and operating conditions. To be applicable in an industrial setting the modelling approaches should allow results to be produced in a short time frame and with reasonable computational resources.

In order to investigate the flame response using BKH results it is first necessary to understand its operation, including the combustor flowfield, the flames produced by the primary injection elements, and the acoustic disturbance produced by the acoustic excitation system. To employ BKH as a numerical test case experimental data must be processed to produce results useful for comparison and validation of numerical models. The specific aims of the project are therefore:

- To numerically investigate the unexcited (steady-state) BKH flow field,
- To characterise and model the acoustic field and the local acoustic disturbance acting upon the flame in BKH experiments,
- To process BKH optical data to identify the flame response and produce results for comparison with numerical models, and

- To model the flame response of BKH injection elements to the local acoustic disturbance during longitudinal and transverse mode excitation.

To address these aims various data processing and numerical modelling approaches are developed and applied to BKH as an experimental and numerical test case. The methods developed in this work are generally applicable to combustion instability experiments and rocket engine combustion chambers. The further analyses of BKH data and numerical results produced in this work also provide further insight into the flame response of coaxial oxygen-hydrogen injectors and combustion instability phenomena.

1.2 Thesis Structure

This thesis begins by providing a background on the relevant oxygen-hydrogen combustion processes and combustion instabilities in liquid rocket engines in Chapter 2. Details of BKH are then introduced and similar research using lab-scale high frequency combustion instability experiments and modelling efforts are summarised. Chapter 2 concludes by stating the objectives of the project.

The remaining chapters of the thesis address the identified aims and objectives. Chapter 3 presents a steady state model of BKH used to describe the chamber flowfield. In Chapter 4 the acoustic field is first characterised and reconstructed from BKH dynamic pressure sensor data. A model of the acoustic field that predicts the disturbance acting upon the flame zone is also presented. In Chapter 5 BKH optical data is processed using DMD analysis to identify the mean flame response during acoustic excitation of the first resonant modes. Finally an approach for modelling the flame response of a single injection element to acoustic disturbances representative of high frequency combustion instabilities is presented in Chapter 6. The main results and conclusions of this thesis are summarised in Chapter 7.

Chapter 2

Background

Combustion instability research is a complex topic with a considerably well documented research history spanning many decades. Current work builds upon this heritage and other work across various research fields. This chapter provides background information on the key topics relevant to this project and the current focus of combustion instability research.

Combustion processes must first be understood before investigating how they respond to acoustic disturbances. This chapter begins by discussing the oxygen-hydrogen propellant combination and combustion chamber processes. The topic of combustion instabilities is then introduced. A brief history, the relevant theories, and a description of the parameters for controlling instabilities, are then provided. The acoustic theory for describing the resonant modes of rocket engine combustion chambers, particularly relevant to the study of high frequency combustion instabilities, is then discussed. Research activities relevant to the current work are then summarised. This includes specialised combustion instability experiments and numerical investigations of combustion instability phenomena conducted by the DLR and various other research groups. This chapter concludes with a summary of the identified research gaps and objectives that are to be addressed in this thesis.

2.1 The Oxygen-Hydrogen Propellant Combination

This thesis is focused on the study of a rocket combustor fuelled with oxygen and hydrogen propellants and therefore the behaviour of both propellants and their products are fundamental to this work. Oxygen and hydrogen propellants are known as liquid fuels due to the fact that both propellants are usually stored in a liquid state for rocket applications. Storing the propellants as liquids reduces their volume allowing for smaller, lighter, and more aerodynamic propellant tanks. As both oxygen and hydrogen are gases at standard atmospheric conditions, the propellants are stored under pressure at cryogenic temperatures to keep them in a liquid state. The challenge of storing cryogenic liquids makes the oxygen-hydrogen propellant combination unsuitable for a variety of applications such as missiles which must be stored for extended periods and launched on short notice. However, it also offers a number of other advantages that make it suitable for various lower and upper rocket stages.

The specific impulse is used to benchmark the efficiency of a propellant combination in a given rocket. The specific impulse represents the force generated by the rocket with respect to the fuel consumption rate. Therefore a higher specific impulse represents higher propellant efficiency. Table 2.1 lists ranges of specific impulse for the various types of chemical rockets and specific values for bipropellant combinations under idealised conditions. Generally, liquid propellants offer superior performance over all other forms of chemical rockets due to their higher specific impulse.

Table 2.1: Specific impulse for chemical rocket engines. Values taken from Sutton [151].

Type of Chemical Rocket	Propellant Combination	Typical Range of Specific Impulse[a]
Liquid bipropellant		250 - 450 s
	Fluorine - hydrogen	410 s
	Oxygen - hydrogen	390 s
	Fluorine - hydrazine	334 s
	Hydrogen peroxide - RP-1[b]	297 s
	Nitrogen tetroxide - A-50[c]	289 s
	Oxygen - RP-1[b]	285 s
	Red fuming nitric acid - RP-1[b]	269 s
Solid propellant		190 - 270 s
Hybrid		230 - 380 s
Liquid monopropellant		184 - 223 s

[a] Values for specific propellant combinations are the maximum theoretical specific impulse at 6895 kPa chamber pressure in an ideal rocket - i.e. stoichiometric mixture ratio, adiabatic combustion, and isentropic, optimum expansion of ideal gas in the nozzle. values are sourced from Tables 2-1 & 5-5 in [151].
[b] RP-1 : Rocket propellant 1, high grade kerosene
[c] A-50 : Aerozine 50, a 50-50 blend of hydrazine (N2H4) and unsymmetrical dimethyl hydrazine (UDMH)

Of the bipropellant combinations listed in Table 2.1 only the fluorine-hydrogen combination offers higher specific impulse than the oxygen-hydrogen combination. However the fluorine-hydrogen combination has a number of disadvantages, such as the prohibitively high cost of fluorine, and the additional handling and storage considerations required to manage the toxic combustion products. While it has only a slightly lower specific impulse, the oxygen-hydrogen propellant combination is both plentiful and environmentally safe. Both oxygen and hydrogen propellants can be produced through electrolysis of water. If renewable energy is used for propellant production then the formation and combustion of oxygen and hydrogen propellants may be carbon neutral. The combustion products are also non-toxic with the main combustion product being water. Due to its superior performance, availability, and environmental concerns, the oxygen-hydrogen propellant combination is likely to remain a popular rocket propellant combination for the foreseeable future.

2.1.1 Injection and Supercritical Conditions

Oxygen and hydrogen are both gases at atmospheric conditions with boiling temperatures of 90 K and 20.4 K, respectively. The pressurised tanks used to store the propellants must be insulated to reduce 'waste' from propellant boil-off. The tanks must also be fitted with pressure release valves to prevent explosions from over-pressurization. The liquid hydrogen is typically circulated around cooling channels in the combustion chamber structure before injection. As the liquid hydrogen is employed to cool the structure it is heated and is injected into the combustion chamber in a gaseous state. Oxygen is typically injected directly into the combustion chamber as a liquid at around 100 K.

Along the coexistence line the liquid and the vapour phase of a chemical species are in equilibrium. The critical point, characterised by the critical pressure and temperature, is defined as the state at which the phases are indistinguishable. Therefore at supercritical conditions phase change phenomena like what is observed at sub-critical conditions do not occur. Supercritical fluid properties change continuously with no phase-boundary between

Table 2.2: Critical properties of oxygen and hydrogen.

Property			O_2	H_2
Critical Temperature,	T_{cr}	[K]	154.59	32.97
Critical Pressure,	p_{cr}	[bar]	50.43	12.93

Table 2.3: Combustion chamber pressures of engines using oxygen-hydrogen propellants as a ratio to the critical pressure of oxygen [98].

Combustor	SSME	LE-7A	Vulcain	Vinci
Launcher	Space shuttle (USA)	H-II (Japan)	Ariane (Europe)	Ariane (Europe)
Stage	first stage	first stage	first stage	upper stage
p/p_{cr}	4.4	2.40	2.28	1.19

the gaseous and liquid phases. The critical pressures and temperatures of oxygen and hydrogen are listed in Table 2.2.

A higher rocket engine combustion chamber pressure results in a higher thrust and specific impulse. For this reason the operating pressure of rocket engine combustion chambers is generally as high as possible. This has lead to many of the rocket engines in use today operating at chamber pressures higher than the critical pressure of one or both of the injected propellants. The operating chamber pressure of the prominent rocket engines that use oxygen and hydrogen propellants are listed in Table 2.3 as a ratio to the critical pressure of oxygen. As listed in the table, all of the engines operate above the critical pressure of both the oxygen and hydrogen propellants.

Figure 2.1.1 shows the change in the state of a propellant as it is injected into a chamber operating at super- and sub-critical pressures. Upon entering the chamber the injected propellants are quickly heated by combustion processes. Liquid propellants injected at sub-critical pressure have a distinct phase boundary where the liquid phase boils into a gaseous state as it is heated. When liquid propellants are injected into a chamber above their supercritical pressure they initially exist as a sub-critical fluid which is below its critical temperature but above its critical pressure. As the fluid is heated above its critical temperature it becomes supercritical. Injection of cryogenic propellants below their critical temperature into chambers above their supercritical pressures is referred to as trans-critical injection.

While there is no distinct phase change at supercritical pressures, as the propellant is heated the density is observed to decrease signficantly over a short temperature range. Oschwald and Schick [97] noted that a peak in the specific heat capacity and thermal expansion coefficient also occur as the density decreases during isobaric heating. Oschwald et al. [98] dubbed this phenomena "pseudo-boiling" due to its similarity to sub-critical vaporisation. Banuti et al. [3] found that the peak in the specific heat capacity distributions move to higher temperatures and becomes wider as the pressure is increased. A pseudo-boiling-line [3], also known as the "Widom-line" [140], is defined as the line defining the crossover between liquid-like and gas-like behaviour. Banuti [5] defined this line as an extension of the vapor-pressure curve at supercritical pressures, as shown in Figure 2.1.1. The Widom-line is defined by the pressure, p_r, and temperature, T_r relation:

$$p_r = exp\left[\frac{T_{cr}}{\theta_{cr}}(T_r - 1)\right], \tag{2.1}$$

where T_{cr} is the critical temperature and θ_{cr} is a constant. For oxygen the fraction T_{cr}/θ_{cr} has a value of approximately 5.5.

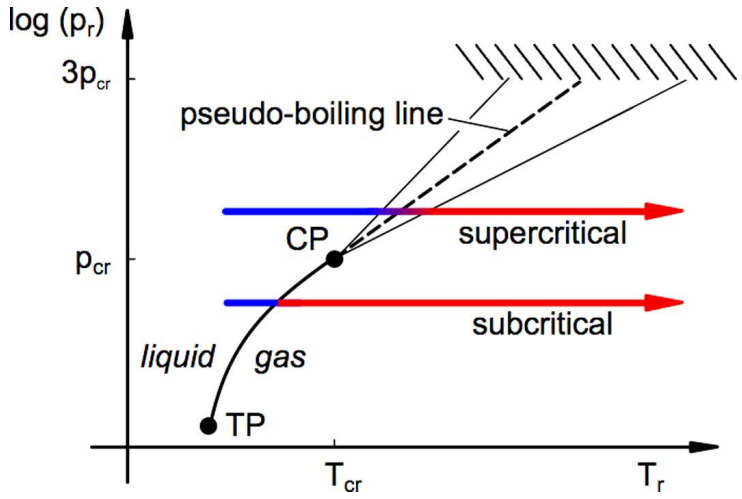

Figure 2.1.1: PT-diagram showing path of propellant injected at supercritical and subcritical conditions [3]. TP and CP denote the triple point and critical point respectively.

Under the operating conditions of modern engines hydrogen is injected and combusted at a supercritical state. Oxygen however may be either sub- or supercritical depending on the chamber pressure of the engine. The current work focuses on experiments and test cases above the supercritical pressure of oxygen. Cryogenic liquid oxygen, known as LOx, is trans-critically injected into a combustor operating at a pressure above the supercritical pressure of oxygen. It is worth noting that the critical pressure of a mixture may be higher than that of the pure components such that a phase transition may occur at pressures above the critical pressures of the pure species involved. The properties of supercritical fluids and pseudo-boiling phenomena are therefore of particular importance to the current work.

2.2 Combustion Chamber Processes

Rocket engine combustion chambers burn propellants to produce hot combustion gases that are expelled through a nozzle in order to generate thrust. To produce sufficient thrust to launch a rocket into orbit combustion chambers must handle immense amounts of energy released from combustion, all while being designed with minimal structural mass to meet the rigorous demands of space flight. Understanding the processes in rocket engine combustion chambers is necessary to design rocket engine combustors that meet these demands while operating reliably. This has motivated a concerted research effort to further the understanding of the processes that occur within the rocket engine combustion chambers.

The main processes that occur during combustion of liquid propellants are injection, atomisation, vaporisation, mixing, and combustion. Each of the aforementioned processes are described in the following subsections.

2.2.1 Injection

Injection refers to how the propellants are introduced into the chamber. Injected propellants are usually fed into a manifold which distributes the flow amongst the individual injection elements. The elements direct the propellants into the chamber and can be designed to control how the propellant streams meet and interact. Various types of injection elements have been designed and experimented with, however coaxial injection elements have become the most common for oxygen-hydrogen combustion [10]. A coaxial injection element features a central tube in which the oxidiser flows, surrounded by an annulus

through which the fuel is injected. The tube separating the oxygen and hydrogen streams is referred to as the LOx post. In this configuration both propellants enter the chamber in parallel with the fuel stream surrounding the oxidiser stream.

The design of the injection system is the main method for controlling all subsequent processes. A number of parameters have been defined to characterise injection regimes and the resulting processes. These parameters and their influence on combustion instabilities are described later in Section 2.3.3.

2.2.2 Atomisation

Liquid propellants enter the chamber as a stream of fluid before breaking down, or "atomising" into smaller structures such as droplets or threads. As the liquid stream breaks down its exposed surface area increases, accelerating other processes such as vaporization and mixing. Therefore atomization has a strong influence on all subsequent combustion processes. Zaller and Klem [168] explain that liquid atomization in coaxial injector sprays is primarily due to the aerodynamic shear of the high-velocity gas stream on the surface of the liquid jet.

The shear stresses acting on the surface of the liquid jet work to overcome the surface tension and viscous forces that hold the liquid stream together. Primary atomisation occurs as ligaments and droplets are shed from the jet surface and mix with the surrounding flow. These ligaments and droplets may then undergo secondary atomisation as they are subjected to the same surface shear forces or through collisions with other separated structures. Through these mechanisms the liquid jet breaks up into finer and finer structures before being fully vaporised.

Sirignano et al. [141] note that below the critical pressure surface tension tends to keep droplets spherical and the droplets can be clearly distinguished from the surrounding gas. However near-supercritical or supercritical pressures the reduced surface tension permits non-spherical shapes and it is no longer possible to distinguish between the two states at the interface. As the surface tension vanishes at supercritical pressures, so do the ligaments and droplets. The process can be described as turbulent mixing rather than break-up. This was first shown by Newman and Brzustowski [87]. Mayer and Tamura [80] identified the same phenomenon experimentally for rocket combustor conditions, observing that the boundary of the liquid jet was not clearly defined and the flame in the shear layer was a turbulent diffusion flame.

2.2.3 Vaporisation

Vaporisation is the process by which liquid propellants evaporate due to heating from nearby combustion processes and enter a gaseous state. Heat is transferred to the liquid via convection from the surrounding high temperature gaseous environment. As surface tension and the heat of vaporisation become negligible at supercritical conditions, the fluid does not form into droplets but separates as fluid structures.

As previously discussed in Section 2.1.1, as the dense liquid stream is heated at supercritical pressures pseudo-boiling occurs. The change in fluid properties over this process should be considered when describing or modelling the flow.

2.2.4 Mixing

Once the propellants are in a gaseous state the gases must mix so that propellant species can interact and chemical reactions can occur. The main methods by which propellants mix is by convection and diffusion. Convection occurs when one propellant stream flows into another. In the case of impinging injectors different propellant streams are pointed

directly into one another. For coaxial and other elements where propellant streams are injected in parallel, turbulence and shear stresses between different propellant streams drives propellant mixing.

In the current work a coaxial oxygen-hydrogen flame is considered. The oxygen and hydrogen meet in the shear layer between the parallel streams. Mayer and Smith [82] and Oefelein [94] suggest that the low gas densities encountered in the reaction zone between the oxygen and hydrogen propellant streams limit the significance of aerodynamic forces and produce a flame that is diffusion-rate limited.

2.2.5 Combustion

Combustion refers to the chemical reactions through which the propellant species are consumed to produce a mix of resulting combustion products. Combustion requires a mixture of propellant species with a suitable oxidiser to fuel ratio and sufficient energy to trigger a self sustaining reaction. An ignition system is used for oxygen hydrogen systems to produce an initial flame kernel which then ignites the surrounding propellants.

In the coaxial injection configuration considered in this work the flame is anchored by the recirculation zone at the LOx post tip. In this zone hot combustion products are mixed with fresh propellants entering the chamber. Detailed numerical studies by Oefelein and Yang [92] and Ribert et al. [115] have shown that combustion of coaxially injected oxygen and hydrogen streams is anchored at the LOx post tip and separates the oxygen and hydrogen streams.

2.3 Combustion Instabilities

When combustion and heat release rates fluctuate with amplitudes greater than the acceptable limits for the given combustion chamber system the combustion is classified as unstable. The fluctuations may produce pressure disturbances or cause combustion efficiency fluctuations that are either merely undesirable or catastrophic. Examples of combustion instabilities exist for a number of industrial burners where temporary flame quenching or extinction lead to a fluctuation of the heat release rate.

A particular type of instability, known as thermo-acoustic instability, is predominant in rocket engines. Thermo-acoustic instabilities refer to a coupling between acoustic and combustion processes that re-enforce one another and may become self-sustaining. In thermo-acoustic instabilities the acoustic disturbance may correspond to one of the natural frequencies of the propellant feed system, engine structure, or combustor volume. If the disturbance is not sufficiently damped it may resonate and its amplitude may continue to increase as it is supported by the unsteady combustion processes. The increasing acoustic disturbance in turn produces larger combustion and heat release fluctuations. This coupling may occur spontaneously by random combustor noise at the right frequencies and become self-sustaining. Thermo-acoustic instabilities are characterised by fluctuations of the combustion chamber pressure at distinct frequencies corresponding to the resonant acoustic phenomena.

Thermo-acoustic instabilities are not unique to liquid propellant rocket systems and have been observed in solid rocket motors and industrial gas turbine systems. There is considerable overlap in all thermo-acoustic combustion instability research, but due to the different propellant properties and combustion regimes in each field the research work has become very specialised. Thermo-acoustic instabilities are so predominant in rocket engines that, in the context of rocket engine combustion, the term combustion instability has become synonymous with thermo-acoustic instabilities. In the context of this thesis

the term combustion instability will hereon be used to refer specifically to thermo-acoustic instabilities in rocket engine combustion chambers.

In liquid rocket engines a significant amount of random combustion noise is always present. Rocket engine combustion is said to be 'smooth' if peak-to-peak pressure fluctuations during steady operation do not exceed 5% of the mean chamber pressure [106]. If pressure fluctuations exceed this limit but are not periodic then combustion is referred to as 'rough'. Periodic fluctuations with amplitudes exceeding 5% of the mean chamber pressure are said to be unstable and evidence of combustion instability. Depending on the level of acoustic damping the disturbance may reach a limit cycle where the instability persists but its amplitude is bounded. If the level of acoustic damping is insufficient the amplitude of the disturbance may grow until it exceeds the limits of the engine leading to a catastrophic failure and loss of the rocket mission.

Liquid rocket engine combustion instabilities are categorised into Low Frequency (LF) and High Frequency (HF) instabilities based on the frequency of the acoustic disturbance. LF instabilities occur at frequencies below 1 kHz. At such frequencies the acoustic wavelength is longer than the chamber, and the disturbance usually corresponds to fluctuations in the propellant feed system. LF instability is often referred to as 'chugging' or 'buzzing' as the fluctuations in the feed system lead to fluctuations in the flow rate of propellant into the chamber causing it to 'chug' and create loud low frequency noise. A large pressure drop across the injection plane is typically employed to acoustically decouple the chamber from the feed system and prevent LF instabilities.

HF instabilities are the most troubling type of instability. At frequencies greater than 1 kHz the acoustic disturbance may correspond to one or more of the resonant modes of the combustion chamber volume. The acoustic fluctuations disturb the flow field within the combustion chamber leading to a variety of problems. For example acoustic velocity fluctuations may disturb the boundary layer flow along the walls of the chamber which protects them from the flame and other hot combustion products. When the boundary layer is disturbed the heat flux to the walls of the chamber increases which can lead to structural damage or failure of the engine. To observe HF combustion instabilities instrumentation that can survive the conditions inside a rocket engine combustion chamber must be employed with high sampling rates. This tests the limits of available technology, ruling out a number of advanced diagnostic methods, and makes the identification and treatment of HF instabilities particularly challenging.

HF instabilities are understood to be caused by a coupling between acoustic and combustion processes. Acoustic processes refer to the acoustic pressure and velocity fluctuations that make up the acoustic field. The combustion processes refer to the combustion chamber processes involved in releasing energy for propellants as described in Section 2.2. How these processes interact to produce and support HF combustion instabilities is not yet fully understood. Until the coupling mechanisms are identified it will not be clear which acoustic disturbances, components, or operating conditions may potentially lead to an instability. This poses a significant challenge to rocket engine designers and necessitates extensive ground testing of new engine designs to ensure stable operation.

Oschwald and Knapp [96] explain that although the basic mechanisms leading to instabilities are known, reliable prediction of stability behaviour is still not possible. Rocket chamber design with respect to stability remains partly reliant on trial and error and experimental stability verification is still a requirement in rocket engine qualification.

If combustion instabilities are detected during testing then they may be treated by a variety of methods. These methods typically involve modifying the chamber to change its resonant frequencies and response to acoustic disturbances. The most popular of these is to divide the internal volume of the chamber by introducing small walls, known as

acoustic baffles, that are positioned to inhibit the acoustic modes that cause the instability. Alternatively, small tuned acoustic cavities designed to damp the acoustic disturbances at the frequencies of interest are employed. Implementing either of these solutions if an instability has been discovered during testing may be difficult or impossible. Both methods also result in additional weight and some loss of performance. Furthermore, the modified engine will most likely need to undergo additional testing to ensure the new "improved" engine is free from instabilities. Testing and retroactively solving combustion instability problems therefore increases both cost and time to market, representing a large part of the risk associated with the development of new engines.

Culick [16] explains that the goal of combustion instability research is to provide a sound basis for reducing the amount of experimentation and testing required. Further understanding of HF combustion instability phenomena may allow for the stability of new engine designs to be predicted prior to construction of the engine. This would reduce the need for experimental stability verification as well as the risk and costs associated with the design of new rocket engine combustion chambers. While analytical solutions can provide general understanding of the processes at hand, numerical analysis is necessary due to the complexity and interdependencies of these processes.

Combustion instability models face various limitations, from the limited understanding of the physical processes involved to the computational power required to complete the analysis. Smith et al [145] note that the utility of CFD to accurately represent multiphase combustion dynamics is limited by the complexity of the physical sub models and the availability of computational resources. Yu et. al. [167] explain that although numerical simulations, enabled by increasing computational power, have rendered detailed studies more feasible, first principles modelling of combustion instabilities remains intractable because of the complex coupling of turbulent flow, combustion, multiple phases, and acoustics. Current research on HF combustion instabilities focusses on identifying and quantifying how acoustic and combustion processes interact to drive combustion instabilities, in order to inform and validate the sub-models and tools needed to predict instability phenomena.

2.3.1 Combustion Instabilities Research History

Evidence of combustion instability phenomena was first noticed in the early 1930s during experiments on the engine for the third Mirak rocket by the German Society for Space Travel (Verein für Raumschifffahrt) [120]. Due to the lack of diagnostic technology at the time, limited insight was possible but a "machine gun staccato" sound was noticed, presumably produced by the engine as it went unstable. Limited insight into the problem was possible with the technology available at the time. Studying the large amplitude high frequency pressure oscillations was not possible until high frequency pressure sensors and diagnostics became widely available and affordable.

Since the 1930s a variety of countries and organisations have been conducting combustion instability research, usually in support of their space programs. As the size of launch vehicles increased, larger propulsion systems were required and combustion instabilities became a greater concern. Research was conducted independently by both the United States of America and Russia during the space race. As their own space programs developed, Europe and Japan have also become leaders in the field.

Culick [16] summarises the history of combustion instability research in the United States of America from the 1930s to 1995. Research into the problem began in the 1940s as part of the development of small tactical solid rocket motors. More significant progress was achieved in the post world war 2 era during the development of larger intercontinental ballistic missiles. A significant body of work was done during the Apollo program in the 1960s as more powerful propulsion systems were needed.

Of note is the development of the F1 engine, developed for the Apollo missions, in which large combustion instability problems were encountered during ground testing [91]. Bombing tests were used to assess the stability of different engine designs. When the problem could not be hastily rectified "Project First" was commenced. Project First studied every component of the engine and reviewed previous instability problems in the Redstone, Atlas, H-1 and E-1 programs to try and find a solution [165]. Oefelein and Yang [91] state that over 2000 tests of the F-1 engine were conducted before a baffle configuration was found to make the engine sufficiently stable for the Apollo program.

After the space shuttle main engine was developed in the 1970s, there was not a great deal of interest in combustion instabilities in the USA until the time came to develop another large propulsion system for the proposed advanced launch system (ALS) in the 1980s. The ALS was subsequently cancelled, but a steady combustion instability research effort has continued in the states. Research groups that continue to investigate combustion instabilities include the Air Force Research Laboratory (AFRL), the Georgia Institute of Technology, and Purdue University.

Russia encountered combustion instabilities during the development of large thrust chambers in the late 1940s and early 1950s [150]. Combustion instabilities have subsequently caused problems during the development of several Russian engines [122]. Russia's combustion instability research let it devise various methods for overcoming instability problems. For example, it was realised that some instability phenomena was more likely to happen in larger engines. By using four smaller engines with an equivalent thrust troublesome vibrations could be overcome. This is part of the reason several Russian liquid propellant engines feature clusters of small thrust chambers [150].

In Europe, combustion instability research activities have been conducted since the early 1980s in support of the Ariane program. The majority of the work is conducted in France and Germany, the two countries most involved in the development and testing of large liquid rocket propulsion systems. In France the National Centre for Scientific Research (CNRS), the National Aerospace Laboratory (ONERA), and CentraleSupélec (a university) all conduct combustion instability research. In Germany combustion instability research is undertaken by the German Aerospace Center (DLR) and the Technical University of Munich (TUM). Airbus-Safran launchers also conduct combustion instability research.

In Japan the Japanese Aerospace Exploration Agency (JAXA) manages combustion instability research in support of the Japanese space program. They have encountered problems with instabilities in the past and have more recently been motivated by the development of the LE-X booster rocket engine for their next generation launch vehicle [71].

Interest in combustion instability research peaks during the development of new rocket engines, especially if instability problems are discovered. In recent times a relatively consistent level of research into combustion instability phenomena has been maintained. This has been assisted by recent technological advances, dedicated combustion instability experiments on new experimental test facilities, and the increased availability of computational power and resources.

2.3.2 Theoretical background

Since its discovery there have been numerous studies into the mechanisms driving combustion instabilities. Simplified models to describe instabilities were developed based on experimental observations. Theories and criteria were developed for quantifying and comparing the relative contribution of different processes to drive combustion instabilities. This section summarises the main combustion instability theories relevant to the current work.

The Rayleigh Criterion

The Rayleigh criterion was first proposed by Lord Rayleigh in 1878 [111]. It states:

> "*If heat be periodically communicated to, and abstracted from, a mass of air vibrating (for example) in a cylinder bounded by a piston, the effect produced will depend upon the phase of the vibration at which the transfer of heat takes place. If heat be given to the air at the moment of greatest condensation, or be taken from it at the moment of the greatest rarefaction, the vibration is encouraged. On the other hand, if heat be given at the moment of greatest rarefaction, or abstracted at the moment of greatest condensation, the vibration is discouraged.*"

This criterion defines how a chamber can become unstable if heat is transferred to or from an acoustic disturbance at the appropriate time. Specifically that heat should be transferred to the acoustic field in phase with the local pressure disturbance. The Rayleigh criterion was verified experimentally by Putnam and Dennis [107, 109] who observed heat release fluctuations in phase with the local acoustic disturbance in a combustor tube setup. Putnam [108] stated the Rayleigh Criterion mathematically as:

$$\int P'Q'dt > 0, \tag{2.2}$$

where P' is the acoustic pressure disturbance and Q' is the heat release fluctuation. Equation 2.2 is not sufficient to describe if a combustor is stable or unstable, as the growth of the acoustic disturbance must overcome acoustic damping and other dissipative forces. Zinn [169] extended the Rayleigh criterion while studying pulse-combustion to address this issue.

$$\int_V \int_{T_s} P'(x,t)Q'(x,t)dtdv \geq \int_V \int_{T_s} \sum_i L_i(x,t)dtdv \tag{2.3}$$

where V is the volume being considered, T_s is the period of the fluctuation, x is the spatial coordinate, and each L_i are damping processes acting to dissipate energy from the instability.

The Rayleigh criterion has been used by various researchers to identify fluctuations that contribute to combustion instabilities. Recent examples include analysis of BKH optical data by Hardi et al. [49, 50] and analysis of unsteady CFD results by Hakim et al. [41] in which Rayleigh source terms were computed to identify regions with fluctuations in phase with the local acoustic disturbance.

Time-lag Theory

The fluctuation of heat release is dependant on the time scales of the combustion processes, and a consequence of the Rayleigh criterion is that similar acoustic time-scales are needed in order for said processes to couple. The time scales of combustion processes have therefore been investigated to assess the potential for coupling with acoustic disturbances. Time-lag theory uses a time delay factor to describe the delay between an acoustic process and the resulting fluctuation in heat release without having to describe the process in detail.

Of note is the $n - \tau$ model proposed by Crocco [15]. The $n - \tau$ model used two parameters, an amplification factor n and a time delay factor τ to describe instabilities. This approach was later refined by Crocco and Cheng [13] to include a sensitive time lag. The sensitive time lag improved upon earlier elements by dividing the total time lag into two parts. The first part is insensitive to the acoustic disturbance and is related to the phenomena shortly after injection. The second part is sensitive to the acoustic disturbance

and represents the effect of the acoustic disturbance on mixing, atomisation, vaporisation, and other processes.

Much of the initial research was focused on the time lag of processes associated with LF instability phenomena. Ivancic and Mayer [61] state that at the temperatures and pressures encountered in liquid propellant rocket engines oxygen-hydrogen flames reach chemical equilibrium within time scales of 1 μs and as turbulence length and time scales decrease downstream further opportunities for coupling arise. This is on order with the time scales of fine turbulent structures near the injection plane but is also much shorter than the acoustic time scales considered in the current work.

The time lag theories depend upon the time lag and amplification factor associated with each of the relevant processes being accurately known. The results of experiments and higher fidelity numerical models may be used to compute values for these factors that can be used in subsequent lower-order modelling approaches.

Response Factors

The orientation and location of an acoustic disturbance determines which components act locally upon the flame. Injection into a pressure antinode would subject the flame to pressure fluctuations with negligible acoustic velocity. Similarly injection into a velocity antinode would subject the flame to acoustic velocity fluctuations without an acoustic pressure disturbance. To quantify the degree of pressure and velocity coupling Heidmann and Weber [56] formulated a response factor, N, which quantifies the net response of a fluctuation in response to a given acoustic disturbance. The response factor represents the gain as a coupling between acoustic and heat release fluctuations, as defined by the Rayleigh Criterion, relative to the magnitude of the acoustic disturbance.

$$N = \frac{\int_V \int_{T_s} P'_N(x,t) Q'_N(x,t) dt dv}{\int_V \int_{T_s} [P'_N(x,t)]^2 dt dv} \tag{2.4}$$

where $P'_N = P'/P_{mean}$ and $Q'_N = Q'/Q_mean$ are non-dimensionalised by dividing by the mean value, so that N is non-dimensional.

The response factors have been applied in a number of studies to quantify the relative contribution of different fluctuations to combustion instability phenomena. As heat release cannot be measured experimentally the fluctuations in high-speed optical data are instead used as an indicator of heat release fluctuations. Examples include the work by Sliphorst [144] who computed response factors for velocity and pressure excitation of oxygen-methane combustion and Hardi et al. [49, 50] who applied the same method to BKH data. This analysis relied upon the reconstruction of the acoustic field, which involved fitting ideal 2D-eigenmode solutions to experimental dynamic pressure sensor data. It also assumed that the fluctuations in optical data were proportional to heat release fluctuations. Response factors are of particular interest in low order modelling approaches where, like the $n - \tau$ factors from time-lag theory, it is used as a simplified representation of the complex interaction between acoustic and combustion processes.

2.3.3 Influence of Injection Parameters

All combustion chamber processes occur at once and are heavily dependant upon one another. However there is limited opportunity to effect combustion processes after injection has occurred. Therefore injector design and the choice of injection conditions are key parameters which are used to control the overall behaviour of the rocket engine. Much of the earlier work was limited by the experimental capabilities available at the time and focused on characterisation of different design parameters and their effect on instabilities.

A number of non-dimensional numbers have been defined and used to categorise injection regimes. These parameters and their influence on combustion instabilities are described in the following paragraphs.

Injection Temperature

The propellant injection temperature determines the state of the fluid. Investigations by Wanhainen et al. [156, 157, 158] studied the influence of hydrogen injection temperatures on combustion instabilities and found that instabilities became more prevalent at lower hydrogen injection temperatures. Wanhainen et al. performed experiments where the temperature of the injected hydrogen was ramped down until instabilites were encountered in order to define a hydrogen temperature stability boundary for the engine. Similar experiments where more recently conducted by Nunome et al. [89, 90] who encountered the same onset of instabilities at low hydrogen temperatures.

However, recent experiments at the DLR by Gröning et al. [38] repeated hydrogen temperature ramping experiments for a temperature range between 40 and 135 K. Gröning et al. found, contrary to the previously published work, that the engine was stable for low hydrogen temperatures, but a transverse instability was excited when injecting with a hydrogen temperature of 100 K. Gröning et al. found that the hydrogen injection temperature changed the speed of sound distribution in the chamber and resulting resonant mode frequencies. Therefore low injection temperatures do not guarantee combustion instabilities will occur, but may affect the resulting acoustic field and disturbance leading to an instability.

Injection Velocity and Momentum Flux Ratios

The injection velocity ratio, VR, and momentum flux ratio, J, are design parameters that have been studied to characterise the injection regime. The velocity ratio describes the relative velocity of the fuel and oxidiser streams.

$$VR = \frac{v_f}{v_{ox}} \tag{2.5}$$

where the subscripts f and ox denotes the fuel and oxidiser respectively.

The momentum flux ratio denotes the relative momentum of the propellants. It is similar to the velocity ratio but also considers the mass of each propellant stream.

$$J = \frac{\rho_f v_f}{\rho_{ox} v_{ox}} \tag{2.6}$$

where ρ denotes the density of the fluid.

Values of the velocity and momentum flux ratios equal to unity indicate that the fuel and oxidiser streams are injected with the same velocity and/or momentum. Values other than unity indicate the difference and the significance of shear stresses at the interface between the streams. It was discovered [52] that a higher axial velocity ratio increased the stability of an engine due to larger shear forcing which control mixing and breakup of the liquid propellant stream.

The Reynolds and Weber Numbers

The Reynolds number is the ratio between inertial and viscous forces and is defined as

$$Re = \frac{\rho v D_0}{\mu} \tag{2.7}$$

where ρ is the density, v is the velocity, D_0 is a characteristic length usually taken as the jet diameter, and μ is the viscosity. The Reynolds number is used to characterises the turbulence state of a flow.

The Weber number describes the ratio between inertial and surface tension forces and is defined as

$$We_L = \frac{\rho v^2 D_0}{\sigma} \tag{2.8}$$

where σ is the surface tension of the liquid.

For coaxial injection of a liquid surrounded by a gaseous propellant the main parameters controlling jet break up have been identified to be the Reynolds number of the liquid stream, Re_L, and the aerodynamic Weber number. The aerodynamic Weber number is defined as:

$$We = \frac{\rho_G D_0 |v_G - v_L|^2}{\sigma} \tag{2.9}$$

where the subscripts G and L represent the gaseous and liquid stream, respectively. The aerodynamic Weber number is the ratio of the momentum difference between the gaseous and liquid streams to the surface tension of the liquid. This project focuses on coaxial oxygen-hydrogen combustion. In this scenario the gaseous stream would correspond to the annular hydrogen injection and the liquid stream would be the central LOx jet.

Chigier and Rietz [11] described and mapped four different jet break up regimes based on the liquid Reynolds and aerodynamic Weber numbers. Hardi [49] states that the liquid Reynolds and aerodynamic Weber numbers of BKH experiments correspond to the fiber-type break up regime. In this regime the jet is propagates steadily with small wave-like surface instabilities. Liquid fibres form from surface instabilities that then separate from the liquid core and break up into individual droplets. Hardi [49] notes that liquid fibers are not visible in the BKH high-speed optical images, indicating that such structures may be consumed rapidly in the presence of a flame.

The Strouhal Number

The Strouhal number is a dimensionless number used to describe oscillating flow. It represents the ratio of the convective time scale to that of a characteristic fluctuation such as vortex shedding. It is defined as:

$$St = \frac{fL}{v} \tag{2.10}$$

where L is a characteristic length, v is the flow velocity, and f is the frequency of the fluctuation.

In combustion instability analysis the Strouhal number is used to relate the convective and acoustic time scales. To study the response of coaxial oxygen-hydrogen to an acoustic disturbance the characteristic length is taken as the LOx jet diameter and the LOx injection velocity is used. The acoustic time scale is represented by the frequency of the acoustic disturbance.

Small or large values of the strouhal number indicate a difference in the convective and acoustic timescales limiting how effectively they couple. It has been shown that acoustic processes interact more strongly with a jet for strouhal numbers between 0.2 and 0.64 [40]. Various numerical studies [129, 42] have looked at the response of jets and coaxial flames to acoustic disturbances at different Strouhal numbers. Such studies are challenging experimentally as the frequency of the acoustic disturbance is dependant on the volume of the chamber which is not easily modified. A characteristic jet shedding frequency, referred to as the preferred mode, occurs at Strouhal numbers close to 0.3. Higher Strouhal numbers closer to unity indicate more rapid fluctuations that do not produce the same characteristic jet-flapping behaviour.

2.4 Acoustics in Combustion Chambers

HF combustion instabilities occur due to a coupling between combustion processes and the resonant modes of the combustion chamber volume. The resonant modes are determined by the internal volume of the chamber, the acoustic properties of the medium, and the acoustic conditions at the chamber boundaries. While only the acoustic disturbance local to a flame may significantly act upon it, to determine the frequency and nature of the local disturbance it is necessary to consider the entire chamber system. In this section mathematical methods for predicting and describing resonant modes and acoustic phenomena are introduced as a basis for later discussion of the models and results presented in this thesis.

Much of combustion instability research focuses on linear acoustics. The justification for this is that the initial small amplitude acoustic disturbance is linear and characterising the linear response of a system may indicate if it will remain stable. Other research, for example by Flando et al. [26, 25] and Jacob [64], focus on non-linear disturbances. The experimental data examined in this thesis is reasonably described by linear acoustic theory and does not exhibit wave-steepening or other phenomena indicative of non-linear acoustics. Therefore non-linear acoustic behaviour is not considered in the current work.

2.4.1 Acoustic Modes

The resonant acoustic modes of simple volumes can be described analytically using the wave equation. A derivation of the wave equation and its application to a cylindrical geometry has been published by Zucrow and Hoffman [173]. A brief summary of the main steps and results are reproduced here.

Beginning with the fundamental equations:
The continuity equation,

$$\frac{\partial \rho}{\partial t} + \nabla \bullet (\rho \mathbf{V}) = 0 \tag{2.11}$$

the momentum equation,

$$\rho \frac{D\mathbf{V}}{Dt} + \nabla p = 0 \tag{2.12}$$

and the speed of sound equation,

$$\frac{Dp}{Dt} - a^2 \frac{D\rho}{Dt} = 0 \tag{2.13}$$

and assuming small perturbations, such that $p = p_\infty + p'$ and $\rho = \rho_\infty + \rho'$ where p_∞ and ρ_∞ are the free stream pressure and density respectively, while p' and ρ' are the fluctuations about the free stream value. $\mathbf{V}$ is the velocity of the gas and a is the speed of sound in the medium.

The general form of the wave equation can be derived.

$$\frac{\partial^2 p'}{\partial t^2} + a^2 \nabla p' = 0 \tag{2.14}$$

The wave equation assumes the following:

1. The amplitude of disturbances are of a sufficiently small scale.

2. The medium through which the acoustic disturbance is travelling is uniform and quiescent.

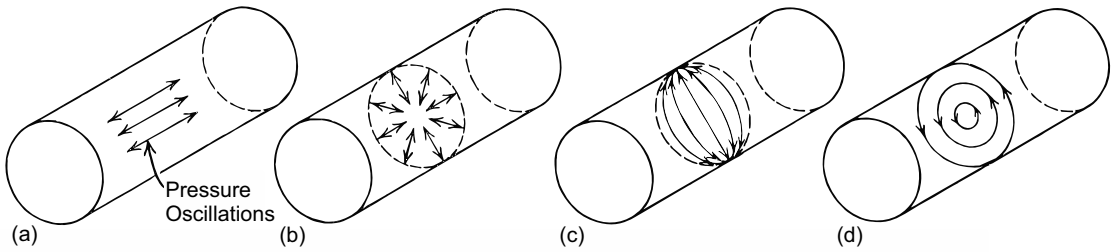

Figure 2.4.1: Acoustic mode orientation for a cylindrical geometry. Figure from Zucrow and Hoffman [173] (a) longitudinal. (b) radial. (c) standing tangential. (d) travelling tangential.

The first assumption deals with the derivation of the wave equation which neglects second order terms, making the equation invalid when large amplitude waves producing non-linear disturbances are present. The second assumption refers to the speed of sound, a, which is assumed to be constant across the medium.

Solutions to Equation 2.14 for different geometries can be determined analytically. For a cylindrical geometry defined in cylindrical coordinates r, θ, and z, and applying separation of variables the solutions to the wave equation given appropriate boundary conditions are of the form:

$$p'(r,\theta,z,t) = \acute{A} J_n\left(\frac{\pi\alpha_{mn} r}{R_0}\right)[\acute{B}e^{jn\theta} + \acute{C}e^{-jn\theta}]\cos\left(\frac{\pi q z}{L}\right)\cos(\omega t + \epsilon), \tag{2.15}$$

where L and R_0 are the length and radius of the geometry respectively, and $\acute{A}$,$\acute{B}$,$\acute{C}$, and ϵ are constants of integration and depend on the particular solution of the problem. α_{mn} is the root of the following equation involving the Bessel function of order n, J_n.

$$\frac{\partial J_n(\pi\alpha_{mn})}{\partial r} = 0 \tag{2.16}$$

Figure 2.4.1 shows the orientation of the mode shapes for each dimension of a cylindrical chamber. Mode shapes are conventionally labelled after the dimension or dimensions that are oscillating during the mode. In cylindrical geometries the dimensions are labelled longitudinal, tangential or transverse, and radial as illustrated in Figure 2.4.1. m, n, and q in Equation 2.15 are the wave numbers in the radial, tangential, and longitudinal directions, respectively. The different mode shapes are designated by their wave numbers as (m,n,q) modes.

Each mode shape corresponds to a different frequency within the chamber. For the proposed solution in Equation 2.15, the frequency at which the (m,n,q) mode oscillates can be calculated via:

$$f_{(m,n,q)} = \frac{a_\infty}{2}\sqrt{\left(\frac{\alpha_{mn}}{R_0}\right)^2 + \left(\frac{q}{L}\right)^2}. \tag{2.17}$$

In reality, waves at a range of frequencies can exist simultaneously. Hence the complete solution is the sum of the pressures for each of the individual excited modes.

The same technique for a cylindrical geometry can be applied to a rectangular geometry to produce the general solution:

$$p'(x,y,z,t) = \acute{A}\cos\left(\frac{\pi m x}{X}\right)\cos\left(\frac{\pi n y}{Y}\right)\cos\left(\frac{\pi q z}{Z}\right)\cos(\omega t + \epsilon). \tag{2.18}$$

where X, Y, and Z are the dimensions of the rectangular volume in cartesian coordinates and m, n and q are now the wave numbers in the x, y, and z axes respectively. Similarly the frequencies for each mode in a rectangular volume can be calculated using:

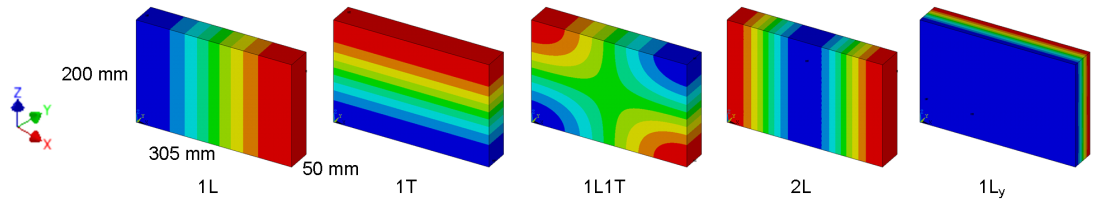

Figure 2.4.2: Acoustic mode pressure distributions for a simple rectangular volume [51].

$$f_{(m,n,q)} = \frac{a_\infty}{2}\sqrt{\left(\frac{m}{X}\right)^2 + \left(\frac{n}{Y}\right)^2 + \left(\frac{q}{Z}\right)^2}. \tag{2.19}$$

The first few modes for a rectangular volume are shown in Figure 2.4.2. The modes are denoted by the wave numbers and the corresponding letter referencing their orientation. For the rectangular geometry shown L represents the longitudinal direction, T the transverse, and L_y the horizontal transverse direction.

While analytical solutions to the wave equations can be determined for simple geometries, complex geometries with non-symmetric features and combustion processes, acoustic damping, and acoustic losses from the nozzle and other components modify the acoustic field so that it may only approximate the analytical solution. Such complex geometries are generally solved using numerical methods that solve the wave equation on a representative numerical domain with appropriate boundary conditions.

2.4.2 Complex Acoustic Notation

Complex notation is used to describe the amplitude, phase, frequency, and damping of an acoustic fluctuation. This section explains how complex valued acoustic properties are employed to describe acoustic phenomena. Complex acoustic notation is used extensively throughout the later chapters of this thesis to describe acoustic and optical intensity fluctuations.

An acoustic pressure and/or velocity disturbance fluctuating inside a given volume is described by the equation:

$$\hat{A}(x)\, e^{i\hat{\omega}t}, \tag{2.20}$$

or

$$\hat{A}(x)(cos(\hat{\omega}t) + isin(\hat{\omega}t)). \tag{2.21}$$

where $\hat{A}$ is a complex amplitude which is dependant on the local spatial coordinates, $\hat{\omega}$ is a complex angular frequency, and t is time. When the complex angular frequency $\hat{\omega}$ is split into its real ω_R and imaginary ω_I components Equation 2.20 has the following form:

$$\hat{A}(x)\, e^{i(\omega_R + i\omega_I)t},$$

or

$$\hat{A}(x)\, e^{i\omega_R t}\, e^{-\omega_I t}. \tag{2.22}$$

From Equation 2.22 it can be seen that the imaginary part of the complex frequency produces a coefficient analogous to an exponential damping function $e^{-\alpha t}$ where α is the damping rate coefficient. The imaginary part of the complex frequency can therefore be interpreted as the damping rate of the acoustic mode. Positive values indicate the mode is damped, while negative values indicate amplification or growth of the disturbance.

The other exponential coefficient of Equation 2.22, $e^{i\omega_R t}$, represents a complex function that traces the complex unit circle in a counter clockwise direction with frequency $f = \omega_R/2\pi$. The product $\hat{A}(x)\, e^{i\omega_R t}$ represents a complex amplitude rotating around the complex plane. The instantaneous physical amplitude of the fluctuation is the the real part of the complex-valued function.

Figure 2.4.3 shows two examples of a complex acoustic fluctuation for different values of $\hat{A}$. When the complex amplitude is a real number, i.e. $\hat{A} = 1$ as in Figure 2.4.3a, then the fluctuation in the real plane has a maximum amplitude of 1 and starts with a phase angle of 0. When $\hat{A} = \frac{1}{2} + i\frac{\sqrt{3}}{2}$, as in Figure 2.4.3b, the fluctuation in the real plane has an amplitude equal to the absolute value of $\hat{A}$ and starts with a phase angle equal to that of $\hat{A}$. The complex amplitude $\hat{A}(x)$ varies spatially and describes both the amplitude and phase of the disturbance at its associated frequency at each point in the field.

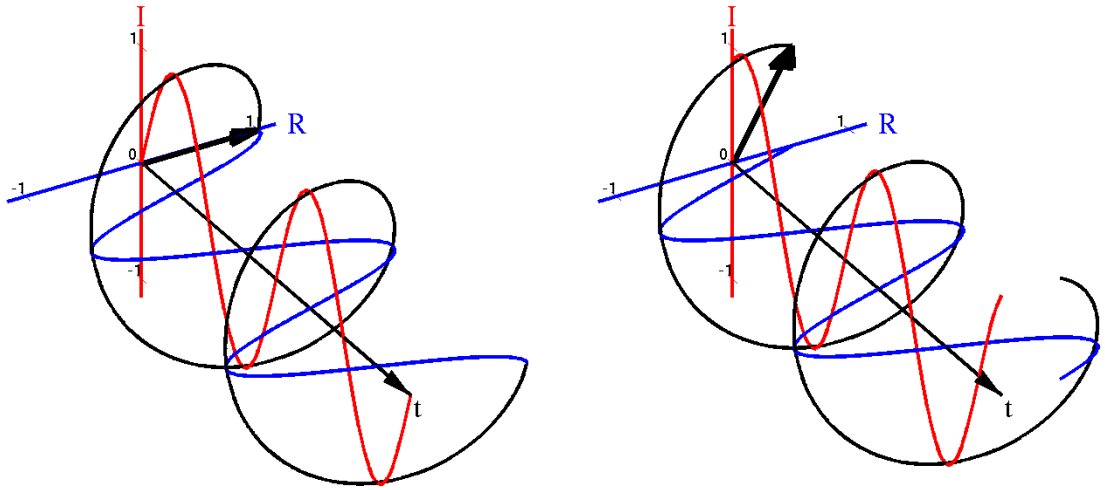

(a) $\hat{A} = 1$ (b) $\hat{A} = \frac{1}{2} + i\frac{\sqrt{3}}{2}$

Figure 2.4.3: Acoustic fluctuations for different complex amplitudes. Black: complex value at time t, Blue: real component projected onto the real plane, Red: imaginary component projected onto the complex plane.

2.4.3 Acoustic Damping and Boundary Conditions

For an instability to occur the acoustic energy being transferred to the acoustic mode must surpass the energy lost from inherent acoustic damping processes. The three main acoustic damping processes described by Zinn and Lieuwen [171] are:

1. transfer of acoustic energy to vortical or entropy disturbances through viscous and heat transfer processes, respectively,

2. convection and or radiation of acoustic energy out of the system, and

3. transfer of energy between acoustic modes.

The first process of energy transfer by turbulence and heat transfer is poorly understood. Oschwald et al. [95] explain that the effects of vortex generation and turbulent dissipation are used in the action of acoustic absorbers. However the tuning of acoustic absorbers is challenging due to our limited ability to control these processes in a changing acoustic environment. The third process involving transfer of energy between acoustic modes is understood to become more prevalent at high acoustic amplitudes leading to wave steepening and non-linear behaviour.

The second process, involving convection or radiation of acoustic energy, is of more direct interest. The resonant modes of the acoustic volume depend on the boundary conditions at the edges of the domain. The understanding the acoustic response of the chamber boundaries is therefore necessary in order to define boundary conditions for numerical

models and predict the resonant modes. Different nozzle and feed systems are characterised by their effective damping and contributing to instabilities. Early investigations[52] found that the nozzle contraction ratio had a strong effect on longitudinal mode instabilities. For linear acoustic problems the transmission of acoustic energy across boundaries is represented by specifying an acoustic impedance or reflectance at the boundary.

Acoustic impedance is analogous to electrical impedance and describes to what degree acoustic propagation is impeded by a flow medium. Acoustic impedance is defined as

$$Z = \frac{p'}{v'} \tag{2.23}$$

where p' and v' are the fluctuating acoustic pressure and velocity, respectively. The impedance of a medium is frequency dependant and can be interpreted as the magnitude of the acoustic pressure fluctuation that is generated by a given vibration of the medium at a specific frequency. The specific impedance z is more often employed.

$$z = \frac{Z}{\rho a} \tag{2.24}$$

A complex impedance may be used to describe the phase change of the reflected acoustic disturbance at the boundary surface. Methods for determining the impedance of surfaces using impedance tube experiments are well established. As the impedance of a boundary or medium is frequency dependant, extensive testing to determine the impedance for all frequencies of interest may be required in order to characterise a system.

Acoustic reflection represents the ratio of the incoming and reflected acoustic disturbance from a boundary. If the incoming wave has amplitude A^+ and the reflected wave has amplitude A^-, then the reflection coefficient R, is computed as:

$$R = \frac{A^-}{A^+}. \tag{2.25}$$

The reflection coefficient is related to the impedance by:

$$R = \frac{z+1}{z-1}. \tag{2.26}$$

The acoustic properties of different boundary conditions are characterised by their acoustic impedance or reflection coefficient. For example, solid boundaries that reflect acoustic disturbances perfectly are prescribed a reflection coefficient equal to 1 and an impedance of ∞.

2.5 Combustion Instability Experiments

A number of dedicated combustor experiments have been developed and employed for studying combustion instability phenomena. The combustors are designed to be robust and accommodate various instrumentation needed to observe both acoustic and combustion processes which would not be practical in a full scale engine. The combustion instability data collected from these experiments consists of high frequency dynamic pressure sensor data to characterise the acoustic disturbance and optical data to observe the flame response.

BKH, which is the focus of this project, is one such combustion instability experiment. Other combustors that share similar features and modes of operation or produce datasets that can be analysed in a manner similar to results from BKH experiments are also discussed in this section. The experiments are divided into two categories: externally excited

Table 2.1: Comparison of different combustion instability experiments.

Combustor	Operator	Fuel	Oxidiser	Operating point
Externally Excited				
BKH	DLR	Hydrogen	Oxygen	Sub- & Supercritical
CRC	DLR	Hydrogen or Methane	Oxygen	Subcritical
MIC	ONERA	Hydrogen	Oxygen	Subcritical
MIC-VHAM	ONERA	Methane	Oxygen	Sub- & Supercritical
Naturally Excited				
BKD	DLR	Hydrogen	Oxygen	Supercritical
CVRC	Purdue	Methane or JP-8	Decomposed H_2O_2	Subcritical
TIC	Purdue	Methane or JP-8	Decomposed H_2O_2	Subcritical

experiments that use an acoustic excitation system to impose an acoustic disturbance, and naturally excited experiments which exhibit spontaneously occurring instabilities. Table 2.1 summarises the propellants and operating points investigated by each combustor experiment. BKH is unique as it is the only externally excited combustor that operates with oxygen and hydrogen propellants at supercritical pressures.

2.5.1 Externally Excited Experiments

Externally excited combustion instability experiments employ acoustic excitation systems to impose a disturbance at a controlled frequency. While electronic speakers have been employed for cold flow investigations of mixing and jet breakup at supercritical pressures [132] they have not been able to match the high amplitudes achieved with mechanical systems. An approach first employed by Lecourt and Foucuad [73] using a toothed exciter wheel to periodically block the flow exiting one or more nozzles of the chamber has become common. Each of the externally excited combustion instability experiments discussed in this section employ a nozzle and exciter-wheel acoustic excitation system.

BKH

BKH (*German: Brennkammer H*) is an experimental combustion chamber developed and operated by the DLR Institute of Space Propulsion in Lampoldshausen, Germany. BKH is used to observe the response of a cluster of coaxial injection elements to an acoustic disturbance which is imposed on the chamber using an external excitation system. The acoustic field is resolved using a distribution of dynamic pressure sensors surface-mounted on the chamber walls, while the flame response is observed by capturing high-speed images of the flame zone through windows in the side of the chamber. BKH diagnostics and experiments are discussed in further detail in Section 2.6.

Hardi [49] conducted the first BKH experiments and used BKH results to investigate the acoustic response of the combustion chamber, the breakup of the LOx core, and the flame response to longitudinal and transverse acoustic excitation. Webster [159] conducted additional BKH experiments to further characterise the response and acoustic dissipation at different operating points and with different injection conditions. The relevant methods and results from this earlier work are summarised in the following paragraphs.

Hardi et al. [51, 49] first characterised the acoustic response of the BKH chamber using the distributed dynamic pressure sensor data to identify the resonant modes. The resonant mode distributions were then predicted by computing the acoustic eigenmodes of the chamber volume assuming a uniform acoustic property distribution. Hardi et al. [50, 49] continued to use acoustic eigenmodes scaled to dynamic pressure sensor data in order to compare the local acoustic disturbance with the observed flame response. Webster [159] investigated the acoustic damping of BKH using a modified sector wheel to impose non-continuous acoustic excitation. Webster found that the damping rates varied considerably between cold and hot-flow conditions, highlighting the need to investigate instabilities at representative conditions.

Hardi et al. [45, 49] presented the first optical data results from the BKH combustor experiments. These were the first published results of optical datasets from externally forced oxygen-hydrogen combustion instability experiments at supercritical pressures. Hardi et al. [44, 49] investigated LOx jet break-up under transverse acoustic excitation using BKH high-speed shadowgraph data. The LOx core length was manually detected in shadowgraph images and was observed to retract towards the injection plane during transverse acoustic excitation. Analysis of instantaneous images was used to highlight shedding from the LOx core during normal operating while a steady length is observed once the core has retracted during acoustic excitation. Trends between the amplitude of acoustic excitation and the length of the LOx core were also identified. The analysis of instantaneous line-of-sight images by Hardi et al. allowed limited insight into the structure of the flame. The random turbulent structures also made it difficult to consistently define features and motion in the instantaneous images.

Hardi et al. [49, 50] also studied the flame response by comparing intensity fluctuations in optical datasets with the local acoustic disturbance determined by scaling an acoustic eigenmode distribution to a single dynamic pressure sensor signal. The flame response was computed by comparing the local acoustic disturbance predicted by the eigenmode solution with the optical intensity fluctuations at the time each frame of optical data was recorded. Through this analysis Hardi et al. were able to compute Rayleigh indices and response factors by integrating the results over multiple acoustic periods.

Hardi et al.[45] found that the longitudinal mode excitation did not deform the flame but produced intensity fluctuations at the excitation frequency. Hardi et al. identified that the peak OH* emission occurs during the peak local pressure disturbance resulting in a positive coupling with acoustic pressure fluctuations during 1L-mode excitation.

Hardi et al. [49, 50] observed the transport of the flame from one side of the chamber to the other during transverse mode excitation. Hardi [49] noted that many of the brightest fluctuations, especially during 1T mode excitation, were a result of the flame moving in and out of different window regions as it was being displaced by the acoustic velocity. Using methods to track the flame as it was displaced Hardi et al. [44] studied the OH* intensity fluctuations during transverse excitation. It was found that when a dynamic window is used to track and follow the displacement of the flame during transverse mode excitation then the peak OH* intensity also occurs during the peak pressure disturbance. Hardi et al. concluded, as had been previously described by Rey et al. [114], that the action of the transverse acoustic velocity was to transport the flame towards a positive pressure antinode thereby satisfying the Rayleigh criterion and supporting an instability. The flame response analysis was again limited by the insight available from the line-of-sight optical data.

Hardi [49] computed pixel-by-pixel cross correlations of the optical intensity fluctuations with the local acoustic disturbance to determine the phase difference between the two signals in an approach similar to Sliphorst [144]. The phase results were used to produce phase distributions showing regions in and out of phase with the acoustic disturbance. As

the eigenmode solution used to determine the local acoustic disturbance had no damping, a phase discontinuity existed at the nodal line of the eigenmode solution. Consequently the results were very dependant on the predicted position of the nodal line in the eigenmode solution.

CRC

The CRC (Common Research Chamber) is a flat disc combustion chamber with a single coaxial injection element jointly developed by DLR and ONERA. Knapp and Oschwald [70] and Knapp et al. [69] used the CRC data to investigate oxygen-hydrogen combustion response to acoustic excitation. Sliphorst et al. [143, 144] used the CRC data to study the breakup and distortion of a methane-oxygen flame.

The single injector is mounted on the circumference and injects LOx and gaseous hydrogen or methane propellants radially toward the center of the chamber volume at pressures up to 10 bar. The main nozzle is located in the center of one side of the disk so that the flow leaving the chamber exits perpendicularly to injection. A number of interchangeable modules for installing instrumentation are located around the circumference of the chamber. One of the modules can also be interchanged with a secondary nozzle and acoustic excitation system. Optical access windows in the sides of the chamber allowed access to the region directly downstream from injection.

Sliphorst et al. [143, 144] analysed CRC dynamic pressure sensor data and identified rotating transverse acoustic modes in the unexcited chamber. Sliphorst et al. [144, 143] and Knapp and Oschwald [70] found that the asymmetry created by the excitation system fixed the orientation of the acoustic field when the chamber was externally excited.

Knapp et al. [69] and Sliphorst [144] fitted eigenmode solutions to the dynamic pressure sensor data from CRC experiments to reconstruct the acoustic field. The flame response was recorded using high-speed shadowgraph and OH* imaging through the optical access windows. The deformation of the spray at subcritical pressures was observed. Pressure and velocity response factors were computed by comparing the local OH* intensity fluctuations with the reconstructed local acoustic disturbance. The fitted eigenmode solution used to represent the acoustic disturbance also assumed a perfectly sinusoidal disturbance in the chamber.

Knapp et al. [69] identified a positive coupling between acoustic pressure and OH* intensity fluctuations. Sliphorst computed the relative phase between acoustic pressure and OH* intensity fluctuations by cross-correlating the intensity fluctuations with the local acoustic disturbance. The OH* images were captured using a window as one side of the chamber allowing the entire chamber volume to be viewed. The results were used to compute response factors for the chamber volume which showed a positive response factor during transverse velocity excitation. However, Sliphorst [144] noted that the low acoustic amplitudes reached in the CRC meant that the calculated response factors were not always statistically significant. A similar method was later applied to BKH by Hardi [49].

Sliphorst [144] analysed shadowgraph imaging to study the oxygen jet including its intact core length and flame spreading angle during acoustic excitation. The CRC contains only a single element and has no secondary injection so clear shadowgraph images were produced which, when binarised, could be used to detect the edges of the LOx core. Sliphorst used the shadowgraph data to correlate relationships between different injection properties and the resulting core properties.

MIC and VHAM

The MIC (Multiple Injector Combustor) was used to investigate the response to an imposed acoustic disturbance using oxygen-hydrogen propellants by Rey et al. [113, 114] and methane-oxygen propellants by Richecoeur et al. [116, 118, 119]. The MIC is a rectangular combustor with a series of five coaxial injection elements arranged in a vertical line along the center of the chamber. The MIC featured a secondary nozzle and exciter wheel acoustic excitation system in the top wall of the chamber and heavily influenced the design of BKH.

To produce larger disturbance amplitudes an improved excitation system, referred to as the VHAM (Very High Amplitude Modulator), was incorporated into the MIC in later experiments reported by Mery et al. [84, 85] studying methane-oxygen flames. The VHAM operated by alternately opening and closing two nozzles located at the end wall of the chamber. The MIC and VHAM experiments were used to study the flame response to transverse acoustic excitation. The flame response was observed through high-speed imaging recorded through optical windows in the side walls of the chamber which allowed line-of-sight access to all five injection elements.

Richecoeur et al. [119] and Mery [83] used OH* and CH* imaging data from MIC and VHAM experiments to study the flame response to acoustic excitation. The optical data showed the deflection of the flame by the acoustic velocity and its retraction during transverse mode excitation. Limited analysis of the optical datasets from the experiments has been published. The optical data have been used for qualitative comparison with the results from combustion instability models, for example by Hakim et al. [41]. The phase of dynamic pressure sensor data from the walls of the chamber and the mean optical intensity fluctuations were also compared, but no analysis of local response distributions, as computed for the CRC and BKH, has been reported.

2.5.2 Naturally Excited Experiments

A reacting flow inside a combustion chamber is said to be naturally excited if an instability occurs spontaneously during its operation without external acoustic forcing or triggering. Naturally excited combustion instability experiments are developed by adapting chambers or design features that are found to produce instabilities for combustion instability research. The underlying instability mechanisms driving naturally unstable experiments are of particular interest as, until the driving mechanisms are understood, similar instabilities could occur in other combustor systems.

Naturally unstable chambers offer a number of unique experimental challenges. The instability frequency and the amplitude of the disturbance may not be controllable. For research purposes the instability must grow to a sufficient amplitude to be studied, while reaching a limit cycle before the combustor is damaged. Care must also be taken when introducing instrumentation and diagnostics not to alter the chamber acoustics significantly enough to 'cure' the instability. The data from such experiments is limited and the study of naturally unstable experiments uses more general observations and results from externally excited experiments to identify the underlying mechanisms.

BKD

BKD (german: *Brennkammer D*) is a research combustor using to investigate naturally excited combustion instabilities. BKD is operated on the P8 testbench at the DLR Institute for Space Propulsion. The chamber is cylindrical with a diameter of 80 mm and 42 coaxial injection elements. It operates with LOx and either liquid or gaseous hydrogen propellants at supercritical chamber pressures ranging from 60 to 80 bar. BKD has been found to

exhibit high frequency combustion instability phenomena with frequencies >10 kHz at specific operating points.

The BKD combustor was not originally designed for instability research and had limited instrumentation. Gröning et al. [34, 35, 37] implemented additional instrumentation into the chamber for studying HF combustion instability phenomena including high frequency dynamic pressure sensors and optical probes. Gröning et al. [36, 37] identified the acoustic disturbances as spinning tangential modes and found that the inclusion of an asymmetric acoustic damping cavity in the side of the chamber fixed the orientation of the acoustic disturbance.

Gröning et al. [34] concluded that high frequency injection coupling was responsible for the instabilities as they occurred at operating points where the tangential chamber mode frequencies matched longitudinal mode frequencies in the LOx posts. This result was later supported by numerical investigations by Urbano et al. [152]. Numerical modelling by Urbano et al. [152] and Douasbin et al. [21] identified a potential coupling with the first radial mode of the chamber volume that occurs at double the transverse mode frequency. The BKD results identified injection coupling as a potential driving mechanism in HF combustion instabilities. It also highlights the additional insight possible through simultaneous experimental and numerical research of instabilities.

CVRC

The CVRC (Continuously Variable Resonant Combustor) is a single element cylindrical combustor operated by Purdue University [142]. The CVRC uses methane or JP-8 as the fuel and decomposed Hydrogen Peroxide (H_2O_2) fed through a catalyst bed as the oxidiser to produce conditions representative of an oxidiser-rich staged combustion cycle. The length of the CVRC oxidiser post can be modified during experiments to change the longitudinal mode frequencies, thereby controlling the frequency of the naturally excited acoustic modes. The acoustic disturbance is monitored using a distribution of dynamic pressure sensors. The flame response is observed using high-speed imaging through a quartz segment that allows optical access to the flame zone.

Bedard et al. [8] measured emission spectra from the CVRC experiments and computed phase averaged results to compare the relative phase of OH* and CH* emission with pressure and heat release fluctuations. This analysis identified the phase difference between acoustic and optical intensity fluctuations, with CH* intensity fluctuations preceding the pressure disturbance by 50° and OH* intensity fluctuations lagging the pressure disturbance by 40°. However Bedard et al. also concluded that the line-of-sight integrated intensity measurements did not sufficiently resolve the spatial and temporal variation of heat release. Bedard et al. note that, despite this, the optical datasets from the CVRC serve to complement and validate model predictions. The availability of optical datasets has facilitated further study of the CVRC as a numerical testcase. In the computational models CH* emmission lead pressure by 60 degrees, while OH* emmission was almost in phase with pressure with a phase lag of only 7 degrees. Bedard et al. explain that the numerical model did not include thermal excitation of OH* which may have a significant effect on the results.

Harvanzinski et al. [53] computed longitudinal mode shapes by filtering pressure data. The mode shapes were used with optical data samples to compute Rayleigh indices for the optically accessible region. Harvazinski et al. also computed relative phase distributions between pressure and optical intensity fluctuations by filtering the optical datasets. Local regions of in- and out-of-phase heat release relative to the local pressure disturbance were identified. However, the global Rayleigh indices computed by Harvazinski et al. was positive for the first three longitudinal modes considered, indicating a positive coupling between acoustic pressure fluctuations and heat release.

Harvazinski et al [55] and Hardi et al. [48] applied DMD analysis to images from the CVRC to qualtiatively compare the combustion response between experiment and simulations. Harvazinski et al. compared CH* chemiluminesence images with heat release results from numerical simulations. Snapshots from the cycle were compared to show that the peak heat release occurs in phase with the local acoustic pressure fluctuation. Hardi et al. compared used phase-locking, POD, and DMD methods to isolate the flame response. The analysis was used to produce reconstructed images of the response which were compared directly with CFD results.

TIC

The TIC (Transverse Instability Chamber) is a multi-element combustor operated by Purdue University that operates with methane or JP-8 and decomposed hydrogen peroxide propellants[104, 160]. The TIC features a flat rectangular volume with seven injection elements arranged in a horizontal line. The six outer swirl-coaxial elements are used to naturally excite a transverse acoustic mode in the chamber. The response of the central study element to the transverse acoustic disturbance is observed through optical access windows in the sides of the chamber. The naturally occuring instabilities in the TIC can reach ampltiudes of up to 72% of the 9.6-bar mean chamber pressure [161].

Pomeroy et al. [103] and Wierman et al. [160] used data from the naturally excited TIC experiment operated at Purdue university to analyse CH* chemiluminesence images during transverse mode excitation. A fit of pressure data to a transverse mode distribution was used to estimate the local acoustic disturbance. Pomeroy et al. [103] processed TIC optical data to compute Rayleigh index and phase distributions showing the response of the central study element. Velocity response factors were then computed by comparing the local acoustic velocity disturbance with the observed optical intensity fluctuations. Wierman [161] noted that the observed transverse acoustic disturbance in the TIC exhibited limit-cycle behaviour with non-linear, steep-fronted waves. Wierman performed POD and DMD analysis of high-speed optical data samples during limit-cycle behaviour to identify coherent structures and the flame response. The time lag between intensity and acoustic fluctuations was computed by cross correlating the optical intensity and dynamic pressure fluctuations.

Wierman et al. [161, 162] also analysed data from the TIC using a variety of mean, global, POD and DMD analyses to study the response to transverse excitation. Wierman et al. found that POD and DMD isolated the transverse displacement of the flame by the acoustic velocity. Global response factors were computed for use in lower-order combustion instability models by calculating the RMS of the selected temporal POD and DMD modes at the frequencies of interest. As the TIC exhibits natural instability phenomena Wierman [161] pre-processed the experimental datasets to identify test periods with relatively constant acoustic amplitudes to be further analysed. This limited the length and duration of the individual samples to be processed. Data from an externally excited experiment with continuous acoustic forcing maintains a relatively constant amplitude allowing longer samples to be processed and the influence of spontaneous fluctuations and other ‘noise’ sources to be reduced.

2.6 BKH

In this section the BKH experimental setup and test sequences is described. BKH was originally developed and is described in more depth by Hardi [49]. The BKH datasets presented in this thesis were collected as part of larger BKH experimental test campaigns, the results of which have been previously reported by Hardi [49] and Webster [159].

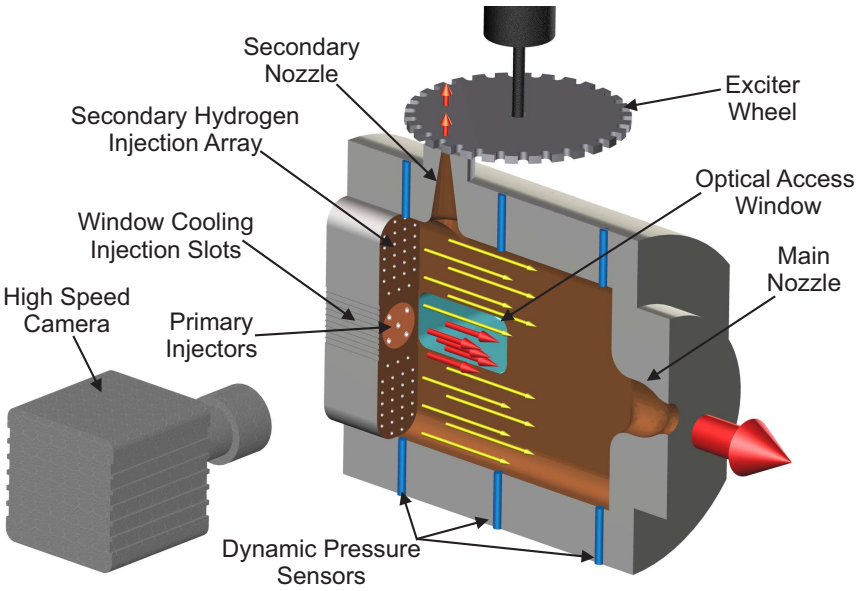

Figure 2.6.1: Concept diagram of BKH.

2.6.1 Description

A diagram showing the major components of BKH are shown in Figure 2.6.1. The chamber volume of BKH is rectangular with dimensions chosen to be representative of an upper stage engine and shown in Figure 2.6.2. The rectangular geometry fixes the orientation of the acoustic modes to the major dimensions of the chamber. The rectangular shape also allows optical windows to be mounted in the side walls of the chamber to provide line-of-sight access to the primary combustion zone. Injection is from left to right in Figure 2.6.1. BKH features two nozzles: a main nozzle mounted parallel to injection in the opposite wall of the chamber, and a secondary nozzle mounted perpendicular to the injection direction in the top wall of the chamber.

The secondary nozzle diameter is approximately $1/10^{th}$ that of the main nozzle and diverts approximately 10% of the flow. During a test the flow through the secondary nozzle is periodically modulated by the motion of a toothed exciter wheel. The teeth of the wheel are positioned so that they pass over the secondary nozzle opening as the wheel is turned by an electric motor. As the teeth interrupt the flow through the nozzle a disturbance is produced which then propagates back into the chamber. This disturbance is used to excite the chamber and impose an acoustic disturbance upon the flames from the primary injection elements.

The secondary nozzle, toothed exciter wheel, and motor are collectively refereed to as the acoustic excitation system. By controlling the speed of rotation of the wheel using the motor the frequency of the resulting acoustic disturbance can be actively controlled during an experiment. The exciter wheel and motor are housed in a specialised casing that is mounted on top of BKH. The casing features a secondary exhaust tube which diverts the flow out of the secondary nozzle so that it mixes with the exhaust from the main nozzle as shown in Figure 2.6.4a.

The primary injection elements that are the focus of BKH experiments are located in the middle of the injection plane as shown in Figure 2.6.1. The primary injectors consist of five shear coaxial injectors arranged in a matrix configuration as shown in Figure 2.6.3. BKH operates using liquid oxygen, referred to as LOx, and gaseous or liquid hydrogen propellants. LOx is injected through the central LOx post of each coaxial element, while hydrogen is injected through the outer annulus. The matrix arrangement of the five injectors is designed to study the interaction between elements as would occur in full scale systems. The central injection element is surrounded on all sides by other elements and is therefore the most representative.

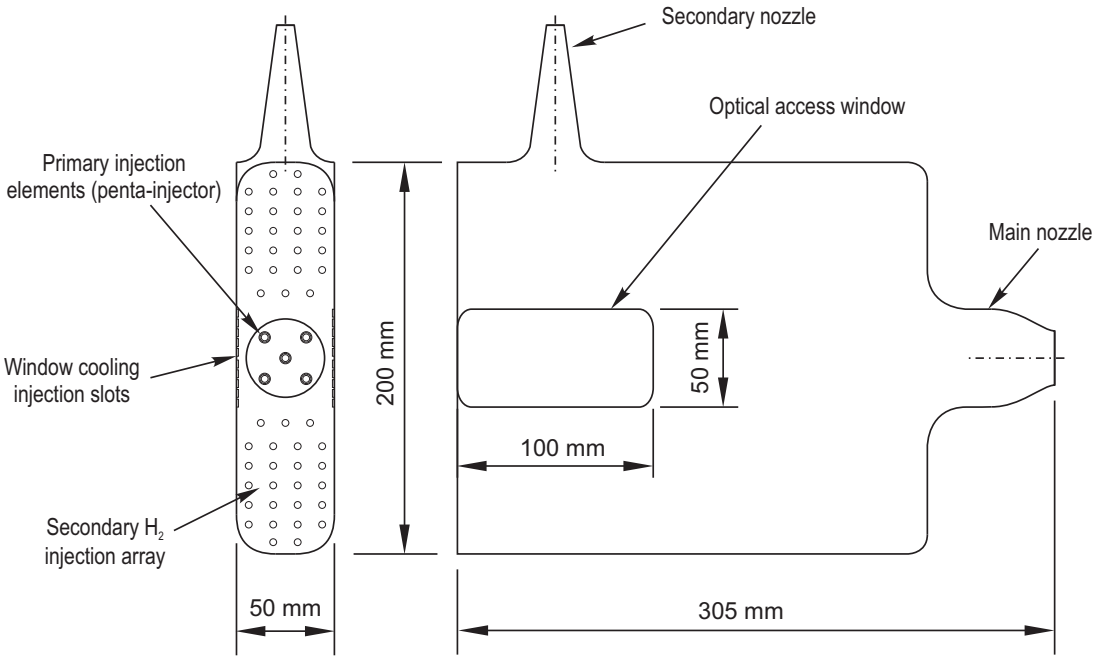

Figure 2.6.2: Diagram of BKH volume with key dimensions [49].

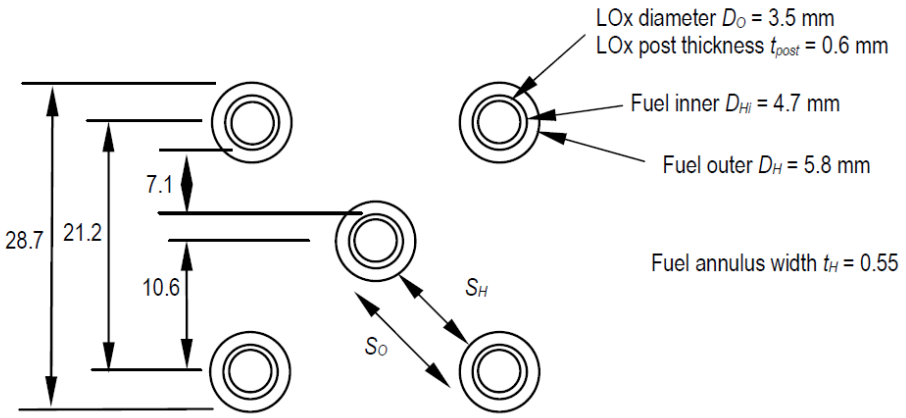

Figure 2.6.3: Diagram of BKH primary injection elements with key dimensions [49].

In addition to the primary injection array, a large amount of secondary injection is employed within BKH. This secondary injection is used to protect the windows and walls of the chamber from the hot combustion gases. It is also intended to prevent recirculation of flow in the top and bottom of the chamber volume which would not be representative of a full scale system. A picture of the assembled BKH injection plane showing the primary and secondary injectors is shown in Figure 2.6.4b. The secondary injection array consists of 50 circular injectors divided evenly above and below the primary injection array to prevent recirculation, and an array of window cooling injectors positioned along each side wall of the chamber spanning the window region. The window cooling injection is used to ensure a protective film of hydrogen gas exists between the primary combustion zone and the optical windows during BKH experiments.

Four different propellant feed manifolds are used to distribute the propellants amongst the individual injection elements as shown in Figure 2.6.5. Two dome-shaped primary manifolds are used for distributing oxygen and hydrogen propellants. One large toroidal manifold is used to distribute the secondary hydrogen injection above and below the primary injectors. A half-disk manifold on each side of the chamber is used to distribute flow amongst the window cooling injector arrays.

A torch igniter is used at the beginning of each test to ensure ignition of the propellants.

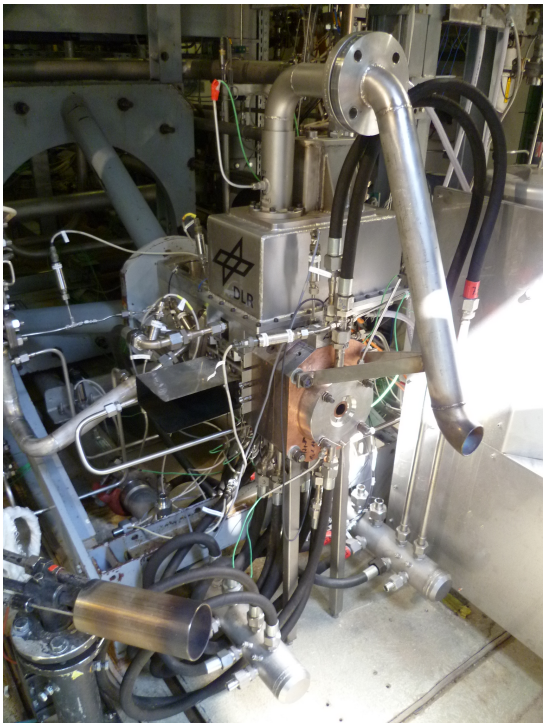

(a) BKH mounted on the P8 testbench[49].

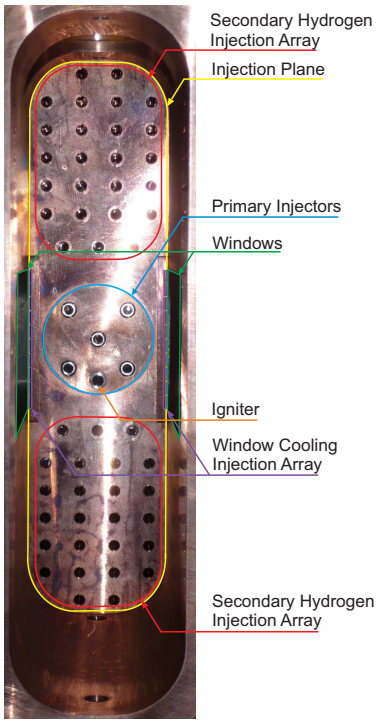

(b) Assembled BKH injection plane viewed from the end of the window segment.

Figure 2.6.4: BKH hardware.

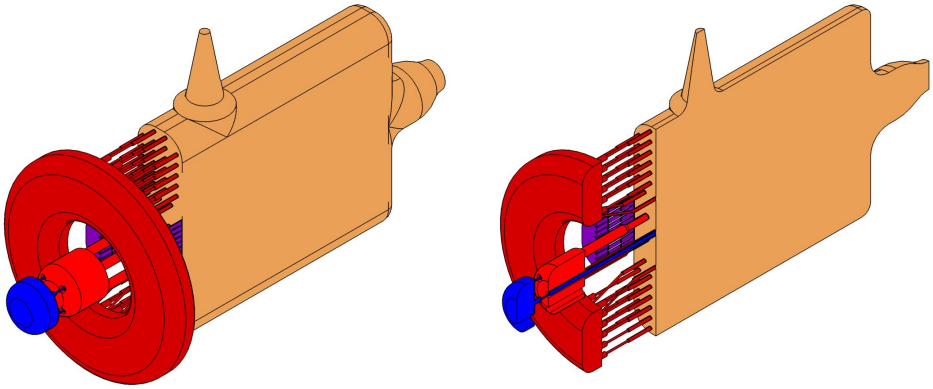

(a) 3D isometric view

(b) 3D isometric view with cut

Figure 2.6.5: BKH volume with injection manifolds. Blue: Oxygen, Red: Primary and Secondary Hydrogen, Purple: Window Cooling, Orange: Chamber volume.

The igniter tube passes through both the primary oxygen and hydrogen manifolds and enters the chamber below the primary injector array. The igniter tube outlet is shown in Figure 2.6.4b.

2.6.2 Instrumentation

BKH features a variety of instrumentation and diagnostics to collect data during experiments. Many of the sensors are used to monitor the operation of the chamber. The most important data for analysing high frequency combustion instabilities are measurements of the acoustic fluctuations and flame response resulting from the acoustic forcing. Specialised dynamic pressure sensors and optical diagnostics featuring high sampling rates are employed for this purpose. The instrumentation installed in BKH are described in the following sections.

Operating Point Diagnostics

The operation of the chamber is controlled by monitoring the mass flow rates of all propellants, their state entering the chamber, the chamber pressure, and the wall temperature of the chamber. For practical reasons, the mass flow rates of each of the different injection arrays are measured upstream of each propellant feed manifold using flow sensors from the P8 test bench. The state of the propellants entering the chamber are monitored using static pressure sensors and thermocouples in each of the propellant feed manifolds. The properties and mass flow rates of each propellant at the injection plane are then computed assuming an equal distribution of propellants through each injection element and continuity between the manifold and the injection plane. The chamber pressure is monitored using a static pressure sensor located downstream from the secondary nozzle in the top wall of the chamber. Thermocouples mounted at various locations in the walls of the chamber are used to monitor the wall temperature. This data is used to ensure that the desired operating conditions are met and that no structural limits are exceeded during operation. The response times of the sensors used to collect the aforementioned data are insufficient for analysis of HF combustion instabilities and are recorded with a sampling rate of 1 kHz.

HF Dynamic Pressure Sensors

The acoustic disturbance produced by the BKH acoustic excitation system is observed using a number of high frequency piezoelectric dynamic pressure sensors. The pressure sensors are surface mounted at various positions on the walls of the chamber volume and in the propellant feed manifolds as shown in Figure 2.6.6.

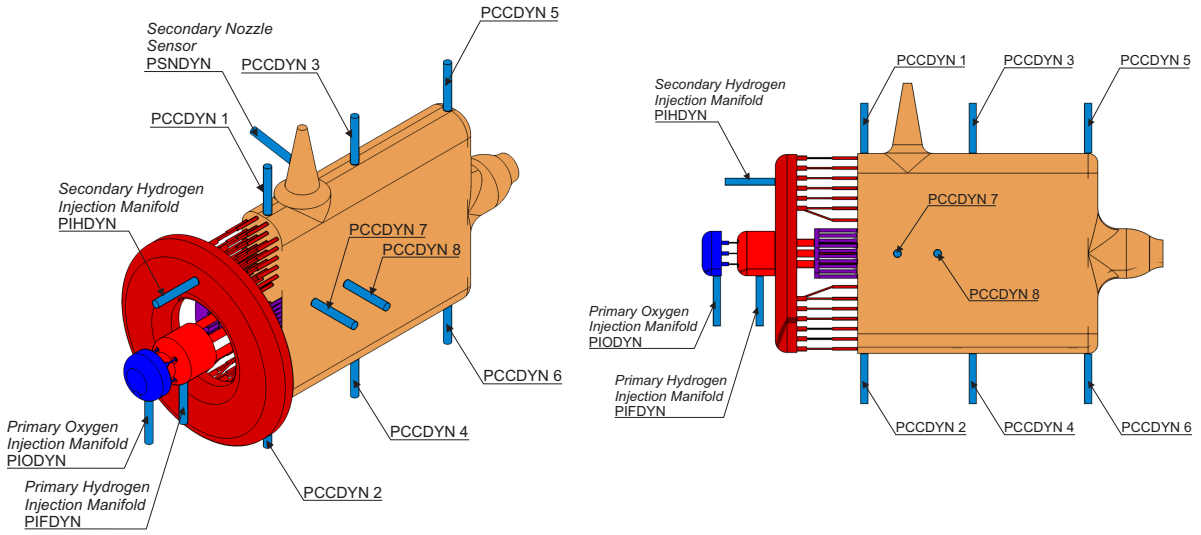

(a) Isometric view (b) Side view

Figure 2.6.6: BKH combustor volume showing position of dynamic pressure sensors.

The chamber sensors PCCDYN1-6 are distributed around the combustion chamber volume so that the distribution of the acoustic field can be determined by comparing the amplitude and phase of the disturbance at each sensor position. Sensors PCCDYN7 & PCCDYN8 are located in a “dummy” window which is sometimes used in place of the optical windows. These sensors are therefore not available when optical diagnostics are being employed. A sensor in the secondary nozzle, labelled PSNDYN, was added in recent BKH experimental campaigns to provide further insight into the disturbance produced by the excitation system.

The sensors located in the propellant feed manifolds are used to monitor if acoustic disturbances from the chamber are propagating upstream through the feed system. The

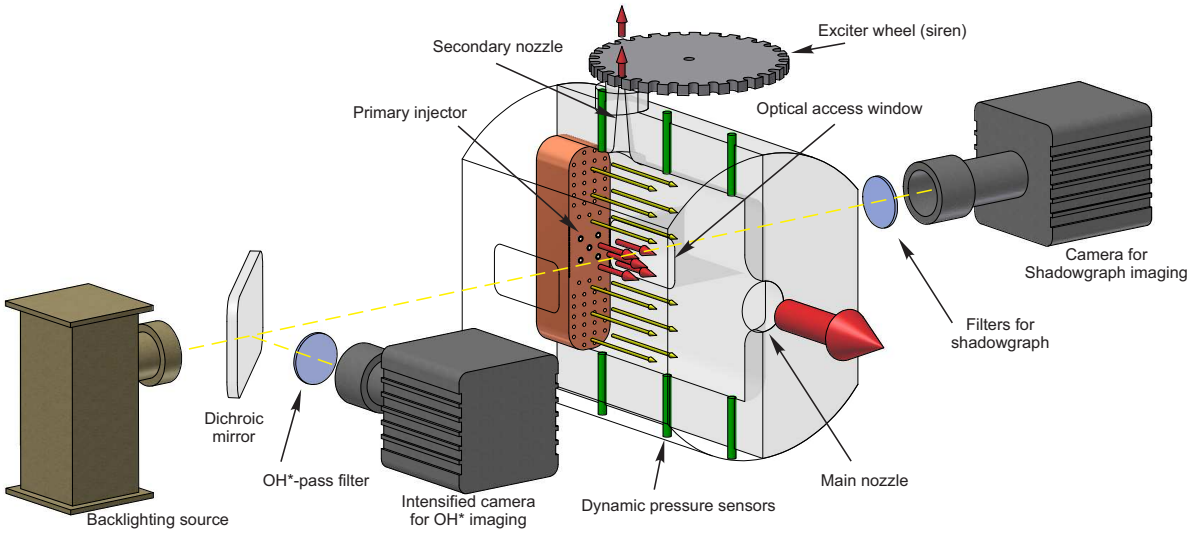

Figure 2.6.7: BKH optical diagnostics setup [49].

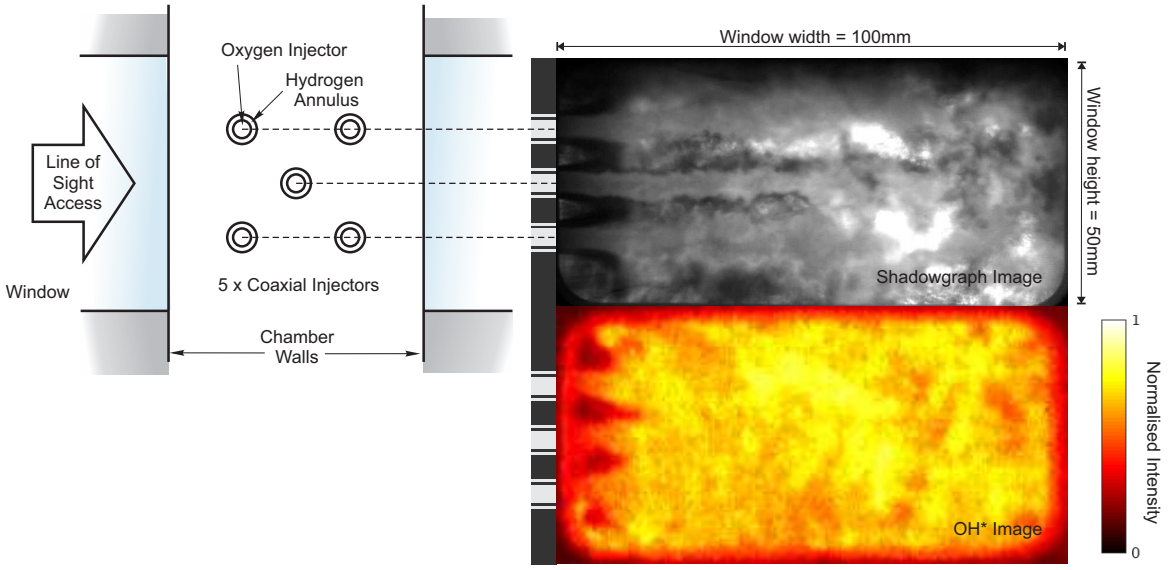

Figure 2.6.8: Visualisation of line-of-sight access in BKH and example images recorded during a BKH test without acoustic excitation [49].

sensors are labelled by the manifold in which they are mounted. No dynamic pressure sensors are located in the window cooling feed system and therefore no information on acoustic propagation through the window cooling feed system is available. The dynamic pressure sensor data is sampled at a rate of 100 kHz. As the resonant modes of interest in BKH experiments occur between 2-5 kHz this allows 20 or more measurements to be recorded over each acoustic cycle.

2.6.3 Optical Diagnostics

The optical diagnostics are used to observe the flame response to acoustic excitation. Simultaneous high-speed OH* and shadowgraph imaging are recorded using the experimental setup shown in Figure 2.6.7. To allow simultaneous imaging a dichroic mirror positioned at 45° to the optical axis is used to reflect ultra-violet light to the OH-imaging camera without interrupting the optical path between the back-lighting source and shadowgraph imaging camera. The optical setup employed during the BKH experiments has been previously described by Hardi [44, 46, 49].

The quartz optical windows in the side of BKH provide line-of-sight access to the primary injector region as shown in Figure 2.6.8. The position of the windows is shown in Figure 2.6.2. The windows are 100 mm wide and 50 mm high, and positioned so that they are midway between the top and bottom of the chamber. One side of the window is flush with the injection plane to view the region directly downstream from the primary injection elements. As the BKH primary injectors are configured in a matrix pattern the line-of-sight access captures only the outer upper and lower injectors and the middle injector directly. These injectors appear as three vertically spaced oxygen streams and flames in the BKH optical images.

A compromise between the sampling rate, resolution, and recording duration of the high-speed camera datasets must be made due to memory limitations. To facilitate a sufficiently high sampling rate to capture the flame dynamics at the resonant frequencies of BKH the image resolution and recording duration is often sacrificed. This allows a high sampling rate (>18,000 fps) to be used for short recording durations. A signal from the P8 test bench is sent to trigger the cameras and begin recording. The camera triggers are part of the test sequence and are selected so that the most scientifically interesting part of the experiments is recorded. The trigger times and cameras vary from test to test depending on the scientific objectives of the campaign. A high frequency feedback signal from the camera is recorded to synchronise the recording time with the other data from the P8 test bench.

Shadowgraph Imaging

When light passes through a medium with different refractive indices it is diffracted by varying degrees. This principle has been used for visualising the density gradients in flow fields. When a back-lighting source is used, the light that is diffracted by the refractive index change at density gradients in the flow field does not reach the other side. The shadows cast as the light is diffracted are recorded in a process known as shadowgraph imaging.

BKH shadowgraph images are collected using a Photron FASTCAM SA5 camera. A back-lighting source is positioned on the opposite side of BKH to the camera and used to illuminate the flame. Light from the back-lighting source passes through the chamber and an additional optical filter before reaching the high-speed camera. The optical filter is designed to block the undesired combustion light emitted by the flame while allowing the light emitted from the back-lighting source to pass through unaffected. The resulting images capture regions of high density gradients in the chamber flow field such as the dense liquid oxygen core produced by the co-axial injection elements.

In the following study data from two BKH campaigns using different back-lighting sources for the shadowgraph images are presented. The shadowgraph imaging from earlier BKH campaigns used a high-power Xenon gas-discharge lamp to provide continuous illumination. A RG850 longpass optical filter was used to block wavelengths shorter than 850 nm in order to suppress combustion light but not the powerful near-infra-red light emitted by the Xenon lamp.

One issue with this configuration was that the lamp was not sufficiently bright to overcome the emitted combustion light and even minor flow gradients were resolved. The oxygen core appeared illuminated rather than as dark structures expected in a traditional shadowgraph image. This was attributed to light emission above the 850 nm wavelength produced on the surface of the LOx core which is not suppressed by the interference filter.

In later BKH campaigns an improved shadowgraph setup was employed which used a high-power green LED as the back-lighting source. A combination of blue-green and yellow optical filters were used to produce a narrow wavelength pass band (528±25 nm) to isolate the light corresponding to the wavelength of the LED. A comparison of shadowgraph

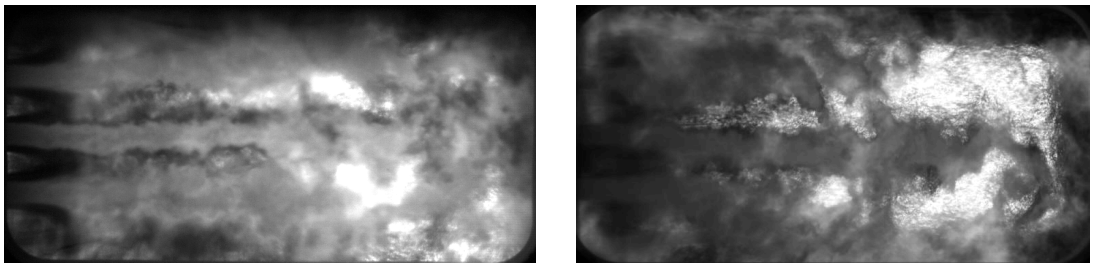

(a) Xenon lamp back-lighting [49]. (b) Green LED back-lighting [159].

Figure 2.6.9: Comparison of shadowgraph images with different back-lighting sources and optical filters.

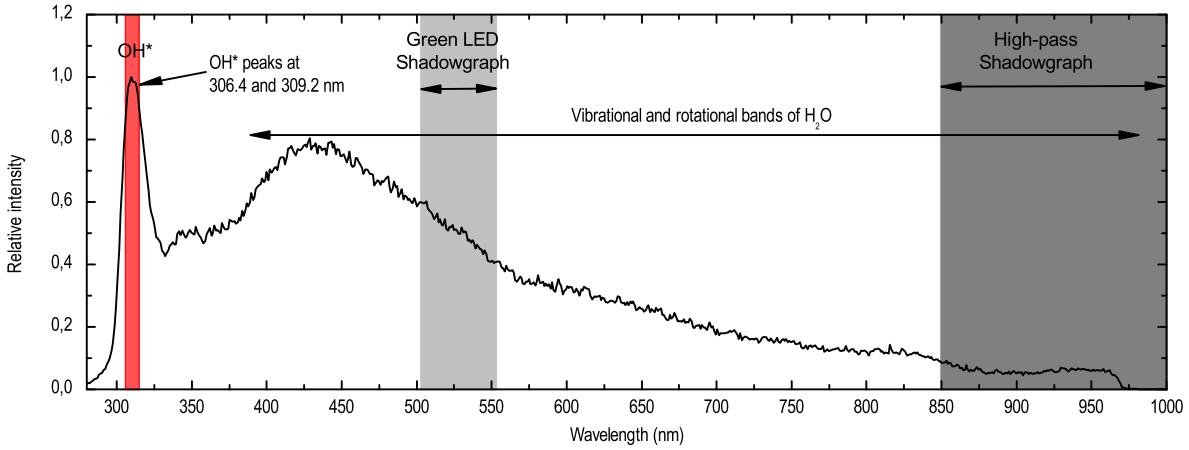

Figure 2.6.10: Emission spectrum from a LOx/H2 sub-scale combustor showing pass bands of optical filters. Modified from [49].

images with the different back-lighting sources is shown in Figure 2.6.9. The optical filter pass bands of both shadowgraph imaging configurations are shown in Figure 2.6.10.

The green LED produced clearer images with less combustion light which allowed better resolution of the end of the dense LOx core. However the shadowgraph images with the green LED are darker near the injection plane and do not show the structure of the LOx core in the near injector region. The undesired combustion light captured using the Xenon lamp setup served to illuminate the structure of the LOx core in the near injector region. Shadowgraph image datasets with both back-lighting sources are analysed in this work.

OH* Imaging

OH* imaging of BKH experiments was designed to capture OH* emission by chemiluminescence. Chemiluminescence refers to the light emitted by excited molecules as they return to their ground state. For oxygen-hydrogen combustion an electronically excited form of the hydroxyl molecule, known as OH*, is used. The hydroxyl molecule is produced during oxygen-hydrogen combustion by chemical reactions such as:

$$O + H + M \rightarrow OH^* + M.$$

where M is another molecule; or by the collision of ground state OH with other molecules:

$$OH + M \rightarrow OH^* + M.$$

Shortly after its formation the OH* radical quickly decays to its ground state by releasing a photon of light at approximately 305 nm. As the formation and decay of the

OH* radical occurs very rapidly during oxygen-hydrogen combustion, it has been used by various research groups as an indicator of where and at what rate combustion, and subsequently heat release, is occurring within a flame [30, 80].

Recent work by Fiala [23] has shown that OH* chemiluminescence is not a good indicator for heat release at high pressure. This is due to the flame being optically thick making it unsuitable for line-of-sight measurements and the hydroxyl molecule undergoing significantly more thermal than chemical excitation. Fiala also concluded that there is no quantitative relation between the OH* intensity and heat release. This conclusion was in light of new research that indicated the OH* intensity was dependant on the local strain rate and other factors making it difficult to relate OH* intensity fluctuations with heat release in turbulent non-premixed flames.

However, Fiala also suggested that OH* intensity may still be used as a qualitative marker of heat release intensity for combustion instability research if the strain rate and other factors are assumed to remain relatively constant. Fiala suggests that the intensity fluctuation in a local region of the flame, where the strain rate may be assumed to be constant over time, is indicative of the heat release. In light of this, the OH* imaging is analysed in this thesis as a qualitative indicator and is used to compute Rayleigh indices and other results that may be used for numerical validation. The calculation of quantitative results, such as response factors, using OH* imaging is not valid based on these findings and is excluded in this project.

A Photron FASTCAM APX-i^2 intensified high-speed camera was used to capture high-speed OH* images during BKH experiments. An optical filter was positioned in front of the camera to filter the light entering the camera to wavelengths corresponding to the OH* emmision wavelengths. The optical filter used had a wavelength pass-band of 305 $\pm$ 5 nm which is centered on the OH* wavelength. Figure 2.6.10 shows the emission spectrum from a LOx/H2 sub-scale combustor and the pass bands of the optical filters. A distinct peak in the spectrum occurs at the OH* wavelengths.

2.6.4 Test Sequences

BKH is operated on the P8 French German cryogenic test facility at the DLR Insitute of Space Propulsion in Lampoldshausen, Germany. The P8 testbench provides cryogenic and gaseous propellants to the combustion chamber at a specified mass flow rate and temperature. The testbench also controls the excitation system and camera triggers. This section describes the operation of BKH experiments and a typical BKH test sequence.

The operating point of the chamber is controlled by the propellant flow provided by the P8 testbench. At the beginning of a test sequence the chamber is purged with gaseous hydrogen to remove air from the chamber volume. After the initial purge the propellants are fed into the chamber with a reduced flow rate and ignited using the chemical igniter. Shortly after ignition the flow rate of propellants are increased to match the desired operating point.

BKH experiments typically have a duration of 40 to 45 seconds. For the experiments considered in this work a single operating point is selected and maintained for the test duration. The excitation system is activated before each test commences and the electric motor is used to accelerate the wheel to a speed corresponding to a specified starting excitation frequency. After the chamber has reached its stable operating point the speed of rotation of the wheel is increased so that the excitation frequency ramps through a specified frequency range. The frequency range covered is typically 2 to 5 kHz, which includes the first longitudinal and transverse modes of the chamber volume.

Figure 2.6.11 shows a spectrogram of the PCCDYN2 dynamic pressure sensor signal from a BKH experiment. The PCCDYN2 sensor, shown in Figure 2.6.6, is positioned near the injection plane on the bottom wall of the chamber and is directly opposite the

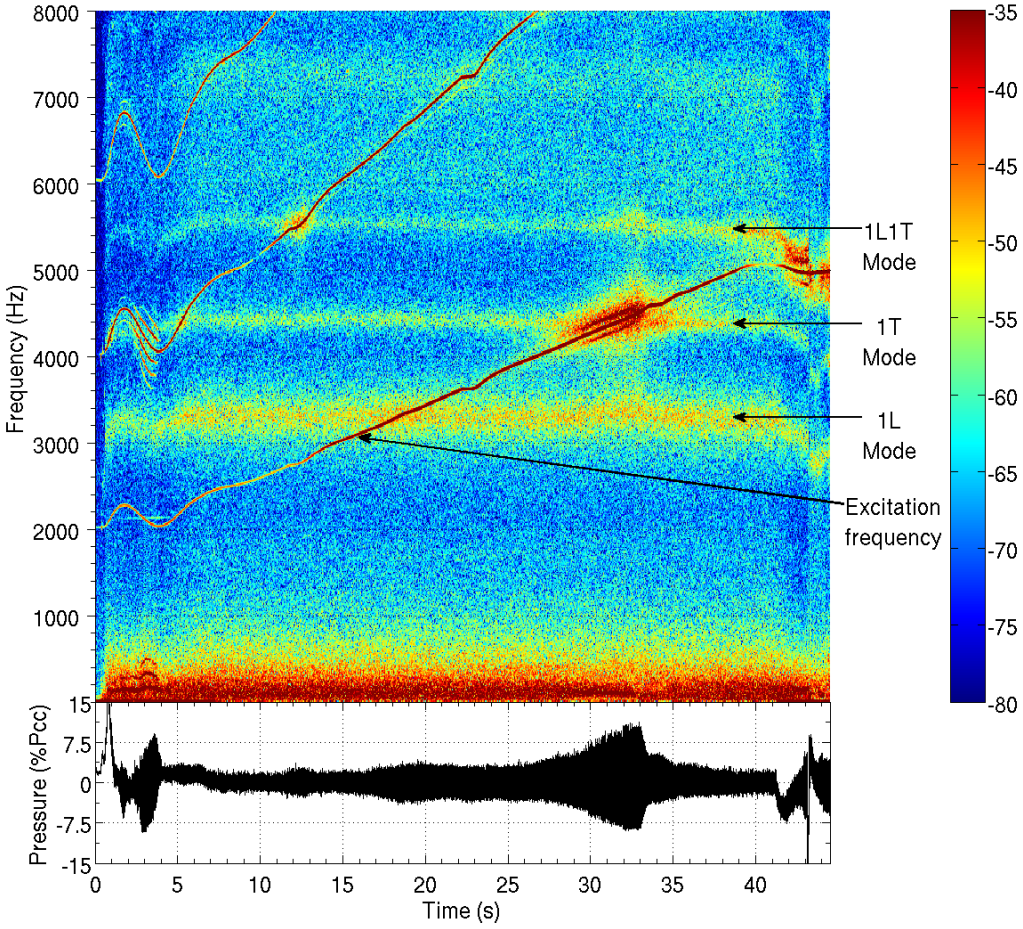

Figure 2.6.11: Spectrogram of PCCDYN2 dynamic pressure sensor data from a BKH 60 bar ROF 6 experiment.

acoustic excitation system. As this sensor is not positioned near a nodal line of a resonant mode it shows each of the resonant mode frequencies and the disturbance produced by the excitation system over the range of the excitation frequency ramp.

The resonant modes of BKH are weakly excited by combustion noise and turbulence even without acoustic excitation. They appear as broad horizontal bands in the spectrum that are labelled in Figure 2.6.11. The excitation frequency starts at 2 kHz at the beginning of the test ($t = 5$ s) and is increased linearly at a rate of 80 Hz/s to ramp through each of the resonant modes, appearing as a diagonal line in the spectrogram.

The raw dynamic pressure signal is shown in the lower plot of Figure 2.6.11. The amplitude of the raw signal shows, aside from initial noise during the start-up and shut-down sequences, that the highest acoustic amplitudes are reached during excitation at the resonant mode frequencies. The triggering of the high-speed optical cameras by the P8 testbench is used to capture the flame response when the excitation frequency matches a resonant mode frequency coinciding with the high amplitude acoustic disturbances. As the excitation is continually ramped during the experiment the data is collected at a stable operating point but continuously varying excitation frequency.

2.7 Combustion Instability Modelling

Combustion instability research aims to address an industrial problem of predicting the stability of new engine designs during the development process. The cost of the highest fidelity methods, such as Direct Numerical Simulation (DNS), is so large that researchers cannot afford to apply them to representative scale problems at the present time. Preference

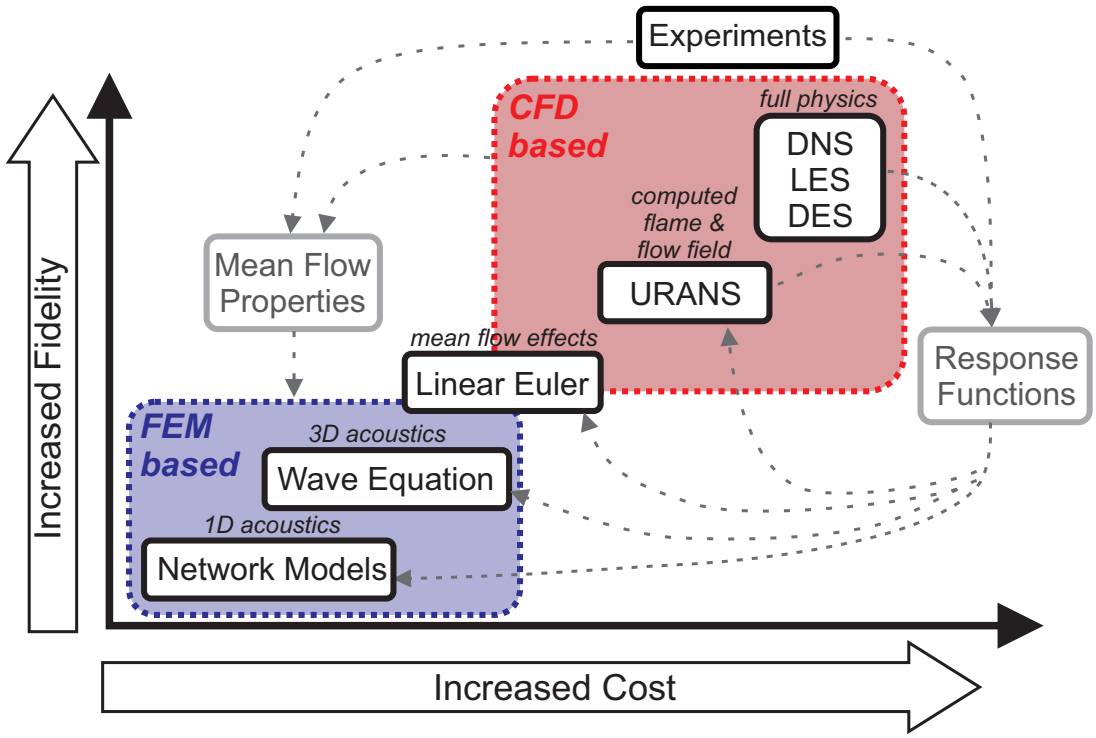

Figure 2.7.1: Hierarchy of combustion instability models. Figure adapted from Portillo et al. [105].

is given to economic and efficient modelling approaches that can produce results sufficient to explain the combustion instability phenomena of interest.

A hierarchy of combustion instability modelling approaches has been developed ranging from simplified acoustic models to full scale simulations of rocket engine combustion chambers. Each model represents a compromise between the fidelity of the model and the associated computational cost, consisting of computational resources and the time required to produce a solution. The different modelling approaches can be ordered by complexity as shown in Figure 2.7.1.

The most inexpensive models currently being investigated are low order models which employ finite element methods (FEM) to solve the linearised Helmholtz or Euler equations to model the acoustic disturbances over a representative domain. Such low order models do not resolve the flame but instead use response functions to model the feedback of the flame to an acoustic disturbance. The response functions may be derived from experimental data or extracted from other higher fidelity models. At the intermediate level are models that solve variations of the linearised Euler equations either to resolve the dynamic disturbance about the mean flow or as a simplified CFD simulation. At the more advanced level are CFD models which resolve the underlying flow field, flame, and acoustic disturbances and their interaction. The following sections discuss these approaches and their application to combustion instability research in more detail.

2.7.1 FEM Based Models

Finite Element Methods (FEM) based combustion instability models focus on resolving the acoustic disturbance of the combustion instability. The acoustic disturbance is modelled by solving the linearised Helmholtz (wave) or Euler equations discretised over the internal volume of the combustion chamber to identify the resonant frequencies and acoustic field distribution. These tools are used to determine the acoustic modes which may contribute to instabilities and to asses how modifications to the chamber may modify the resonant modes in order to reduce or prevent the instability. The combustion response may be

included via representative time-lag or response factors as discussed in Section 2.3.2.

By not resolving the flame or tubulent structures of the underlying flow field FEM based models have a significantly reducing the complexity. This reduces the computational resources required to solve the equation set and the resolution of the numerical grid. However neglecting the underlying flowfield ignores the influence of intantaneous and mean flow effects such as a change in the distribution of acoustic properties and mean flow velocity which affect the acoustic modes of the chamber. The response of the flame that supports or dampens the acoustic disturbance is also not captured in the model. To overcome this FEM based models may use inputs from experiments and higher fidelity models to represent these phenomena. For example, the acoustic property distribution and flow velocity in the chamber may be imported from a higher fidelity CFD simulation. As a consequence the models are dependant on the accuracy of the employed flame response functions. Smith et al. [145] explain that such models are useful when there is high quality test data so that appropriate response functions, suitably accurate for the depth of analysis, may be designed.

Acoustic Network Models

The simplest FEM models are acoustic network models which discretise a combustion chamber system into a 1-D system of discrete acoustic volumes in a network, known as the lumped-parameter method. Each acoustic volume represents a constant cross section volume or cavity that is connected to neighbouring components by acoustic boundary conditions. The acoustic boundary conditions assure mass conservation and continuity but may also take the form of an acoustic impedance or admittance. An acoustic equation is solved to compute the resonant mode frequencies and distributions of the system of coupled volumes. Acoustic network models are typically used to study low frequency instabilities which occur due to feed system hydraulic-modes at frequencies of a few hundred Hz [20, 60]. Huber [59] has also used acoustic network models to study feed system coupling in gas turbine systems.

Acoustic network models are very fast to compute and adapt to new systems. But inherently rely on the assumption that the reduced 1-D system of simply connected volumes is representative of the complex combustion chamber system, that appropriate acoustic boundary conditions can be determined for each interface, and the accuracy of the response functions employed to model the response of the flame. An additional assumption often used is that the flame is compact, meaning that the flame is contained within a length that is significantly shorter than the acoustic wavelength. The compact flame assumption simplifies the application of response functions as only the local acoustic disturbance at this location needs to be considered. The flames considered in the current work occupy half the length of the chamber volume and therefore do not satisfy this assumption.

Wave Equation Models

The acoustic wave equation has been previously described in Section 2.4. Wave equation models solve the wave equation to predict the frequencies and distributions of the resonant acoustic modes. Modelling approaches have been developed that solve the linearised wave equation over 2D or 3D numerical domains. The effect of different designs or the influence of acoustic damping devices on the acoustic field may also be determined. Yu et al. [167] explain that wave equation models require the least computational resources and may be enhanced by including non-linear source terms. This has led wave equation models to be the most commonly adopted approach to access combustion instability. The FAME model developed by Rey et al. [114] was a wave equation based model used to describe

the transverse transport of the flame. Another example of a wave equation model is the AVSP solver developed by Cerfacs [84, 88, 153].

For combustion chambers filled with a mixture of burnt and unburnt propellants the speed of sound and other acoustic properties may vary considerably across the chamber volume. These effects may be included by including acoustic property distribution by approximating it from experimental observations or extracting it from a CFD simulation. The linear wave equation assumes small pressure disturbances and that the local velocity is significantly lower than the speed of sound of the medium. Yu et al. [167] investigated the impact of the mean flow velocity on the resonant frequencies and found minimal variation for mach numbers $\leq$0.3 while higher order modes are more strongly affected. As the mean flow velocity is not considered in the wave equation, this effect is neglected and limits its applicability. Shimizu et al. [138] solve a potential flow formulation of the linear wave equation to include the effect of the mean flow velocity. This approach resolved the influence of the mean flow velocity on the propagation of transverse and longitudinal acoustic modes.

2.7.2 LEE Models

Linearised Euler Equation (LEE) models solve a linearised form of the system of conservation equations for mass, momentum, and energy. The advantage of the LEE equations over simpler models is that they inherently include the influence of high Mach number compressible flows. The LEE equations are solved to determine either the dynamic acoustic fluctuations about the mean flow state or the underlying mean flow with viscous and turbulent effects. LEE models produce solutions which are less computationally expensive than the numerical results of full CFD modelling techniques.

Pieringer et al. [101] and Sattelmayer et al. [125] solved a derivative of the linearised Euler equations known as the Acoustic Perturbation Equations (APEs). The APEs describe acoustic wave propogation in nonuniform mean flows without convection of vorticity or entropy modes. The mean flow was computed using an Euler equation solver and the mean flow velocity was used to apply acoustic admittance boundary conditions. A flame model proposed by Crocco and Cheng [13] was used which treats the flame as a concentrated combustion front and the heat release from the flame is modelled using an $n - \tau$ model.

Researchers at Purdue University [27, 145, 167] have applied 1D LEE models to predict longitudinal instabilities in the CVRC. The flow within the chamber was modelled by dividing the chamber into upstream and downstream sections containing either propellants or combustion products with a combustion zone defined at the interface. In more recent work Frezzotti et al. [27] defined the combustion zone as an additional longitudinally distributed region in the numerical domain. Smith et al. [145] collected additional CVRC experimental data that was used to refine and validate each model.

The main limitation of LEE models is that they still require response functions to model the flame response and combustion dynamics. The choice of how to represent the combustion zone and its response to acoustic excitation to suit each particular case limit the general applicability of simplified modelling approaches without higher fidelity results to tune and validate each model.

2.7.3 CFD Models

CFD models of rocket engine combustion instability aim to resolve the unsteady turbulent flow field in detail to recover the response of the flame to the local acoustic disturbance. The flow field is resolved by computationally solving the Navier-Stokes equations. CFD models may include additional sub-models to represent other phenomena such as combustion, multi-phase fluids and droplets, and real-gas thermodynamics. To resolve the turbulence,

combustion, and other scales of interest in the flow the grids used for CFD modelling are significantly finer than lower order models. The increased complexity, additional sub-models, and larger meshes required for CFD computations make the computational costs to obtain a solution magnitudes larger than simpler modelling approaches. The high computational requirements made CFD modelling intractable during early combustion instability research, limiting its adoption and focusing research efforts on the development of simpler analytical tools and modelling approaches. The additional insight possible with fully resolved CFD results has motivated CFD modelling to complement experimental research activities.

Modern computing advances and the increased availability of computational resources have allowed researchers to begin applying CFD methods to study combustion instability problems. Research has focused on modelling specialised rocket engine combustion instability experiments to incrementally validate and build confidence in the employed modelling tools and approaches before applying them to study larger more complex systems. The experimental test cases can generally be divided into cold flow experiments which study acoustic phenomena and its influence on liquid jet breakup, and hot flow experiments studying the response of flame elements to imposed acoustic disturbances. Some CFD modelling of naturally unstable combustion instability experiments has also been conducted.

The main CFD approaches being applied to model combustion instabilities are URANS (Unsteady RANS) and LES (Large Eddy Simulation). URANS resolves the distribution and fluctuation of mean flow properties and models all turbulence scales while LES resolves turbulence to the grid scale and may model finer scales using sub-grid scale models. The scales being resolved determine the level of grid refinement needed with LES models requiring finer grids and more resources than URANS. The following sections discuss URANS and LES combustion instability modelling in more detail.

URANS models

RANS models take an ensemble average of the Navier-Stokes equations to produce a time-averaged steady-state solution. URANS models are RANS models that are made time accurate by ensuring that the associated time step is uniform across the computational domain. This is typically achieved using a dual time stepping method. The inherent assumption of URANS is that the turbulent fluctuations being modelled occur over far shorter time scales than the mean flow property fluctuations being resolved. This assumption is a problem for jet flows where the turbulent and mean flow scales may be similar. However, if repetitive cyclic motion is being studied and we consider the average cycle, then the turbulent motion at particular points in the cycle may disappear. Under this assumption URANS may be used to resolve the phase-averaged response of a flow undergoing periodic motion that is not being driven by turbulence.

Schmid et al. [128, 129], Ramcke et al [110], and Schulze et al. [134] have used URANS models to study the response of single injection elements to subjected to acoustic forcing. Acoustic forcing was imposed via fluctuating mass source terms at the boundaries of the single injector numerical domain. Schmid et al. [129] studied the response of a cold flow supercritical nitrogen jet subjected to acoustic pressure fluctuations. A Peng-Robinson equation of state [99] was used to model real gas nitrogen. Deformation of the dense nitrogen jet was produced by the acoustic pressure disturbance. By studying a variety of injector configurations Schmid et al. identified a range of Strouhal numbers at which the jet would respond significantly to the imposed acoustic disturbance.

Schmid et al. [128] and Ramcke et al. [110] studied the response of coaxial hydrogen oxygen injection to acoustic disturbances using the same URANS excitation method as for the cold flow computations applied to a subcritical 10 bar combustion test case. Schmid

et al. [128] modelled a subcritical gaseous oxygen-hydrogen flame and studied the model's response to both pressure and velocity forcing. Fluctuations in heat release coinciding with acoustic pressure fluctuations were observed.

Ramcke et al. [110] modelled a gaseous hydrogen and liquid oxygen flame where the liquid flow was modelled as a cone representative of the potential liquid core. A Euler-Lagrange model was used to study LOX droplets being injected through the cone into the domain. Evaporation rate Transfer Functions (ETFs) describing the influence of the acoustic disturbance on the vaporisation of the liquid droplets and Flame Transfer Functions (FTFs) to characterise overall response of the flame were computed from the numerical results.

The same approach has more recently been used by Schulze et al. [134] as part of a combined CFD/CAA approach. The linear stability of four operating points of BKD were assessed by computing FTFs of BKD injectors subjected to acoustic pressure and velocity disturbances from URANS results. The species were modelled as an Euler continuum using the Soave-Redlich Kwong equation of state [147] for real gases. Turbulent combustion was modelled using an Eddy-Disipation Model (EDM) with 2-step chemistry. The resulting FTFs from the URANS computations were used in a Computational Aero-Acoustics solver to assess the linear stability of the system. The same method has been employed to study BKD by Kaess et al. [65], and to study the response of NTO/MMH injection to acoustic disturbances [125, 126, 127].

URANS single injector model results have not yet been validated against experimental data. It is therefore unclear if the URANS models capture the flame dynamics sufficiently to describe the flame response and if the resulting FTFs used for the subsequent hybrid CFD/CAA analysis are representative of the physical system. The ability of URANS to propagate acoustic disturbances at the frequencies of interest has also not been demonstrated. These issues need to be addressed before URANS models can be relied upon for further combustion instability analysis and research.

LES models

Large Eddy Simulation (LES) is the highest-order modelling approach that has currently been applied by multiple research groups to study combustion instability phenomena. LES has been applied to study specific test cases of interest or fundamental experiments to provide further insight into physical phenomena than can be observed experimentally. Recent LES modelling by Urbano et al. [153] of the BKD are the first LES computations of a representative subscale combustor. However Urbano et al. [153] note that a coarse LES grid was used to reduce the computational cost and permit multiple computations.

Examples of LES applied to rocket engine combustion instability are the research activities undertaken by JAXA [79], by Purdue University [54, 86, 139, 146], and by various french research organisations using the AVBP LES code jointly developed by Cerfacs, IFPEN, and EM2C [153, 41, 42, 33]. The work of the french research groups is the most comprehensive, with focused research to address acoustic boundary conditions[113, 102, 68, 137], validation against cold flow experiments [33, 132], single injector studies[42], and modelling of representative sub-scale systems at supercritical pressures[41, 152, 153]. Other researchers have focused directly on applying LES tools to study combustor experiments with naturally excited instabilities.

Selle et al. [137] explain that the acoustic reflectivity of CFD boundary conditions requires special consideration to ensure they do not change the resonant modes of the system or introduce additional disturbances. Proper acoustic boundary conditions are a particular challenge for LES due to the low level of numerical dissipation allowing disturbances to persist within the numerical domain for considerable periods of time. For many purposes non-reflecting boundary conditions are desired and an approach based

on characteristic treatment of the Euler equations was devised by Poinsot and Lele [102]. Kaufmann et al. [68] extended this approach to work with boundary conditions for imposing acoustic excitation via flow forcing. Rey et al. [113] developed boundary conditions for studying transverse acoustic motion by modulating the flow velocity on alternative sides of the numerical domain. This numerical excitation method has since been employed in a number of studies using AVBP [33].

Schmitt et al. [132] and Gonzalez-Flesca et al. [33] studied the response of coaxial transcritical nitrogen injection subjected to external acoustic excutation using AVBP. Varicose motion - fluctuations in the jet thickness - was identified both experimentally and as axisymmetric vortex shedding in the LES results when the jet was positioned in a pressure antinode. Transverse acoustic velocity forcing produced a sinusoidal motion of the jet and asymmetric vortex shedding. The inner liquid jet was found to be relatively insensitive to the imposed acoustic disturbance which was at almost double the frequency of the preferred mode of the jet. Schmitt et al. compared the LES results with experimental data from a specialised cold flow experiment. Gonzalez-Flesca et al. [33] modelled a configuration representative of MIC experiments but had no data for numerical validation.

Hakim et al. [41, 42] applied AVBP to model the LOx-methane MIC experiments at supercritical pressures. Both representative single injector [42] and full chamber models[41] were computed. The single injector models were used to predict the response to transverse acoustic forcing for Strouhal numbers of 0.8 and 3.2. The Soave-Redlich-Kwong equation of state to include real gas effects and a combustion model assuming equilibrium chemistry were employed. The chemical characteristic time for methane combustion (4×10^{-7} s) being smaller than the modulation period (125 μs) was used to justify the equilibrium chemistry model. A transverse acoustic disturbance was imposed using the method proposed by Rey et al. [113]. The MIC chamber model computed by Hakim et al. [41] included the VHAM configuration with the complete chamber internal volume, all five coaxial injection elements, and both exhaust nozzles. Acoustic forcing was imposed by modulating the flow exiting the domain through each of the nozzles analogous to the operation of the VHAM.

The LES results from Hakim et al. [42] predicted the vertical transport and retraction of the LOx core and flame during transverse excitation observed during MIC experiments. A strouhal number of 0.8 produced a sinusoidal structure with asymmetric shedding and large scale flapping of the light oxygen jet as counter rotating vortices are produced and convected downstream. Hakim et al. suggest that the counter rotating vortices increase mixing between the oxygen and methane streams with the frequency of vortex shedding dependant on velocity difference between the dense LOx core and lighter outer gaseous streams. A Strouhal number of 3.2 produced asymmetric corrugations on the surface of the LOX core while the center of the jet was largely unaffected. The dense jet is rapidly flattened and smaller counter rotating vortices are produced at its edges.

Hakim et al. [42] resolved the local heat release and used it to compute Rayleigh index distributions. The near injector region where the flame remains cylindrical was found to be the most important as the difference in velocities between the two propellant streams leads to higher strain rates. Similar results were produced for the multi-injector configuration. The results from the chamber model were compared with experimental optical data and measurements and good qualitative agreement was obtained. The LES results were then further analysed and provided additional insight into the experiment such as the increased intensity of light emmision observed between flame elements caused by the flattening of the flame surface. Hakim et al. [41] report that 8.5 million CPU hours on high performance computing resources were required to compute the MIC chamber model.

The BKD LES model computed by Urbano et al. [152, 153] using the AVBP LES solver included the full 3D geometry of the chamber, all 42 injector elements, and all propellant

manifolds. Real-gas properties were modelled using the Soave-Redlich-Kwong equation with transport properties computed using the corresponding-state model of Chung et al. [12]. Oxygen-hydrogen combustion was modelled assuming equilibrium chemistry with a β-pdf model using the filtered mixture fraction as the progress variable.

The model was used to study one stable and one unstable BKD operating point. The LES model did not reproduce the spontaneously occurring instabilities observed experimentally and predicted that both points were stable. However Urbano et al. [153] produced self-supporting instabilities after applying an initial transverse acoustic disturbance distribution to perturb the model and trigger the instability. Using this method Urbano et al. were able to show that the unstable load point was stable until an initial disturbance with an amplitude of 8% P_{CC} was prescribed. Urbano et al. state that spontaneous occurrence of the instability may not be recovered due to the LES mesh, which was coarsened to reduce the computational requirements of the LES computations, and may not have being sufficiently resolved to reproduce driving mechanism. It is unclear if a similar triggering disturbance is produced by random combustion noise to trigger the instability during BKD experiments.

By analysing the spectrum and acoustic disturbance distribution in the LES results Urbano et al. [152] found that the first radial mode of the BKD chamber volume was simultaneously being excited and contributing to the instability. The excitation of the radial mode could not be identified experimentally due to the placement of pressure sensors in the experiment. Urbano et al. computed a local Rayleigh index for each injection element by considering a small control volume for each injector. The Rayleigh index results were used to compute FTFs. The FTFs were later applied in a Helmholtz solver which reproduced the 1T and 1R BKD modes identified in the LES [152].

LES has been applied by a number of groups to study the CVRC. The CVRC is an attractive numerical testcase as acoustic boundary conditions are defined by sonic conditions at the inlet and outlet of the chamber. The CVRC has been modelled by Smith et al. and Harvasinski et al. using DES (Detached Eddy Simulation) [146, 54] and hybrid RANS/LES [55] approaches, by Garby [29] using AVBP, and by Srinivasan et al. [149]. These studies identified an interaction between acoustic fluctuations and flow dynamics.

The CFD results from each group reproduced the instability observed experimentally and identified a vortex shedding phenomena at the end of the oxidiser post which supported the instability. Many of the aformentioned CFD studies used the CFD results to compute transfer functions for acoustic solvers which were then able to reproduce the acoustic frequencies and mode distributions. LES has also been applied to successfully model instability in the TIC by Shipley [139] and Morgan et al. [86] with results compared with optical data from the experiment.

LES results provide further insight into combustion instability phenomena that can be used to inform lower order modelling techniques. However only qualitative validation of LES results has been completed, partly due to the difficulty of quantitatively comparing LES results directly with instantaneous optical images. The high computational requirements of LES also forces researchers to make various compromises in grid resolution and sub-model complexity. Sardeshmukh et al. [124] found that detailed kinetic mechanisms are needed to accurately capture combustion response, while most of the LES computations previously discussed assume equilibrium chemistry. Current computational resources do not facilitate multiple large scale computations or parametric investigations with LES.

2.8 Research Gaps and Objectives

The background information provided in this chapter described the key topics relevant to this project and the current depth of experimental and numerical research on HF combustion instabilities. Due to the difficulty of collecting experimental data at representative conditions, limited insight has been gained from experimental investigations of rocket engine flames. The increased availability of computational resources has facilitated higher-order modelling which has provided additional insights and understanding. However, the models need to be validated before they can be used as predictive design tools with confidence. Data collected from BKH experiments provides unique opportunities to produce data and identify phenomena for validating numerical models. However a number of research gaps need to be addressed in order to prepare the data from BKH and other combustion instability experimental combustors to be suitable as numerical testcases.

The underlying acoustic and combustion processes must first be understood before coupling processes may be investigated. The previous analyses of optical data from BKH and other experiments have identified the structure and distribution of oxygen-hydrogen flames at supercritical pressures from line-of-sight experimental data. However complementary numerical modelling is needed to better understand the operation of each experiment and to further interpret the line-of-sight experimental data. These models must capture the trans-critical injection and combustion of oxygen-hydrogen propellants. The models must also be robust and computationally inexpensive to facilitate parametric studies to inform the design of new rocket engine combustion chambers.

Methods for predicting and reconstructing the acoustic disturbance excited during a combustion instability are still limited. Previous analysis of BKH and other experimental data has focused on scaling idealised eigenmode solutions to sensor data to reconstruct the acoustic field. The eigenmode solutions are only valid at specific resonant frequencies. They also do not capture acoustic damping which is needed to accurately characterise the phase difference between acoustic and combustion processes.

To validate numerical results high quality experimental data is needed. However the analysis of optical data has focused on instantaneous analysis of individual frames or filtered optical data. This analysis has identified the motion and response of the flame but not in a consistent or statistically relevant manner useful for numerical validation. Methods for comparing the observed response to the local acoustic fluctuations are needed to identify key features to be reproduced numerically and their phase relationship to the local acoustic disturbance.

Finally, validated models that can reproduce the flame response to acoustic excitation are needed. These models can be used to produce further insight into the flame response and to produce response functions to inform lower-order modelling approaches. A validated approach that is less computationally expensive may allow more rapid research and development. URANS models have been previously applied for this purpose, but have not yet been validated against experimental data.

2.8.1 Thesis Objectives

The objectives of this thesis address the identified research gaps by studying BKH as an experimental and numerical testcase. The objectives are:

- To model the BKH flowfield and flame structure using a RANS model with real-gas capability to providing further insight into the experiments and demonstrating the applicability of the employed modelling approach to study trans-critical injection of oxygen-hydrogen propellants at supercritical pressure,

- To develop methods for experimentally reconstructing and numerically predicting the local acoustic disturbance acting upon the flame zone in BKH,
- To process BKH optical data to isolate the mean response of the flame to acoustic excitation and produce results for numerical validation, and
- To model the response of a BKH injection elements to acoustic excitation and to compare the results with data from BKH experiments.

The methods and modelling approaches developed to meet these objectives are designed to be generally applicable to other combustion instability experiments. The results will provide further insight into the BKH experiments and combustion instability phenomena.

Chapter 3

Steady-state Modelling

Before investigating the interaction of acoustic and combustion processes the unexcited steady-state operation of the BKH chamber must first be understood. A 3D steady-state CFD model of the chamber would allow the flowfield to be investigated in detail. The numerical results would also allow further interpretation of the line-of-sight experimental data. For the model results to be relied upon, it must capture the trans-critical injection and combustion of oxygen-hydrogen propellants and reproduce the features identified in BKH experimental datasets.

In this chapter a specialised release of DLR TAU code is employed to compute a steady-state model of BKH. The specialised release includes a real-gas model for accurately capturing the change in properties of cryogenic liquid oxygen as it is injected into a combustor at supercritical pressures. The model results provide further insight into the BKH flow field than is available from the experimental data alone. In particular, the effect of the secondary hydrogen and window cooling flows on the resulting flame distribution produced by the primary injection elements is investigated. The application of this model to BKH serves to demonstrate its ability to describe the flow and relevant processes before applying the same model to investigate the flame response to acoustic excitation in Chapter 6. The acoustic property distributions from the steady-state model are also used in later chapters to model the acoustic field.

This chapter begins by first describing the specialised release of the DLR TAU code and its application to modelling LOx/H2 combustion. The modelled operating point and numerical setup of the steady-state combustor model is then defined. The results of the steady-state chamber model are presented and relevant flow field features are identified. The numerical results are compared against optical data from an equivalent BKH experiment.

3.1 CFD Solver: The DLR TAU code

The DLR TAU code is an in-house CFD code developed by the DLR. The standard release of the TAU code has an perfect gas flow solver for the compressible Euler and Navier-Stokes equations. It uses a Godunov-type finite-volume method and works with hybrid structured-unstructured grids. As such the TAU code is capable of modelling viscous or inviscid flows, complex geometries, and low subsonic to hypersonic flow regimes. The TAU code also features grid partitioning algorithms for parallel computing. The DLR TAU code has been validated for a range of steady and unsteady flow cases [31, 77, 135, 136] and is further described in [43, 67, 136].

Turbulence models ranging from RANS one- and two-equation models to Detached and Large Eddy Simulations have been implemented in TAU. The one-equation Spalart-Allmaras [148] turbulence model was selected for the current work due to its simplicity

and ease of implementation. This turbulence model yields satisfactory results for a wide range of applications while being numerically robust and computationally inexpensive. The Spalart-Allmaras model is known to over-predict the spreading rate when modelling round jet free shear flows but captures mixing layer flows well [6, 163].

Second order spatial accuracy is obtained using a MUSCL [154] reconstruction. Stabilization, if necessary for the computation of high density ratio shear layers, is carried out by reducing the spatial order to 1.95. The acceptable small increase of numerical dissipation was required to stabilize the solution and to damp oscillations in the vicinity of large density gradients. For the current work an explicit 3rd order Runge-Kutta scheme was used for time integration. A MAPS+ Riemann solver by Rossow [121] is also used to handle the low Mach number flows and high density gradients which are a challenge to a compressible flow solver.

In the current study a specialised release of the TAU code [4] is employed to model injection and combustion of cryogenic propellants. This specialised release has two main extensions to the standard TAU code to provide the necessary functionality: A finite-rate chemistry model to model combustion processes, and a real gas capability to model injection of cryogenic propellants. The model and these capabilities are described in the following sections.

3.1.1 Governing Equations

In this model the flow is treated as a reacting mixture of thermally perfect gases and one real gas component. A dedicated transport equation is solved for each chemical species S. The governing equations are the Navier-Stokes equations for a mixture of compressible ideal reacting gases. The equations can be written in their integral form as:

$$\frac{\partial}{\partial t}\int_V \vec{U}\mathrm{d}V + \int_S \vec{F}^{inv} n\mathrm{d}S = \int_S \vec{F}^{visc} n\mathrm{d}S + \int_V \vec{Q}\mathrm{d}V \tag{3.1}$$

where, in the case of thermal equilibrium, $\vec{U}$ is the vector of conservative variables:

$$\vec{U} = \begin{pmatrix} \rho_s \\ \rho\mathbf{V}^T \rho E \end{pmatrix}, \tag{3.2}$$

$\vec{F}^{inv}$ is the matrix of inviscid (Euler) fluxes:

$$\vec{F}^{inv} = \begin{pmatrix} \rho_s\mathbf{V}^T \\ \rho\mathbf{V}\mathbf{V}^T \\ \rho E\mathbf{V}^T \end{pmatrix} + \begin{pmatrix} 0 \\ pI_n \\ p\mathbf{V}^T \end{pmatrix}, \tag{3.3}$$

$\vec{F}^{visc}$ is the matrix of the viscous (Navier-Stokes) fluxes:

$$\vec{F}^{visc} = \begin{pmatrix} \rho D\nabla\frac{\rho_S}{\rho} \\ P_v \\ \kappa\nabla^T T + \rho D\sum_S h_S \nabla^T \frac{\rho_S}{\rho} + (P_v\mathbf{V})^T \end{pmatrix}, \tag{3.4}$$

and $\vec{Q}$ is the source vector describing the contribution from chemical reactions:

$$\vec{Q} = \begin{pmatrix} \omega_S \\ 0 \\ \dot{q} \end{pmatrix}. \tag{3.5}$$

The viscous stress tensor P_v is modelled according to stokes hypothesis:

$$P_v = \mu\left(\nabla\mathbf{V}^T + (\nabla\mathbf{V}^T)^T\right) - \frac{2}{3}\mu(\nabla^T\mathbf{V})I_n. \tag{3.6}$$

The system is closed via an equation of state, such as the ideal gas equation:

$$p = \sum_S \rho_S R_S T. \tag{3.7}$$

3.1.2 Laminar Transport Coefficients

Karl [67] describes the calculation of the laminar transport coefficients in the TAU code. The laminar viscosity of each species is calculated using Blottner curve fits [39].

$$\mu_S = 1 \left(\frac{N_S}{m^2}\right) \mathrm{e}^{C_S T^{(A_s \ln(T) + B_S)}} \tag{3.8}$$

The laminar viscosity of the mixture is then computed using the mixture rule of Wilke[164].

$$\mu = \sum_S \frac{n_S \mu_S}{\sum_m n_S \phi_{S,m}} \tag{3.9}$$

with

$$\phi_{S,m} = \frac{1}{\sqrt{8}} \left(1 + \frac{M_S}{M_m}\right)^{-1/2} \left[1 + \left(\frac{\mu_S}{\mu_m}\right)^{1/2} \left(\frac{M_m}{M_S}\right)^{1/4}\right]^2 \tag{3.10}$$

The thermal conductivity of each species is computed via the Eucken correction [22] in the modified version of Hirschfelder [57].

$$\kappa_S = \mu_S \left(\frac{5}{2}(c_v)_S^{\mathrm{t}} + \frac{(c_v)_S^{\mathrm{rot}} + (c_v)_S^{\mathrm{vib}} + (c_v)_S^{\mathrm{e}}}{\mathrm{Sc}}\right) \tag{3.11}$$

The total heat conductivity of the mixture is computed using the mixture rule of Zipperer and Herning[172].

$$\kappa = \sum_S \frac{n_S \kappa_S}{\sum_m n_S \sqrt{M_m / M_S}} \tag{3.12}$$

The diffusion fluxes are calculated from the viscosity and a constant Schmidt number using Fick's law. The diffusion coefficient D is then calculated via:

$$D = \frac{\mu}{\rho} \frac{1}{\mathrm{Sc}} \tag{3.13}$$

3.1.3 Finite-rate Chemistry Model

The finite-rate chemistry model in the TAU code is described by Hannemann [43] and Karl [67]. a brief summary of the model is presented here.

The chemical sources ω_S in Equation 3.5 are produced by sets of chemical reactions involving the species X_S and the stoichiometric coefficients α_S and β_S:

$$\sum_S \alpha_S^r X_S \underset{k_r^f ; k_r^b}{\longleftrightarrow} \sum_S \beta_S^r X_S. \tag{3.14}$$

A chemical source term, ω_S for each species is computed from the law of mass action by summation over all participating reactions:

$$\omega_S = M_S \sum_r (\beta_S^r - \alpha_S^r) \left[k_r^f \prod_S (n_s)^{\alpha_S^r} - k_r^b \prod_S (n_s)^{\beta_S^r}\right], \text{where } n_S = \frac{\rho_S}{M_S}. \tag{3.15}$$

The forward reaction rate is evaluated using a modified Arrhenius law:

$$k_r^f = a_r^f \left(\frac{T}{1\mathrm{K}}\right)^{b_r^f} \exp\left(-\frac{c_r^f}{T}\right). \tag{3.16}$$

Where a_r^f, b_r^f, and c_r^f are the Arrhenius coefficients. The backward rate is determined from the equilibrium constant:

$$k_r^b = \frac{k_r^f}{K_r^{eq}}. \tag{3.17}$$

The equilibrium constant is determined from the partition functions of the participating species:

$$K_r^{eq} = \prod_S \left(\frac{Q_S}{VN_A}\right)^{\beta_S^r - \alpha_S^r}. \tag{3.18}$$

Hannemann [43] describes the use of partition functions in the TAU code.

3.1.4 Kinetic Scheme

A six-species and seven-step reaction scheme for oxygen-hydrogen combustion published by Gaffney et al. [28] has been used in the current work. This kinetic scheme includes the species H_2,O_2,H,O,OH, and H_2O. The Arrhenius coefficients and third body efficiencies of the reaction mechanism are summarised in Appendix A.1. The results with this kinetic scheme were compared against those produced using a more detailed mechanism with 8 species and 17 reactions first published by Jachimowski [63] and described by Lempke et al.[75]. Negligible differences in the results were found when including the trace species H_2O_2 and HO_2 in the detailed mechanism and the reduced 6 species mechanism was therefore deemed suitable for the current work.

The existence of other species within the combustion chamber is ignored in the present work. This is justified, as the chamber is purged briefly before each test with gaseous hydrogen. The only other species that may be present within the combustion chamber in significant quantities is Nitrogen. Nitrogen is used to pressurize the oxidizer tank of the P8 testbench, and the injected LOx therefore contains a small percentage of nitrogen. While nitrogen is known to participate in third body reactions with oxygen and hydrogen species, this effect is assumed to be small and is ignored in this work.

3.1.5 Turbulent Combustion Modelling

The effect of turbulence on combustion processes must also be considered. Karl [67] implemented a Gaus-β pdf turbulent combustion model in the DLR TAU code based on the model by Gerlinger et al [32]. However, Lempke et al. [76] reported that the turbulent combustion model did not significantly alter the results of computations with finite rate chemistry for oxygen - hydrogen combustion. Similar results have been shown more recently by Karl when modelling the Penn State combustor experiment using the DLR TAU code [62]. For this reason an explicit turbulent combustion model is not used in the current work.

Turbulence combustion interaction is implicitly included in the current modelling approach by the addition of a turbulent contribution to the laminar diffusion coefficient and thermal conductivity for each species. This approach is described by Karl [67]. In the transport equation for each species S the diffusion flux is modelled using Fick's law. An averaged Diffusion coefficient D is prescribed for all species using the viscosity, μ, and a constant Schmidt number, Sc.

$$-\rho D \nabla \frac{\rho_s}{\rho} = -\left(\frac{\mu}{Sc}\right) \nabla \frac{\rho_s}{\rho} \tag{3.19}$$

The employed Spalart-Allmaras turbulence model describes turbulence using an eddy viscosity term, μ_T. The increase of diffusion velocities in the presence of turbulence is modelled by adding the turbulent contribution, $\frac{\mu_T}{Sc_T}$, to the laminar diffusion coefficient:

$$-\rho D \nabla \frac{\rho_s}{\rho} = -\left(\frac{\mu}{Sc} + \frac{\mu_T}{Sc_T}\right) \nabla \frac{\rho_s}{\rho}. \tag{3.20}$$

Increased turbulence causes an increase in the species diffusion velocities, increasing the rate at which propellants mix, which increases the rate of combustion. Combustion of oxygen and hydrogen under the investigated conditions is essentially an equilibrium process and can be assumed to be infinitely fast. Unsteady variations of the temperature therefore have only marginal effect on reaction rates. This means that the rate controlling process is the turbulent mixing process which provides the reactants to the reaction zone. By modelling the transport of the species individually the significant rate controlling step is captured in the numerical model.

Turbulence also acts to increase the local thermal conductivity. In the employed release of the DLR TAU code the influence of turbulence on the thermal conductivity was computed by adding a turbulent contribution κ_T to the laminar thermal conductivity κ. The turbulent contribution to the thermal conductivity is computed via:

$$\kappa_T = \kappa_{lam} \frac{\mu_T}{\mu_{lam}} \frac{\mathrm{Pr}_{lam}}{\mathrm{Pr}_T}. \tag{3.21}$$

The Prandtl number ratio $\mathrm{Pr}_{lam}/\mathrm{Pr}_T$ is the ratio of the laminar Pr_{lam} and turbulent Pr_T Prandtl numbers. The Prandtl number ratio is prescribed as a parameter of the model.

This approach for computing the turbulent thermal conductivity is a legacy of the combustion model's original implementation focused on supersonic combustion modelling. The approach is different to that employed by other groups using RANS and URANS approaches for modelling oxygen-hydrogen flames that typically specify a constant turbulent Prandtl number and compute the turbulent thermal conductivity using this value. The currently implemented approach permits the turbulent Prandtl number to change as the laminar properties of the mixture vary. A limitation of the current implementation is that the Prandtl number ratio is specified as a single model parameter and is therefore constant over the entire computational domain. The choice of the Prandtl number ratio was found to have a significant impact on resulting flame temperature and break-up of the LOx core in the numerical model. A Prandtl number ratio of 2 was prescribed in the current work. This Prandtl number ratio was found to result in reasonable flame temperatures and jet breakup that agreed with experimental observations. Further development and a more involved treatment of the problem of modelling turbulent thermal conductivity is outside the scope of the current project.

A limitation of the assumptions inherent in the employed RANS and URANS modelling approaches in this work is that the unsteady flame surface will not be resolved in detail. Instantaneous fluctuations in the flame surface will be averaged over time and only the fluctuations of the mean properties will be resolved. The flame front predicted by the RANS model represents a statistical mean of the flame position and flow field properties. This model also neglects the effect of fluctuations finer than the grid scale on chemical production rates. Excluding such fluctuations may be partly responsible for higher flame temperatures.

3.1.6 Real Gas Capability

As previously described in Section 2.1 cryogenic oxygen at supercritical pressures exists as a supercritical fluid with a single phase. As cryogenic oxygen is heated its density decreases in a processes referred to as pseudo-boiling. The change in properties of oxygen, and in particular the high density of LOx, is not accurately described using an ideal gas equation of state. These effects may be captured by modelling the properties of the fluid using a real gas equation of state.

A real gas equation of state was first implemented in the DLR TAU code by Calvo [7]. The original implementation modelled a single species and was focused on studying cooling channel flows of a single species. Banuti [2, 4] extended the real gas capability in the TAU code for modelling multiple reacting species in order to model rocket engine combustion chambers. A specialised release of the TAU code with the real gas capability implemented by Banuti is used in the current work.

Banuti [2, 4] explains that there are two distinct features of the current real gas implementation in TAU: A dedicated equation of state is used for each species, and a multi-fluid mixing model is used to determine the properties of the mixture. The dedicated equation of state for each species allows those species that are not reasonably approximated by an ideal gas equation of state to be modelled using their own dedicated equation of state. Those species that can be approximated as ideal gases may therefore still be modelled using a computationally inexpensive ideal gas law. With this approach only the high fidelity and computationally expensive equation of state is used for those species that require it. The real gas properties are precomputed and stored in a tabular library that is iterated over during runtime. Precomputing the library reduces the time needed to evaluate the equation of state allows a high fidelity real-gas equation of state to be used with no additional computational cost.

Once the properties of each species have been determined using an appropriate equation of state, the properties of the mixture are computed using a mixing model. The current real gas implementation uses a multi-fluid mixing model which is an extension of the two-fluid mixing model described by Pfennig [100] extended to multiple species. The thermodynamic variables are computed in a mass weighted fashion.

$$\phi_{\text{mix}} = \frac{\sum_i \rho_i \phi_i}{\sum_i \rho_i} \tag{3.22}$$

where ρ_i and ϕ_i are the partial densities and individual species properties, respectively. The employed multi-fluid mixing model is different to the more commonly used single fluid mixing models which describe a virtual pure fluid that exhibits the same properties as the mixture. Single fluid mixing models evaluating fluid coefficients a, b, and the specific volume v as a weighting factor in a single equation of state describing the virtual pure fluid. The difference between single- and multi-fluid mixing models is illustrated in Figure 3.1.1.

The multi-fluid mixing model assumes that the mixture can be described by the implemented ideal mixing laws which limit its wider applicability. The single fluid mixing model is valid for general mixtures of real components and can model mixing of inert propellants with real gas properties, while the multi fluid mixing cannot. The multi-fluid model is therefore only applicable for modelling mixtures where real-gas effects only need to be considered in a pure-fluid state, and not for predicting the properties of cold transcritical mixtures. However, the application of the multi-fluid mixing model in the current work to oxygen-hydrogen combustion is physically justified. Numerical studies by Oefelein [93, 94] have noted the flame produced by a coaxial injection element in an oxygen-hydrogen liquid propellant rocket engine effectively isolates the fuel and oxidiser streams. This agrees with similar experimental observations made by Oschwald et al. [98]

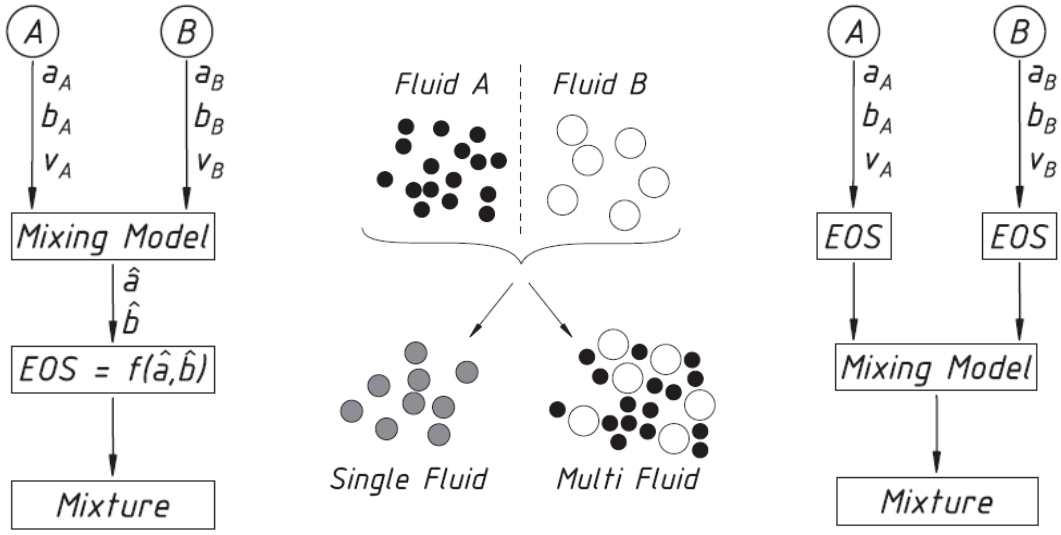

(a) Single Fluid Mixing Model (b) Multi Fluid Mixing Model

Figure 3.1.1: Illustration of Single Fluid Mixing and Multi Fluid Mixing models [4].

and many others. Numerical studies of representative reactive cryogenic shear layers [9] by Bellan and 1D counterdiffusion flames by Ribert et al. [115] and Lacaze et al. [72] have shown that mixing in the hot reaction zone occurs under ideal gas conditions.

Banuti et al. [4, 1] found that, for oxygen-hydrogen combustion at supercritical pressures, the LOx transitions from a liquid-like to a gaseous state under pure fluid conditions, where essentially all real fluid effects are confined to the LOx core. Thus for diffusion flames as encountered in the present work, ideal mixing is an appropriate model.

The fluid in the numerical domain is assumed to exist as a continuous Eulerian mixture with no discrete phases or phase changes. This approach is sometimes referred to as an Euler-Euler or continuum-based model. Recent work from Oefelein and colleagues has addressed the lack of a proper definition of the transition from two-phase flow to diffusion-dominated mixing. They developed a theory to explain the mechanisms of transition at the boundary between multicomponent fluids [18]. The model is based on a Knudsen-number criterion, and shows that at high subcritical temperatures the interface thickens and the mean free molecular path decreases, causing the interface to enter the continuum length scale regime where transport processes dominate and the phase transition is continuous.

When applied to the oxygen-hydrogen system for the range of typical liquid-propellant rocket engine conditions, the model predicts the persistence of classical, two-phase spray dynamics up to high supercritical pressures for hydrogen temperatures below 350 K[19]. The operating point focused on in this study, with a chamber pressure of 60 bar and a hydrogen injection temperature of 280-300 K, is below the theoretical Knudsen number threshold of $Kn = 0.1$. Below this threshold diffusion dominated mixing occurs and the assumption of a continuous Eulerian mixture is valid. The nature of the transition phenomena precludes the use of classical real-gas thermodynamics to calculate transport properties, which means no information is yet available on the time scales of the transition process [17]. Such information would be required to be able to formulate models capturing the effect in continuum-based CFD approaches.

In this work an ideal gas equation of state is solved for the species H_2, OH, H_2O, O, and H, while the only species treated with a real gas equation of state is oxygen, O_2. Real gas properties for oxygen are computed from the high fidelity modified Benedict-Webb-Rubin equation of state of Younglove [166], described in Appendix A.2. Thermodynamic state variables, such as pressure, enthalpy, heat capacities, and speed of sound, are all computed consistently from the real gas equation of state and stored in a library during

a preprocessing step. Real gas corrections to the transport coefficients are evaluated following Lemmon and Jacobsen [74].

The real gas model and its validation is further described by Banuti et al. [2, 4]. The model has been validated by comparison with NIST, 0D vaporization of liquid oxygen, 1D combustion with CEA, and real gas injection of the A60 Mascotte single injector test chamber. Its application to study BKH in the current work is the first application of the model to a multi-element oxygen-hydrogen combustor operating at supercritical conditions.

3.2 CFD Model Description

In this section the application of the numerical method described in the previous section to the BKH combustor is described. The operating point of the BKH experiment to be modelled is first defined. The geometry of the numerical domain and boundary conditions used for the computations are then presented. The mesh used for the CFD computations is also described.

3.2.1 Operating Point Definition

As previously discussed in Section 2.6, BKH can operate at a range of pressures and ROFs. A single operating point was chosen to be the focus of the current work. This operating point corresponds to a chamber pressure of 60 bar and an ROF of 6 (referred to hereon as the 60 bar ROF 6 operating point). The 60 bar chamber pressure was chosen as it is the highest chamber pressure consistently reached during BKH experiments. This pressure is greater than the critical pressure of both propellants and is therefore trans-critical. By choosing this operating point with a pressure above the critical point of the injected propellants, the oxygen will be the only propellant species injected at a subcritical state. As previously discussed, it will quickly transition to a supercritical state upon entering the chamber and before mixing with other species. Therefore all species within the chamber can be assumed to exist as either a pure-fluid real-gas, or as a mixture of ideal and supercritical gases and the assumptions inherent in the employed Euler-Euler real gas model are justified.

The ROF value of 6 was chosen as it is the largest ROF reached during the BKH experiments and also the most representative of upper stage engines. An additional reason for selecting the 60 bar ROF 6 operating point was the availability of validation data from BKH experimental campaigns. Test data had been captured at the 60 bar ROF 6 operating point during multiple BKH tests providing the most comprehensive dataset for numerical comparison and validation.

The 60 bar ROF 6 operating point is reached by controlling the mass flow rates into the chamber. Table 3.1 lists the mass flow rates and properties of the propellant streams entering the chamber. The temperature and pressure of the propellants are measured prior to injection in the feed system domes. The chamber pressure is measured by a static pressure sensor located in the top wall of the chamber. The propellant mass flow rates are measured via upstream mass flow sensors on the P8 test bench. Additional values characterising the chamber operating point may be computed using the measured values defined in Table 3.1 and details of the chamber geometry. The calculated values are listed in Table 3.2.

Individual element mass flow rates are computed assuming an equal distribution of propellant between each of the elements. The injection density, velocity, and Reynolds numbers are computed assuming conservation of mass and that the injected propellants enter the chamber at the chamber pressure while still at the same temperature measured

Table 3.1: Propellant flow rates and properties defining the modelled operating point.

Measured Values		**Value**	**Unit**	**Uncertainty**
Combustion Chamber Pressure	P_{CC}	60.7	bar	±1%
Oxygen				
Mass flow rate	$\dot{m}_O$	566	g/s	±3%
Dome Temperature	T_O	127	K	±1.25 K
Dome Pressure	P_O	80.9	bar	±1%
Primary Hydrogen				
Mass flow rate	$\dot{m}_H$	95	g/s	±3%
Dome Temperature	T_H	279	K	±1.25 K
Dome Pressure	P_H	69.7	bar	±1%
Secondary Hydrogen				
Mass flow rate	$\dot{m}_{H2}$	933	g/s	±3%
Dome Temperature	T_{H2}	278	K	±1.25 K
Dome Pressure	P_{H2}	94.9	bar	±1%
Window Cooling Hydrogen				
Mass flow rate	$\dot{m}_{WC}$	260	g/s	±3 %
Dome Temperature	T_{WC}	281	K	±1.25 K
Dome Pressure	P_{WC}	86.3	bar	±1%

Table 3.2: Calculated values for the modelled operating point

Calculated Values		**Value**	**Unit**	**Uncertainty**
Oxygen				
Element mass flow rate	$\dot{m}_{Oi}$	113.2	g/s	±3%
Injection Density	ρ_O	955.1	kg/m^3	±1.4%
Injection Velocity	V_O	12.3	m/s	±4.4%
Injection Reynolds no.	Re_O	4.5×10^5		
Primary Hydrogen				
Element mass flow rate	$\dot{m}_{Hi}$	19	g/s	±3%
Injection Density	ρ_H	5.08	kg/m^3	±1.4%
Injection Velocity	V_H	412.0	m/s	±4.4%
Injection Reynolds no.	Re_H	2.7×10^5		
Secondary Hydrogen				
Element mass flow rate	$\dot{m}_{H2i}$	18.7	g/s	±3%
Injection Density	ρ_{H2}	5.10	kg/m^3	±1.4%
Injection Velocity	V_{H2}	380.19	m/s	±4.4%
Injection Reynolds no.	Re_{H2}	7.9×10^5		
Window Cooling Hydrogen				
Element mass flow rate	$\dot{m}_{WCi}$	13	g/s	±3%
Injection Density	ρ_{WC}	5.05	kg/m^3	±1.4%
Injection Velocity	V_{WC}	660.31	m/s	±4.4%
Injection Reynolds no.	Re_{WC}	3.1×10^5		
Primary Injector Properties				
Ratio of oxidiser to fuel	ROF	5.95		±3%
Velocity Ratio	VR	33.4		±8.8%
Momentum flux Ratio	J	5.95		±9.9%
Aerodynamic Weber no.	We	3.5×10^5		
Mean Chamber Properties				
Ratio of oxidiser to fuel	ROF_{CC}	0.44		±3%

at the propellant manifold. Therefore these values do not take into account heat transfer to the propellant between the dome and injection plane, pressure loses, and the resulting state of the fluid entering the chamber.

The primary injector properties listed in Table 3.2 were previously defined in Section 2.3.3 and are computed by considering only the primary oxygen and hydrogen flows passing through the five coaxial injection elements in the center of the chamber. As stated previously, the resulting ROF through the central injection elements is approximately 6. The calculated velocity and momentum flux ratios are somewhat higher but still representative of full scale systems. The calculated Aerodynamic Weber number has been computed assuming a value of surface tension of 4×10^{-3} N/m for the liquid oxygen stream. This value is based on a study by Vieille, Chauveau and Gökalp [155] who measured the surface tension of LOx droplets in helium atmospheres at supercritical pressures. The large value of the aerodynamic Weber number and Reynolds numbers suggests that, if multiple phases do exist, shear break up of the liquid jet would occur.

3.2.2 Numerical Domain and Boundary Conditions

The domain chosen for the steady-state model of the BKH combustor is shown in Figure 3.2.1. The domain features the large rectangular chamber volume and both the main and secondary nozzles. A volume downstream of each nozzle is included in the domain to ensure that the choked flow through the nozzle is captured. The outflow boundaries at each of the nozzle extensions are specified to be at atmospheric pressure. The nozzle extensions are representative of the BKH experiment which has no nozzle expansion section downstream of either the primary or secondary nozzles. The primary nozzle exit exhausts directly to open atmosphere and is therefore at atmospheric pressure. The secondary nozzle exhausts into a specially designed pipe within the excitation system housing that redirects the flow into the main exhaust. For the current work it is assumed the exit pressure at this boundary, which in actuality is in the excitation system housing, is also atmospheric. BKH is vertically symmetric and a symmetry plane in the XY plane is used to model one half of the chamber and reduce the size of the computational domain.

The BKH propellant feed system features a large number of injectors and distribution domes making the internal geometry very complex. A limitation of the current implementation of the DLR TAU code for real gases is that only a single species can be treated as a real gas. As oxygen was chosen to be treated as real gas species, all other species including hydrogen are modelled using an ideal gas equation of state. The ideal gas equation of state for hydrogen predicts the density of hydrogen at the temperatures in the hydrogen feed system with an error of 5-6%. This would introduce errors in the partial volume of the injected hydrogen and therefore modelling the pressure drop and flow through the various geometric features of the hydrogen feed system could not be accurately computed with the current model. For this reason only small sections before the injection plane of the primary, secondary, and window cooling injectors is included in the numerical domain. This also serves to reduce the size and complexity of the numerical domain. For the primary and secondary hydrogen injectors only the last 2 mm of each injector is included.

While the pressure drop along the oxygen post could be accurately modelled using the real gas model, it is not of particular interest for the steady-state operation of the chamber. To reduce the complexity of the model only 10mm of the primary oxygen injector is included in the numerical domain.

The boundary conditions imposed at each of the injection elements were specified to match the measured and calculated values in tables 3.1 and 3.2. Dirichlet boundary conditions were prescribed at each of the hydrogen injector inlets specifying the inlet density, velocity, and temperature. A mass flow boundary was prescribed at the oxygen inlet specifying the mass flow rate and injection temperature across the boundary. The

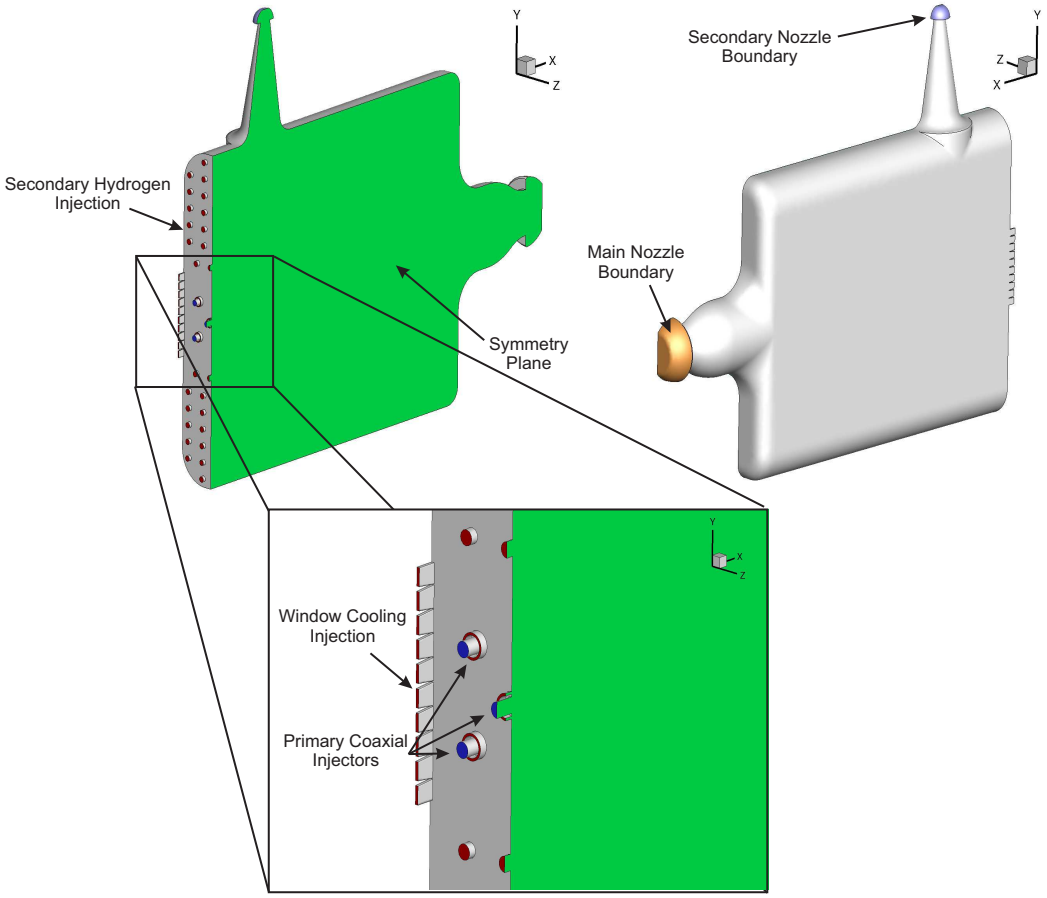

Figure 3.2.1: Domain used for steady-state chamber model.

flows through each of the separate hydrogen and oxygen arrays was therefore assumed to be divided equally amongst each of the injection elements.

All of the walls of the chamber were treated as adiabatic viscous walls. The viscous boundary conditions were found to affect the resulting flowfield significantly due to the high speed window cooling flow along either side of the chamber. The assumption of adiabatic walls is a limitation of the current implementation of TAU. In the BKH experiment the walls are actively cooled which would extract energy from the chamber and reduce the chamber pressure. Therefore the model results are expected to over-predict the chamber pressure.

3.2.3 Mesh

The numerical domain was meshed using the commercial meshing software Centaur. An unstructured mesh was used to simplify mesh development and to adapt to the various features of the BKH chamber such as its multiple nozzle geometries and multiple injection elements. A quadrilateral boundary layer mesh was prescribed to all viscous boundary surfaces. Tetrahedra elements were then used to fill the remaining volume of the numerical domain. The boundary layer mesh was found to be necessary to resolve the boundary layer flow along the walls of the chamber, particularly along the side walls of the chamber directly downstream of the window cooling injection array.

The size of mesh elements was controlled by defining various geometric sources. The sources were positioned around the flame zone and in particular near the LOx post tip of each injection element to resolve the flame. A stretching factor of 1.25 was defined for increasing the size of tetrahedra elements away from the refined regions. A maximum element size of 2 mm was defined for the mesh. The stretching factor and large element size lead to small regions of poor quality with high aspect ratios (>800) at locations away

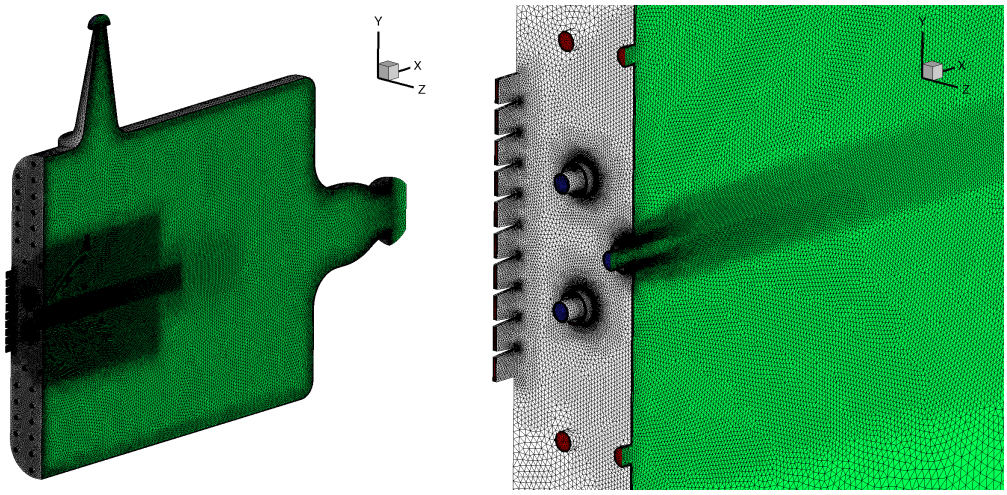

(a) Domain (b) Near injector region

Figure 3.2.2: Mesh used for steady-state chamber model.

from the primary flame zone. These aspect ratios were within acceptable limits (<1000 [139]) and a mesh refinement study demonstrated these regions had negligible impact on the final solution. The mesh is shown in Figure 3.2.2. The mesh has approximately 2.6 million nodes and 10.8 million elements. The mesh size and element distribution was selected based on experience modelling single coaxial injection elements under similar conditions.

Mesh independence was demonstrated by investigating different levels of mesh refinement using the same geometry. The mesh of the flame zone in the 100 by 50 mm window region directly downstream of injection was investigated separately on a representative sub-domain. Consistent results were produced on a mesh with approximately one third as many points in the primary flame zone. The length and structure of the LOx jets was consistent as was the resulting chamber pressure and flame distribution. The final mesh had the highest level of refinement which was used to better resolve the OH mass fraction distribution between the oxygen and hydrogen streams.

3.3 Numerical Results

A RANS steady-state model of the BKH combustion chamber was computed using the DLR TAU code. The steady-state model was initiated by interpolating a pre-computed and relatively inexpensive single injector model result to each of the BKH injection element positions and assuming a uniform mixture of combustion products throughout the rest of the numerical domain. The interpolated result converged relatively quickly as the flame and chamber pressure were already established within the numerical domain. This approach was suitable for time-averaged steady-state RANS computations as initial disturbances produced by discontinuities between the interpolated solution and the surrounding numerical domain were quickly dissipated by the numerical scheme. Convergence was assessed by a global normalized residual output from TAU which reduced by 3 orders of magnitude and by monitoring the convergence of the flame distribution, chamber pressure, and maximum flame temperature within the domain. The final result presented here converged after 200,000 iterations on the full chamber domain which required approximately 48,000 CPU hours on 16 Intel Xeon 5560 processors.

In this section results describing the BKH flow field and the modelled operating point are first presented. The flame zone downstream from the five primary coaxial elements is then studied in detail. The results of the steady-state model are compared against observations from the BKH experiments. The steady-state results are post processed for

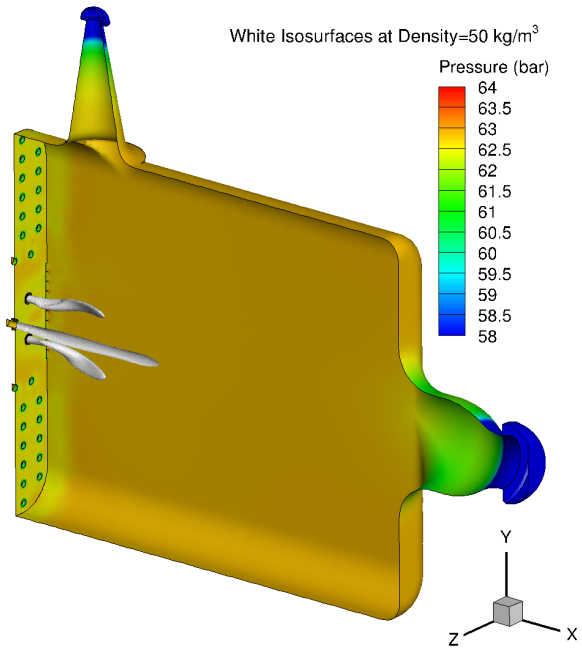

Figure 3.3.1: Pressure distribution with density isosurfaces showing position of LOx core.

comparison against optical data and the wall temperature distribution is compared with markings identified from inspection of BKH hardware.

3.3.1 Flow field

Figure 3.3.1 shows the pressure distribution throughout the chamber which is approximately uniform. The pressure at the equivalent position to the static pressure sensor measurement in the BKH experiment is 62.3 bar. This pressure is higher than the measured experimental chamber pressure (60.7 bar $\pm 1\%$). As previously discussed, the higher chamber pressure may be attributed to the adiabatic boundary conditions prescribed to the chamber walls. The walls are actively cooled during operation resulting in additional heat losses which would reduce the chamber pressure.

Density isosurfaces in the center of Figure 3.3.1 show the positions of the dense liquid oxygen core. As only half of the chamber was modelled only 2.5 LOx jets are shown. The dense liquid oxygen which enters the chamber propagates into the middle of the chamber as several individual jets. The central jet propagates directly along the centerline of the chamber and is longer than the outer jets. The outer jets are deflected towards the center plane of the chamber by the strong window cooling flow which will be discussed later in this section.

Figures 3.3.2 shows streamlines painted with temperature seeded at various locations across the chamber volume. The streamlines show that the flow field in BKH is stratified into 3 distinct layers. In the center of the chamber is the primary flame zone which causes a significant amount of recirculation and redirection of the flow as hot combustion products expand in the center of the chamber. The hot combustion products travel horizontally and exhaust through the main nozzle resulting in a central layer of high temperature combustion products. Above and below this layer is a cooler flow produced by the secondary hydrogen injection. The secondary hydrogen also flows horizontally across the chamber volume before redirecting to pass through the main nozzle with minimal recirculation in the downstream corners of the chamber. A small part of the secondary flow on the top of the chamber exits through the secondary nozzle.

Figure 3.3.3 shows the OH mass fraction distribution throughout the chamber. The

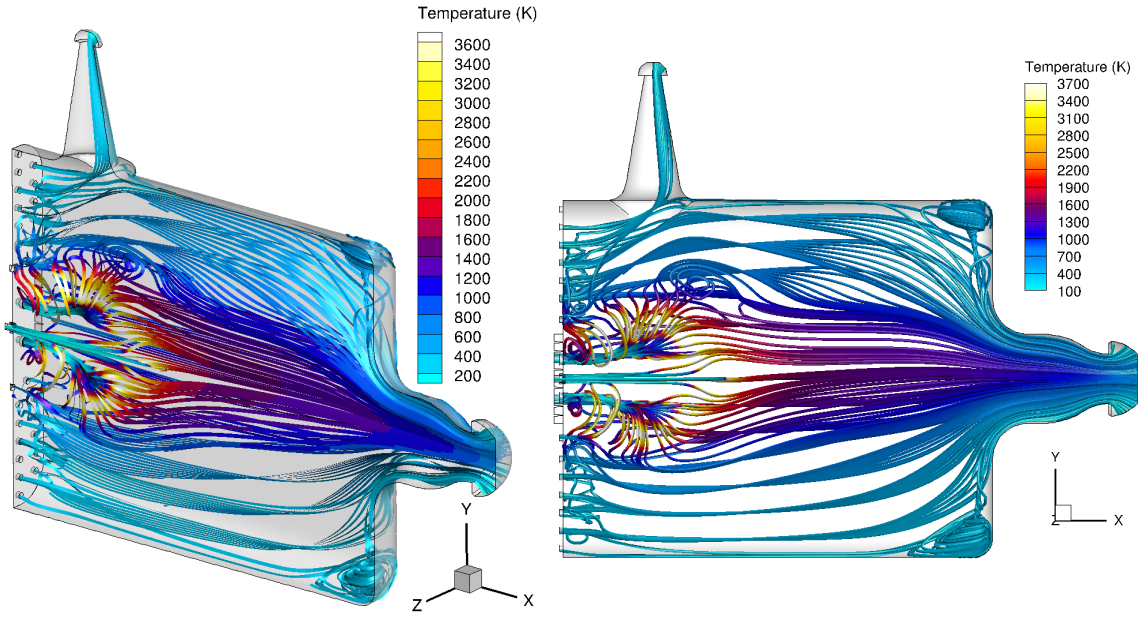

(a) Isometric View (b) Side view

Figure 3.3.2: Streamline plots showing chamber temperature distribution.

OH distribution is indicative of the flame position and envelopes the oxygen flow injected through the primary injection elements into the fuel rich chamber environment. While the individual injection elements can be distinguished near the injection plane, downstream the flames from different elements intersect, creating a single continuous OH mass fraction distribution. Figures 3.3.3a and 3.3.3b show an isosurface of the OH mass fraction distribution across the chamber volume. The isosurface shows that the flames from the outer primary injection elements follow the path of the dense oxygen jets, shown in Figure 3.3.1, and are similarly deflected towards the centerplane of the chamber. As the oxygen jets intersect, a single flame front is formed between the surrounding fuel rich chamber environment and the central flow of dense liquid oxygen.

OH* radiation is used as a marker of heat release in BKH and other combustion instability experiments. The heat release distribution of the steady-state model is shown in Figure 3.3.4. The heat release is calculated by considering the chemical source terms of each species in the finite rate chemistry scheme. Integrating the heat release over the chamber volume results in a net heat release rate of 4.4 MW or 8.8 MW for a complete chamber with 5 elements. This value agrees with values computed from CEA based on the flow rate of the injected propellants. The heat release distribution is shown with a logarithmic scale. Figures 3.3.3 and 3.3.4 show that the distribution of high heat release follows the position of the peak OH mass fraction distribution.

3.3.2 Flame Zone

The steady-state half chamber model result is mirrored at the centerplane to produce a result representative of the BKH experiment. Figure 3.3.5 shows density isosurfaces from the five primary coaxial elements. As previously mentioned, the outer jets are deflected towards the centerplane of the chamber. The deflection of the jets is attributed to the influence of the high speed window cooling flow along the side walls of the chamber. The X velocity distribution shown in Figure 3.3.5 shows the window cooling flow parallel to the primary injection elements.

Figure 3.3.6 shows the propagation of the dense oxygen jets and OH mass fraction distribution in the window region. The OH mass fraction distribution envelopes the oxygen distribution. The OH mass fraction distribution is very thin in the shear layer near the

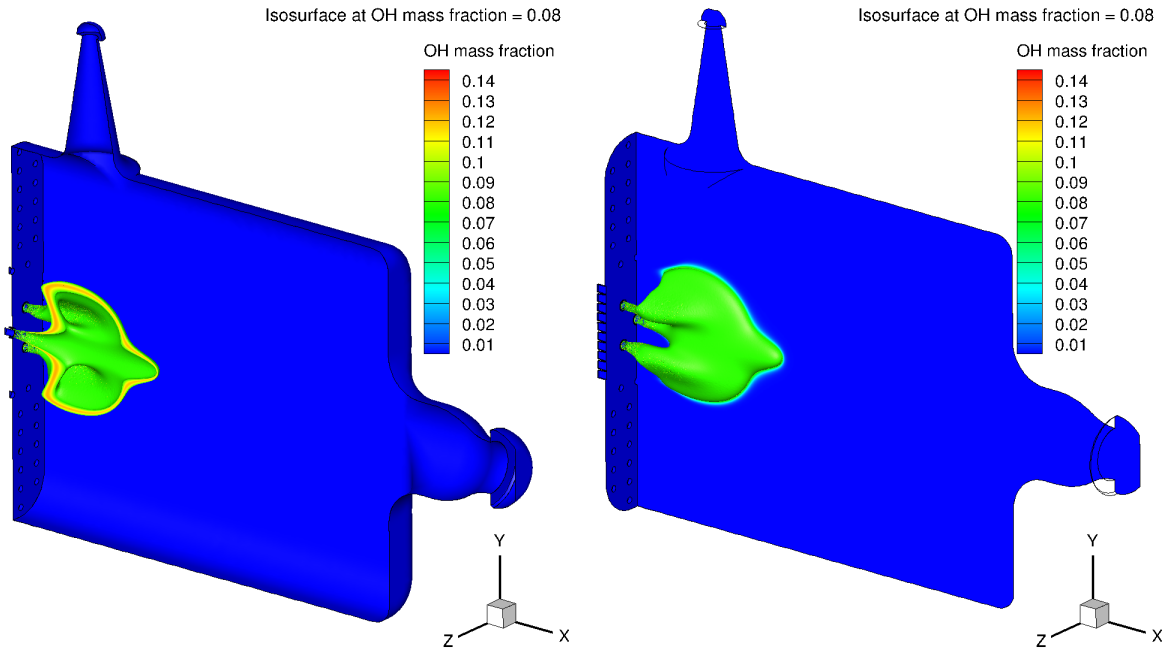

(a) Internal view (b) Outer view

Figure 3.3.3: OH mass fraction distribution of steady-state chamber model.

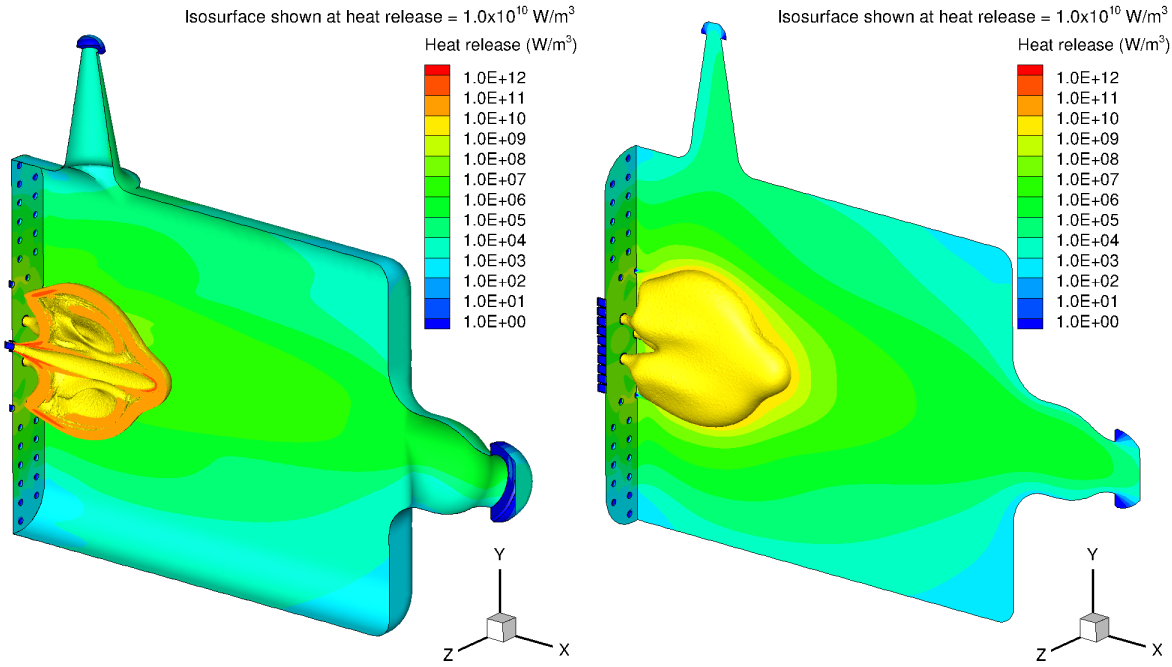

(a) Internal view (b) Outer view

Figure 3.3.4: Heat release distribution of steady-state chamber model.

injection plane, but thickens downstream as warmer gaseous oxygen mixes more readily with the surrounding fuel rich environment. The vertical distribution of the oxygen jets shown in 3.3.6b shows that the central element propagates almost undisturbed along the centerline of the chamber. The end of the central LOx core is slightly deflected towards the top of the chamber. The outer primary jets are vertically deflected away from the central jet. The top elements are deflected slightly further away from the central element by the additional flow out of the secondary nozzle at the top of the chamber. The deflection of the outer primary element flames is shown clearly in Figure 3.3.6a. This phenomenon cannot be observed from the line of sight imaging of the flame zone from BKH experiments.

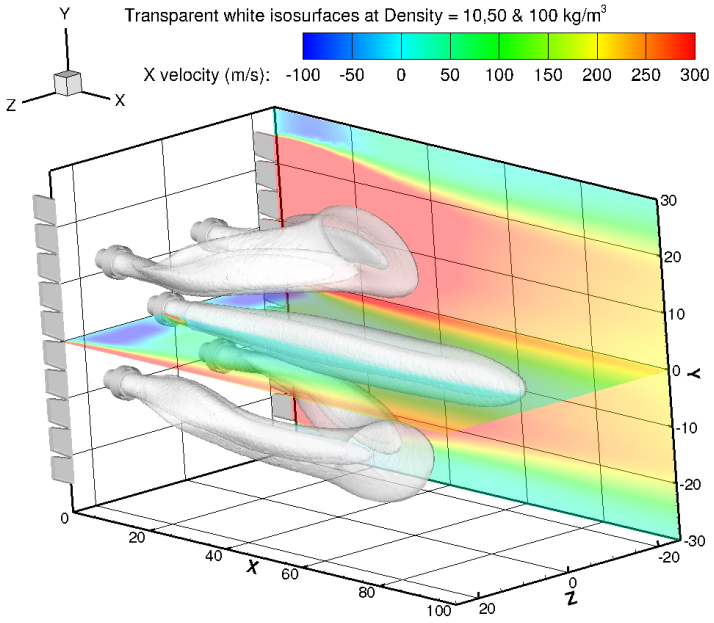

Figure 3.3.5: Isometric view of mirrored density distribution in center of chamber. Slices at horizontal center plane and side wall showing x velocity distribution.

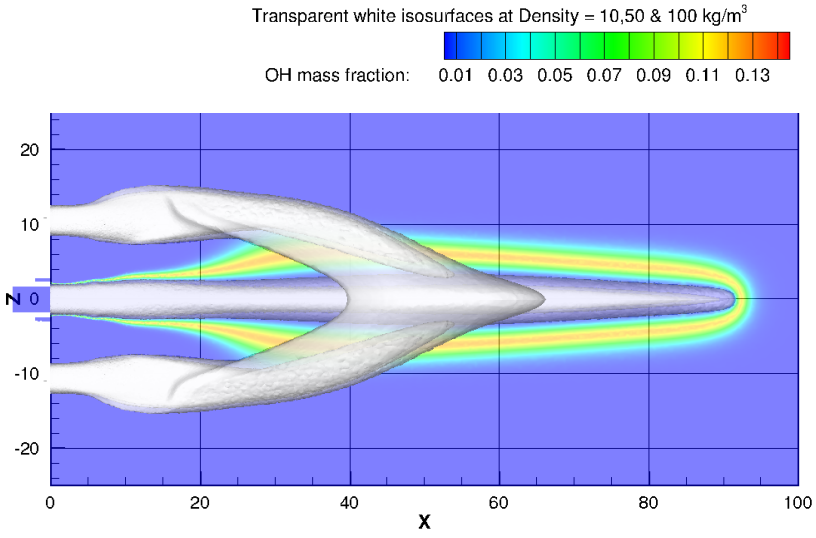

(a) Overhead view

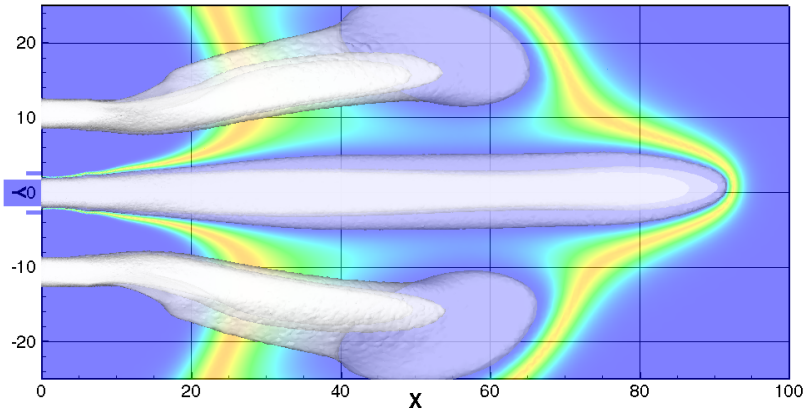

(b) Side view

Figure 3.3.6: Density isosurfaces and OH Mass fraction distributions at vertical and horizontal centerplanes.

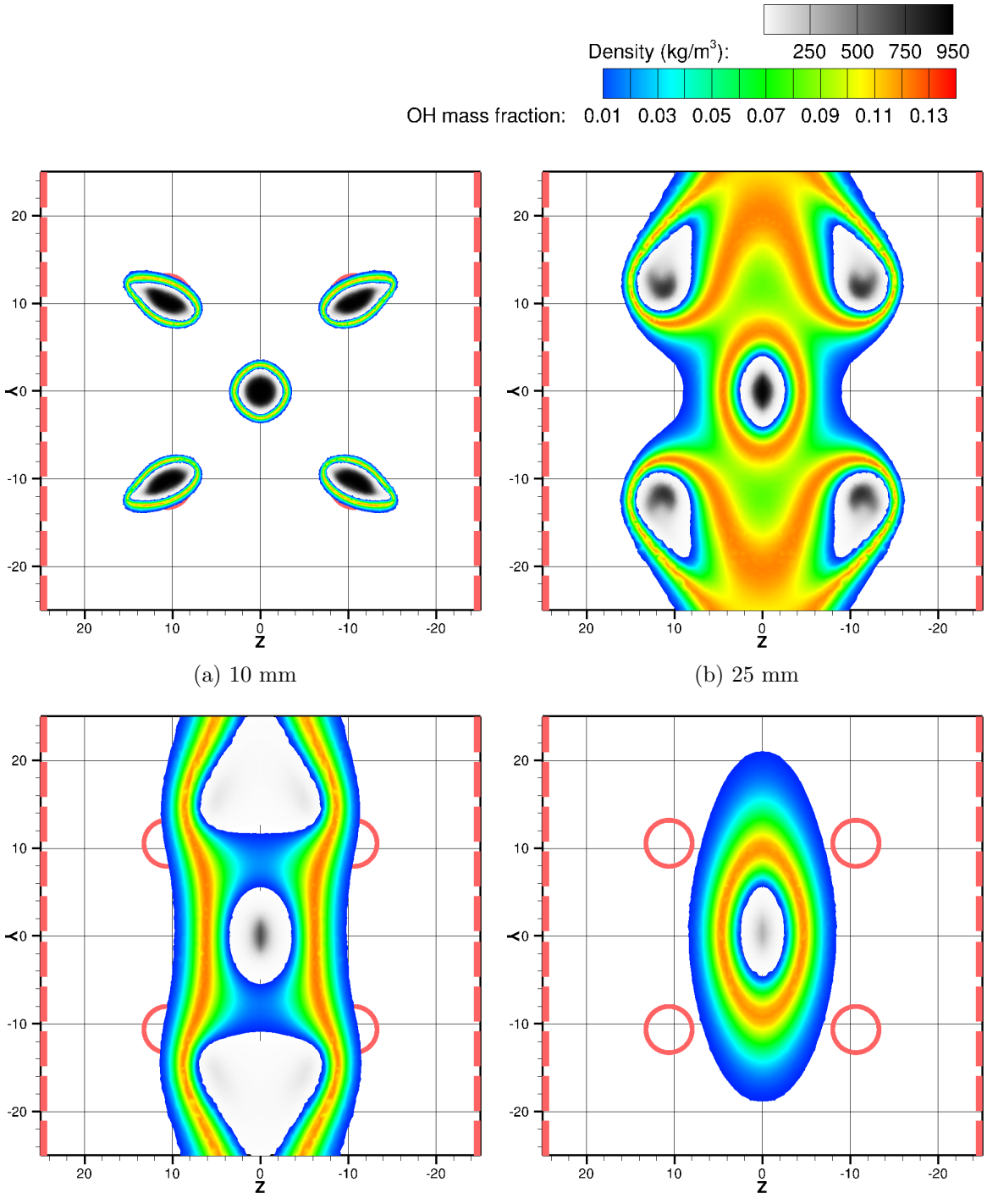

(a) 10 mm

(b) 25 mm

(c) 50 mm

(d) 75 mm

Figure 3.3.7: Slices showing mirrored OH mass fraction and density distributions at various distances from the injection plane. The hydrogen injection array is shown in red.

Comparing figures 3.3.6a and 3.3.6b it can be seen that the central element is broader in the horizontal than the vertical direction. This is again attributed to the strong window cooling flow and indicates that the outer primary elements do not perfectly protect the central element from the surrounding chamber flowfield.

Cross sections of density and OH mass fraction at various distances from the injection plane are shown in Figure 3.3.7. The cross sections show the development of the flame as it propagates into the chamber. At a distance of 10 mm (Figure 3.3.7a) from the injection plane the outer primary elements are deflected away from the central injection element with tear-drop shaped cross-sections. the central injection element is almost perfectly circular. At 25 mm from the injection plane (Figure 3.3.7b) the outer jets have been further deflected away from the central injection element, but the window cooling flow

now causes the jets to deflect back towards the vertical centerplane of the combustor. The central injection element has also been deformed and has an elliptic cross section.

At 50 mm from the injection plane (Figure 3.3.7c) the outer jets have been deflected into each other and mix in the centerplane of the combustor. Instead of multiple discreet flames, a single combustion zone exists which encloses all of the oxygen jets and separates them from the surrounding fuel rich flow. By 75 mm from the injection plane (Figure 3.3.7d), the outer injection elements are no longer visible, and the central jet has a larger elliptical cross section.

3.3.3 Comparison with Experimental Optical Data

Optical data has been collected from an unexcited BKH test at the modelled 60 bar ROF 6 operating point. During the particular test of interest the excitation system was not operating and both the main and secondary nozzles were unobstructed for the duration of the test. The optical setup of BKH experiments is described in Section 2.6.3. Shadowgraph and OH* chemiluminesence images from the unexcited BKH test have been time averaged for comparison with the steady-state RANS results in this chapter. Similarly, the 3D unstructured CFD solution is post processed to produce representative images for comparison with the experimental datasets.

Shadowgraph Imaging

Instantaneous and time averaged shadowgraph images from the unexcited BKH test are shown in Figure 3.3.8. The shadowgraph images were captured using a high-power Xenon gas-discharge lamp and a RG850 long pass optical filter positioned between the camera and the flame to block wavelengths shorter than 850 nm. The shadowgraph images therefore capture the infra-red light emitted by the lamp that passes through the chamber and is not obscured by density gradients in the flow. Ideally the dense LOx core of each injector would be identifiable as dark structures in the resulting shadowgraph images. However it was found that the lamp was not overly bright compared to the flame which is also emitting infra-red combustion light that passes through the optical filter. Combustion light emission from the surface of the LOx core results in the dense jets appearing as lighter structures in the images. The coaxial hydrogen injection appears as dark shadows surrounding the oxygen streams near the injection plane. Further downstream the shadowgraph imaging works as intended with lighter sections appearing between the oxygen streams allowing the edges of the LOx core to be identified.

The central and outer injection elements are visible in Figure 3.3.8. Turbulent breakup and shedding at the end of the central jet make it difficult to define the jet length in the instantaneous image in Figure 3.3.8a. Consequently it is also difficult to define the steady-state jet length in the time averaged image in Figure 3.3.8b. Study of the instantaneous image sequence has shown that the jet remains intact for almost the entire length of the window with periodic shedding near the end of the jet, usually about 90 mm from the injection plane. The outer jets are visible and travel parallel to the central jet near the injection plane before being deflected towards the top and bottom of the chamber.

Figure 3.3.9 shows results from the steady-state chamber model that have been post-processed for comparison with the experimental shadowgraph images. One issue with comparing experimental and numerical results is that the density value corresponding to the edge of the jet in the shadowgraph images is not defined. Figure 3.3.9a shows transparent white isosurfaces at different levels of oxygen partial density. The isosurfaces have been rendered in white to match the experimental images where the LOx streams appear as a lighter structure in the shadowgraph images. The length of the central jet is not significantly affected by the choice of density cut off value, with the dense part of

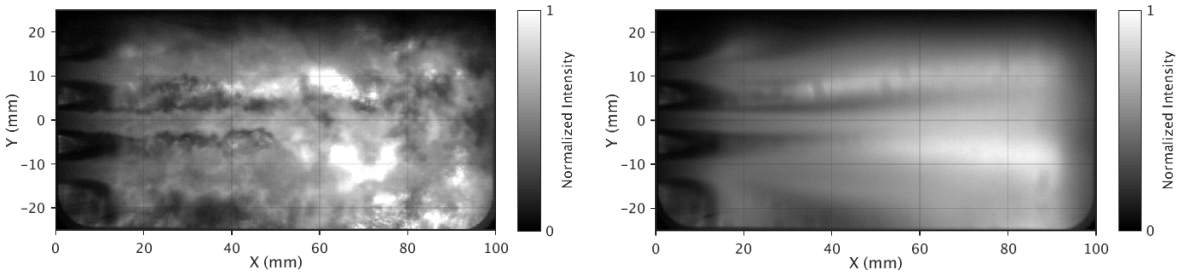

(a) Instantaneous image (b) Time averaged image

Figure 3.3.8: Shadowgraph images from an unexcited 60 bar ROF 6 BKH experiment [49].

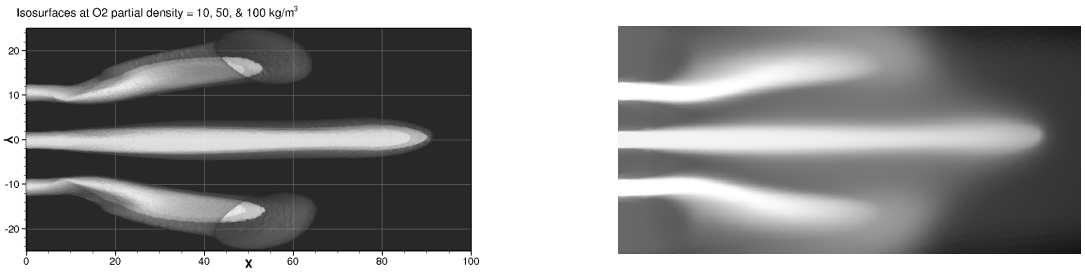

(a) Density isosurfaces (b) 1D integration of density

Figure 3.3.9: 2D post-processed images of steady-state chamber solution for comparison with shadowgraph images.

the jet (>100 kg/m^3) propagating almost the full length of the window. The 2D view of density isosurfaces shows that the deflection of the outer jets in the steady-state result matches the deflection of the outer jets observed experimentally. The outer jets are more diffuse than the central jet and there is a larger difference between the density isosurfaces at 10 and 50 kg/m^3.

Figure 3.3.9b shows a line-of-sight image produced by computing a 1D integration of density horizontally across the numerical domain. A 3D rectilinear grid is defined with width and height matching the window dimensions and a resolution matching the experimental shadowgraph images. A hundred regularly spaced points are defined in the horizontal 'Z' direction. After the steady-state solution has been interpolated to the grid, a 1D integration in the horizontal direction is computed to produce a 2D image comparable to the experimental shadowgraph images. The scale of the image is arbitrarily adjusted to highlight the features of the image. The result in Figure 3.3.9b shows the dense oxygen streams from the central and outer injectors. The deflection of the outer jets and the recirculation near the injection plane can also be seen. The 1D integrated image shows the diffuse breakup of the oxygen jet as lighter distributions surrounding the LOx streams which are not visible in the isosurface image. This diffuse breakup is comparable to the time-averaged shadowgraph image shown in Figure 3.3.8b.

OH* Imaging

Figure 3.3.10 shows an instantaneous and time-averaged OH* image recorded during the steady-state unexcited BKH experiment. At this operating point the OH* intensity distribution fills the entire window region except for a few regions on the left side near the injection plane. These less intense regions match the vertical spacing between the injection elements in the penta-injector configuration. Approximately 15 mm from the injection plane the flame from neighbouring injection elements meet and can no longer be distinguished. Some recirculation is observed along the top and bottom edges of the window near the injection plane.

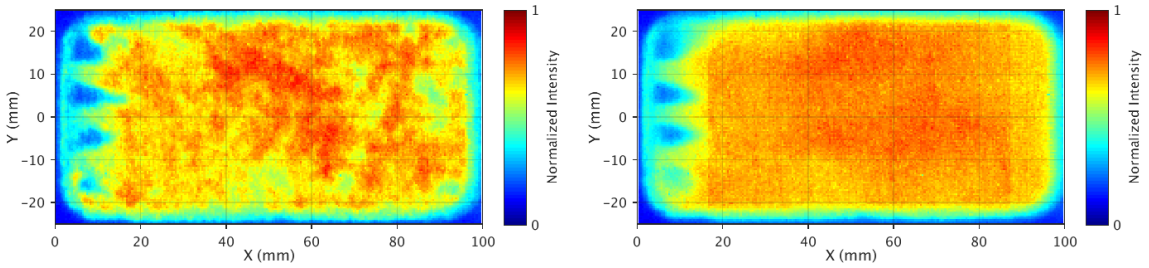

(a) Instantaneous image

(b) Time averaged image

Figure 3.3.10: OH* images from an unexcited 60 bar ROF 6 BKH experiment [49].

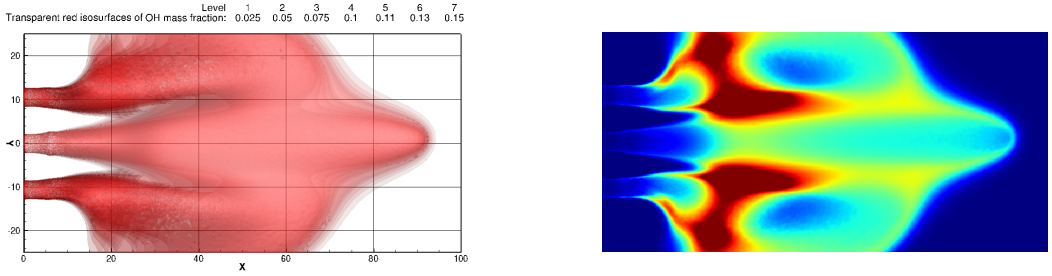

(a) OH mass fraction isosurfaces

(b) 1D integrated OH partial density

(c) 1D integrated [OH*]

(d) 1D integrated [OH*] with optically thick flame assumption

Figure 3.3.11: 2D post-processed images of steady-state chamber solution for comparison with OH* images.

The instantaneous image (Figure 3.3.10a) shows various turbulent structures downstream on the surface of the flame. These structures are not visible in the time averaged image (Figure 3.3.10b). Recent work studying OH* emission by Fiala [23] and Sardeshmukh et al. [123] have indicated that OH* emission is absorbed and re-emitted by other OH molecules making it optically thick. Therefore what is visible in the instantaneous image is most likely the turbulent structures on the outside surface of the flame. The time averaged image shown in Figure 3.3.10b has a more uniform intensity. Two lobes with a slightly higher intensity are visible near the middle of the window corresponding to the region between the central and outer oxygen streams.

Figure 3.3.11 shows comparable OH* chemiluminesence images produced by post-processing the steady-state chamber model result. For comparison purposes OH* chemiluminesence imaging is typically compared with the OH distribution. Figure 3.3.11a shows red transparent isosurfaces at multiple levels of OH mass fraction and indicates the OH distribution within the window region. As previously discussed, the OH distribution envelopes the dense oxygen streams from the coaxial injection elements. The vertical spacing between the injection elements is visible as regions with low intensity OH near the injection plane. Between 15 and 20 mm from the injection plane the flames from neighbouring elements meet and the OH distribution fills the height of the window region. A key difference in the numerical and experimental results is that the OH distribution does not continue to the end of the window in the steady-state model. Instead, the OH

distribution ends shortly after the oxygen jet has been consumed. This difference indicates that the oxygen is consumed too rapidly in the current model, but may also be due to additional transport and OH* excitation not being captured with the current approach.

1D integration of the OH partial density distribution was computed to produce representative line-of-sight images as for the pseudo-shadowgraph image in Figure 3.3.9b. The regions of highest intensity occur around the outer injection elements, which is most likely due to the 1D integration not including the effect of optically thick OH. Without absorption and re-emission the line-of-sight integration captures all of the OH along the 1D integration path. The points passing through the outer elements passes through the flame from 2 coaxial injection elements resulting in higher total intensity in these locations.

Fiala and Sattelmayer [23, 24] studied OH* chemiluminesence in high pressure O2/H2 flames and discovered that the majority of OH* emission at these conditions is caused by thermal, rather than chemical, excitation. Fiala and Sattelmayer suggested a method for post processing numerical results for better comparison with chemiluminesence imaging called the Equilibrium Filtered Radiation Model (EFRM). The EFRM assumes that the concentrations of OH* and OH are in thermal equilibrium and can be related using statistical thermodynamics.

$$[\mathrm{OH}^*] \sim [\mathrm{OH}] \cdot exp\left(-\frac{hc}{k_b \lambda T}\right) \tag{3.23}$$

where [OH*] is the concentration of thermally excited OH*, h is the Planck constant, c is the speed of light, k_b is the Boltzmann constant, $\lambda = 308.5$ nm is the wavelength of OH* emission, and T is the temperature.

Equation 3.23 was used to compute [OH*] from the steady-state chamber model results. 1D integration of the xOH^*_{Therm} distribution was computed to produce a representative line-of-sight image which is shown in Figure 3.3.11c. As the optical thickness of OH is again ignored there is very little difference between the 1D integrated xOH^*_{Therm} and OH distributions. The resulting [OH*] distribution matched the original OH distribution almost identically once the scale was adapted to show the same features in the image.

The 1D integration method essentially sums the mass of OH along horizontal lines in the Z direction in Figure 3.3.7. To approximate the absorption and re-emission of OH* radiation by OH molecules an optically thick flame is assumed. The 1D integration method is modified to weight the [OH*] distribution by the mass of OH along the 1D integration path. Therefore the points nearest the outer surface of the flame have a high weighting, while points in the center of the flame whose emission may be absorbed by the OH along the 1D path to the window, have a reduced weighting. The resulting 1D line of sight integrated image is shown in Figure 3.3.11d.

The intensity distribution in Figure 3.3.11d is more uniform and better matches the experimental results than the images that do not assume an optically thick flame. High intensity regions still exist where the central and outer injection elements intersect at approximately 20mm from the injection plane. The vertical spacing of the primary injectors is clearly seen and comparable with the experimental images in Figure 3.3.10. The lighter parts of the distribution at the edges of the image suggest that some of the OH is being recirculated towards the injection plane at the left corners of the image. The downstream distribution also extends slightly further towards the end of the window. This result indicates the importance of considering the optical path when producing line of sight images. Ray tracing algorithms which include such effects may produce results that are more readily compared with experimental datasets.

3.3.4 Wall Temperature Distribution

The steady-state chamber model is computed assuming adiabatic conditions at all solid boundary surfaces. Therefore, the wall temperatures of the steady-state chamber model are unphysically high compared to the BKH experiment which is actively cooled. Despite this, the temperature distribution at the walls of the chamber is of interest to assess the effectiveness of the window cooling flow and identify areas of high thermal load. The wall temperature distribution from the steady-state chamber model is shown in Figure 3.3.12.

The regions with the highest temperatures in the wall temperature distribution of the steady-state model are comparable to patterns of discolouration on the chamber walls and window segments. The discolouration is caused by temperatures near the annealing temperature of the copper alloy chamber walls (371-649°C). The images presented here were photographed during disassembly of BKH after a test campaign. As such, the pattern of discolouration is the result of multiple BKH tests with various operating points and sequences. However, as the 60 bar ROF 6 operating point is the highest pressure and ROF condition reached it should therefore have the highest heat flux and cause the most significant discolouration.

Figure 3.3.13 compares the temperature distribution of the steady-state chamber model with discolouration of the BKH injection faceplate. The steady-state model results predict that the surface with the highest wall temperature is located on the injection plane above and below the primary injection elements. This region, between the primary injectors and the innermost secondary hydrogen injectors, sees the recirculation of warm combustion products towards the injection plane. The pattern of discolouration in the same regions of the faceplate from BKH experiments, shown in Figure 3.3.13b, matches the predicted temperature distribution.

The side wall temperature distribution is shown in Figure 3.3.14. The side wall temperature distribution shows the action of the window cooling to protect the side walls, and in particular the 100 × 50 mm window region adjacent to the primary combustion zone. Downstream from the window cooling injection a higher temperature zone is observed above the window cooling flow than below. This difference is caused by the slight deflection of the primary flame elements and flow towards the secondary nozzle. The modelled temperature distribution suggests that hot combustion gases may interact with the downstream top and bottom edges of the window. This is supported by observations of discolouration at the edges of steel dummy windows which indicate a similar flow pattern as shown in Figure 3.3.15.

3.4 Discussion

The steady-state model has been successfully employed to model the flow field inside BKH. The inclusion of the real gas model to capture the breakup of the dense liquid oxygen core produced results which agree well with experimental observations. An outcome of this work is to assess the validity of the assumptions made and their impact on the final results. A number of key points have been identified that may be addressed in future work as the model is further developed and applied to additional test cases. These are primarily related to the choice of parameters and employed boundary conditions, the ability of the RANS model to capture the unsteady breakup of the LOx jet, and the methods by which experimental and numerical results are compared. These points are discussed in the following paragraphs.

The RANS modelling approach is dependant on a number of parameters that are chosen empirically. The choice of Prandtl number ratio was found to have a significant impact on the break up of the dense LOx core and the resulting flame temperatures

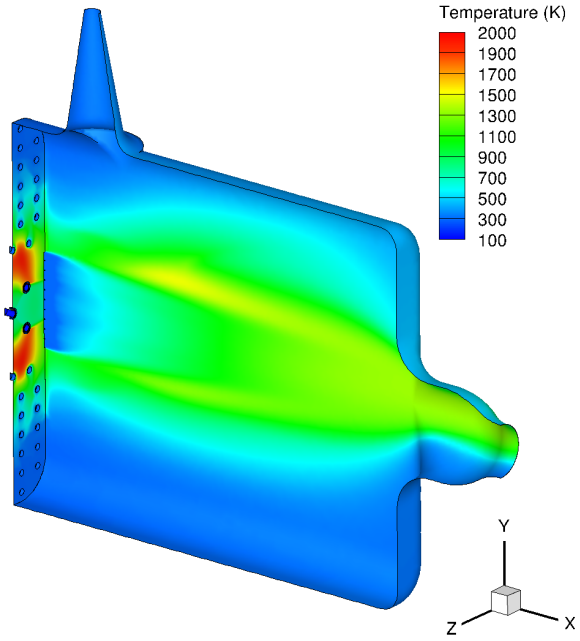

Figure 3.3.12: Modelled wall temperature distribution.

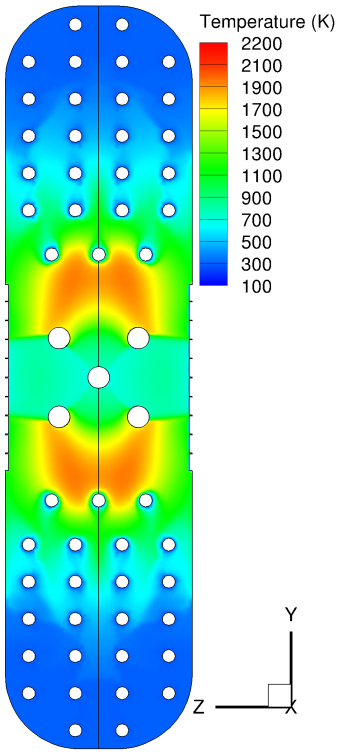

(a) Modelled temperature distribution at the injection plane

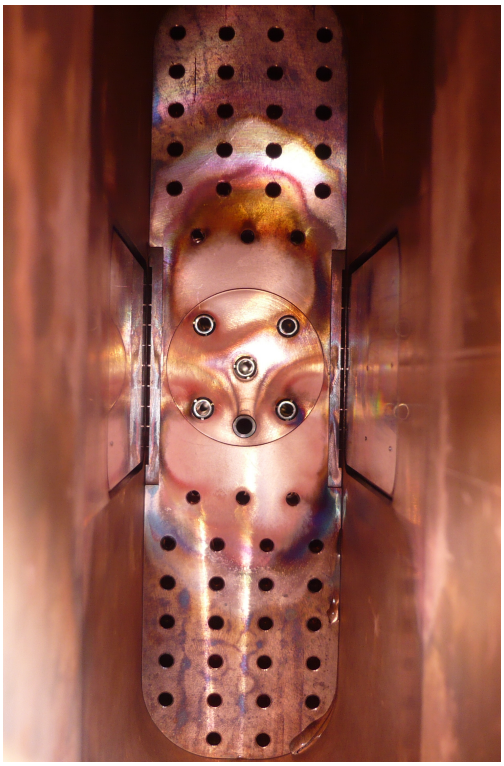

(b) Discoloration of the injector faceplate after a BKH campaign.

Figure 3.3.13: Comparison of injection plane temperature distribution and discolouration of BKH faceplate after BKH test campaign.

in the current model. The turbulent Prandtl number ratio implementation in the TAU code comes from the its heritage as a high-speed aerodynamics code which uses partition functions to compute the thermodynamic properties, while most other codes appear to use look-up tables. The Prandtl number ratio value of 2, chosen for the current work, is a compromise between high thermal conductivity for larger values, and high flame

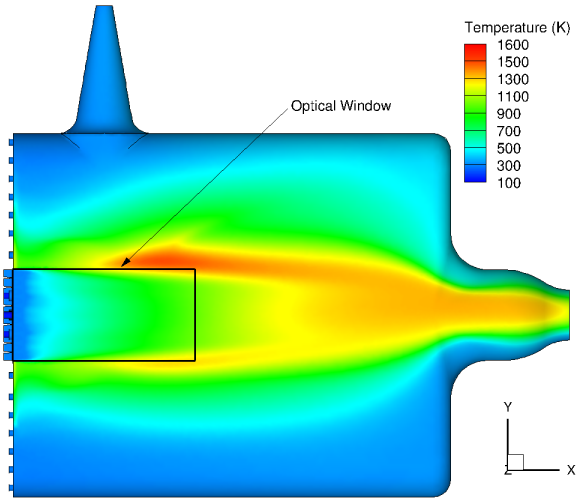

Figure 3.3.14: Side wall temperature distribution.

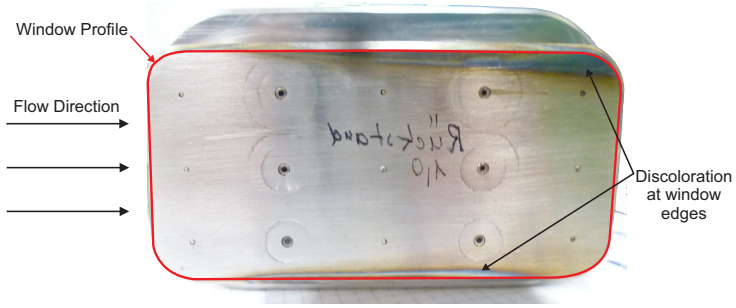

Figure 3.3.15: Discolouration of dummy window after BKH test campaign.

temperatures for lower values. It is higher than the appropriate Prandtl number ratio value of 0.8 for ideal gases, but also lower than the appropriate value to describe the dense oxygen jet. A different formulation for computing the Prandtl number ratio, or the ability to specify the turbulent Prandtl number independently from the laminar Prandtl number, would increase the flexibility and applicability of the TAU code for modelling cryogenic injection.

An additional point identified while studying the impact of the Prandtl number ratio was the absence of suitable experimental data to inform an empircal choice of the thermal conductivity and other parameters that control the breakup of the LOx core during coaxial injection with combustion. Experimental density profiles for combustion cases, similar to those produced using Raman imaging of supercritical cold flow nitrogen injection by Mayer et al. [81], would address this gap. Due to the difficulty of applying Raman spectral imaging to combustion cases new experimental methods and results may need to be developed before this can be addressed. The results of higher order modelling and simulations may also be used to evaluate appropriate turbulent Prandtl numbers.

Despite the identified issues with the Prandtl number ratio, the chosen parameters produced results that match experimental observations of the jet length, flame, and temperature distribution. The results are expected to under-predict the LOx core length as the unsteady shedding is not captured by the RANS modelling approach. The steady-state result should instead be compared with the mean length of the jet. However, the mean length of the jet cannot be readily identified in the time averaged shadowgraph image. Assuming a cut-off density of 100 kg/m^3, the steady-state model predicts that the central jet extends 85 mm from the injection plane. This agrees well with experimental observations where periodic shedding from the end of the jet is observed at the same location.

The comparison of the numerical result with available experimental optical data required the numerical results to be post-processed to produce comparable line of sight images. In this work a simplified 1D integration across the 3D numerical domain is used to collapse the 3D numerical dataset into representative 2D images. While crude, this approach produced results suitable for qualitative comparison of the experimental and numerical results. The 1D integration method could readily be improved by implementing more advanced interpolation methods or using a higher level of grid refinement for sampling of the 3D numerical result.

The difference in the representative OH* imaging results when the optically thick flame assumption is employed show that the optical path must be considered when post-processing numerical results for comparison with experimental data. Ray-tracing algorithms should be employed to generate representative line of sight images from the numerical data. The development and application of such algorithms is outside the scope of the current work.

The adiabatic boundary conditions prescribed to the walls of the chamber domain have affected the final chamber pressure and temperature distribution. Applying isothermal walls or a heat flux representative of the active water cooling in BKH would more accurately represent the experimental configuration. Limitations in the current implementation of the TAU code for real gases did not permit such boundary conditions to be used in the current work. The extensive secondary hydrogen injection in BKH mean that accurately capturing the heat transfer through the walls of the chamber is not significant in the current work. This effect would be more significant in other combustion chambers where hot combustion products meet the wall of the chamber.

3.5 Summary

In this chapter a RANS based CFD model of BKH has been presented. This model is the first steady-state model of BKH computed and was used to demonstrate the applicability of the employed modelling approach and to provide further understanding of the flowfield in BKH. The model uses a specialised implementation of the DLR TAU code for modelling fluids with real-gas properties. The employed modelling approach relies upon the assumption that as the modelled operating point is above the critical pressure of all species so that only a single supercritical phase exists within the chamber.

The model results show good agreement with available BKH optical datasets. The predicted OH mass fraction distribution filled the window region and showed similar spacing between the individual injection elements near the injection plane. The real-gas modelling capability captured the propagation of the dense LOx cores into the center of the chamber volume. The line-of-sight density distribution showing the position of the LOx cores was compared directly with shadowgraph images. The predicted LOx core length and the deflection of the outer jets agreed with the available experimental data.

The model provides further insight into the BKH flowfield that was not previously possible with the limited experimental data available. The model shows the flowfield around the flame zone and in the corners of the chamber. The model predicts that the window cooling flow has a strong influence on the primary flame zone, deflecting the outer jets towards the centerplane of the chamber. This deflection affects the breakup of the outer and central LOx streams and is undesirable as it is not representative of real flight hardware. The results also show no signs of recirculation zones in the downstream corners of the rectangular BKH volume. The predicted temperature distributions showed the effectiveness of the window cooling flow and the recirculation of combustion products towards the injection plane. These findings may be used for the design of more representative experiments in the future.

The comparison of the steady-state chamber model results with available experimental data provides justification for using the same approach for more advanced analysis. The supercritical real-gas modelling approach is employed in Chapter 6 to compute unsteady models of BKH injection elements subjected to acoustic forcing. The steady-state model results, in particular the distribution of acoustic properties over the chamber volume, are further utilised in Chapter 4 as part of a lower-order acoustic model.

Chapter 4

Acoustic Analyses and Modelling

Analysis of the flame response requires knowledge of the acoustic disturbance acting locally upon the flame. However the acoustic field, which determines the local acoustic disturbance, is dependant on the entire chamber system. Therefore determining the local acoustic disturbance requires consideration of the entire chamber geometry and acoustic boundary conditions.

Previously applied methods for determining the local acoustic disturbance in BKH assume idealised eigenmode solutions which are then fitted to dynamic pressure sensor data. The local acoustic disturbance is then extracted from the fitted solution. However, the applicability of these methods are limited as the eigenmode solutions are only valid at specific resonant frequencies. The computed solutions should also be validated against experimental data before they are relied upon.

The challenge of predicting the local acoustic disturbance acting upon the flame is addressed in this chapter via two methods. The first method involves extracting the local acoustic disturbance from a reconstruction of the acoustic field using dynamic pressure sensor data, which is presented in Section 4.1. A new method is developed for reconstructing the acoustic field from experimental data. The new method uses a complex acoustic amplitude formulation and improves upon previous analyses by allowing the acoustic field to be reconstructed at all excitation frequencies of interest. The new reconstruction method allows new insight into how the acoustic field and the local acoustic disturbances acting upon the flame in BKH varies over a range of excitation frequencies. The new results produced as part of this analysis are also useful for validation of numerical models.

Section 4.2 addresses the challenge of predicting the acoustic field of a rocket combustor analogous to an industrial application in which high fidelity experimental data may not be available. Modal analysis is used to predict the acoustic eigenmodes of the chamber volume. Unlike previous work, in this study the distribution of acoustic properties is considered by implementing the steady-state chamber model solution presented in Chapter 3. Additional modelling of off-resonance frequencies is used to show that the model accurately predicts the evolution of the acoustic distribution over the range of excitation frequencies covered during BKH experiments.

4.1 Experimental Data Analysis

To investigate the acoustic disturbances in BKH experiments, data is collected from a number of dynamic pressure sensors located on the walls of the chamber and injection manifolds. The chamber sensors are positioned along the top and bottom walls of the chamber and spaced along its length to spatially resolve both longitudinal and transverse acoustic modes. The locations of the chamber sensors are shown in Figure 4.1.1.

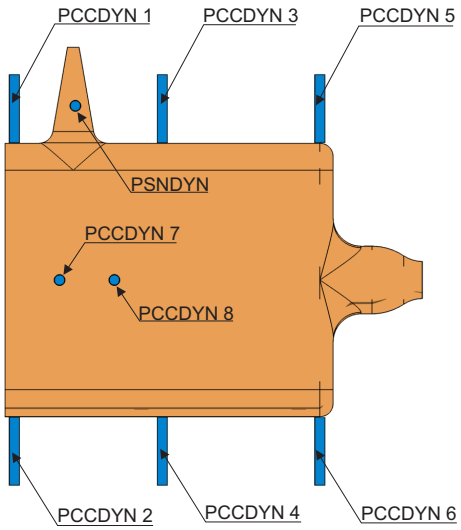

Figure 4.1.1: Dynamic pressure sensor positions in BKH.

Experimental data has been collected from BKH tests at various operating conditions. Hardi et al. [49, 51] previously analysed BKH dynamic pressure sensor data and identified the relevant acoustic modes by comparing the amplitudes and phase of each signal. In this section a new method of analysing the dynamic pressure sensor data using a complex amplitude formulation of the acoustic field is presented. The complex amplitude formulation is used to reconstruct the acoustic field for the range of frequencies covered experimentally by the BKH excitation frequency ramp. The results of this analysis are used to assess the accuracy of the acoustic model of BKH presented in Section 4.2.

The complex amplitude formulation has a number of features making it suitable for combustion instability analysis. In particular, the local distribution of acoustic pressure, velocity, and phase can be readily extracted from the complex acoustic distribution. The complex amplitude formulation and reconstruction method is employed in Section 5.3 to calculate the spatially resolved acoustic disturbance in the window region corresponding to observed intensity fluctuations in optical data.

4.1.1 Dynamic Pressure Sensor Data

All of the dynamic pressure sensor data presented in this section are taken from BKH experiments operating at the 60 bar ROF 6 operating point which was defined in Section 3.2.1. Figure 4.1.2 shows raw dynamic pressure sensor data from a BKH experiment without acoustic excitation. In this experiment the optical windows were installed in the chamber and the secondary nozzle sensor was not installed so only data from 6 dynamic pressure sensors on the upper and lower walls of the chamber are available. The raw data shows random fluctuations produced by combustion noise and turbulence with amplitudes less than 1% of the mean chamber pressure indicative of stable combustion.

Figure 4.1.2b shows a PSD plot of the unexcited dynamic pressure sensor data with the resonant modes labelled. Peaks in the PSD of each sensor signal correspond to the resonant frequencies of the combustor which stand out above the background noise. The peak at approximately 3250 Hz corresponds to the 1L mode and sensors PCCDYN3 and PCCDYN4 which are located near the 1L pressure nodal line do not show this peak. The peak at approximately 4400 Hz corresponds to the 1T mode, and all of the 6 wall sensors show a peak at this frequency. Additional peaks have been identified as the 1L1T mode, and a strong sensor artefact at a frequency of 2500 Hz which was remedied and not observed in later BKH experiments.

Figures 4.1.3 and 4.1.4 show dynamic pressure sensor data from a BKH experiment with acoustic excitation at the 1L and 1T mode frequencies, respectively. In this experiment

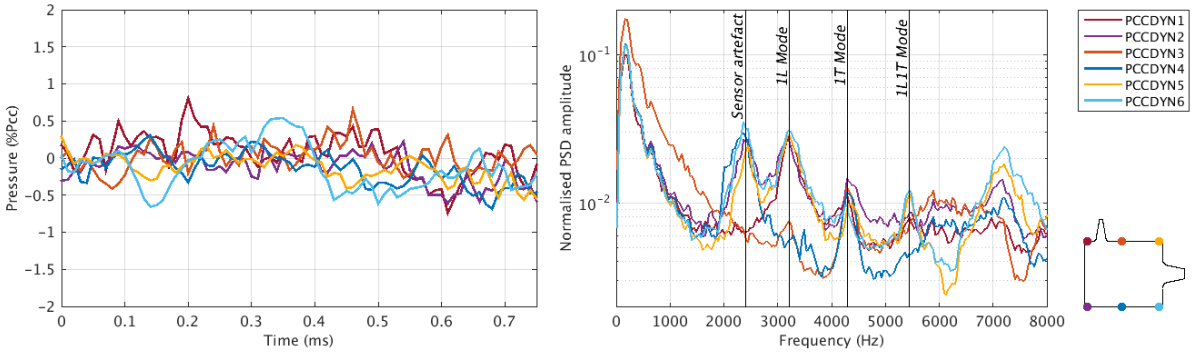

(a) Raw sensor data

(b) PSD plot of sensor data

Figure 4.1.2: BKH dynamic pressure sensor data during a test period without acoustic excitation.

the window sensors PCCDYN7 and PCCDYN8 and the secondary nozzle sensor PSNDYN were installed resulting in 9 dynamic pressure sensor signals. Figures 4.1.3a and 4.1.4a show raw dynamic pressure sensor signals. Large pressure fluctuations are observed at both resonant frequencies with amplitudes greater than 2.5% of the mean chamber pressure for the 1L mode, and amplitudes greater than 9% of the mean chamber pressure for the 1T mode. The orientation of the excitation system on the BKH combustor favours excitation of the 1T mode so that higher amplitudes are reached during excitation of the 1T mode than the 1L mode. A different scale has been used for Figures 4.1.3 and 4.1.4 to account for this. The phase of the pressure fluctuations between sensor locations matches the expected longitudinal and transverse mode distributions.

Figures 4.1.3b and 4.1.4b show the phase locked signals that have been computed by sorting data points into phase intervals corresponding to the phase of a reference signal at the time that each data point was recorded. A sufficiently long data sample is analysed to ensure an even number of data points in each phase interval. All data points corresponding to the same phase interval are averaged and the results are ordered to produce a phase locked cycle corresponding to the mean fluctuation at the reference frequency. Figures 4.1.3b and 4.1.4b were computed by analysing 0.1 s periods of test data using the phase of the PCCDYN2 dynamic pressure sensor signal fluctuation which had been filtered to the excitation frequency. The phase locked results closely resemble the original experimental data. This result confirms that the imposed acoustic excitation in BKH produces consistent acoustic fluctuations at the frequency of interest. Moreover, as a consistent amplitude is reached, the amplitude reached is the limit cycle of the acoustic excitation system whereby the acoustic forcing of the excitation system is balanced by the acoustic damping in the chamber.

For the current work it is important to differentiate between the resonant mode frequencies of the unexcited chamber and the peak response frequencies observed during experiments with acoustic excitation. The peak response frequencies are the frequencies at which the largest acoustic response is observed over the excitation frequency ramp performed during BKH experiments. The acoustic excitation can affect the flow field inside the chamber and thereby change the resonant mode frequencies. As such, the resonant mode frequencies of the unexcited chamber are different to the peak response frequencies of the excited chamber. This effect is more significant for transverse modes where the acoustic velocity acting across the flame zone changes the temperature and speed of sound distribution in the chamber significantly. Unforced resonant mode frequencies are determined by computing the PSD of the dynamic pressure sensor data and identifying the peak frequencies as shown in Figure 4.1.2b. The peak response frequencies of each mode are determined by identifying the frequency at which the largest pressure disturbance was

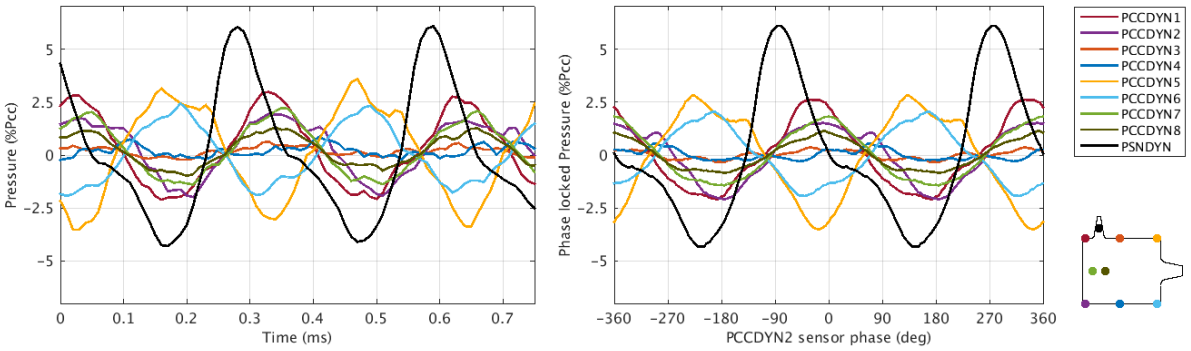

(a) Raw sensor data (b) Phase locked sensor data

Figure 4.1.3: BKH dynamic pressure sensor data during 1L mode excitation.

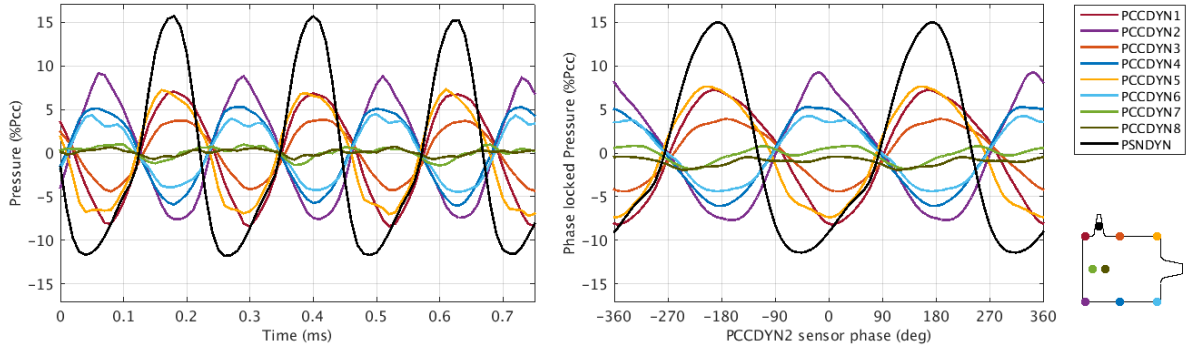

(a) Raw sensor data (b) Phase locked sensor data

Figure 4.1.4: BKH dynamic pressure sensor data during 1T mode excitation.

Table 4.1: BKH resonant and peak response frequencies.

Mode	**Resonant Mode Frequency (Hz)**	**Peak Response Frequency (Hz)**
1L	3250	3330
1T	4350	4480

observed across all sensor positions with the correct acoustic distribution. The resonant mode and peak response frequencies are listed in Table 4.1.

Hardi [49] and later Webster [159] have previously identified and discussed the difference in resonant mode and peak response frequencies in BKH. Hardi and Webster hypothesised that the difference between the resonant and peak response 1T mode frequencies was caused by the retraction of the flame due to acoustic velocity fluctuations acting upon the flame zone during transverse mode excitation. As the flame retracts a higher proportion of the chamber is then occupied by warm combustion products and the mean volumetric speed of sound in the chamber is increased. The higher speed of sound increases the 1T mode frequency and this occurs as the BKH excitation frequency ramp approaches the 1T mode. Similarly the redistribution of warm combustion products during 1L mode excitation may have produced a similar effect to a lesser degree.

At some particular frequency after the 1T mode frequency the flame has reached its minimum length. As the excitation frequency increases the flame does not retract further and the mean speed of sound and the associated 1T mode frequency no longer increase. The increasing BKH acoustic excitation frequency transitions above the 1T mode frequency

and the acoustic disturbance no longer imposes a transverse velocity fluctuation across the flame. The flame quickly extends back to its undisturbed length which also decreases the mean speed of sound. The decreased speed of sound further lowers the resonant mode frequency below the current excitation frequency. The excitation frequency is then no longer exciting a resonant mode and the acoustic amplitude rapidly decreases. Therefore, the peak response frequencies at which the highest acoustic amplitudes are reached occur at frequencies above the resonant mode frequencies.

4.1.2 Calculation of Acoustic Amplitude and Phase

A method for determining the amplitude and relative phase of the acoustic disturbance at the excitation frequency has been developed. The amplitude and phase of the acoustic disturbance is used to study the evolution of the acoustic field over a range of frequencies corresponding to the BKH excitation frequency ramp. The results of this analysis are used to identify the resonant mode frequencies of the chamber with acoustic excitation and as part of the acoustic field reconstruction method described in Section 4.1.3.

Determination of Acoustic Amplitude

To compare the amplitude of the pressure disturbance recorded at each sensor position a sliding root mean square (RMS) is computed for each sensor signal. Equation 4.1 defines the RMS of a signal p with zero mean and n samples.

$$p_{RMS} = \sqrt{\frac{1}{n}\sum_{i=1}^{n}(p_i)^2} = \sqrt{\frac{p_1^2 + p_2^2 + ... + p_{n-1}^2 + p_n^2}{n}} \tag{4.1}$$

The RMS is a measure of the averaged amplitude of a signal over a period of time. The RMS of a sinusoidal signal can be shown to be equal to $\frac{1}{\sqrt{2}}$ times the amplitude of the original signal. The relationship between the RMS of other non-sinusoidal signals and their amplitude is not so straightforward, but it is still often used to compare amplitudes of fluctuating signals. The RMS result represents the mean amplitude of the dominant disturbance produced by the excitation system and is not strongly affected by noise. This is preferential to peak-to-peak measurements of dynamic pressure sensor amplitudes which are more strongly affected by signal noise from other frequencies within the chamber.

A sliding RMS is computed by dividing a signal p into windows containing $n = 20000$ samples and computing the RMS of each window. The magnitude of the sliding RMS is therefore proportional to the mean amplitude over the duration of each window. Figure 4.1.5 compares RMS results with raw signal data. The raw signal (shown in grey) has a considerable amount of low frequency noise. This low frequency noise can be removed by applying a high pass filter to the data with a cut off frequency of 1 kHz. A sliding RMS of the raw signal tracks the amplitude of the acoustic disturbances over the test duration. The sliding RMS was computed using $n = 20,000$ samples (0.2 seconds) per window and a 50% overlap of each subsequent window with the last. A better match of the amplitude can be achieved by assuming the signal is harmonic and adjusting the RMS amplitude by a factor of $\sqrt{2}$.

The RMS results are unfiltered and contain additional content at frequencies different to the excitation frequency. To isolate the acoustic amplitude of the fluctuation at the excitation frequency a combination of a sliding RMS calculation and band pass filtering is used which is referred to as BPRMS. The mean excitation frequency of each RMS window is determined using a frequency tracking algorithm which identifies the acoustic excitation frequency for each RMS window. The data for each window is then band pass filtered around the excitation frequency before the RMS calculation is computed.

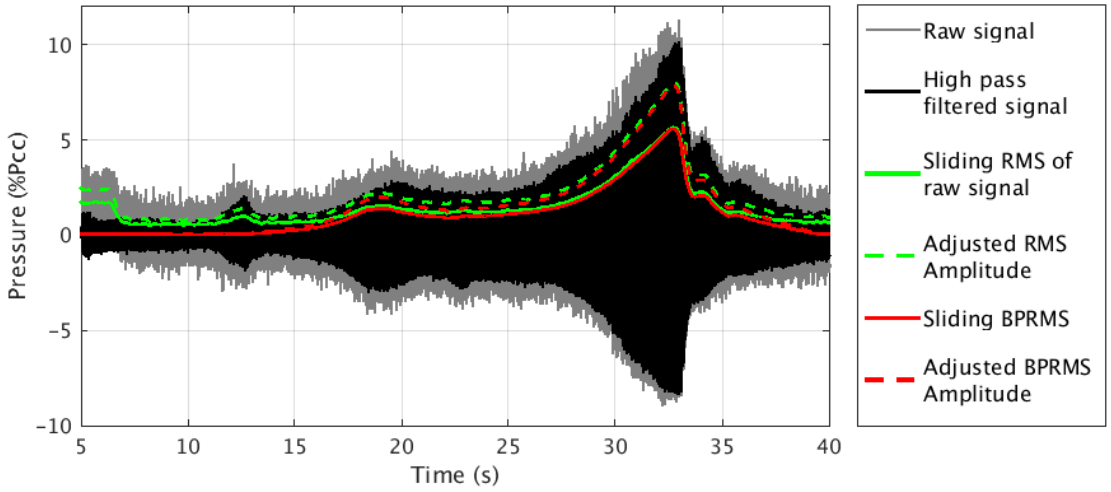

Figure 4.1.5: Raw data and RMS results versus test time for a PCCDYN2 dynamic pressure sensor signal from a BKH hot flow experiment.

The difference between the sliding RMS and sliding BPRMS results is evident at 12.5 seconds in Figure 4.1.5. At this time an overtone of the excitation frequency is exciting the 1L1T mode in the chamber. The sliding RMS captures this disturbance, but the sliding BPRMS does not. Therefore the sliding BPRMS effectively isolates the acoustic disturbance at the excitation frequency.

Figure 4.1.5 shows that over the period between excitation of the 1L mode at 18 seconds and excitation of the 1T mode at 32 seconds the sliding RMS and sliding BPRMS agree very closely. This indicates that the most significant fluctuations in the signal correspond to those at the excitation frequency. As the passband of the band pass filter is relatively small it can also be assumed that the BPRMS result is from a monofrequent harmonic signal. A better estimate of the amplitude can then be attained by adjusting the BPRMS amplitude by a factor of $\sqrt{2}$.

In this work the acoustic amplitude of the disturbance at the excitation frequency will be computed as the adjusted BPRMS amplitude. The BPRMS calculation uses a band pass filter with a pass band of 400 Hz centered on the mean excitation frequency for the RMS window. The sliding BPRMS is calculated using 0.2 s long samples with 50% overlap, or 20,000 data samples, for each RMS window. The amplitude of the BPRMS calculation is then adjusted by a factor of $\sqrt{2}$ to match the amplitude of a mono-frequent harmonic signal. Figure 4.1.6 shows the evolution of the acoustic amplitude and phase versus excitation frequency from a 60 bar ROF 6 experiment. The 1L- and 1T-mode frequencies can be identified from Figure 4.1.6 as the peaks at 3290 and 4480 Hz, respectively.

The relative acoustic amplitudes of each sensor in Figure 4.1.6 matches the expected acoustic mode distributions at the resonant frequencies. At the 1L-mode frequency sensors 3 and 4 are located in a pressure antinode and have lower acoustic amplitudes than the other sensors at either end of the chamber. Similarly during 1T-mode excitation Sensors 7 and 8 which lie along the centerline of the chamber are positioned in the nodal line and have much smaller amplitudes than the other sensors which are located at the top and bottom walls of the chamber.

The amplitude and phase distributions in Figure 4.1.6 are smooth, suggesting a gradual transition and re-orientation of the acoustic disturbance as the excitation frequency transitions from one resonant mode frequency to the next over the course of the frequency ramping. However, a rapid decrease in the amplitude is seen as the excitation frequency increases past the 1T-mode frequency.

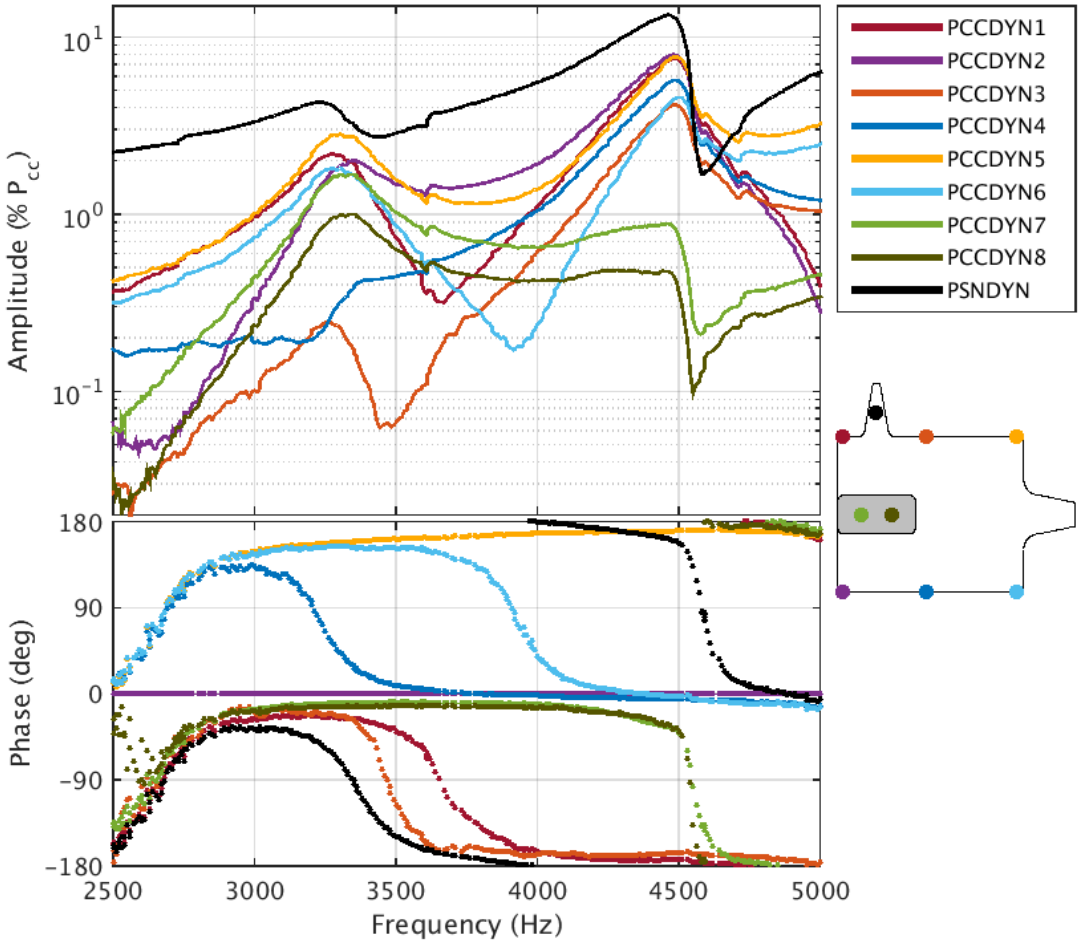

Figure 4.1.6: Amplitude and phase computed from dynamic pressure sensor data versus excitation frequency from a BKH 60 bar ROF 6 experiment.

Determination of Acoustic Phase

A method for extracting the phase of BKH dynamic pressure sensor signals relative to one another has been developed. This method uses a similar windowing approach to the sliding BPRMS calculation. In each window the data is band-pass filtered about the excitation frequency with a pass band of 400 Hz. The mean phase is then determined by computing the phase at the center of the window of the approximately mono frequent signal. The phase from different sensor positions is normalised against the phase of the PCCDYN2 sensor signal for comparison. The normalised phase convention is taken so that a negative phase angle indicates that the peak amplitude is reached before the peak PCCDYN2 pressure disturbance, while positive phase angles indicate how that the signal lags behind the PCCDYN2 signal.

The lower part of Figure 4.1.6 shows phase results for the same experiment. It can be seen that the phase relationship between sensors transitions relatively smoothly over the frequency ramp. This suggest that the large disturbance imposed by the excitation system organises the acoustic fluctuations in the chamber at the excitation frequency. The relative phase between sensors indicates a 1L mode distribution at frequencies between 3200 and 3400 Hz which surround the peak amplitude frequency of 3290 Hz. Between 4100 and 4500 Hz the phase distribution resembles a 1T mode distribution with top and bootom wall sensor having a 180 degree phase difference. This suggests the acoustic disturbance resembles a 1T mode at frequencies leading up to the 1T frequency. The 180 degree phase shift in sensor 7 and 8 at 4500 Hz indicates that these sensors have crossed a nodal line of an acoustic mode. This is the same frequency at which the amplitude of all sensors decreases.

4.1.3 Acoustic Field Reconstruction Method

In this section, a method for reconstructing the acoustic field inside the combustion chamber from dynamic pressure sensor data is presented. This method is used to gain insight into how the acoustic field changes with excitation frequency. It is also used to estimate the acoustic disturbance acting upon the flame zone. In past work [49, 50], the acoustic field was reconstructed from pressure data by scaling a 2D eigenmode solution to match the amplitude of the disturbance at individual sensor positions. This approach was useful for analysing the acoustic field when the chamber was being excited at the resonant frequency of an acoustic mode. However, it had limited application and could not describe the acoustic field at other frequencies. The new method presented here, referred to as the complex reconstruction method, addresses this problem and allows the structure and phase of the instantaneous acoustic field to be visualised at all excitation frequencies reached during BKH experiments.

The acoustic field is reconstructed using the complex formulation of an acoustic disturbance as described in Section 2.4.2. The reconstruction involves:

1. Determining the amplitude and relative phase of each sensor.
2. Calculating the complex acoustic amplitude.
3. Interpolating the complex acoustic amplitude over a representative domain.

All acoustic properties of interest can then be determined from the interpolated complex acoustic amplitude distribution.

To calculate the complex acoustic amplitude it is assumed that the acoustic disturbance takes the form of a harmonic pressure disturbance:

$$p = \hat{P}\, \mathrm{e}^{i\hat{\omega}t}. \tag{4.2}$$

where $\hat{P}$ is the complex amplitude, $\hat{\omega}$ is the complex frequency, and t is time. The complex amplitude of a field consists of real and imaginary components (Equation 4.3) at each position in the field.

$$\hat{P}_{(x,y,z)} = P_{R(x,y,z)} + iP_{I(x,y,z)} \tag{4.3}$$

The two components of the complex amplitude are then determined using the following two relations:

$$|\hat{P}| = |P_R + iP_I| = \sqrt{\frac{\sum_1^n p_n'^2}{n}} \cdot \sqrt{2} = p'_{BPRMS} \cdot \sqrt{2}, \tag{4.4}$$

and

$$\angle\hat{P} = \angle(P_R + iP_I) = \angle p'. \tag{4.5}$$

Equation 4.4 states that the magnitude of the complex amplitude should equal the amplitude of the pressure fluctuation. Equation 4.5 relates the phase angle of the complex amplitude with the phase of the mono frequent signal. The amplitude and relative phase of each sensor signal is determined as described in Section 4.1.2. i.e. The amplitude is taken as the adjusted result of a sliding BPRMS calculation (top figure, Figure4.1.6), and the relative phase computed by normalizing the phase of each signal to the PCCDYN2 sensor signal phase (bottom figure, Figure 4.1.6).

The real and complex parts of the amplitude are calculated from equations 4.4 and 4.5. These values are then interpolated over an area representing the combustor volume. As the BPRMS result captures only disturbances close to the excitation frequency, we assume that the disturbance is monofrequent and should take the form of an acoustic eigenmode. Therefore the distribution should exhibit no discontinuities and can be approximated by

interpolating a spline distributions between the sensor positions. The employed spline interpolation assumes zero pressure gradient at the walls of the chamber where applicable.

The interpolated result describes the complex amplitude $\hat{P}$ from Equation 4.2. To animate the reconstructed acoustic field it must be modulated by $e^{i\hat{\omega}t}$ where $\hat{\omega}$ is the excitation frequency. The phase can also be computed from the complex amplitude for any point using Equation 4.5.

Of particular interest is the direction and magnitude of the acoustic velocity. The relationship between the acoustic velocity and pressure field can be derived by considering the linearised equation for the conservation of momentum [144].

$$\rho\frac{\mathrm{d}u}{\mathrm{d}t} + \nabla p = 0$$

or

$$\frac{\mathrm{d}u}{\mathrm{d}t} = -\frac{1}{\rho}\nabla p \tag{4.6}$$

Here ρ is assumed to be constant across the domain. The right hand side of Equation 4.6 is integrated with respect to time using the complex notation for p (Equation 4.2).

$$\begin{aligned}
-\int \frac{1}{\rho}\nabla p dt &= -\int \frac{1}{\rho}\nabla\hat{P}\,\mathrm{e}^{i\hat{\omega}t}dt \\
&= -\frac{1}{\rho}\nabla\hat{P}\int \mathrm{e}^{i\hat{\omega}t}dt \\
&= -\frac{1}{\rho}\nabla\hat{P}\frac{1}{\hat{\omega}i}\mathrm{e}^{i\hat{\omega}t} \\
&= \frac{i}{\rho\hat{\omega}}\nabla\hat{P}\,\mathrm{e}^{i\hat{\omega}t}
\end{aligned} \tag{4.7}$$

The velocity is then determined from the complex amplitude via:

$$v = \frac{i}{\rho\hat{\omega}}\nabla\hat{P}\,\mathrm{e}^{i\hat{\omega}t}. \tag{4.8}$$

The complex coefficient i in Equation 4.8 represents the 90° phase shift between acoustic pressure and acoustic velocity fluctuations.

4.1.4 Acoustic Field Reconstruction Results

The complex reconstruction method described in Section 4.1.3 was used to reconstruct the acoustic field from dynamic pressure sensor data over the duration of a BKH 60 bar ROF 6 test. To calculate the acoustic velocity a constant uniform chamber density of 3 kg/m^3 was assumed based on the mean volumetric density predicted by the steady-state chamber model presented in Chapter 3. Snapshots of this reconstruction at different excitation frequencies are shown in Figures 4.1.7 and 4.1.8. The scales shown in the figures are consistent across all plots and have been chosen to show the evolution of the field also when low amplitude disturbances are present. As such, at some frequencies the magnitude of the disturbance exceeds the color scale of the plots.

The reconstruction images show the evolution of the acoustic field with varying excitation frequency over the course of the BKH excitation frequency ramp. As the excitation frequency approaches the 1L mode frequency the acoustic wavelength becomes short enough to fit within the combustion chamber volume. Acoustic disturbances are reflected by solid boundaries at either end of the chamber volume and higher disturbance amplitudes are reached. As the excitation frequency increases from the 1L to the 1T mode

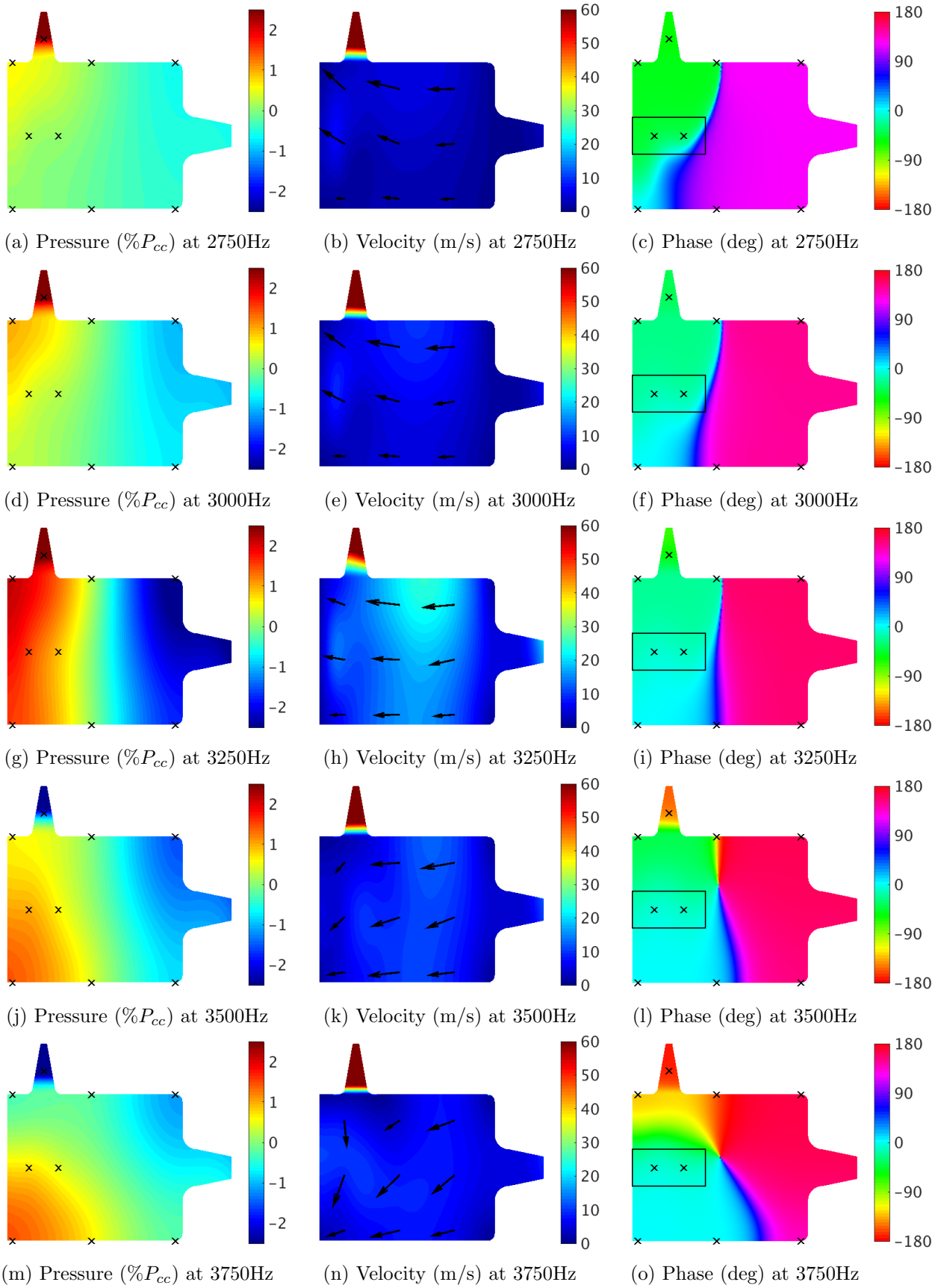

(a) Pressure (%P_{cc}) at 2750Hz (b) Velocity (m/s) at 2750Hz (c) Phase (deg) at 2750Hz

(d) Pressure (%P_{cc}) at 3000Hz (e) Velocity (m/s) at 3000Hz (f) Phase (deg) at 3000Hz

(g) Pressure (%P_{cc}) at 3250Hz (h) Velocity (m/s) at 3250Hz (i) Phase (deg) at 3250Hz

(j) Pressure (%P_{cc}) at 3500Hz (k) Velocity (m/s) at 3500Hz (l) Phase (deg) at 3500Hz

(m) Pressure (%P_{cc}) at 3750Hz (n) Velocity (m/s) at 3750Hz (o) Phase (deg) at 3750Hz

Figure 4.1.7: Reconstructed acoustic field from BKH dynamic pressure sensor data. Excitation Frequencies between 2.5 and 4 kHz.

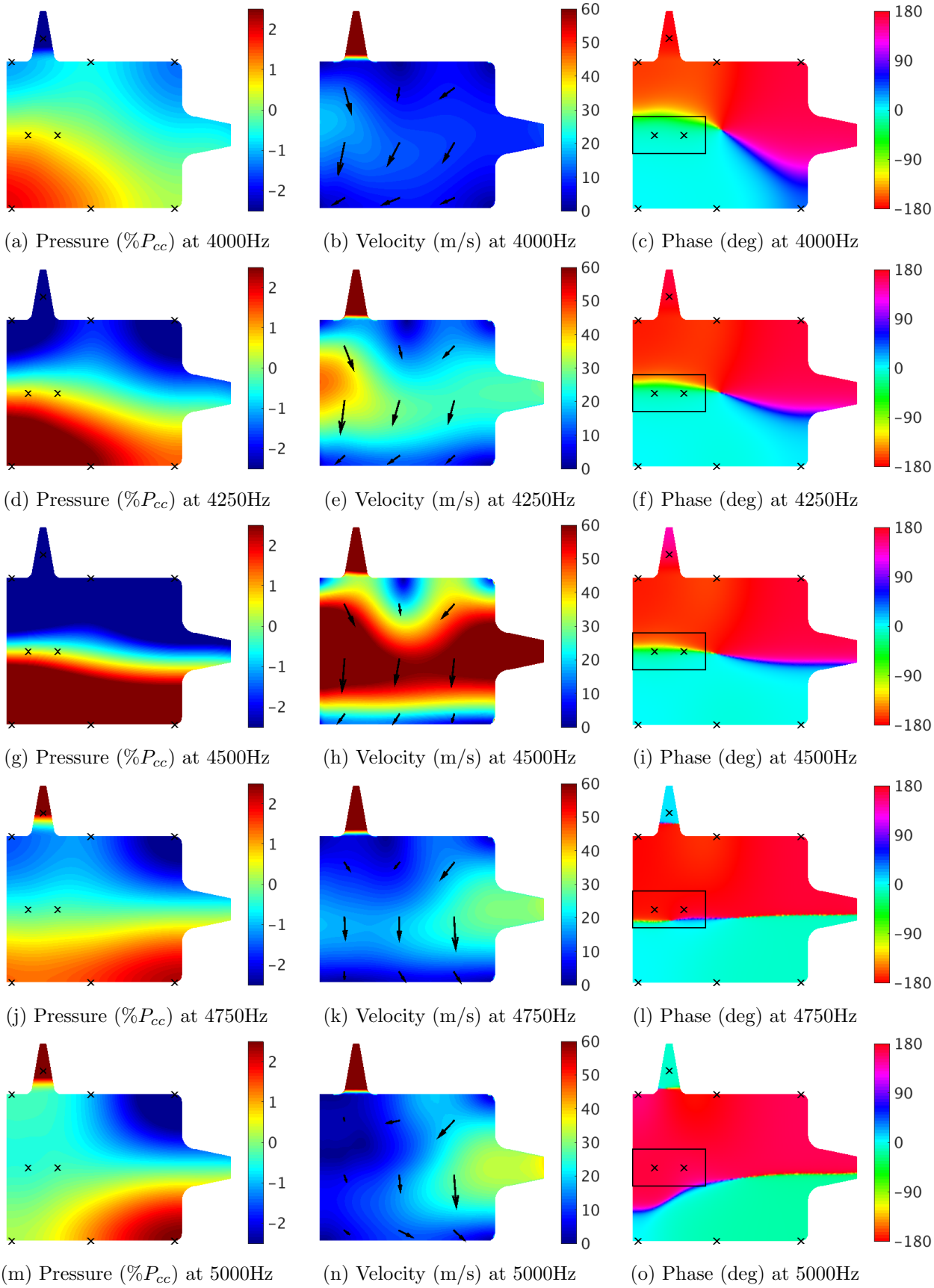

(a) Pressure (%P_{cc}) at 4000Hz (b) Velocity (m/s) at 4000Hz (c) Phase (deg) at 4000Hz

(d) Pressure (%P_{cc}) at 4250Hz (e) Velocity (m/s) at 4250Hz (f) Phase (deg) at 4250Hz

(g) Pressure (%P_{cc}) at 4500Hz (h) Velocity (m/s) at 4500Hz (i) Phase (deg) at 4500Hz

(j) Pressure (%P_{cc}) at 4750Hz (k) Velocity (m/s) at 4750Hz (l) Phase (deg) at 4750Hz

(m) Pressure (%P_{cc}) at 5000Hz (n) Velocity (m/s) at 5000Hz (o) Phase (deg) at 5000Hz

Figure 4.1.8: Reconstructed acoustic field from BKH dynamic pressure sensor data. Excitation Frequencies between 4 and 5 kHz.

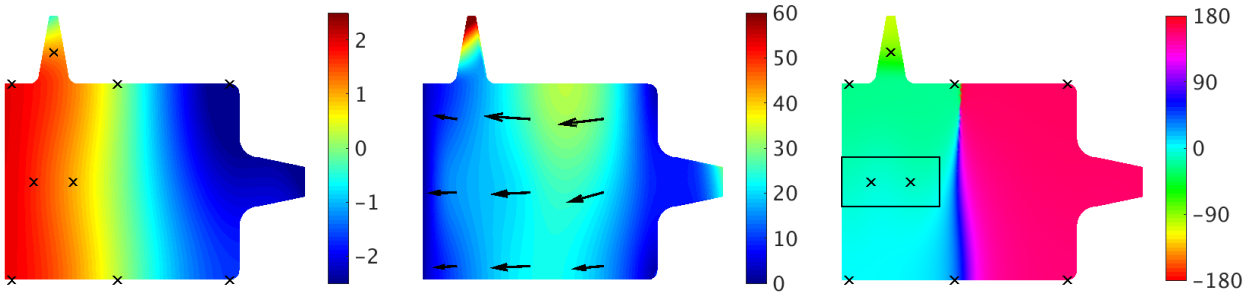

(a) Pressure (%P_{cc}) at 3330Hz (b) Velocity (m/s) at 3330Hz (c) Phase (deg) at 3330Hz

Figure 4.1.9: Reconstructed acoustic field from BKH experimental data at the 1L mode peak response frequency.

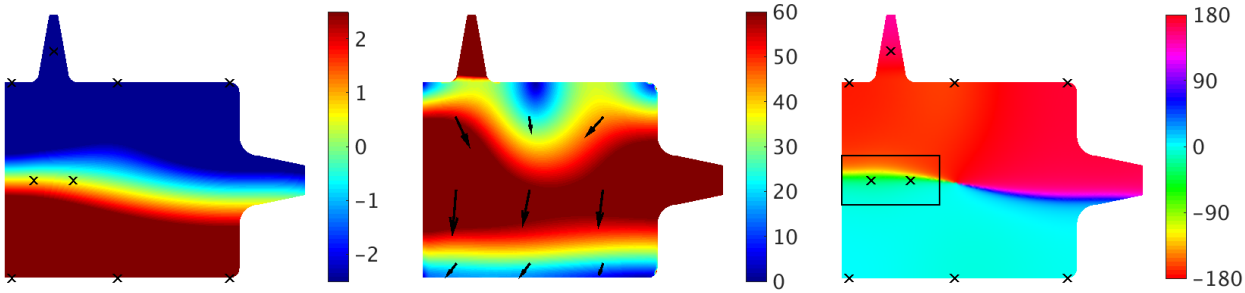

(a) Pressure (%P_{cc}) at 4480Hz (b) Velocity (m/s) at 4480Hz (c) Phase (deg) at 4480Hz

Figure 4.1.10: Reconstructed acoustic field from BKH experimental data at the 1T mode peak response frequency.

frequency the orientation of the acoustic disturbance rotates from a vertical to a horizontal distribution.

The rotational behaviour of the acoustic field is attributed to the geometry of the chamber volume, with the acoustic disturbance rotating to the orientation with the least acoustic damping at each frequency. The orientation with the least acoustic damping occurs where the solid walls of the chamber are located one acoustic wavelength apart. The rotation of the acoustic field as the excitation frequency varies indicates how the acoustic modes can appear as bands in the spectrograms covering a range of frequencies.

The phase distribution shows that the phase of the secondary nozzle leads the disturbance in the chamber. At the 1T mode and peak response frequencies the secondary nozzle sensor is still in phase with the top wall sensors as shown in Figure 4.1.8i. Above the 1T peak response frequency the acoustic wavelength is shorter than the shortest cross-section of the chamber volume and the disturbance in the secondary nozzle is out of phase with the top wall sensors as shown in Figure 4.1.8l. The amplitude of the disturbance also quickly decreases above the 1T peak response frequency but begins to rise again as the excitation frequency approaches the 1L1T mode.

Identification and reconstruction of the peak 1L- and 1T-mode distributions is of particular interest. Based on the earlier analysis of sensor amplitudes shown in Figure 4.1.6 the 1L- and 1T-mode peak response frequencies occur approximately at frequencies of 3330 and 4480 Hz, respectively. The reconstruction of the acoustic field at these frequencies are shown in Figures 4.1.9 and 4.1.10.

4.1.5 Calculation of the Local Acoustic Disturbance

The acoustic disturbance acting locally upon the flame zone at each excitation frequency can then be interpolated from the reconstructed acoustic field. in Section 5.3 The local acoustic disturbance is compared with optical data to determine the relationship between

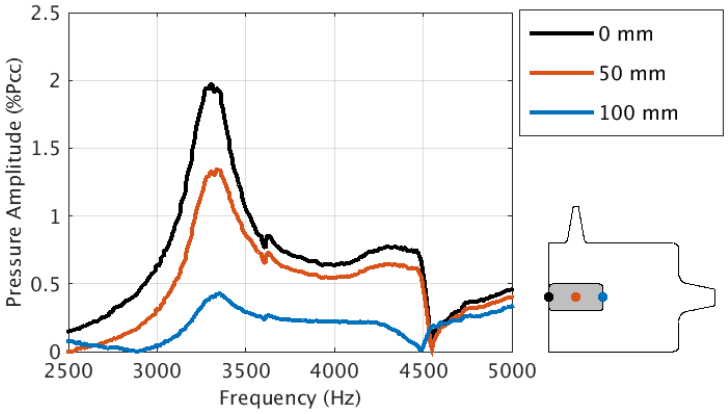

(a) Window pressure disturbance amplitudes.

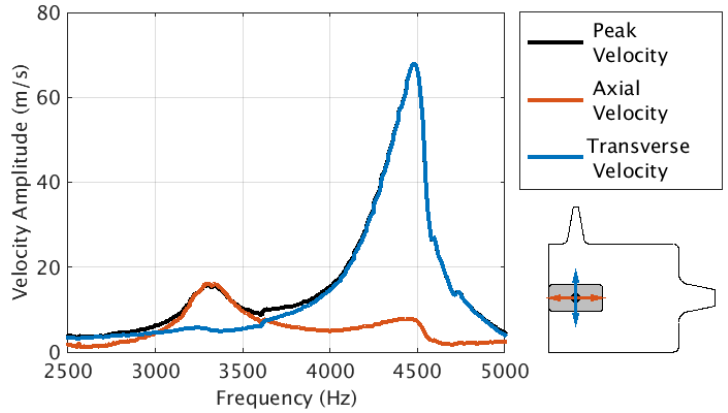

(b) Window velocity disturbance amplitudes.

Figure 4.1.11: Amplitude of acoustic disturbance in the center of the BKH window region. Data was extracted from the acoustic field reconstruction of the BKH hot flow experiment.

acoustic and intensity fluctuations. Knowledge of the local acoustic disturbance acting upon the injection elements is used to determine representative numerical disturbances for modelling of BKH experiments.

Figure 4.1.11 shows the amplitude of the local acoustic pressure and velocity disturbances in the BKH optical window region versus excitation frequency. These results have been extracted from the reconstructed acoustic field for all frequencies assuming a uniform chamber density of 3 kg/m^3. Figure 4.1.11a shows the amplitude of the pressure disturbance at 0, 50, and 100 mm from the injection plane corresponding to the start, middle, and end of the window, respectively. It can be seen that pressure fluctuation at the injection plane are larger than the pressure fluctuations downstream, particularly during excitation of the 1L mode. It can also been seen that pressure fluctuations are observed at the center of the window-region during excitation of the 1T mode between 4100 and 4500 Hz. This indicates that the pressure nodal line of the 1T mode is not located precisely in the middle of the flame zone and window, but is most likely offset slightly above the center of the window due to the asymmetry of the chamber volume caused by the secondary nozzle.

Figure 4.1.11b shows the velocity fluctuation extracted from a point 50mm from the injection plane at the center of the window region. Near the 1L frequency, the window is subjected to axial velocity fluctuations with amplitudes up to 18 m/s at this particular point. Much larger transverse velocity fluctuations occur during excitation of the 1T mode. The amplitude of the acoustic velocity is linearly dependant on the local value of density, with lower densities producing higher velocity amplitudes. The hot combustion products in the window region may have densities as low as 2.3 kg/m^3 resulting in a maximum 1T velocity amplitudes of 90 m/s in the center of the window region. Alternatively the

LOx jet has a density 2 orders of magnitude higher and there would effectively be no acoustic velocity disturbance in this dense medium. The value of 3 kg/m^3 used to produce the results presented in this work is believed to be representative of the gaseous medium surrounding the central combustion zone.

4.2 Acoustic Modelling

To be applicable in an industrial setting, a method for predicting combustion instabilities would have to function relying only upon the specifications and operating conditions of an engine as inputs such as details of the chamber geometry and its intended operating point. To have confidence in the results the method would need to be demonstrated and validated against representative test cases. It is also important that the method can produce results quickly and efficiently in order to be applicable in an industrial setting.

In this section, the industrial challenge of predicting the acoustic modes of a rocket engine combustion chamber is addressed. Modal analysis is used to model the BKH acoustic field and predict the resonant acoustic mode frequencies and distributions. The employed method assumes knowledge of the chamber geometry and operating point so that a CFD solver can be used to determine the steady state distribution of acoustic properties in the chamber. For this work, the steady state result presented in Chapter 3 is used. Modal analysis is performed using the acoustic property distribution from the CFD result to model the chamber and identify its resonant modes. The frequency domain model employed is inexpensive making it suitable for industrial application. The results of the model are compared with the BKH experimental data presented in the previous section.

Modal analysis of the BKH combustion chamber has previously been undertaken by Hardi et. al. [51, 49]. The previous work employed a FEM acoustic solver in ANSYS to calculate the acoustic modes. The results were compared with experimental data. In the work by Hardi et. al. the model did not consider a variation of the acoustic properties within the chamber volume. Instead the properties of the combustion products estimated from CEA were assumed to be representative of the properties of the chamber domain. The frequencies of the acoustic modes were compared with the frequency spectrum of pressure sensor data and found to agree well. The current work aims to improve upon the previous results by consideration of the acoustic property distribution within the chamber using the steady state model results discussed in the previous chapter. The predicted resonant mode distributions are compared against sensor data from BKH experiments. The acoustic disturbance at non-resonant frequencies is also modelled and compared with the experimental results presented in Section 4.1.2.

4.2.1 Numerical Method

The commercial software package COMSOL Multiphysics is used for the present work. An implemented wave equation solver, referred to as the pressure acoustics model, is used to compute the acoustic eigenmodes of the chamber and to perform a modal analysis over a frequency range comparable to the excitation frequency ramp in BKH experiments.

The pressure acoustics model solves the wave equation for a time harmonic acoustic wave:

$$p(x,t) = p(x)e^{i\omega t}, \tag{4.9}$$

where p is acoustic pressure, x is the spatial coordinate, t is time, and ω is the complex angular frequency. The time harmonic acoustic wave assumption is used to reduce the wave equation to an inhomogeneous Helmholtz equation.

$$\nabla\Big(-\frac{1}{\rho_c}(\nabla p - q_d)\Big) + \frac{\omega^2 p}{\rho_c c_c^2} = Q_m \tag{4.10}$$

where q_d is a dipole source, Q_m is a monopole source, and ρ_c and a_c are the mean flow density and mean flow speed of sound, respectively. The subscript "c" is used here to indicate that the speed of sound and density may also be complex valued. Complex values of these properties may be used to represent acoustic attenuation in porous materials or highly viscous fluids.

For an eigenfrequency calculation, Equation 4.10 is formulated as an eigenvalue problem.

$$\nabla\Big(-\frac{1}{\rho_c}\nabla p\Big) + \frac{\lambda^2 p}{\rho_c a_c^2} = 0 \tag{4.11}$$

where $\lambda = i2\pi f = i\omega$ is the eigenvalue to be solved for. The eigenfrequency formulation neglects the acoustic source terms in Equation 4.10. Therefore no acoustic forcing is included in the eigenfrequency calculation.

For a frequency domain modal analysis calculation, the wave number, k_{eq}, is introduced and Equation 4.10 is reformulated in the frequency domain.

$$\nabla\Big(-\frac{1}{\rho_c}(\nabla p - q_d)\Big) + \frac{k_{eq}^2 p}{\rho_c} = Q_m \tag{4.12}$$

$$k_{eq}^2 = \Big(\frac{\omega}{a_c}\Big)^2 \tag{4.13}$$

k_{eq} includes the ordinary wave number k and other out-of-plane or circumferential contributions if applicable. Modal analysis is used to compute the response over a range of frequencies using harmonic loads and sources. The wave number at each frequency is computed using Equation 4.13 and substituted into Equation 4.12 to compute the resulting acoustic pressure disturbance.

A number of boundary conditions have been implemented in the pressure acoustics model. In the present work three different boundary conditions are employed: the sound hard boundary condition, the impedance boundary condition, and the velocity boundary condition. The sound hard boundary condition is a perfectly reflecting boundary condition with no acoustic velocity fluctuation normal to the boundary surface and is representative of solid boundary surfaces.

The impedance boundary condition relates the amplitude of the pressure and velocity fluctuations at the boundary. The specific impedance $Z_i = \rho_c c_c$ is prescribed at the boundary and Equation 4.14 is applied normal to the boundary surface.

$$-\frac{1}{\rho_c}\nabla p = \frac{i\omega}{Z_i} \tag{4.14}$$

where ω is the angular frequency. The impedance boundary condition is an intermediate condition between the perfectly reflecting sound hard ($Z_i = 0$) and the perfectly non-reflecting sound soft ($Z_i = \infty$) boundary conditions. It is used to represent internal fluid boundaries connected to volumes that are not acoustically decoupled from the volume being considered.

The velocity boundary condition prescribes a harmonically oscillating velocity disturbance normal to the boundary surface. The velocity fluctuates at the frequency of the modal analysis. The amplitude of the velocity disturbance, v_d, is specified and Equation 4.15 is applied normal to the boundary surface.

$$-\frac{1}{\rho_c}\nabla p = i\omega v_d \tag{4.15}$$

Two different studies using the pressure acoustics model have been computed. The first study identifies the resonant frequencies of the chamber by computing the acoustic eigenmodes of the chamber model. The eigenmode solutions describe the resonant mode frequencies and distributions. To model the acoustic field in the chamber over the frequency range of the BKH excitation frequency ramp a frequency domain study is also computed. The frequency domain study computes the response of the model to harmonic excitation at specific frequencies. A MUMPS solver was used in both studies to solve the pressure acoustic model using direct LU decomposition. The MUMPS direct solver requires more RAM than other iterative methods but is more robust and ensures convergence of well conditioned models.

4.2.2 Model Description

In this section the application of the pressure acoustic model presented in Section 4.2.1 to model BKH is described. The model is computed for the 60 bar ROF 6 operating point described in Section 3.2.1. The domain used for the model consisted of the chamber volume and the converging sections up to the throat of both the main and secondary nozzles. A symmetry condition was prescribed at the horizontal center plane of the chamber to reduce the size of the numerical domain. The geometry of the injection elements was excluded and the injection plane was a treated as uniform flat surface. The area of the exit of each injection element on the injection plane were defined as separate boundary surfaces in order to apply impedance boundary conditions at each injector. The domain is shown in Figure 4.2.1.

All boundaries of the domain corresponding to chamber walls were treated as sound hard boundaries. At the 60 bar ROF 6 operating point both the main and secondary nozzles would be choked and can therefore be approximated to first order as a solid wall

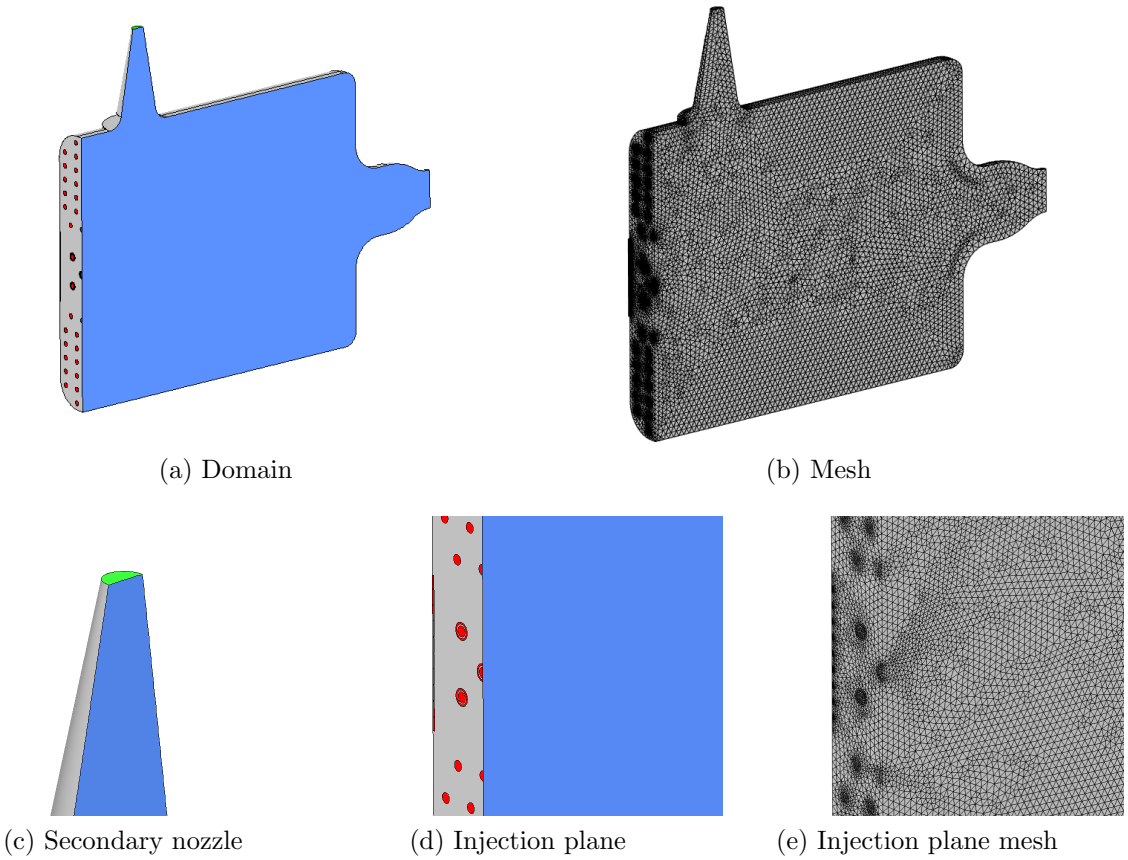

(a) Domain (b) Mesh

(c) Secondary nozzle (d) Injection plane (e) Injection plane mesh

Figure 4.2.1: Domain and mesh used for chamber acoustic model.

[78]. Therefore the boundaries at the throat of the main and secondary nozzles were also prescribed as sound hard boundaries in this work. An alternative would be to prescribe a complex impedance condition representing the nozzle. Methods for determining complex impedances representative of the internal boundary of a rocket combustor nozzle have been identified by Crocco and Sirignano [14] and experimentally by Zinn et al. [170]. Schulze et al. [133] has also studied new methods of modelling the acoustic admittance. These works have focused on rocket engine nozzles where the diameter of the nozzle is comparable to the cross section of the chamber. It is unclear if the same analysis can be applied to the nozzles of the BKH chamber where the area of the nozzles are a fraction of the total chamber cross section.

An impedance boundary condition was applied to the surface area of each injection element on the injection plane. Physically, each injection element would respond to the fluctuations in the chamber differently. To model the response of each injector accurately the complex impedance of each element for each excitation frequency would need to be determined. As this is not in the scope of the current work a real-valued specific impedance was instead defined at each injector inlet boundary. The value of the specific impedance was computed using the values of density and speed of sound at each injector inlet from the steady state CFD solution. The applied real specific impedance is equivalent to partial reflection with no phase shift at each injector inlet surface.

For calculations with acoustic excitation, a velocity boundary condition was prescribed to the secondary nozzle throat boundary surface instead of a sound hard wall boundary condition. A velocity disturbance amplitude equal to one quarter of the sonic flow velocity at the secondary nozzle throat was applied for all excitation frequencies. This velocity disturbance was found to produce disturbance amplitudes similar to those observed during BKH experiments.

An unstructured tetrahedral mesh with 1.35 million elements was used to mesh the numerical domain. Geometric clustering was used to refine the mesh about the injector inlets in order to resolve the boundary surfaces. The mesh for acoustic models must be sufficiently fine to resolve the acoustic wavelengths of interest and are typically coarser than meshes used for CFD. For this work a very fine mesh was used with a maximum element size of 2.5 mm. The fine mesh was necessary to resolve the variations in acoustic properties interpolated from the steady state model. The mesh is shown in Figure 4.2.1b.

A real gas fluid model is not currently implemented in the pressure-acoustics solver. In the current work the linear elastic fluid model was chosen and the density and speed of sound were specified as distributed real-valued properties. Therefore the medium inside the chamber is modelled as a lossless compressible fluid. The linear elastic fluid model was the best available model for approximating the acoustic behaviour of the medium containing both gaseous combustion products and dense liquid oxygen.

The speed of sound and density distributions from the steady state BKH chamber model presented in Chapter 3 were imported into the model to be utilised in Equations 4.10 and 4.12. A custom inverse distance weighted interpolation function was developed to map the results from the steady state chamber model to each point in the mesh of the chamber acoustic model. The imported speed of sound and density distributions are shown in Figure 4.2.2. The speed of sound distribution shows the horizontal stratification of the flow in BKH with ambient temperature secondary hydrogen injection above and below the warmer central combustion zone.

The results of two BKH chamber acoustic calculations are discussed in the current work. An eigenfrequency calculation was used to identify the resonant mode frequencies and distributions of the chamber volume. A frequency domain modal analysis calculation with acoustic excitation at the secondary nozzle was then used to perform a parametric frequency sweep over the 2.5 to 5 kHz frequency range covered by the BKH excitation

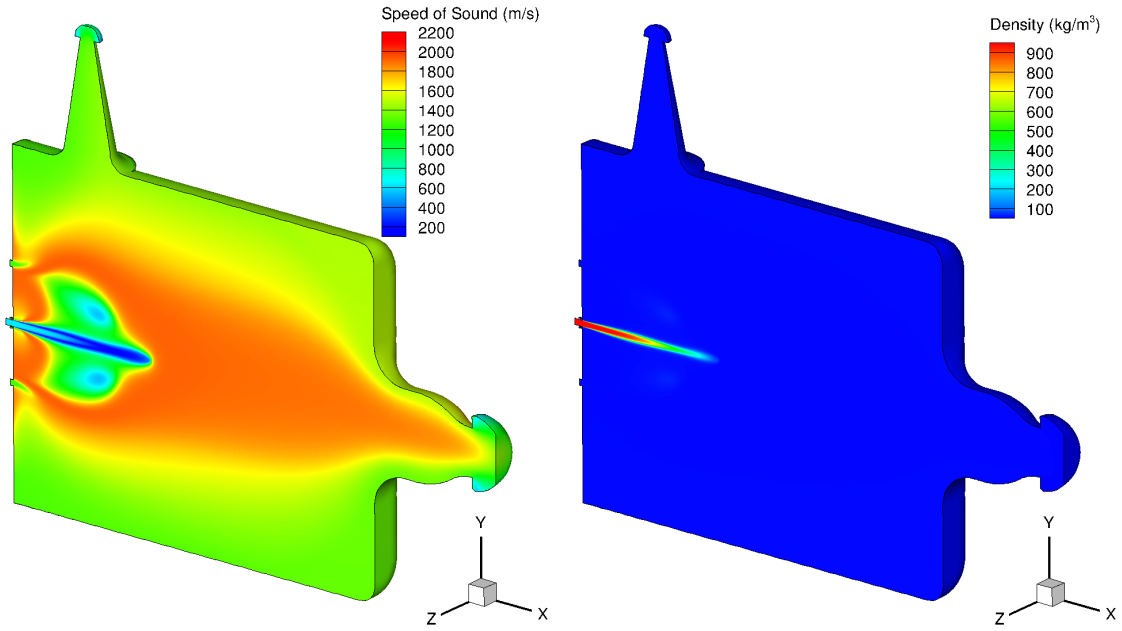

(a) Speed of sound distribution (b) Density distribution

Figure 4.2.2: Acoustic property distributions from the steady state chamber model.

Table 4.1: Predicted eigenfrequency and experimental unexcited resonant mode frequencies.

Mode	Predicted Frequency (Hz)	Experimental Frequency (Hz)	Error (%)
1L	3272	3250	0.7
1T	4433	4350	2.1
1L1T	5318	5450	2.4

frequency ramp. The computations on the fine mesh using the direct MUMPS solver required over 50 GB of RAM and were computed using two 16 core AMD opteron 6274 processors. The eigenmode study required 96 CPU hours to compute the first 12 eigenmodes of the chamber, while the frequency domain study required an average of 8.5 CPU hours per computed frequency.

4.2.3 Results of Eigenfrequency Calculation

The resonant mode frequencies were predicted using an eigenmode calculation. The experimental resonant mode frequencies were determined by computing the PSD of pressure sensor data from an unexcited BKH experiment and identifying the peaks corresponding to each resonant mode. The predicted and experimental resonant mode frequencies are listed in table 4.1. The predicted frequencies of the first 3 resonant modes are all within 3% of the experimental frequencies.

Figures 4.2.3, 4.2.4, and 4.2.5 show the pressure, velocity, and phase distributions at the center plane of the predicted 1L, 1T, and 1L1T modes, respectively. The amplitude and phase distributions have been normalised relative to the disturbance at the PCCDYN2 sensor position. The velocity has also been normalised so that it is representative of a $5\%P_{cc}$ amplitude disturbance at the PCCDYN2 sensor position. The pressure and phase distributions match the expected resonant mode distributions. The influence of the 3D steady-state flow field is clearly seen in the velocity distributions. The dense liquid oxygen

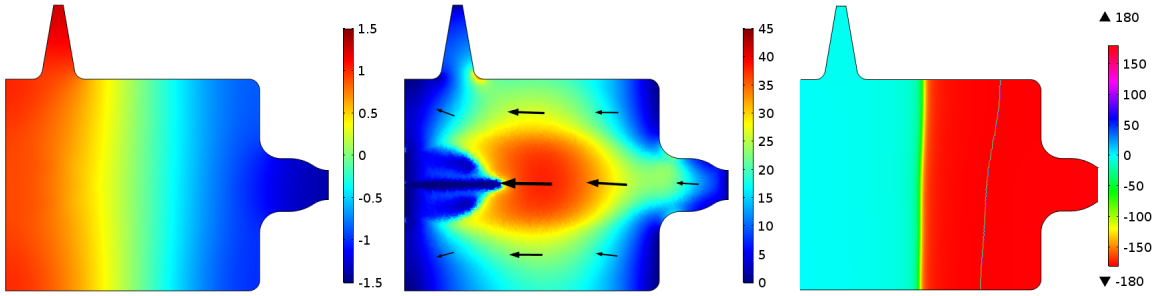

(a) Pressure distribution (b) Velocity distribution (m/s) (c) Phase distribution (deg)

Figure 4.2.3: Centerplane 1L eigenmode distributions.

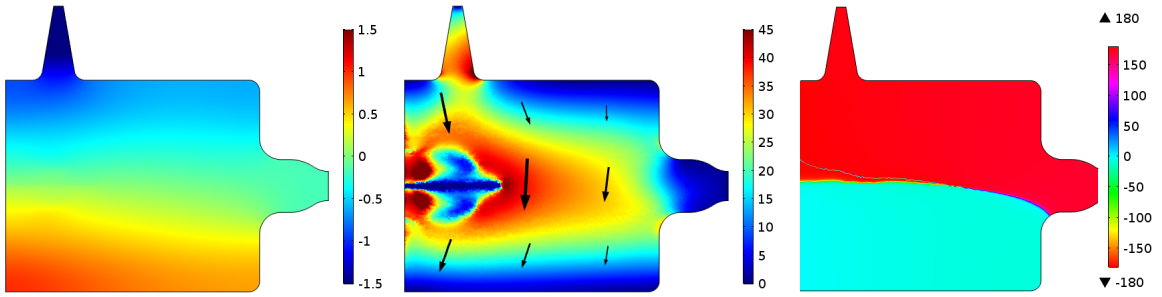

(a) Pressure distribution (b) Velocity distribution (m/s) (c) Phase distribution (deg)

Figure 4.2.4: Centerplane 1T eigenmode distributions.

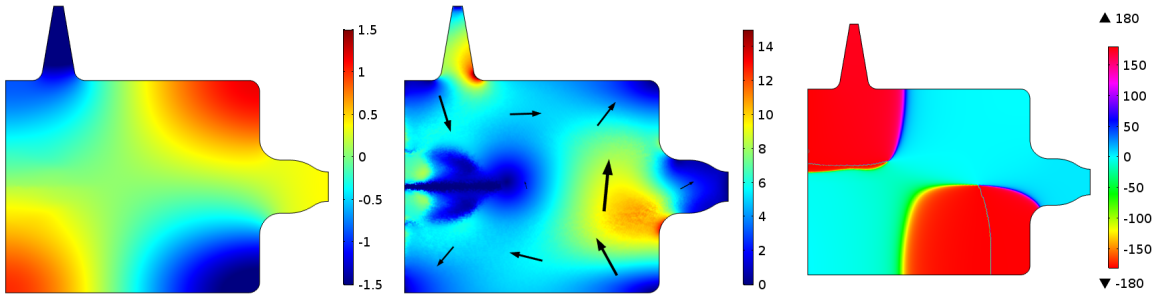

(a) Pressure distribution (b) Velocity distribution (m/s) (c) Phase distribution (deg)

Figure 4.2.5: Centerplane 1L1T eigenmode distributions.

at the center of the chamber has a much lower speed of sound than the hot combustion products that fill the rest of the chamber volume. The inertia of the high density oxygen prevents it from being transported by the acoustic disturbance and results in negligible acoustic velocity in this region.

Figures 4.2.6 and 4.2.7 show mirrored cross sections of the acoustic disturbances of the 1L and 1T modes normal to the chamber centerplane. These distributions show that the predicted acoustic distributions are 3D, like the interpolated steady state flow field. The negligible center plane acoustic velocity in the locations of the dense oxygen in Figures 4.2.3, 4.2.4, and 4.2.5, are not representative of the acoustic disturbance acting upon the gaseous combustion products surrounding the central flame zone.

The disturbance surrounding the flame zone is similar to that of a chamber with uniform acoustic properties suggesting that the presence of the dense oxygen has minimal impact on the overall mode distribution. The acoustic velocity distributions either side of the flame zone are comparable to the distributions predicted by the acoustic field reconstruction in Section 4.1.4. This is expected, as the acoustic field reconstruction assumed a uniform density of 3 kg/m^3 which is representative of the medium either side of the flame zone.

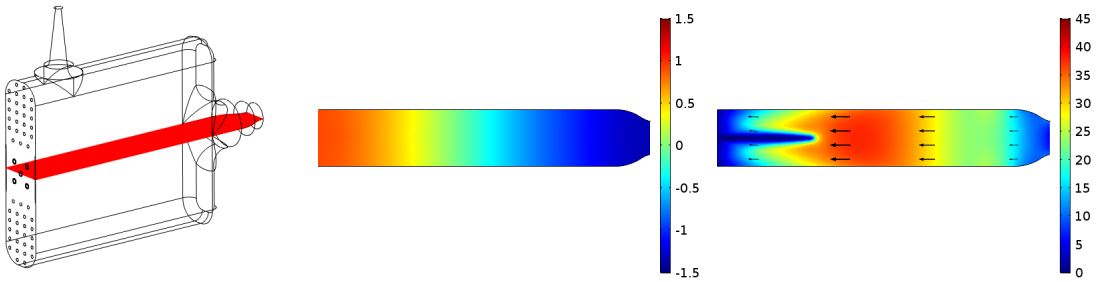

(a) Plane position (b) Pressure distribution (c) Velocity distribution (m/s)

Figure 4.2.6: 1L eigenmode distributions on a horizontal plane at the center of the BKH chamber.

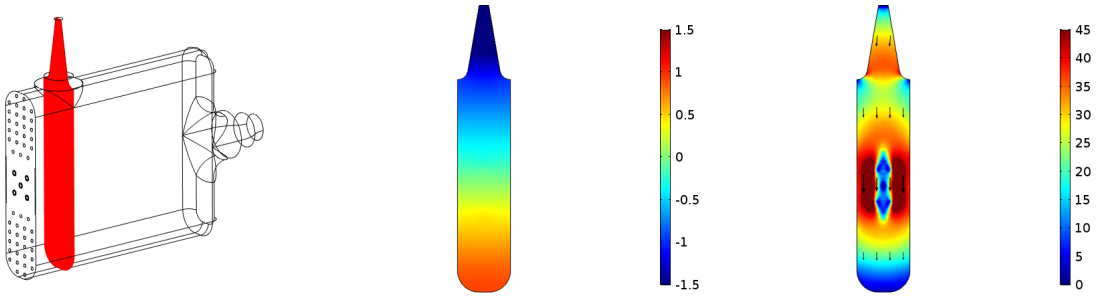

(a) Plane position (b) Pressure distribution (c) Velocity distribution (m/s)

Figure 4.2.7: 1T eigenmode distributions on a vertical plane 50 mm from the BKH injection plane.

The accuracy of the predicted eigenmode distributions is assessed by comparing the distributions with the relative amplitude of dynamic pressure sensor data from BKH experiments. Figures 4.2.8 and 4.2.9 compare the acoustic amplitude along vertical and horizontal lines extracted from the eigenmode solutions and the amplitudes of the distributed BKH dynamic pressure sensor data. The amplitudes of the eigenmode distributions and pressure sensor data have been normalised by the amplitude of the PCCDYN2 sensor signal. The experimental amplitude is determined as the result of the adjusted BPRMS calculation described in Section 4.1.2 at the 1L peak-response frequency of 3330 Hz and 1T peak response frequency of 4480 Hz.

The error bars shown in Figures 4.2.8 and 4.2.9 indicate 2 normalised standard deviations of the pressure amplitude in the 0.1 second RMS window used for the BPRMS calculation. Therefore the size of the error bars indicates how much the amplitude varied over the RMS window. Higher amplitude acoustic fluctuations are reached during 1T mode excitation of the BKH chamber. The large amplitude disturbance organises the acoustic motion within the chamber and more consistent amplitudes are reached resulting in small error bars. At the 1L-mode frequency the acoustic disturbance is weaker and less organised resulting in a higher normalised standard deviation and larger error bars.

Figures 4.2.8 and 4.2.9 also show that vertical and horizontal acoustic distributions can be reasonably approximated by a spline fit between the sensor positions. This is the basis for the acoustic reconstruction method described in Section 4.1.3. The only significant discrepancy is the influence of the secondary nozzle on the longitudinal 1T distribution shown in Figure 4.2.9a, but as sensors PCCDYN7 and PCCDYN8 confirm, the disturbance at the secondary nozzle does not significantly effect the acoustic distribution at the flame zone and this effect can be ignored.

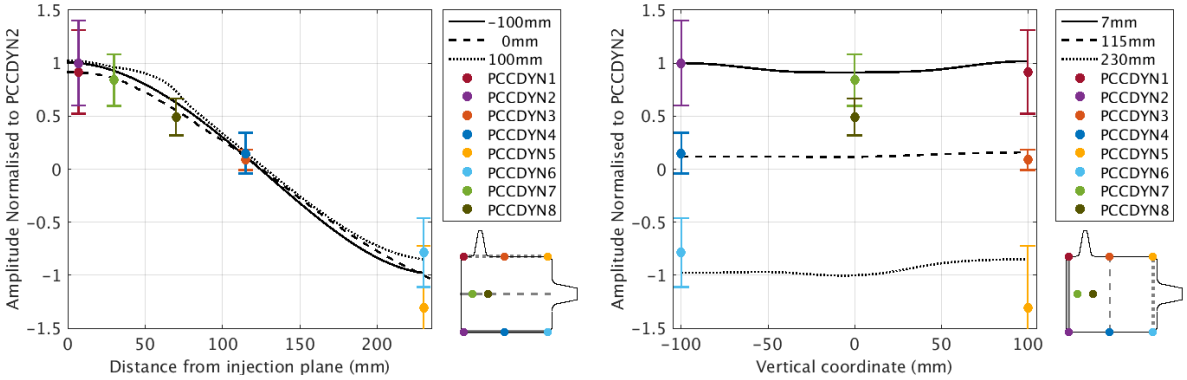

(a) Longitudinal distribution (b) Transverse distribution

Figure 4.2.8: Comparison of predicted and experimental 1L mode pressure distributions

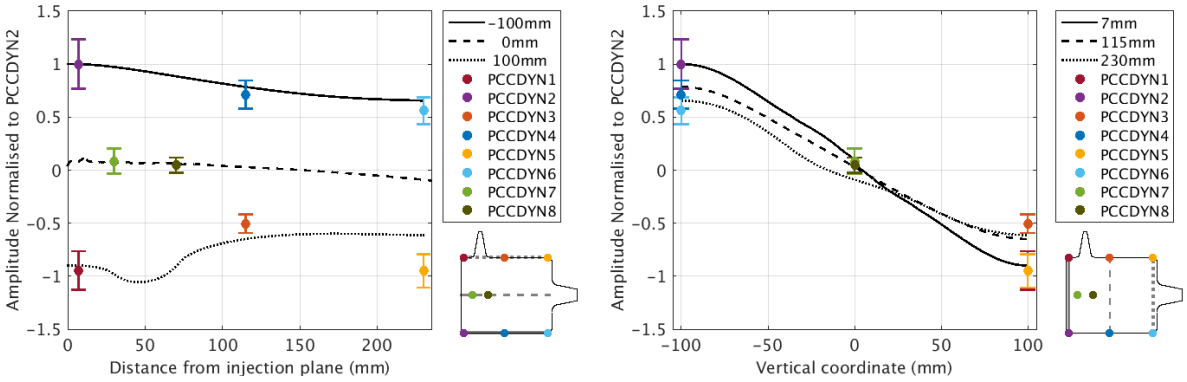

(a) Longitudinal distribution (b) Transverse distribution

Figure 4.2.9: Comparison of predicted and experimental 1T mode pressure distributions

4.2.4 Results of Modal Analysis Calculations

The modal analysis calculations were used to model the evolution of the acoustic field with varying excitation frequency. A parametric frequency ramp was used to study the 2500 to 5000 Hz frequency range covered experimentally by the BKH excitation frequency ramp.

To compare with the experimental data analysis previously presented in Section 4.1.2, the amplitude and phase at each of the BKH dynamic pressure sensor positions is extracted from the modal analysis results for each frequency computed. Figure 4.2.10 shows the acoustic pressure amplitude and phase versus excitation frequency and is comparable with the experimental results shown in Figure 4.1.6. The peak response occurs at the predicted 1L and 1T mode eigenfrequencies listed in table 4.1. The underlying acoustic property distribution used for the modal analysis is not affected by the acoustic disturbance. Therefore the speed of sound distribution is not modified as in the experiment and the shift of the 1T mode frequency is not reproduced in the model. Comparing Figures 4.2.10 and 4.1.6 it can be seen that the modal analysis has predicted the relative amplitudes of the acoustic disturbance at all sensor positions for both resonant and non-resonant frequencies.

The resulting amplitude of the disturbance is proportional to the amplitude of the harmonic velocity disturbance prescribed at the secondary nozzle. A velocity disturbance amplitude of one quarter the sonic flow velocity was used to produce the current results. One assumption of this model is that the same velocity disturbance is prescribed at all excitation frequencies. It is expected that the flow through the secondary nozzle takes some time to re-establish after the tooth of the siren wheel has stopped blocking the nozzle.

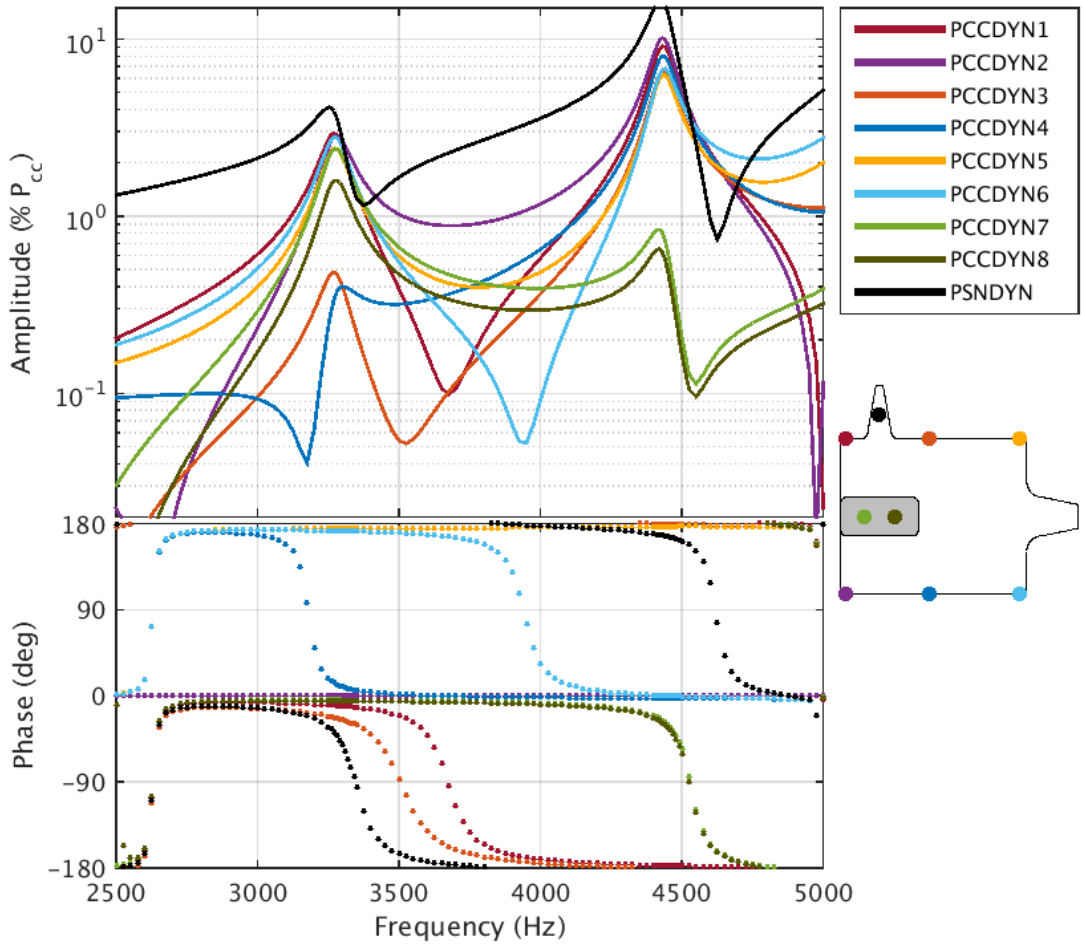

Figure 4.2.10: Amplitude and phase at dynamic pressure sensor position versus excitation frequency predicted by modal analysis. Comparable to experimental results shown in Figure 4.1.6.

Analysis of dynamic pressure sensor data from the secondary nozzle sensor has also shown a secondary peak which occurs after the flow has becomes sonic. The assumption of a harmonic velocity disturbance with the same amplitude at all frequencies is a considerable simplification and means that these effects are neglected in the current modelling approach.

The lower part of Figure 4.2.10 shows the phase of the acoustic pressure disturbance at the dynamic pressure sensor positions relative to the phase at the PCCDYN2 pressure sensor location and is comparable with Figure 4.1.6. The same shift of phase between sensor positions versus excitation frequency observed experimentally are seen in the modal analysis results.

The phase plot also shows the influence of the impedance boundary condition which is the only source of acoustic damping or dissipation in the model. The introduction of the impedance boundary condition results in a complex-valued solution for the acoustic field. Without the impedance boundary condition the acoustic field would be only real valued and a phase discontinuity would exist at the nodal line of the acoustic distribution. The relative phase on either side of this nodal line would be either 0° or 180°. With the acoustic impedance boundary condition the acoustic field is complex, the phase at the nodal line becomes continuous, and the transition of the relative phase between sensor positions that has been observed experimentally occurs.

While the real valued acoustic impedance imposed in the current approach has reproduced a similar trend, further consideration of impedance boundary conditions may improve the agreement with experimental data. Determination of better boundary condition parameters by further studying the acoustic properties of the injection system may

improve agreement between numerical and experimental results. Applying representative impedances at the main and secondary nozzle boundaries may also improve experimental agreement. Determining suitable impedance values would require dedicated experiments which are outside the scope of the current work. Thermal, viscous, and other losses have also been neglected in this study.

The acoustic distribution predicted by the modal analysis at various excitation frequencies are shown in Figures 4.2.11 and 4.2.12. The predicted distributions are comparable to the reconstructions from BKH dynamic pressure sensor data shown in Figures 4.1.7 and 4.1.8. As seen in the reconstruction from experimental data, at intermediate frequencies between the 1L and 1T mode the predicted acoustic pressure distribution rotates from a horizontal to a vertical distribution. The acoustic velocity distributions show the locations of the dense oxygen jets in the center plane of the chamber, as seen in Figures 4.2.11 and 4.2.12. Unlike the predicted eigenmode distributions in Figures 4.2.3 and 4.2.4, the velocity distributions predicted by the modal analysis show the high amplitude velocity forcing at the secondary nozzle. Despite this difference, the predicted acoustic disturbances in the flame zone at the resonant frequencies predicted by the modal analysis are very comparable to the results from the eigenfrequency calculation.

The acoustic phase distributions in Figures 4.2.3 and 4.2.4 show that despite the acoustic impedance boundary condition, a distinct nodal line still exists at all frequencies. More appropriate acoustic boundary conditions may improve the agreement between the predicted phase distributions and the acoustic reconstruction. The change in the phase of the secondary nozzle relative to the chamber volume that occurs above the 1T mode frequency is also predicted by the modal analysis.

4.2.5 Predicted Local Acoustic Disturbance

The predicted local acoustic disturbance acting upon the flame zone was extracted for each frequency computed in the modal analysis. The local acoustic pressure and velocity disturbances acting in the window region are shown in Figure 4.2.13. Data was extracted from the same axial and transverse positions as the results extracted from the reconstruction from experimental data discussed in Section 4.1.5 and presented in Figure 4.1.11.

The acoustic pressure disturbances shown in Figure 4.2.13a are taken from the center of the chamber. At this location, in the dense LOx core, the acoustic velocity is negligible. The acoustic velocity disturbances shown in Figure 4.2.13b are extracted from a point in the outer gaseous flow, 5mm from the side wall of the chamber. The predicted local acoustic disturbances shown in Figure 4.2.13 are very similar to the results from the acoustic reconstruction shown in Figure 4.1.11. The amplitude difference could be reduced by adjusting the amplitude of the imposed velocity disturbance in the acoustic model to better match the experimental amplitudes at the frequency of interest. Similarly the difference in acoustic velocity could be improved by selecting a different density value for the calculation of the acoustic velocity when reconstructing from experimental data.

4.3 Summary

In this chapter the BKH acoustic field produced by the acoustic excitation system has been described using experimental results and predicted with a low-order modelling approach. Dynamic pressure sensor data was analysed to identify the resonant modes and the evolution of the acoustic field with varying excitation frequency. A new complex reconstruction method improved upon previous methods by allowing the acoustic field to be reconstructed from experimental data for all frequencies of interest. The complex reconstruction results provided new insight into how the acoustic field rotates and transitions between the 1L

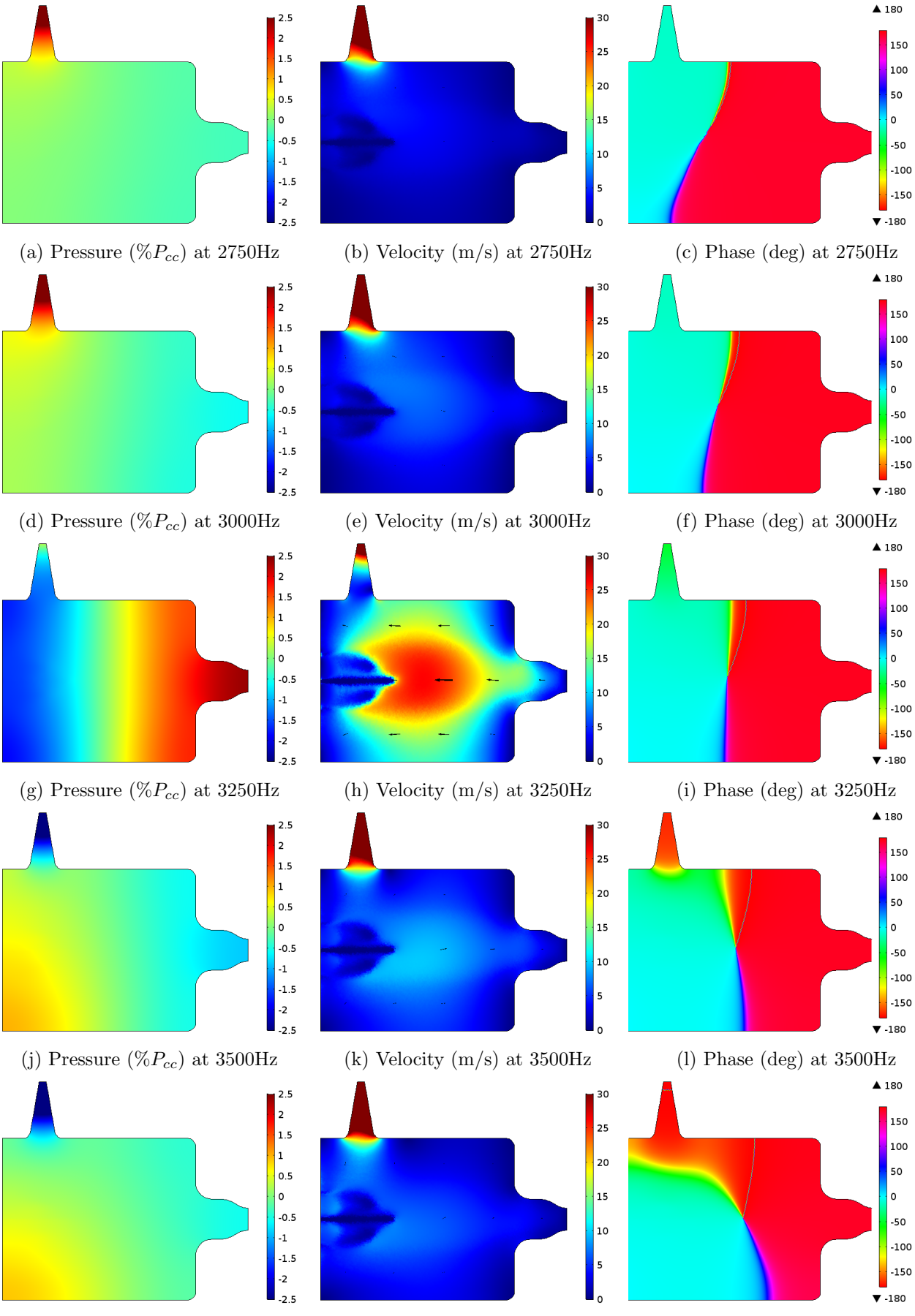

(a) Pressure (%P_{cc}) at 2750Hz (b) Velocity (m/s) at 2750Hz (c) Phase (deg) at 2750Hz

(d) Pressure (%P_{cc}) at 3000Hz (e) Velocity (m/s) at 3000Hz (f) Phase (deg) at 3000Hz

(g) Pressure (%P_{cc}) at 3250Hz (h) Velocity (m/s) at 3250Hz (i) Phase (deg) at 3250Hz

(j) Pressure (%P_{cc}) at 3500Hz (k) Velocity (m/s) at 3500Hz (l) Phase (deg) at 3500Hz

(m) Pressure (%P_{cc}) at 3750Hz (n) Velocity (m/s) at 3750Hz (o) Phase (deg) at 3750Hz

Figure 4.2.11: Evolution of the acoustic field predicted by the frequency domain modal analysis. Excitation Frequencies from 2.75 and 3.75 kHz.

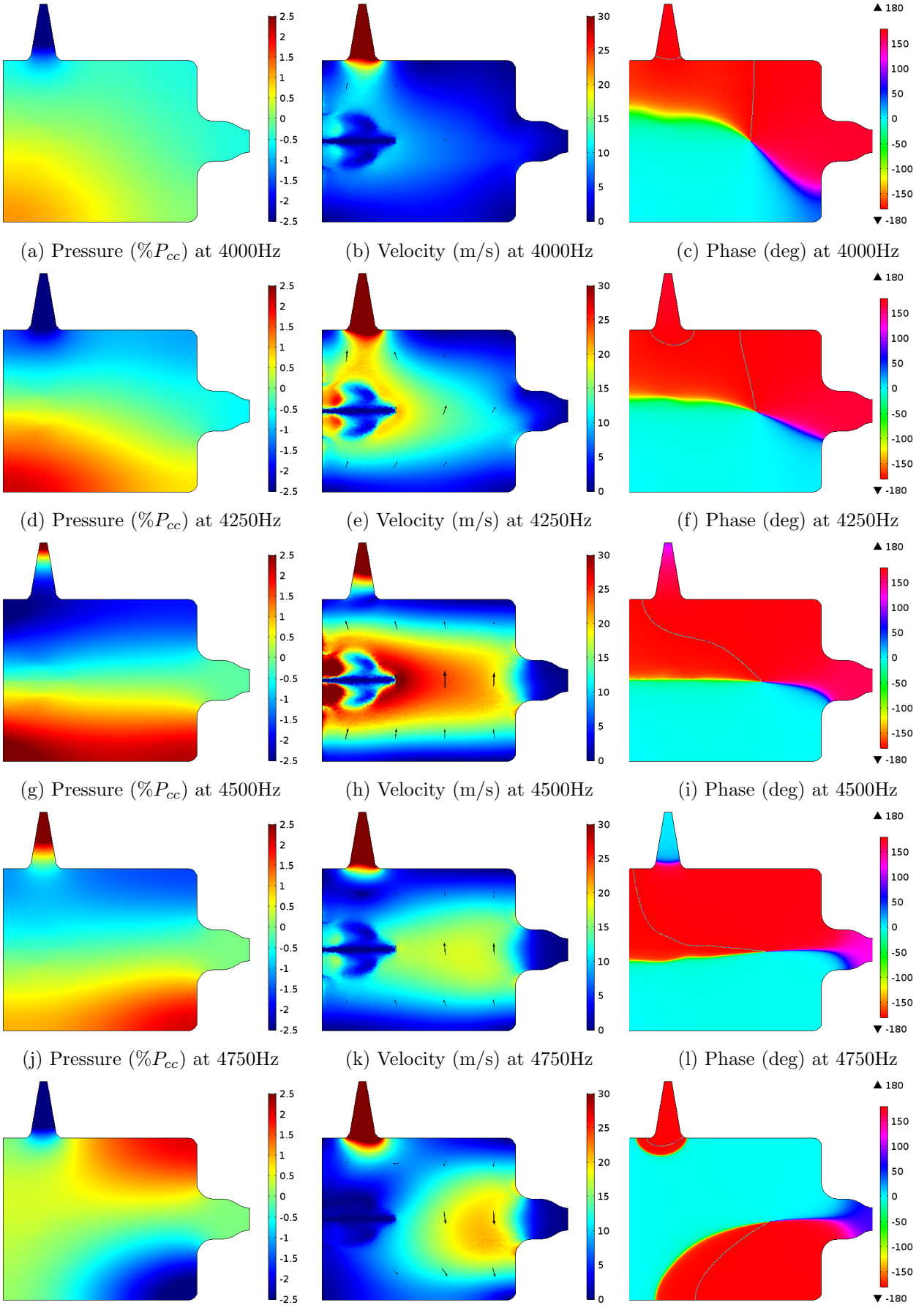

(a) Pressure (%P_{cc}) at 4000Hz (b) Velocity (m/s) at 4000Hz (c) Phase (deg) at 4000Hz

(d) Pressure (%P_{cc}) at 4250Hz (e) Velocity (m/s) at 4250Hz (f) Phase (deg) at 4250Hz

(g) Pressure (%P_{cc}) at 4500Hz (h) Velocity (m/s) at 4500Hz (i) Phase (deg) at 4500Hz

(j) Pressure (%P_{cc}) at 4750Hz (k) Velocity (m/s) at 4750Hz (l) Phase (deg) at 4750Hz

(m) Pressure (%P_{cc}) at 5000Hz (n) Velocity (m/s) at 5000Hz (o) Phase (deg) at 5000Hz

Figure 4.2.12: Evolution of the acoustic field predicted by the frequency domain modal analysis. Excitation frequencies from 4 to 5 kHz.

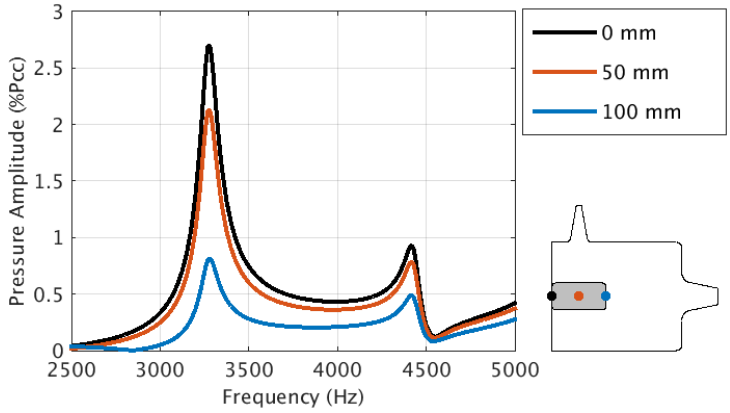

(a) Pressure Disturbance Amplitude

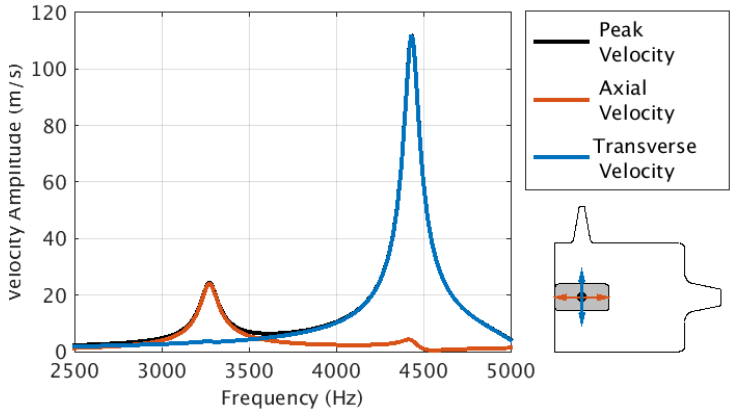

(b) Velocity Disturbance Amplitude

Figure 4.2.13: Amplitude of acoustic disturbance in the center of the BKH window region. Data was extracted from the acoustic field reconstruction of the BKH hot flow experiment.

and 1T resonant modes. The rotation of the acoustic field as the excitation frequency varies explains why the acoustic modes can appear as wide frequency bands in pressure data spectra.

The results of the complex reconstruction method also identified a phase difference between sensor positions which is the result of the acoustic admittance of the boundaries of the BKH chamber volume. By reconstructing the acoustic field using the complex acoustic amplitude the resulting phase distribution across the chamber volume can be recovered. The results of this analysis serve as valuable validation data for acoustic models of rocket engine combustion chambers.

The acoustic modelling of BKH demonstrated an approach using a low-order numerical modelling method able to predict the acoustic disturbance at resonant and non-resonant frequencies in a time scale suitable for industrial application. This approach relied upon having an informed estimate of the acoustic property distribution in the chamber volume from a CFD solution. The results of this modelling approach reproduced the evolution of the acoustic field with varying excitation frequency. The model improved upon previous works by including an impedance boundary conditions at the injector inlets that produced phase distributions that better matched the new experimental results. By including a realistic 3D acoustic property distribution from the steady-state chamber model solution, the model also predicted the variation in the acoustic disturbances acting around the primary flame zone.

Despite various simplifications and assumptions in both approaches, good agreement between experimental and numerical results were obtained. Importantly, the results of both approaches describe the local acoustic disturbance acting upon the flame zone. The new complex reconstruction method is employed again in Chapter 5 to predict the local

acoustic disturbance distribution in the window region in order to analyse the flame response using BKH optical data.

Chapter 5

Optical Data Analyses

Optical data from combustion instability experiments is used to investigate and describe the flame response. The response of flames to acoustic excitation has qualitatively been identified by a number of research groups. Typically a uniform combustion response is found to occur in phase with acoustic pressure fluctuations and the transport of the flame during acoustic velocity forcing from low to high pressure regions produces a positive coupling between combustion and acoustic processes. Results such as response factors are used for low-order tools, while Rayleigh indices and phase distributions serve as a point of comparison for validation of higher-order numerical models and simulations. However most results are still qualitative and describe general trends and observed behaviour rather than quantitative results that can be used for numerical validation. The analysis of optical data from combustion instability experiments therefore provides only limited insight and is often seen as complementary to numerical research.

There are a number of challenges that must be addressed before quantitative results can be produced. Chief among them is a thorough understanding of flame emission at high pressure which will inform and allow better interpretation of experimental results. Other challenges include developing methods for determining the local or representative disturbance acting upon the flame, isolating the response of the flame to the imposed acoustic disturbance, and analysing transient unsteady motion to produce results that can be compared quantitatively with numerical results.

The current study focuses on addressing the identified challenges besides flame emission. Similar BKH optical datasets to those analysed in this work have previously been studied by Hardi et al. [49, 50]. The previous analysis focused on comparing individual images with the instantaneous acoustic disturbance. The acoustic disturbance was assumed to take the form of an acoustic eigenmode which meant that the analysis could only be applied to samples excited at the resonant frequency.

The current analysis improves upon the previous results by Hardi et al. by using DMD analysis to isolate the response to the imposed acoustic disturbance at the frequencies of interest. This improved analysis also uses the new complex reconstruction method for reconstructing the acoustic field from dynamic pressure sensor data presented in Chapter 4. Additionally, a complex amplitude formulation is used for both the acoustic and optical intensity fluctuations. The complex amplitude formulation allows the mean phase difference between acoustic and optical intensity fluctuations to be quantified in a more consistent manner than previous cross-correlation methods. The identified phenomena provide further understanding of combustion instabilities and new results for validation of numerical models.

5.1 BKH Optical Data

The optical setup has been previously described in Section 2.6.3. For the current study optical data collected from BKH experiments at the 60 bar ROF 6 operating point have been analysed. The optical datasets were collected as part of larger BKH experimental test campaigns whose results have been previously reported by Hardi [49] and Webster [159]. A summary of the datasets is provided in Table 5.1. Each dataset contains a sequence of at least 1000 images at the specified sampling rate and resolution. The spatial resolution indicates how much of the window area is represented by a single pixel in each dataset. The original images typically capture the window and a region surrounding it. The spatial resolution of the image stated in Table 5.1 is the resolution after the images have been cropped to include only the 100 × 50 mm window region.

Table 5.1: Summary of analysed optical datasets.

Test	**Excitation**	**Camera**	**Sampling Rate (fps)**	**Spatial Resolution (mm^2/pixel)**
A	1L	Shadowgraph	20,000	0.018
		OH*	30,000	0.212
	1T	Shadowgraph	20,000	0.018
		OH*	30,000	0.212
B	1T	Shadowgraph	20,000	0.023
		OH*	24,000	0.245
C	1L	Shadowgraph	18,000	0.003

Test A in Table 5.1 was from a later BKH campaign which used the green LED as the back-lighting source for shadowgrpah imaging. During this test simultaneous shadowgraph and OH* images were captured during periods of both 1L- and 1T-mode excitation. Tests B and C in Table 5.1 were from an earlier BKH campaign where the Xenon lamp was used as a back-lighting source for the shadowgraph imaging. The optical datasets from 1T-mode excitation in test 2 better resolve the near injector region. The optical dataset from Test C is a specially chosen sample from a test where the shadowgraph camera was zoomed in to focus on the shear layer of the central BKH injector. The camera settings were modified between different BKH tests and campaigns to try and better resolve the flame. Therefore, only the 1L and 1T samples from Test A are directly comparable to one another as the same camera settings were employed for both optical datasets.

All of the optical datasets to be analysed are from 60 bar ROF 6 experiments with acoustic excitation. For comparison, samples of shadowgraph and OH* images from a 60 bar ROF 6 experiment without acoustic excitation are shown in Figure 5.1.1. Without acoustic excitation the liquid oxygen stream from the central injection element continues along the length of the window. The OH* image show the flames from the individual coaxial injection elements in the near injector region. Shortly downstream the flame fills the height of the window region with almost uniform intensity. Lighter lobes are visible between the central and outer injectors near the middle of the window.

5.1.1 1L Mode Optical Data

During 1L-mode excitation the flame zone is subjected to acoustic pressure fluctuations and axial velocity forcing. Figure 5.1.2 shows simultaneously recorded shadowgraph and OH* images from the Test A 1L sample. The shadowgraph images show that the oxygen jets are not significantly affected by the longitudinal acoustic disturbance. Similarly the

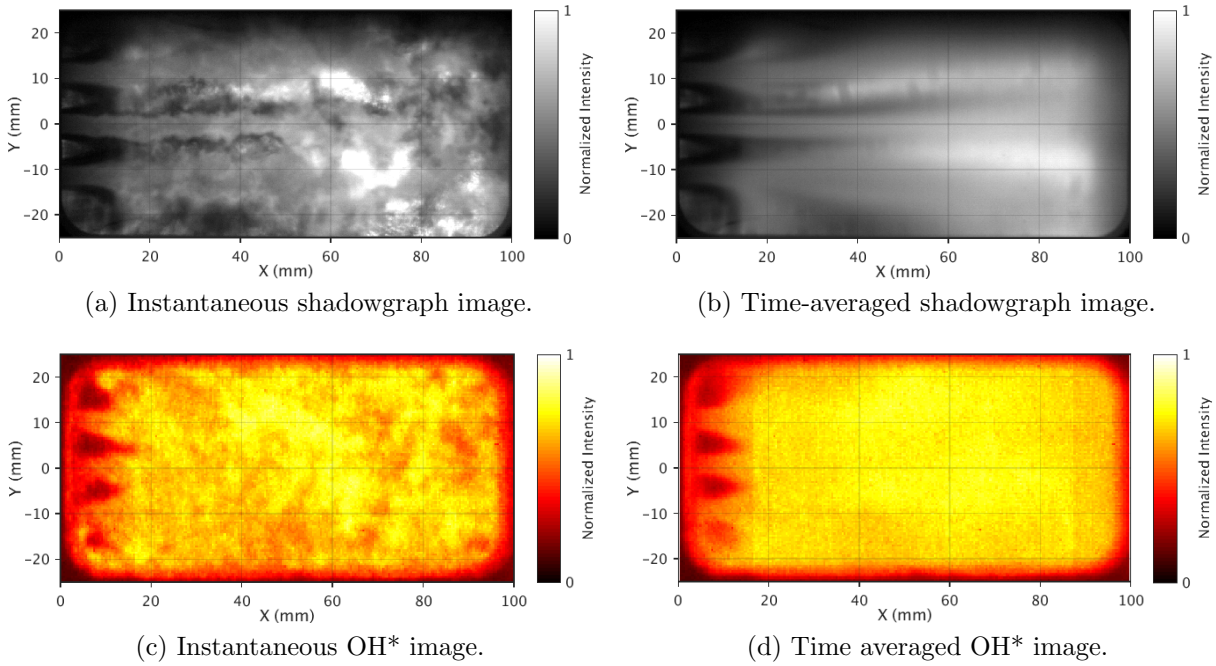

(a) Instantaneous shadowgraph image.

(b) Time-averaged shadowgraph image.

(c) Instantaneous OH* image.

(d) Time averaged OH* image.

Figure 5.1.1: Simultaneously recorded instantaneous and time-averaged optical images from a test without acoustic excitation [49].

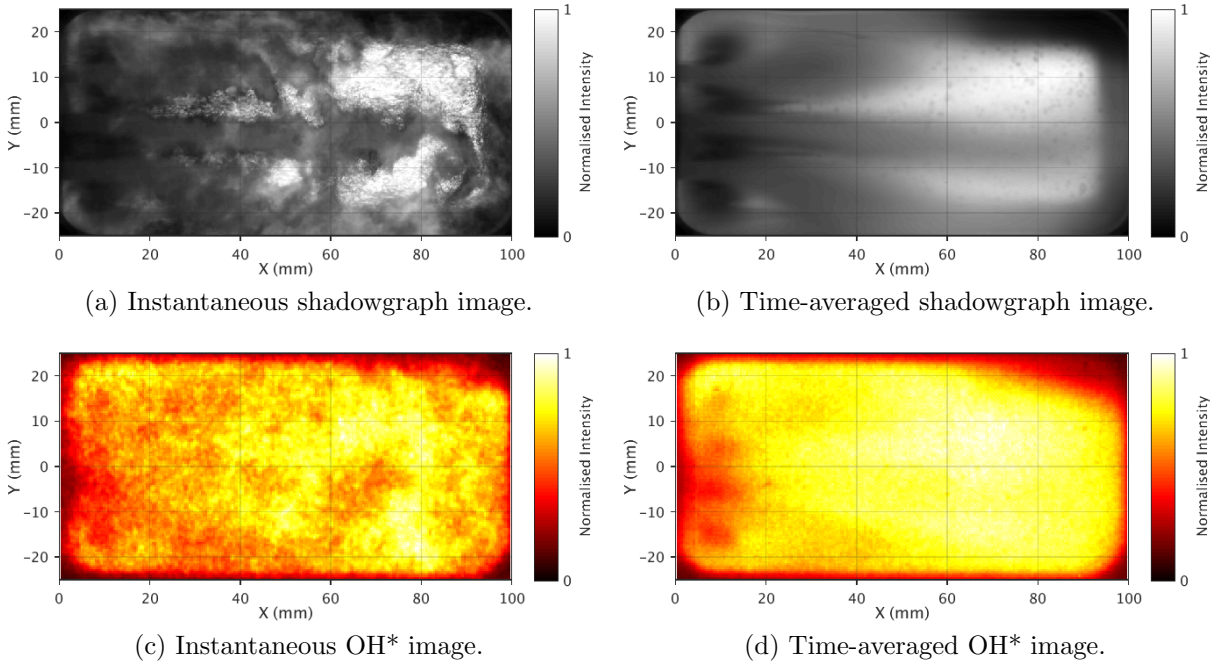

(a) Instantaneous shadowgraph image.

(b) Time-averaged shadowgraph image.

(c) Instantaneous OH* image.

(d) Time-averaged OH* image.

Figure 5.1.2: Samples of instantaneous and time-averaged optical images from Test A 1L-mode excitation [159].

OH* intensity distributions show that the flame fills the window region as for the unexcited case. In this set of OH* images the brightest part of the image occurs above and below the ends of the central injector oxygen stream.

Figure 5.1.3 shows the shadowgraph sample from Test C during 1L mode excitation. This test has an enhanced spatial resolution in order to resolve the shear layer of the central oxygen jet. There is some uncertainty in the exact dimensions of the image as there are no geometric features to identify its position or scale precisely. For this study these images have been scaled so that features in the image match the expected position and diameter of the LOx post and hydrogen annulus in the experiment. Fluctuations on the surface of the LOx jet are visible in the instantaneous image which are not present in the time-averaged image.

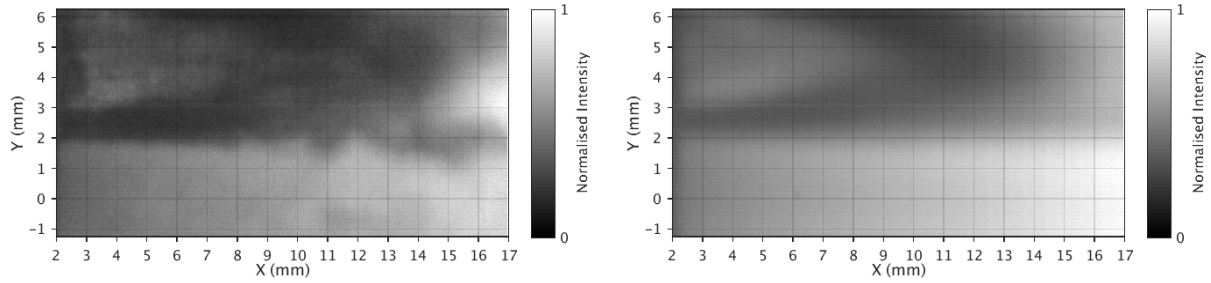

(a) Instantaneous shadowgraph image.

(b) Time-averaged shadowgraph image.

Figure 5.1.3: Samples of instantaneous and time-averaged optical images from Test C 1L-mode excitation [49].

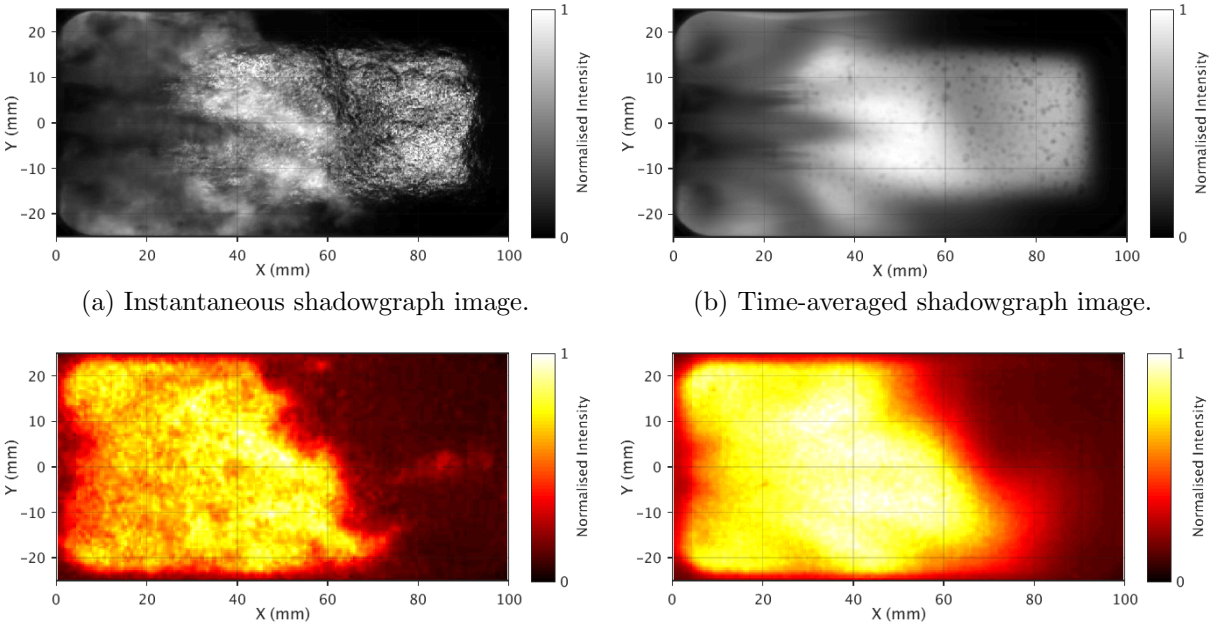

(a) Instantaneous shadowgraph image.

(b) Time-averaged shadowgraph image.

(c) Instantaneous OH* image.

(d) Time-averaged OH* image.

Figure 5.1.4: Instantaneous and time-averaged optical images used from Test A 1T-mode excitation [159].

5.1.2 1T Mode Optical Data

During 1T-mode excitation the acoustic velocity acts across the injection plane. The transverse acoustic velocity disturbs and displaces the dense liquid oxygen core and surrounding flame zone. The acoustic motion also increases mixing of the oxidiser and fuel streams and the flame is observed to retract towards the injection plane. Figure 5.1.4 shows simultaneously captured shadowgraph and OH images from Test A during 1T-mode excitation. The shadowgraph images show that the oxygen jets have retracted towards the injection plane with the central jet propagating less than 40 mm into the chamber. The OH* images show that the flame zone has retracted with the oxygen jets and the downstream region of the window has very low OH* intensity. Four bright lobes appear in the time-averaged OH* image above and below the ends of each of the oxygen jet positions. These bright regions are caused by the flame being transported by the acoustic velocity which has been thoroughly discussed by Hardi [49].

Figure 5.1.5 shows simultaneously recorded shadowgraph and OH* images recorded during Test B with excitation of the 1T mode. This data is from a period where the excitation frequency was below the 1T peak response frequency and had a lower acoustic amplitude than the Test A 1T sample. The flame has retracted towards the injection

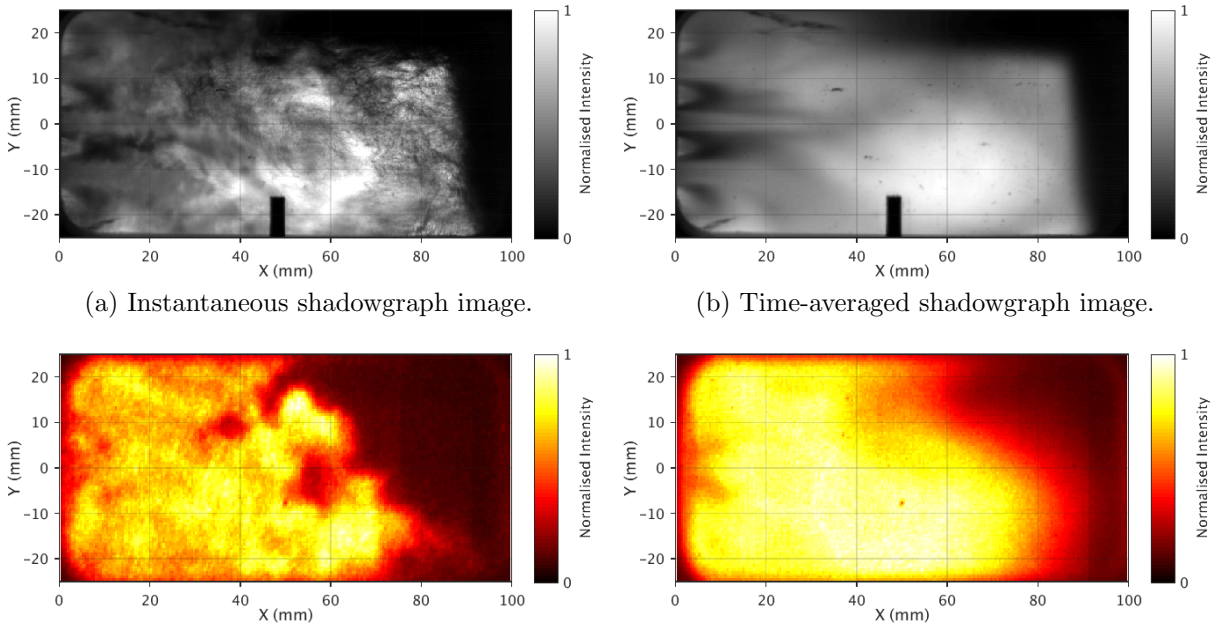

(a) Instantaneous shadowgraph image.

(b) Time-averaged shadowgraph image.

(c) Instantaneous OH* image.

(d) Time-averaged OH* image.

Figure 5.1.5: Samples of instantaneous and time-averaged optical images from Test B 1T-mode excitation [49].

plane, but not to the same degree as the Test A 1T sample shown in Figure 5.1.4. The flames resulting from seperate injection elements can be distinguished in the instantaneous OH* image, yet the flame appears as a single uniform distribution in the time-averaged image. The OH* images show that the region at the end of the window has a very low OH* intensity.

5.2 DMD analysis

The experimental optical data shows a variety of unsteady turbulent motion. To provide a better comparison with numerical results the optical data is processed to extract the mean response of the flame to the imposed acoustic disturbance. Dynamic Mode Decomposition (DMD) is described by Schmid et al.[130] and is useful for identifying and sorting coherent fluctuations of data at different frequencies. DMD is often applied to study periodically fluctuating phenomena and has been previously used in combustion instability research in order to detect coherent fluctuations of flame visualisation data [47, 48, 55, 162].

5.2.1 DMD method

Schmid [130] and Huang et al. [58] describe the DMD method. DMD is one specific application of matrix decompositional methods which are generally applied to a data matrix D consisting of n columns of spatial data points with m rows of temporal data collected from each spatial location with a time step of $\triangle t$. The matrix D is decomposed into

$$D = ABC \tag{5.1}$$

where $A \in \mathbb{C}^{n \times m}$, $B \in \mathbb{C}^{m \times m}$ is a diagonal matrix, and $C \in \mathbb{C}^{m \times m}$. Schmidt [131] explains that the diagonal matrix B serves to separate the spatial and temporal structures allowing coherent motion to be isolated. The spatial information is contained in the m columns of A while the temporal information is contained within the corresponding m rows of C.

An additional constraint is needed to make the decomposition unique. If the matrix A is constrained so that the m columns are orthonormal, that is, the spatial structures are orthogonal and normalised, then the decomposition becomes equivalent to the single value decomposition of the matrix and is known as proper orthogonal decomposition (POD). The constraint that the spatial modes are orthogonal in general means that the temporal modes may contain a number of different frequencies. POD is therefore useful for identifying dominant coherent spatial structures but is not useful for studying the response to specific frequencies or for identifying weaker motion that is coherent.

DMD isolates the coherent motion at individual frequencies by imposing the constraint that the time signal contained in each row of the temporal matrix C consists of a fluctuation at a single complex frequency. Using complex notation, each row of C should contain snapshots of a complex function $z_i = e^{j\omega_i \triangle t}$ with $j = \sqrt{-1}$.

$$C = \begin{bmatrix} 1 & z_1(\triangle t) & z_1(2\triangle t) & ... & z_1(m\triangle t) \\ 1 & z_2(\triangle t) & z_2(2\triangle t) & ... & z_2(m\triangle t) \\ \vdots & \vdots & \vdots & \ddots & \vdots \\ 1 & z_m(\triangle t) & z_m(2\triangle t) & ... & z_m(m\triangle t) \end{bmatrix} \tag{5.2}$$

Due to the formulation $z_i = e^{j\omega_i \triangle t}$, C can be rewritten as

$$C = \begin{bmatrix} 1 & z_1 & z_1^2 & ... & z_1^m \\ 1 & z_2 & z_2^2 & ... & z_2^m \\ \vdots & \vdots & \vdots & \ddots & \vdots \\ 1 & z_m & z_m^2 & ... & z_m^m \end{bmatrix}. \tag{5.3}$$

C is now in a form known as a Vandermode matrix. Vandermode matrices can be diagonalized via:

$$CKC^{-1} = \wedge. \tag{5.4}$$

Where $\wedge$ is a diagonal matrix and K is a companion matrix of the form:

$$K = \begin{bmatrix} 0 & & & a_1 \\ 1 & \ddots & & a_2 \\ & \ddots & 0 & \vdots \\ & & 1 & a_m \end{bmatrix}. \tag{5.5}$$

Substituting B for $\wedge$ and equation 5.4 into equation 5.1 produces:

$$\begin{aligned} D &= ABC \\ &= A(CKC^{-1})C \\ &= ACK \\ &= D'K \end{aligned} \tag{5.6}$$

where D' is the combination of the unknown matrices A and C. From knowledge of the companion matrix K it can be seen that columns 2:m of D' are the columns 1:m-1 of D. It can also be shown that the unknowns $a_1 : a_m$ represent a linear combination of the m columns of D' to produce the original data matrix D. The values of $a_1 : a_m$ are unknown and must be found so that the matrix K can be used to calculate the decompositional matrices A, B, and C.

Schmid [131] presents an algorithm for solving this DMD problem using the single value decomposition. V_1^m is used to denote a data matrix containing v_i evenly spaced temporal snapshots. An unknown matrix P is introduced which propagates any snapshot v_i by one time step $\triangle t$.

$$Pv_i = v_{i+1} \tag{5.7}$$

Over an entire sequence V_1^m:

$$\begin{aligned} PV_1^m &= P\left[v_1, v_2, \ldots, v_m\right] \\ &= \left[Pv_1, Pv_2, \ldots, Pv_m\right] \\ &= \left[v_2, v_{3,} \ldots, v_{m+1}\right] \\ &= V_2^{m+1} \end{aligned} \tag{5.8}$$

V_2^{m+1} is analogous to D and V_1^m is analagous to D' in equation 5.6. So that:

$$PV_1^m = V_2^{m+1} \approx V_1^m K, \tag{5.9}$$

or

$$PV_1^m \approx V_1^m K. \tag{5.10}$$

The single value decomposition of $V_1^m = U\Sigma V^H$ is used to transform the data snapshots into an orthogonal basis U, which is equivalent to propagating the snapshot sequence V_1^m onto its POD-modes (U). The unknown propagation matrix P is propagated onto the POD basis to form $U^H PU$ where the superscript H denotes the complex conjugate transpose.

Pre-multiplying equation 5.10 by U^H produces:

$$\begin{aligned} U^H PV_1^m &\approx U^H V_2^{m+1} \\ U^H PUU^H V_1^m &\approx U^H V_2^{m+1} \\ U^H PU\Sigma V^H &\approx U^H V_2^{m+1} \\ U^H PU &\approx U^H V_2^{m+1} V\Sigma^{-1} \\ S &\approx U^H V_2^{m+1} V\Sigma^{-1} \end{aligned} \tag{5.11}$$

The $m \times m$ matrix S introduced in the last step replaces the companion matrix K, and the eigenvalues and eigenvectors of S characterize the dynamics of the propogation matrix P. The eigenvalues λ_i of S are the values z_i of the Vandermode matrix and can be used to compute the temporal matrix C in equation 5.3. The complex valued angular frequency of each temporal mode, ω_i can be extracted from the eigenvalues via:

$$\omega_i = \frac{log(\lambda_i)}{\triangle t}. \tag{5.12}$$

The physical frequency of each temporal mode can then be computed.

$$f_i = \frac{|(\omega_i)_I|}{2\pi} \tag{5.13}$$

Two modes exist at each physical frequency corresponding to conjugate values of ω_i. The temporal component of each mode traverses the unit circle in C in opposite directions such that the complex part of each mode is cancelled by its conjugate.

The spatial matrix A is the projection of the eigenvectors X of S onto the spatial POD matrix U.

$$A = UX \tag{5.14}$$

Finally the diagonal matrix B can be determined.

$$B^{-1} = CV\Sigma^{-1}X \tag{5.15}$$

As A and C are unitary matrices the diagonal entries of the matrix B define the magnitude of each mode where a higher magnitude indicates greater coherence. For

simplicity, in the following work the matrix A will be denoted as the spatial matrix Φ containing the spatial modes ϕ_i. The remainder of the decomposed matrix D will be denoted the temporal mode Ψ which contains temporal modes ψ_i for each spatial mode ϕ_i.

$$\Psi = BC \tag{5.16}$$

Note that the temporal modes t_i contain both the magnitude and temporal information for the DMD mode i. Furthermore, as the temporal information of each mode corresponds to the rows of the matrix C in 5.3, each may be expressed as:

$$\psi_i(t) = B(i,i)e^{j\omega_i t}. \tag{5.17}$$

To analyse optical data from the BKH experiments, the data is first sorted into snapshots by rearranging $m+1$ frames of optical data with $X \times Y$ pixels into a matrix $D(n \times m+1)$ with $n = X \times Y$ spatial points for $m+1$ temporal snapshots. Due to the assumption that each DMD mode is a harmonic fluctuation at a particular frequency, first the mean image $\bar{I}$ of the optical data sample is subtracted from each frame so that changes in intensity will be observed as harmonic fluctuations about a zero value.

The previously described algorithm is then applied to decompose the data matrix D into spatial, Φ, and temporal, Ψ , matrices. Afterwards the spatial matrix Φ is reshaped so that each column corresponds to a $X \times Y$ image representing the spatial distribution of the mode ϕ_i. ϕ_i is complex and describes the amplitude and relative phase of each pixel in the image being modulated by the complex temporal mode t_i. This means that the phase of the spatial mode is consistent between each of the points in the same spatial mode, but the phase of different DMD spatial modes at different frequencies is arbitrary unless the phase has been normalised to a common reference phase using the corresponding temporal mode of each spatial mode. The phase of the results presented in this section have been normalised against the phase of the PCCDYN2 sensor signal. The phase of modes at overtones of the excitation frequency have been reduced to a -90∘:+90∘ interval as the fluctuations occur twice per acoustic cycle. The relative phase of the DMD modes and the local acoustic disturbance is discussed as part of the flame response analysis in Section 5.3.

The original optical data image I at time t can be reconstructed by multiplying all spatial DMD modes ϕ_i with the corresponding temporal DMD modes t_i at time t and addition of the mean image.

$$I(t) = \bar{I} + \sum_{i=1}^{m} \phi_i t_i(t) \tag{5.18}$$

The primary interest of the current study is to isolate the response of the flame at specific frequencies of interest. As the temporal component of each DMD mode is monofrequent, the response at specific frequencies can be identified by selectively studying the DMD modes corresponding to the acoustic excitation frequency and its overtones. It is also possible to isolate motion at the frequencies of interest by reconstructing images using only the desired DMD modes. DMD analysis of the BKH optical datasets listed in Table 5.1 are presented in the following sections.

5.2.2 DMD Results

The DMD of the optical data samples described in Section 5.1 was computed using a matlab routine. The DMD modes were sorted by the frequency of the mode and prescribed a mode number. The DMD modes of interest were identified by comparing the magnitude

of the DMD modes with one another. As expected the modes with the highest magnitudes, indicating the strongest coherence, corresponded to the frequency of acoustic excitation and its overtones. Figure 5.2.1 shows example DMD mode magnitudes versus frequency plots resulting from the DMD calculation of the Test B 1T-mode shadowgraph and OH* image samples.

The shadowgraph sample DMD mode magnitude spectrum shown in Figure 5.2.1a exhibits clear peaks at the excitation frequency and its overtone. The OH* sample result shown in Figure 5.2.1b has peaks at the same frequencies and additional large peaks at various frequencies. The additional peaks have been identified as artefacts resulting from poor internal synchronization between the built-in image intensifier and the photodetector chip in the high-speed camera. The fluctuations caused by these artefacts are not of interest to the current work, and the optical data samples presented in this thesis were extracted from periods when the excitation frequency did not match any of the identified camera artefact frequencies to ensure minimal interference.

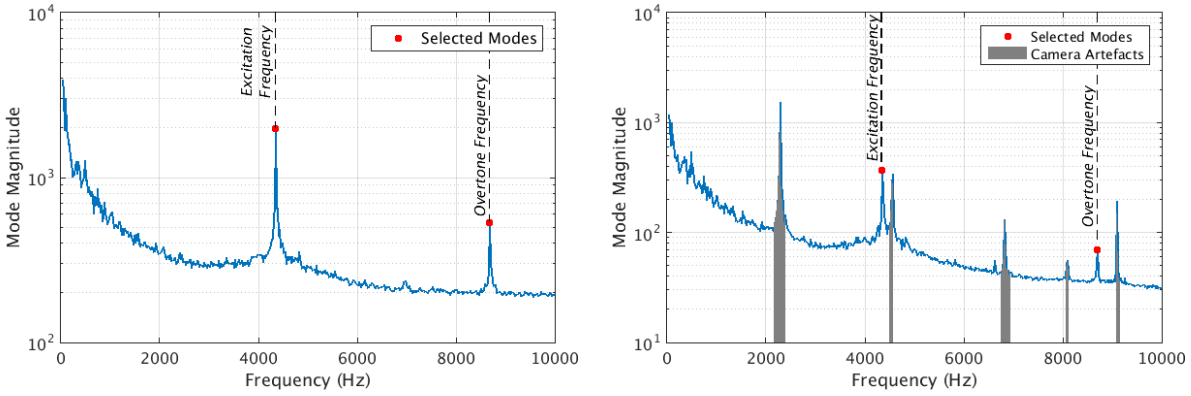

(a) Shadowgraph (b) OH*

Figure 5.2.1: Mode magnitude versus frequency plots from DMD calculations of Test B optical data samples.

The DMD mode pairs corresponding to the peak mode magnitudes at the excitation frequency and its overtone are identified and selected for further analysis. The DMD modes at the excitation frequency isolate the response at the same frequency as the acoustic pressure fluctuations. While the acoustic velocity fluctuates at the same frequency as the acoustic pressure disturbance, the modulus of the acoustic velocity fluctuates twice per acoustic cycle. The DMD modes at the overtone frequency therefore isolate the response at double the excitation frequency which are related to acoustic velocity fluctuations. The following sections describe and interpret the DMD results during BKH 1L- and 1T-mode excitation.

1L-Mode Excitation

The samples of BKH optical data recorded during 1L-mode excitation listed in Table 5.1 were processed using the DMD method described in the previous section. The DMD mode magnitude spectrum of the Test A shadowgraph and OH* 1L samples are shown in Figure 5.2.2. The DMD modes at the excitation frequency and the first overtone of the excitation frequency were identified. The DMD modes at the excitation frequency had high magnitudes indicating large coherent motion. The DMD modes at the overtone of the excitation frequency had low magnitudes and showed no significant structures or motion. This is expected, as the flame zone is located in a pressure anti-node and velocity node of the 1L-mode acoustic distribution. Therefore no significant fluctuations are observed at the overtone of the excitation frequency.

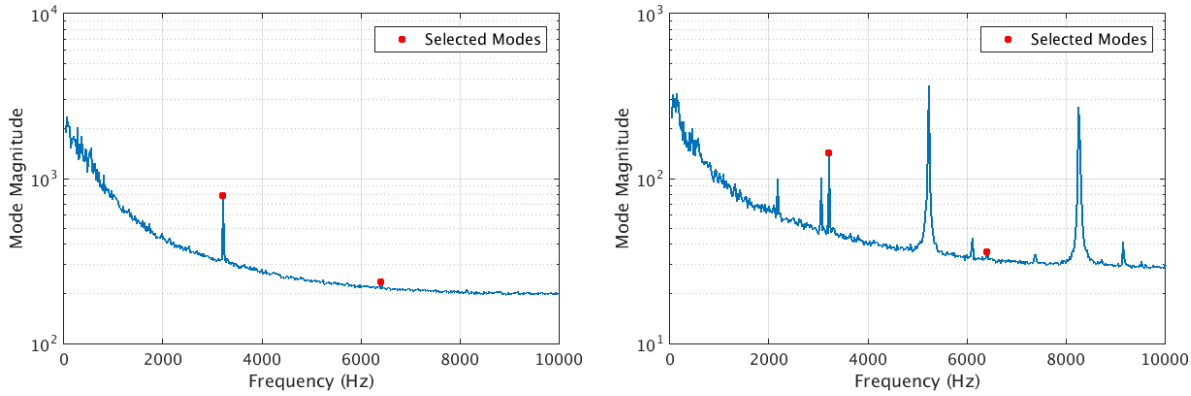

(a) Shadowgraph (b) OH*

Figure 5.2.2: Mode magnitudes versus frequency plots from DMD calculations of Test A 1L-mode optical data samples.

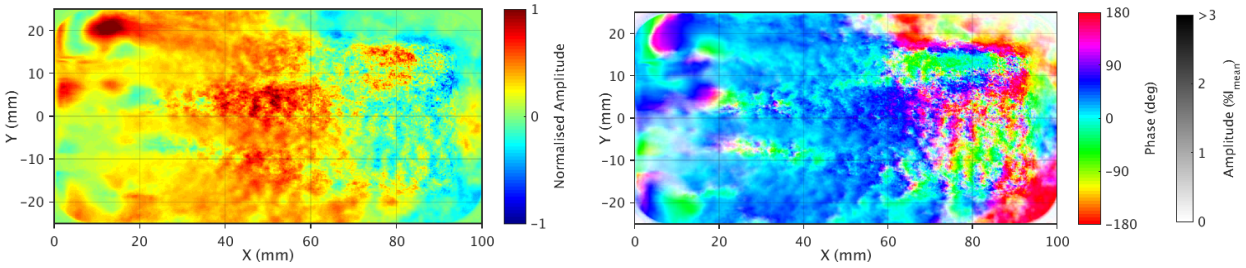

(a) Real part of spatial mode (b) Phase of spatial mode relative to PCCDYN2

Figure 5.2.3: Spatial DMD mode of Test A 1L-mode shadowgraph sample at the excitation frequency.

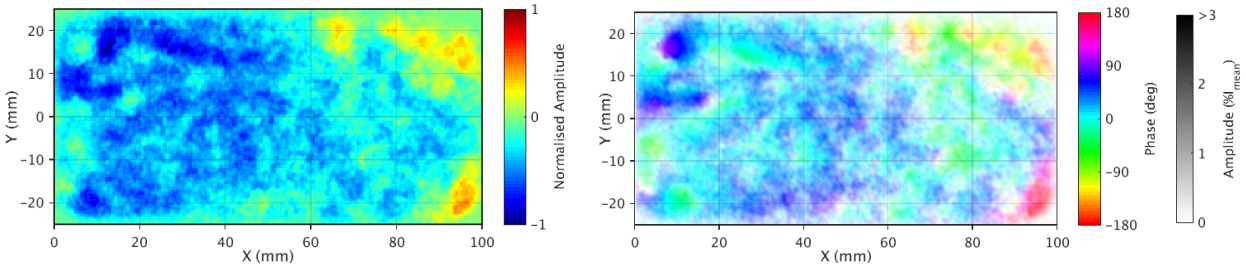

(a) Real part of spatial mode (b) Phase of spatial mode relative to PCCDYN2

Figure 5.2.4: Spatial DMD mode of Test A 1L-mode OH* sample at the excitation frequency.

Figures 5.2.3 and 5.2.4 show the spatial mode distributions of the DMD modes at the 1L excitation frequency from the Test A shadowgraph and OH* 1L samples. The spatial modes are complex and must be modulated by the complex temporal modes to reconstruct the original image data. The real part of the spatial modes indicate the distribution and relative intensity of the fluctuations at the mode frequency. The phase is computed as the phase angle of the complex spatial mode and has been normalised to the phase of the PCCDYN2 sensor signal. The colour of the phase distributions have been scaled so that regions of low amplitudes appear transparent (white) in order to highlight the regions of high amplitude fluctuations corresponding to significant disturbances.

The real part of the DMD modes shown in Figures 5.2.3 and 5.2.4 show a bulk fluctuation across the window region. The phase distributions also show that the fluctuations throughout the window region are in phase with the PCCDYN2 dynamic pressure sensor signal. The spatial DMD mode of the OH* sample indicates a uniform intensity fluctuation

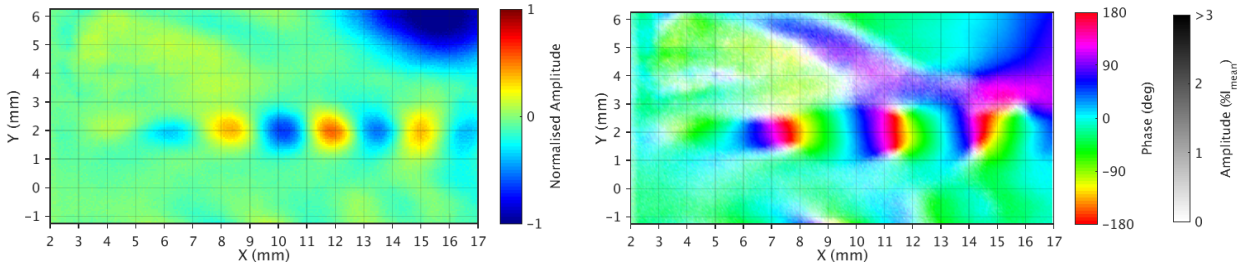

(a) Real part of spatial mode (b) Phase of spatial mode relative to PCCDYN2

Figure 5.2.5: Spatial DMD mode of Test C 1L-mode shadowgraph sample at the excitation frequency.

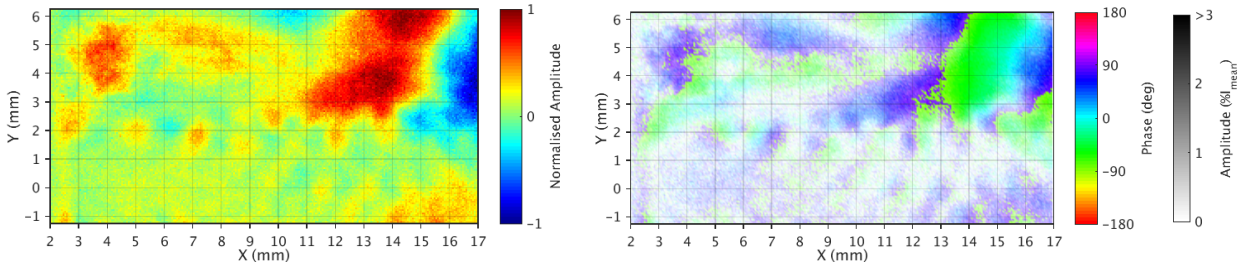

(a) Real part of spatial mode (b) Phase of spatial mode relative to PCCDYN2

Figure 5.2.6: Spatial DMD mode of Test C 1L-mode shadowgraph sample at the first overtone of the excitation frequency.

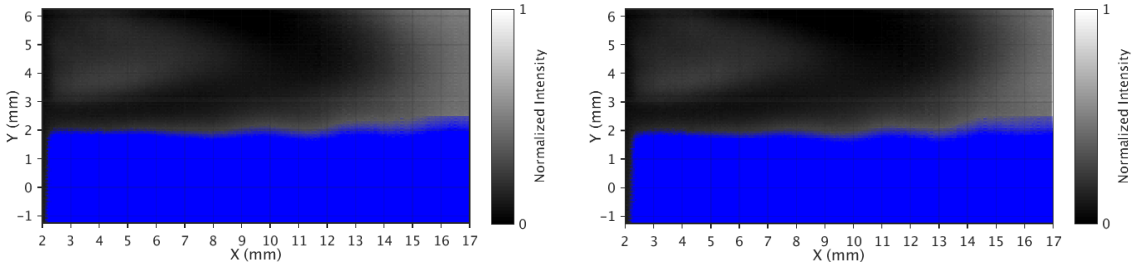

(a) PCCDYN2 phase=0 (b) PCCDYN2 phase=π

Figure 5.2.7: Instantaneous reconstructions of Test C 1L-mode shadowgraph sample using selected DMD modes at excitation and overtone frequencies. Results shown at different phase angles of the acoustic cycle determined by the phase of the PCCDYN2 sensor. Blue highlighting shows the position of the LOx core.

to acoustic pressure which has previously been reported by Hardi [49]. A similar bulk fluctuation in intensity is observed in the shadowgraph DMD mode at the excitation frequency. Instantaneous images show that the LOx jet is not significantly deformed during 1L mode excitation and the observed fluctuations in the DMD modes are attributed to increased combustion light being emitted during acoustic pressure fluctuations rather than motion of the oxygen jets.

The 1L shadowgraph DMD spatial mode distributions shown in Figure 5.2.3 exhibit regularly spaced fine vertical structures. These structures are spaced approximately 4.2 mm apart and the mean excitation of the sample is approximately 3350 Hz. The vertical structures therefore correspond to motion travelling at 14.5 m/s from left to right in the image, which closely matches the oxygen injection velocity. These structures suggest that the breakup of the LOx core is affected by the acoustic pressure and the resulting disturbance propagates downstream.

The breakup of the LOx core is studied in more detail by analysing the sample of shadowgraph data during 1L mode excitation from Test C which resolved the shear layer

of the central oxygen injector. The DMD of the sample was computed and the spatial modes at the excitation frequency and its overtone were identified. The distributions of the spatial modes at the excitation frequency and its overtone are shown in Figures 5.2.5 and 5.2.6, respectively. The phase of the DMD mode at the overtone frequency has been reduced to a -90° $\sim$ +90° interval as the fluctuations occur twice per acoustic cycle. A clear alternating pattern is observed in the spatial distribution of the DMD mode at the excitation frequency in the shear layer between the oxygen and hydrogen streams. This alternating pattern indicates deformation of the LOx jet surface at the excitation frequency. A similar pattern is shown at the overtone frequency, indicating that these fluctuations relate to the propagation of structures on the surface of the LOx jet.

Figure 5.2.7 shows reconstructed images using the selected DMD modes at the excitation frequency and its overtone at different phase angles of the acoustic cycle. The LOx core was identified in each image by adjusting the contrast of the image to isolate its features. The isolated image was then used as a mask to highlight the core, which is shown in blue. The reconstructed images show wave-like structures on the surface of the oxygen jet which propagate downstream. The spacing of the neighbouring waves matches the excitation frequency indicating that these structures are formed by the acoustic pressure fluctuations at the injection plane.

The 2D line-of-sight data does not allow 2- and 3-dimensional structures to be distinguished. Therefore the experimentally observed structures may be the result of a helical disturbance. However, these structures are reproduced numerically in Chapter 6 of this thesis using an axisymmetric model. The model results indicate that these structures are axisymmetric and related to the first longitudinal mode frequency of the LOx post. These fluctuations in the post produce wave-like deformations on the surface of the LOx core which continue propagating downstream. This result is useful for numerical validation. The propogation of these structures may also be responsible for the fine vertical structures identified in Figure 5.2.3.

The flame response analysis of 1L-mode optical data samples has identified a number of interesting phenomena. The approximately 45° phase lag between the peak pressure disturbance and the peak optical intensity emission is of primary interest. This phase lag was observed consistently between OH* and shadowgraph imaging results from multiple BKH experiments. The phase lag may be the result of a number of factors, with thermal excitation producing additional emission after the peak combustion response being a likely candidate. Better fundamental understanding of the emmission of flames at high pressure is needed to assist interpretation of the results.

1T Mode Excitation

The DMD modes of the Test A and 2 1T-mode Shadowgraph and OH* samples listed in Table 5.1 were computed. The modes of interest at the excitation frequency and its first overtone were identified by comparing the magnitude of each of the DMD modes. Figure 5.2.8 shows the mode magnitude versus frequency for the Test A shadow graph and OH* samples. The mode magnitude versus frequency plots of the Test B samples have been shown previously in Figure 5.2.1.

The shadowgraph mode magnitude plot shows distinct peaks at the excitation frequency and its overtone. The overtone frequency stands out clearly from the other modes as the velocity disturbance from transverse excitation acts across the flame zone twice per acoustic cycle. The OH* mode magnitude plot shows a number of camera artefacts. These artefacts occur at the same frequencies as those from the 1L-mode OH* sample from the same test. As no artefacts occur at the excitation frequency and its overtones they do not interfere with the DMD modes of interest and can be safely ignored.

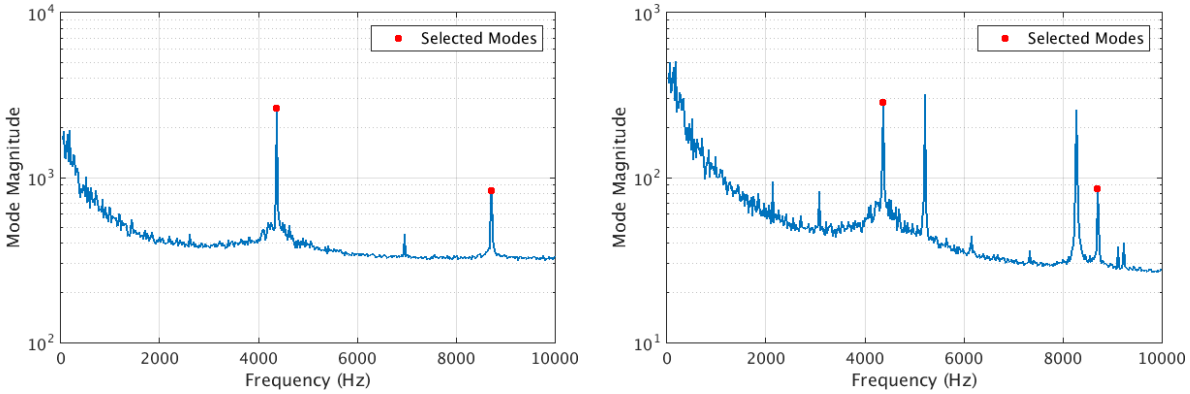

(a) Shadowgraph (b) OH*

Figure 5.2.8: Mode magnitudes versus frequency plots from DMD calculations of Test A 1T mode optical data samples.

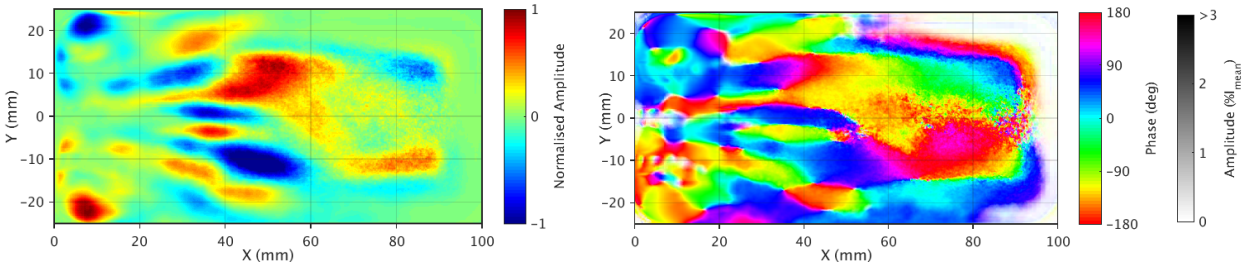

(a) Real part of spatial mode (b) Phase of spatial mode relative to PCCDYN2

Figure 5.2.9: Spatial DMD mode of Test A 1T-mode shadowgraph sample at the excitation frequency.

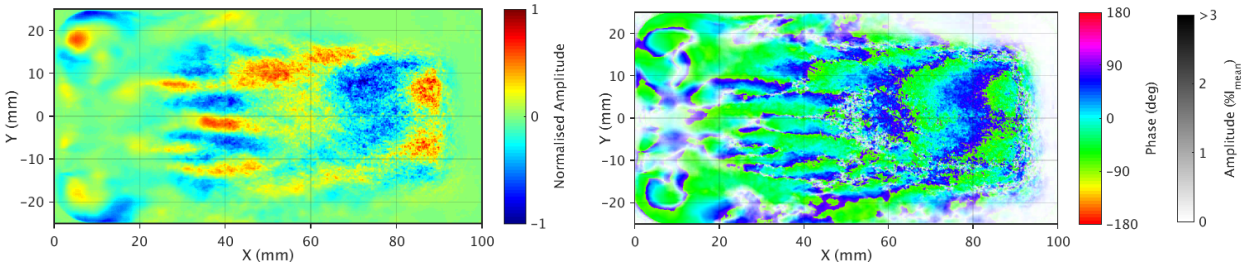

(a) Real part of spatial mode (b) Phase of spatial mode relative to PCCDYN2

Figure 5.2.10: Spatial DMD mode of Test A 1T-mode shadowgraph sample at the first overtone of the excitation frequency.

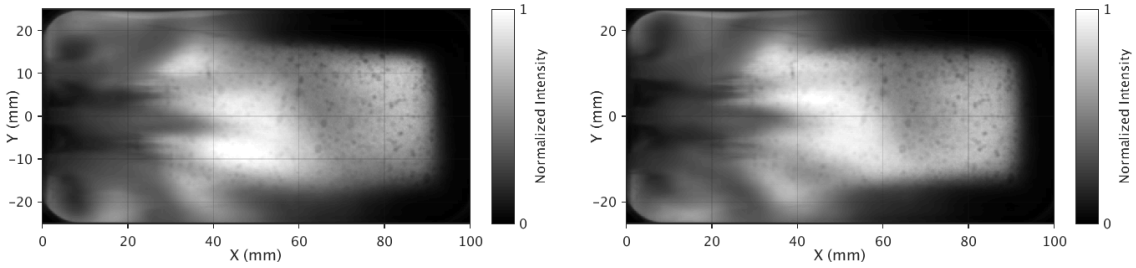

(a) PCCDYN2 phase=0 (b) PCCDYN2 phase=π

Figure 5.2.11: Instantaneous reconstructions of Test A 1T-mode shadowgraph sample using selected DMD modes at excitation and overtone frequencies. Results shown at different phase angles of the acoustic cycle determined by the phase of the PCCDYN2 sensor.

The spatial modes of the Test A shadowgraph 1T-mode sample at the excitation and overtone frequencies are shown in Figures 5.2.9 and 5.2.10, respectively. The spatial modes show horizontal structures repeating across the height of the window between 30 and 60 mm from the injection plane. As similar structures exist in the spatial mode at the overtone of the excitation frequency it is clear that these structures are a result of the transverse motion of the flame due to the acoustic velocity fluctuations. Focusing on the central injector, two small structures occur at 35 mm from the injection plane above and below the line in the center of the window (Y=0 mm). This is the region around the end of the oxygen core in the mean image (Figure 5.1.4b). These small structures are a result of the motion of the dark oxygen core and indicate the extent of the deflection of the core by the acoustic velocity.

The larger lobes above and below the central core correspond to the lighter part of the image around the oxygen core which also follows the acoustic velocity. This is more readily observed by studying the reconstructed images using the selected DMD modes at different phase angles of the acoustic cycle as shown in Figure 5.2.11. These larger downstream structures correspond to a larger gaseous structure enveloping the oxygen core and appearing as a lighter region in the reconstructed images. This gaseous structure is also being transported by the acoustic velocity. As it is lighter than the surrounding regions of the shadowgraph image it may either be less dense, or additional combustion light may be emitted in this region. Because this region is seen to obscure the shadow of the window in the background, the latter is deemed most likely.

The relative phase of the structures in the spatial modes of the Test A 1T-mode shadowgraph samples show a similar layered structure. The structures corresponding to the fluctuation of the dark oxygen core tip and lighter surrounding gases are almost 180 degrees out of phase. This phase shift is due to the convention that dark values correspond to a negative fluctuation in the DMD modes. Therefore, the dense jet and surrounding gaseous medium are moving together. A horizontally repeating pattern is visible in the near injector shear layer regions in the phase plots. These fluctuations have a very low intensity in this shadowgraph sample and are later investigated using the 1T-mode shadowgraph sample from Test B.

Figures 5.2.12 and 5.2.13 show the spatial modes at the excitation and overtone frequencies of the Test A 1T-mode OH* sample. Horizontal structures are visible at both frequencies corresponding to the motion of the flame by the transverse acoustic velocity. Comparing with the shadowgraph images, the structures in the spatial modes of the OH* sample are located above and below the surface of each of the oxygen streams. These regions appear in the spatial modes as 4 maximum and minimum structures alternating across the height of the image. The four structures are more readily observed in the reconstructed images shown in Figure 5.2.14. These regions follow the dense oxygen jet and match the lighter surrounding gaseous structures identified in the Test A 1T shadowgraph sample.

The Test B 1T-mode samples are recorded with different camera settings that better resolve the LOx jet and near injector region. Figures 5.2.15 and 5.2.16 show the spatial DMD modes at the excitation and overtone frequencies of the Test B 1T shadowgraph sample. Similar horizontal structures are observed as for the Test A shadowgraph sample. The high pass optical filter employed for shadowgraph imaging in Test B permitted more combustion light to reach the camera which resolved the oxygen core in greater detail.

Figure 5.2.17 shows a zoomed-in view of the spatial mode at the excitation frequency around the central injector. The phase plot in Figure 5.2.17b shows a repeating pattern in the shear layer region about the central and lower injectors. The shear layer fluctuations have a low normalised amplitude in the spatial mode as other larger motions such as transport of combustion products from one region to another dominate the distribution.

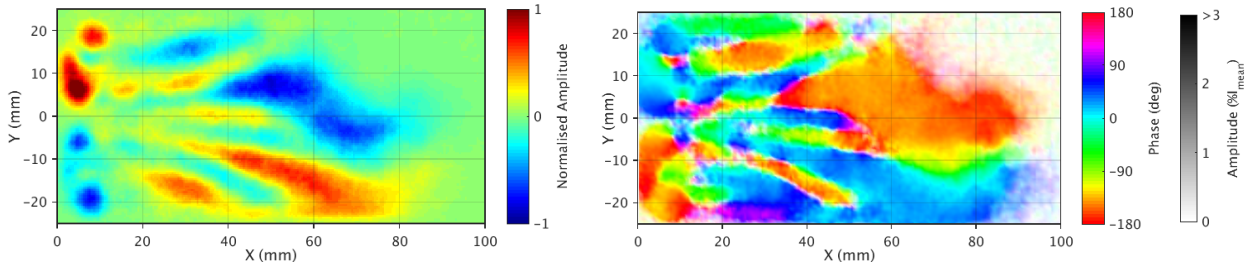

(a) Real part of spatial mode (b) Phase of spatial mode relative to PCCDYN2

Figure 5.2.12: Spatial DMD mode of Test A 1T-mode OH* sample at the excitation frequency.

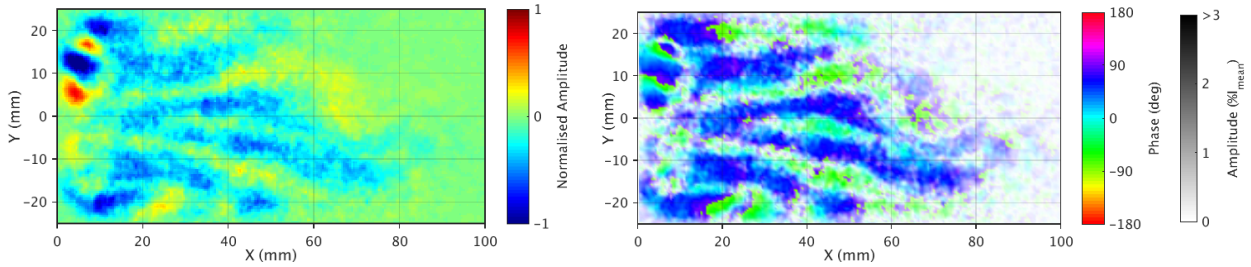

(a) Real part of spatial mode (b) Phase of spatial mode relative to PCCDYN2

Figure 5.2.13: Spatial DMD mode of Test A 1T-mode OH* sample at the first overtone of the excitation frequency.

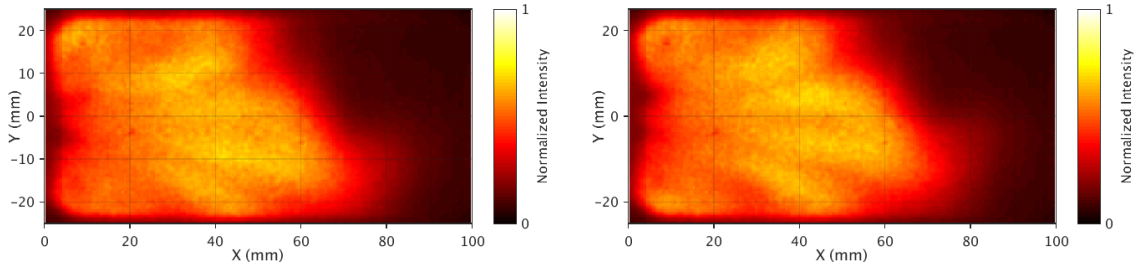

(a) PCCDYN2 phase=0 (b) PCCDYN2 phase=π

Figure 5.2.14: Instantaneous reconstructions of Test A 1T-mode OH* sample using selected DMD modes at excitation and overtone frequencies. Results shown at different phase angles of the acoustic cycle determined by the phase of the PCCDYN2 sensor.

Figure 5.2.18 shows the same region in the reconstructed images. Using the same method as for Figure 5.2.7, the LOx core has been highlighted by creating a mask from a high contrast image of the images. Figure 5.2.18 shows that the pattern identified in the spatial mode results from alternating fluctuations on the top and bottom surfaces of the oxygen core that propagate downstream. The spacing of the waves corresponds to the oxygen injection velocity and excitation frequency. The wave-like structures are clearly visible up to 15 mm from the injection plane. After 15 mm from the injection plane the surface of the oxygen core becomes less distinct and the surface structures are no longer clearly visible. The motion of the flame about the central oxygen core can also be seen as the light structure moving from below to above the central oxygen stream in the reconstructed images.

The spatial DMD mode of the Test B 1T OH* sample at the excitation and overtone frequencies are shown in Figures 5.2.19 and 5.2.20, respectively. In this sample a large recirculation region downstream is the most recognizable feature in the spatial mode at the excitation frequency. The recirculation regions near the injection plane are also clearly visible in the spatial mode distribution. Similar horizontal structures are visible

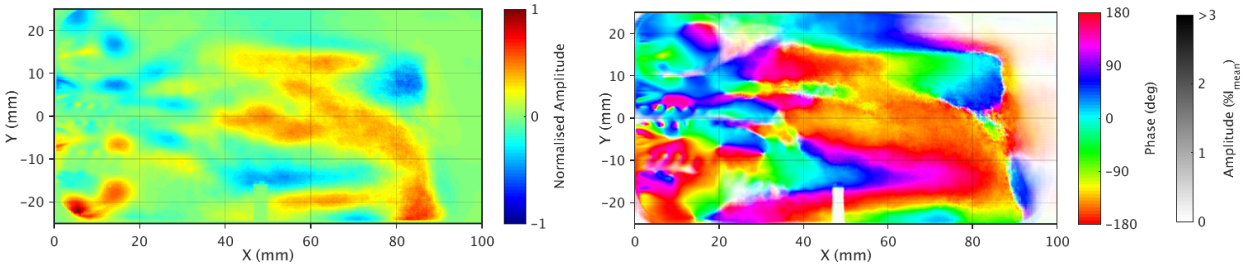

(a) Real part of spatial mode (b) Phase of spatial mode relative to PCCDYN2

Figure 5.2.15: Spatial DMD mode of Test B 1T-mode shadowgraph sample at the excitation frequency.

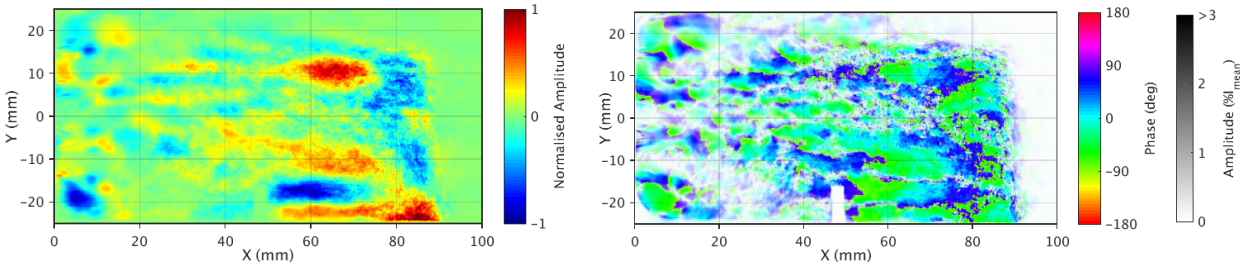

(a) Real part of spatial mode (b) Phase of spatial mode relative to PCCDYN2

Figure 5.2.16: Spatial DMD mode of Test B 1T-mode shadowgraph sample at the first overtone of the excitation frequency.

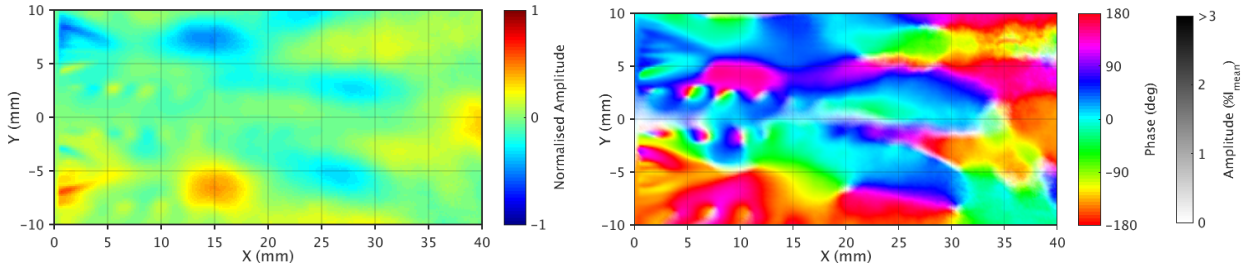

(a) Real part of spatial mode (b) Phase of spatial mode relative to PCCDYN2

Figure 5.2.17: Near injector region of spatial DMD mode of Test B 1T-mode shadowgraph sample at the excitation frequency.

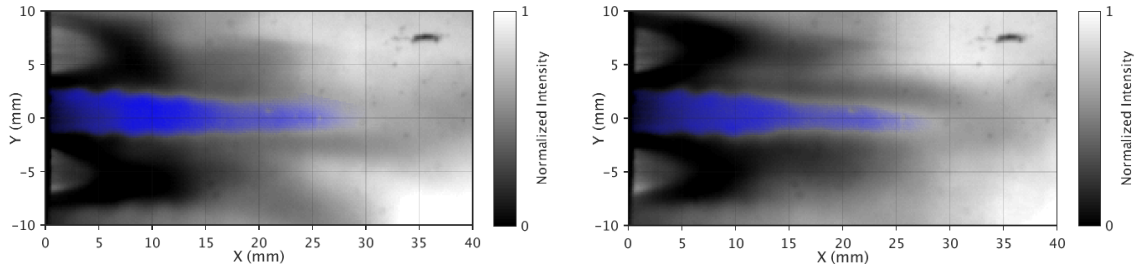

(a) PCCDYN2 phase=0 (b) PCCDYN2 phase=π

Figure 5.2.18: Instantaneous reconstructions of Test B 1T-mode shadowgraph sample near injector region using selected DMD modes at excitation and overtone frequencies. Results shown at different phase angles of the acoustic cycle determined by the phase of the PCCDYN2 sensor.

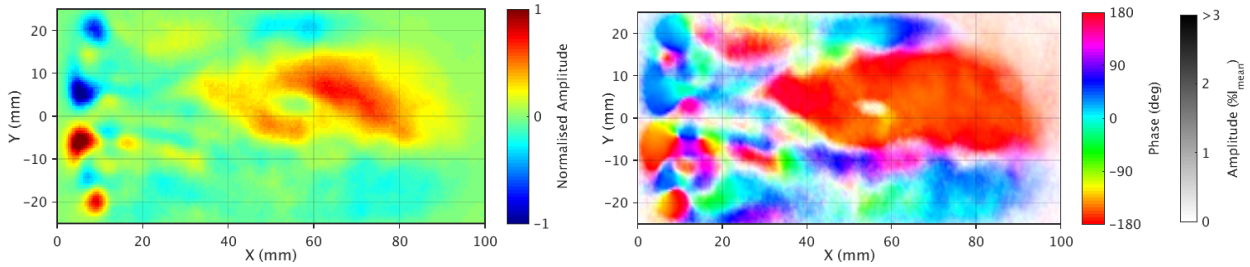

(a) Real part of spatial mode (b) Phase of spatial mode relative to PCCDYN2

Figure 5.2.19: Spatial DMD mode of Test B 1T-mode OH* sample at the excitation frequency.

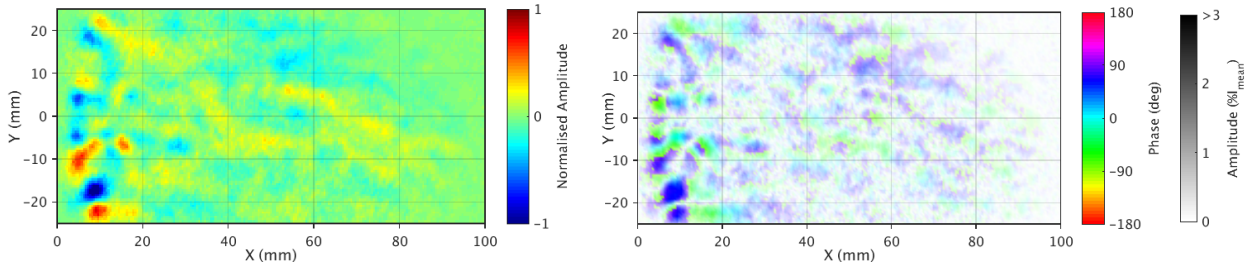

(a) Real part of spatial mode (b) Phase of spatial mode relative to PCCDYN2

Figure 5.2.20: Spatial DMD mode of Test B 1T-mode OH* sample at the first overtone of the excitation frequency.

as those observed in the Test A 1T-mode OH* sample between 15 mm and 35 mm from the injection plane. The horizontal structures are also visible in the spatial mode at the overtone frequency and indicate the transverse displacement of the flame by the acoustic velocity.

5.3 Flame Response Analyses

To analyse the response of the flame to the acoustic disturbance the amplitude and phase of the fluctuations in the optical data previously identified by the DMD analysis are compared against the local acoustic disturbance. To determine the local acoustic disturbance in the window region corresponding to the DMD results a new approach using a multi-variable DMD method is employed.

This approach incorporates the dynamic pressure sensor signals from the BKH experiments into the DMD analysis of the optical data samples. The spatial points of the resulting DMD modes that represent dynamic pressure fluctuations are isolated and used to reconstruct the acoustic disturbances corresponding to the identified DMD fluctuations discussed in the previous section. The reconstructed acoustic disturbances are converted to a complex amplitude formulation and used to reconstruct the acoustic field using the same method described in Section 4.1.3. The local acoustic disturbance in the window region is extracted from the reconstruction and compared with the identified optical intensity fluctuations at the same frequency. The response of the flame is studied using the properties of the DMD results to compare the amplitudes and relative phase of the acoustic and optical intensity fluctuations.

This method isolates and compares the acoustic and optical disturbances at the particular frequencies of interest. The results are representative of the mean response over the sample duration and can be used to validate the mean response of numerical models instead of comparing on a frame-by-frame basis. Similarly, the computed Rayleigh index

and phase distributions are representative of the mean response and are less susceptible to experimental noise.

5.3.1 Multi-variable DMD method

The multi-variable DMD method incorporates different diagnostics and measurements to construct the data matrix D of the DMD calculation. Simultaneously recorded data are ordered into a single spatial snapshot (column) of the DMD data matrix D. The resulting DMD modes are a common basis for all variables included in the DMD calculation. Once the DMD is computed, the points in the DMD modes corresponding to each variable can be separated and reordered to match the original input data. The multi-variable DMD method has been previously applied to combustion instability data by Richecoeur et al. [117] who studied simultaneous dynamic pressure and PIV data. In this work, the multi-variable DMD is applied to process simultaneously recorded dynamic pressure sensor data with the shadowgraph and OH* optical data samples from BKH.

The dynamic pressure sensor data are appended to the DMD data matrix as additional spatial points for each temporal snapshot. Each temporal snapshot then consists of the $X \times Y$ pixels of an image reordered into a 1D vector with n_s additional spatial points corresponding to the dynamic pressure sensor data measurements recorded at the same instant appended to the end. The appended dynamic pressure sensor data is re-sampled to match the lower sampling rate of the optical data. Once the DMD is computed the n_s points in the DMD spatial modes corresponding to the dynamic pressure sensor signals are separated before re-ordering the remaining points to represent the original $X \times Y$ frames of optical data. The original input dataset can be reconstructed using equation 5.18. The multi-variable DMD method is illustrated in Figure 5.3.1.

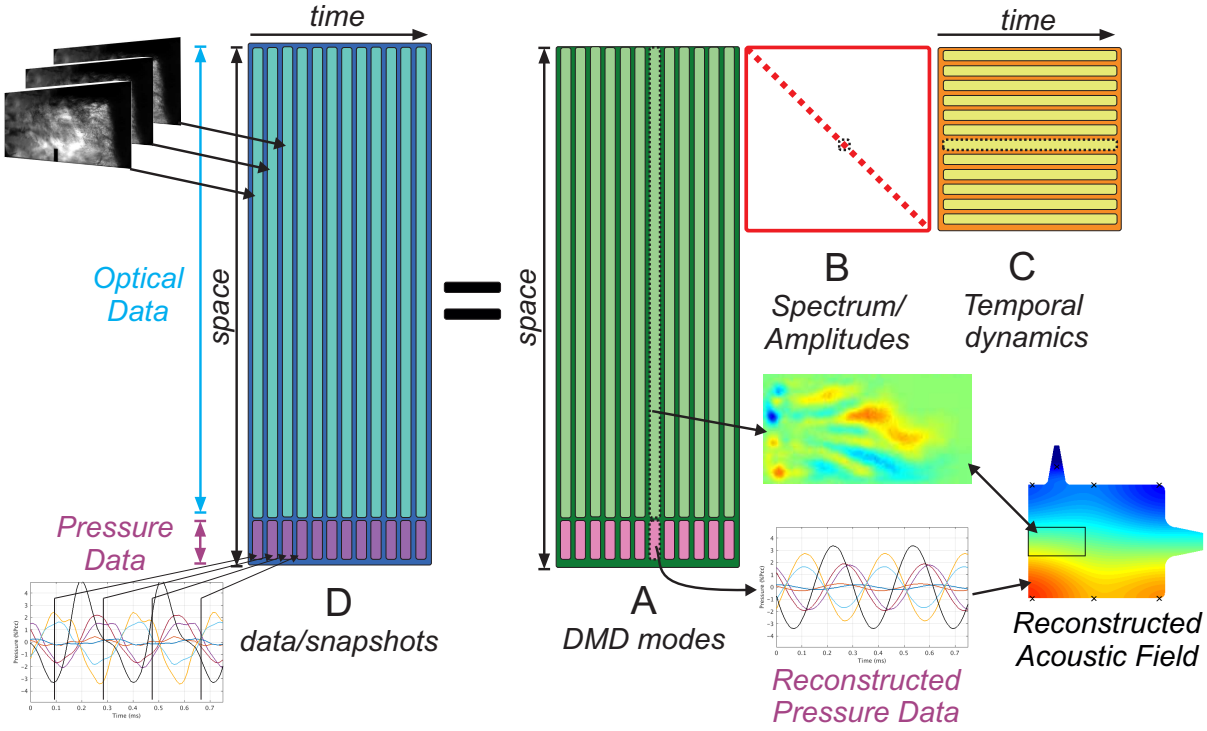

Figure 5.3.1: Application of multi-variable DMD method to BKH experimental data.

The optical data can then be reconstructed by combining all DMD modes with the corresponding temporal modes and the original mean values subtracted to ensure harmonic fluctuations as described in Equation 5.18. For this study the fluctuations at specific frequencies of interest are isolated by selecting the relevant DMD modes.

Calculation of the Complex Amplitude from DMD Results

A complex amplitude formulation is used to compare the relative phase and amplitudes of the DMD results with the acoustic field. The complex amplitude has been described previously in Section 2.4.2. The complex amplitude of the fluctuation at a particular frequency can be computed by considering the corresponding DMD modes.

The computed DMD modes occur as pairs with each member of a pair having the same frequency with opposite sign. Therefore the temporal modes of each member of the mode pair traverses the circumference of the complex unit circle in opposite directions and are the complex conjugate of one another. To reconstruct the original data from the DMD modes, the sum of all mode pairs is computed resulting in a real valued result to match the input data, with each member of the mode pair contributing 50% of the real-valued total disturbance at the associated frequency.

To convert the DMD results to a complex amplitude, first modes at the frequency of interest are selected. Then the mode in each mode pair that has a temporal component traversing the complex plane in an anti-clockwise direction is identified by the derivative of its temporal phase and selected. The amplitude of the mode is then doubled making its real part representative of the sum of the original mode pair and the physical optical intensity fluctuation. The reconstructed data from the scaled mode is a complex amplitude representing the mode pair and the disturbance at the frequency of interest.

Calculation of the Relative Phase and Rayleigh Index

The instantaneous phase of a spatial point at a particular time can be computed as the phase angle of the reconstructed complex amplitude at the time of interest. The relative phase between each spatial point and a reference signal is computed as the difference between the reference signal and the reconstructed complex amplitude. Therefore a relative phase of -90° indicates that the maximum positive real value occurs a quarter of an acoustic cycle before the maximum positive value of the reference signal. Similarly a relative phase difference of 0° indicates that the peak fluctuations of both signals are perfectly in phase.

The Rayleigh index was previously described in Section 2.3.2 and is used as an indicator of coupling between heat release and acoustic processes. The optical instensity fluctuation, I', is assumed to be representative of the heat release. Using the complex amplitude formulation the Rayleigh Index is computed as:

$$\text{Rayleigh Index} = |I'||p'|cos(\theta_{I'} - \theta_{p'}). \tag{5.19}$$

Where $\theta_{I'}$ and $\theta_{p'}$ represents the phase angle of the optical intensity and acoustic pressure fluctuations, respectively.

In the following analyses the frequency resolution of the DMD sufficed such that the disturbance of interest is isolated in a single DMD mode pair. This greatly simplified analysis as the fluctuations at all other frequencies could be ignored and the Rayleigh index and phase distributions can therefore be computed by analysing a single spatial DMD mode. This also allowed the identified camera artefacts to be separated and removed from the data of interest.

The optical data has 256 bit intensity values while the dynamic pressure sensor data is recorded in bar and has lower absolute amplitudes than the optical data. Therefore the inclusion of the dynamic pressure sensor data in the multi-variable DMD analysis produces negligible difference in the spectrum of the DMD modes.

5.3.2 Flame Response Results

The optical data samples listed in Table 5.1 were analysed along with simultaneously recorded pressure data using the multi-variable DMD method and the same modes at the

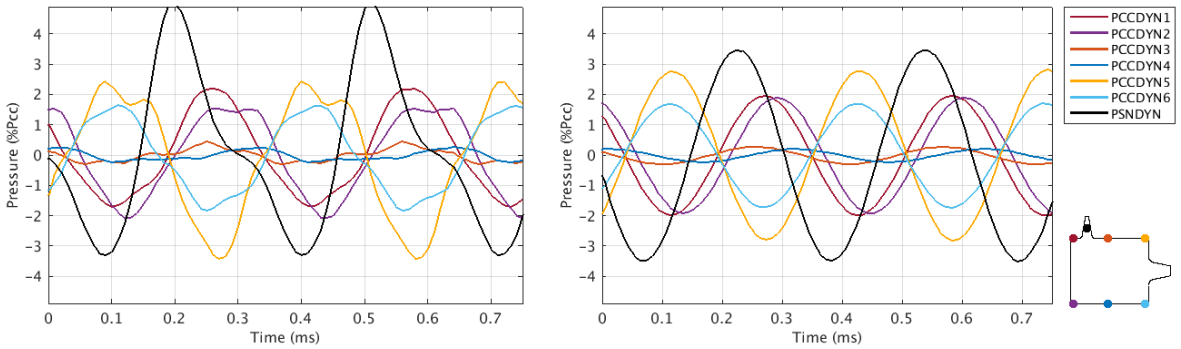

(a) Phase locked data

(b) Band-pass filtered data at excitation frequency

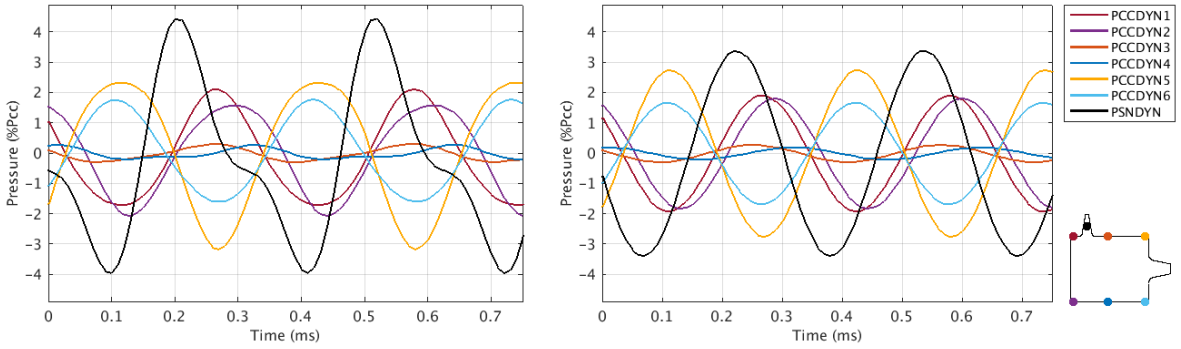

(c) Reconstrucuted data using DMD modes at excitation and overtone frequencies

(d) Reconstrucuted data using only DMD modes at excitation frequency

Figure 5.3.2: Comparison of original and reconstructed sensor data during 1L-mode excitation.

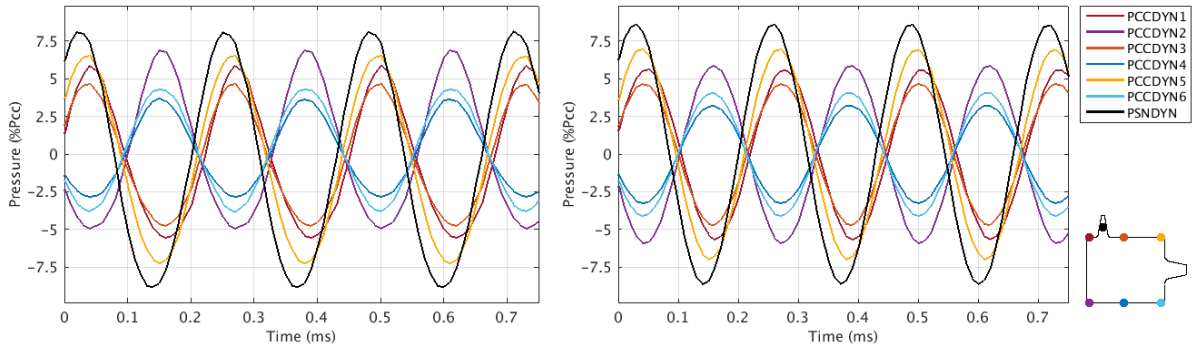

(a) Phase locked data

(b) Reconstrucuted data using only DMD modes at excitation frequency

Figure 5.3.3: Comparison of original and reconstructed sensor data during 1T-mode excitation.

excitation and overtone frequencies were identified. The spatial points corresponding to the dynamic pressure sensor data were then separated from the spatial points representing intensity fluctuations in the optical data.

The dynamic pressure sensor data was reconstructed from the identified DMD modes to verify that the reconstructed disturbance was representative of the original acoustic disturbance. Figure 5.3.2 shows the raw and reconstructed pressure sensor signals from the multi-variable DMD calculation of the Test A 1L samples. The phase locked experimental data shows the mean disturbance over the sample period. The band-pass filtered data was computed using a filter with a pass band of ± 200 Hz about the excitation frequency. It can be seen that, despite a slight offset in the phase locked data, the reconstructed DMD results reproduce the dynamic pressure sensor data with the same amplitude and phase.

Figure 5.3.3 shows a comparison between phase locked experimental data and the reconstructed pressure sensor signals from the Test B 1T-mode optical samples. As the original data is very close to monofrequent, the pressure data can be reproduced by reconstructing with only the DMD modes at the excitation frequency. These results were produced by reconstructing using just the modes at the frequencies of interest and demonstrate the application of the multi-variable DMD method to isolate the mean pressure disturbance.

The dynamic pressure sensor data is reconstructed as a complex amplitude using the method described in Section 5.3.1. The reconstructed complex amplitude can then be used to reconstruct the mean acoustic disturbance over the sample period. The relative phase distribution is computed relative to the reconstructed PCCDYN2 sensor signal. The local acoustic disturbance acting upon the window region is then determined by interpolating from the reconstructed acoustic field. Using this method the mean local acoustic and intensity fluctuations over a sample period can be compared at the pixel coordinates of the optical data. This method is applied to the 1L and 1T DMD results previously presented in Section 5.2.2.

1L Mode Excitation

The multi-variable DMD method was also applied to the Test A 1L optical data samples. The dynamic pressure sensor data was reconstructed as a complex amplitude using the DMD mode at the excitation frequency. The resulting complex amplitude formulation of the dynamic pressure sensor signals was then used to reconstruct the acoustic disturbance in the chamber using the reconstruction method described in Section 4.1.3. The resulting acoustic field is shown in Figure 5.3.4 and matches the expected 1L mode distribution.

The local acoustic disturbance in the window region is shown in Figure 5.3.5. As discussed previously, during 1L mode excitation the flame zone and window region are located in a pressure anti-node. The phase distribution in the window region shows that the acoustic disturbance in the window region is almost uniformly in phase. The acoustic forcing propagating from the secondary nozzle causes the disturbance in the top of the window to slightly lead the disturbance near the bottom of the window.

The calculated local acoustic disturbance is compared with the local intensity fluctuations at the same frequency represented by the DMD mode. The results of this comparison for the Test A 1L-mode shadowgraph sample are shown in Figure 5.3.6. The intensity amplitude shows that the brightest fluctuations occur near the center of the window region with an intensity amplitude of 4-10% of the mean image intensity.

The relative phase plot in Figure 5.3.6b shows that the peak intensity occurs between $-90°$ and $90°$ relative to the PCCDYN2 sensor signal. However when the phase is computed relative to the local acoustic disturbance, as shown in Figure 5.3.6d, intensity fluctuation can be seen to lag behind the local acoustic disturbance in most locations by $40° \sim 50°$. It is therefore important to use the local phase instead of the PCCDYN2 sensor phase for Rayleigh index calculations.

The shadowgraph image intensity fluctuations suggest that a significant amount of combustion light is being captured. A Rayleigh index is computed for the shadowgraph sample and is shown in Figure 5.3.6c. Despite the phase lag between pressure and optical intensity fluctuations, the Rayleigh index is positive over the window region. As the peak emission occurs after the pressure peak in the acoustic cycle, when the highest rate of combustion is expected, the emitted light captured by the shadowgraph images may be caused by thermal emission from water and other species as the flame temperature increases.

Figure 5.3.7 shows the results produced from the analysis of the Test A 1L OH* sample. Like the shadowgraph images, the peak intensity occurs in phase with the PCCDYN2

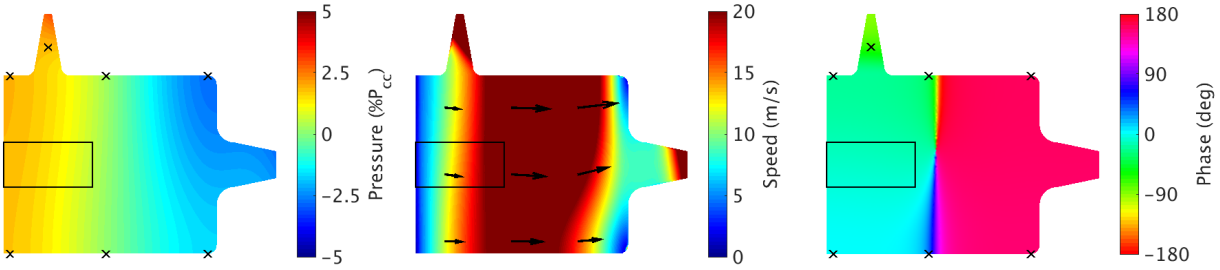

(a) Peak pressure disturbance (b) peak velocity disturbance (c) Relative phase

Figure 5.3.4: Reconstructed acoustic field during Test A 1L-mode sample.

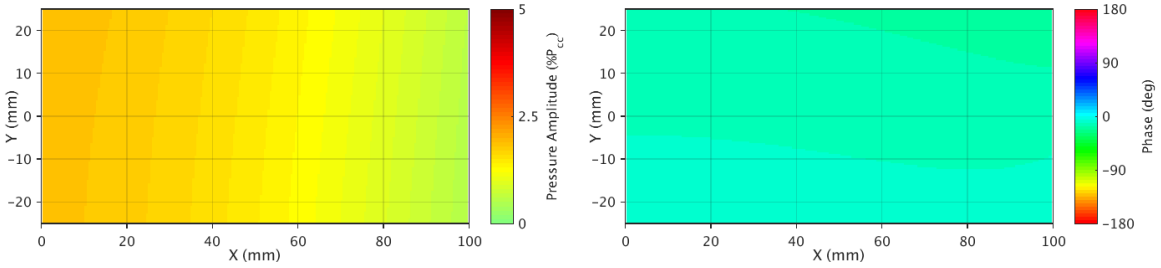

(a) Pressure amplitude (b) Acoustic pressure phase relative to PCCDYN2

Figure 5.3.5: Acoustic pressure field distribution in optical data region during Test A 1L-mode sample.

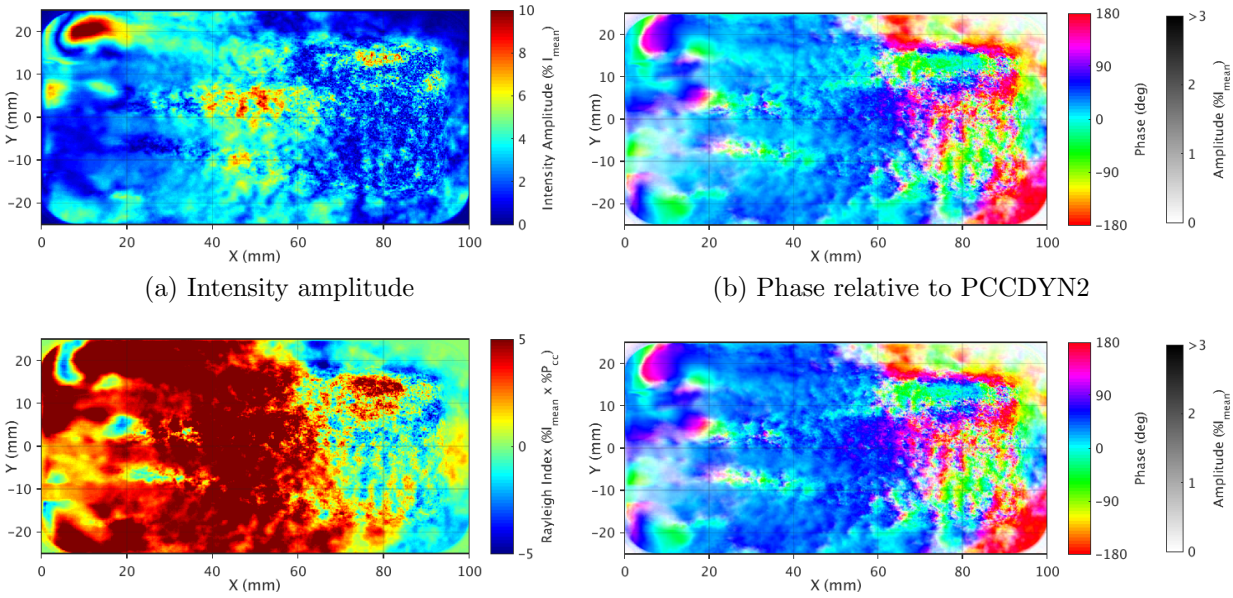

(a) Intensity amplitude (b) Phase relative to PCCDYN2

(c) Rayleigh index (d) Phase relative to local acoustic pressure

Figure 5.3.6: Flame response distribution computed for DMD mode at the excitation frequency for Test A 1L-mode Shadowgraph sample.

signal and the local acoustic pressure disturbance. The intensity amplitude distribution shows that the amplitude of the intensity fluctuations increases towards the injection plane. This corresponds to the local pressure disturbance amplitude shown in Figure 5.3.5a and suggests a direct response to the local pressure fluctuations.

The phase distribution shown in Figure 5.3.7b shows that the intensity fluctuations are in phase with the PCCDYN2 sensor. Figure 5.3.7d shows that the intensity fluctuations are in phase with, or lag slightly, behind the local acoustic disturbance. The slight phase lag between pressure and OH* emission could be the result of thermal excitation of OH* as the flame temperature increases after the acoustic pressure peak. The Rayleigh index computed for the Test A 1L OH* sample shown in Figure 5.3.7c shows predominantly

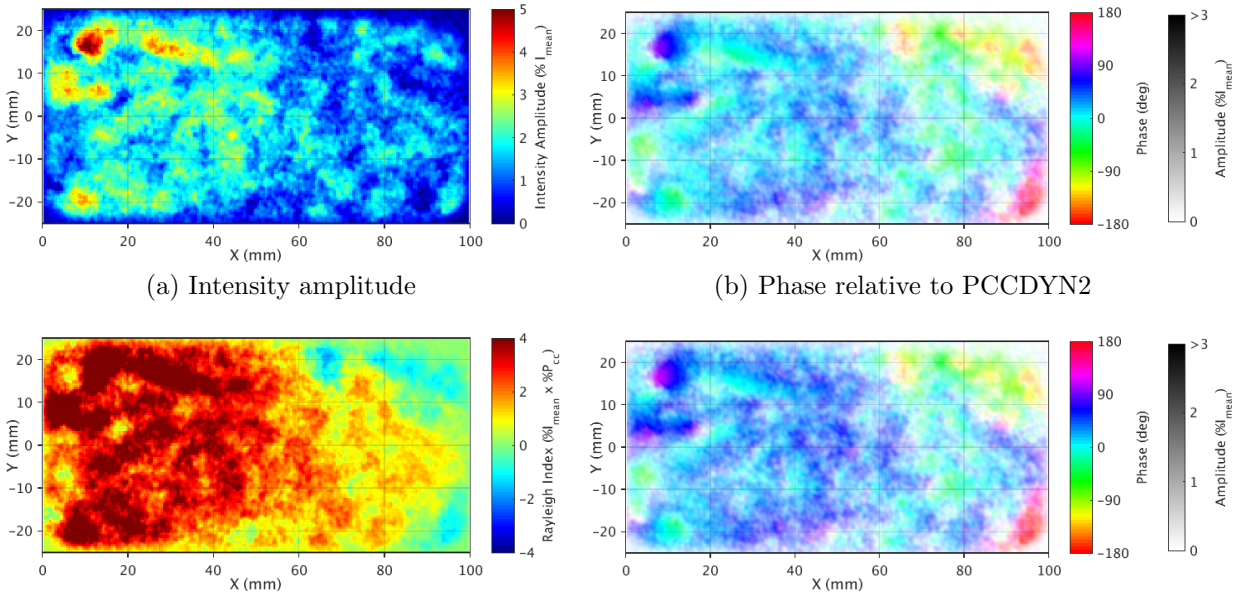

(a) Intensity amplitude

(b) Phase relative to PCCDYN2

(c) Rayleigh index

(d) Phase relative to local acoustic pressure

Figure 5.3.7: Flame response distribution computed for DMD mode at the excitation frequency for Test A 1L-mode OH* sample.

positive values and agrees with previous results and analysis by Hardi [49].

Figure 5.3.8 shows the reconstructed acoustic field for the Test C 1L-mode shadowgraph sample. The local acoustic disturbance in the region captured by the Test C 1L-mode shadowgraph sample is shown in Figure 5.3.9. The region captured is very small as the camera was zoomed in to focus on the shear layer region and is subjected to a uniform pressure disturbance with negligible acoustic velocity. The acoustic field reconstruction shows that the phase of the acoustic disturbance in this region slightly leads the pressure disturbance at the PCCDYN2 location.

Figure 5.3.10 shows the calculated intensity, relative phase, and Rayleigh index of the Test C 1L-mode shadowgraph sample. All plots show a distribution following the shear layer of the oxygen core at 2 mm above the centerline of the chamber. The intensity amplitude distribution shows regions which, compared with the relative phase distributions, occur slightly after the acoustic pressure peak. The Rayleigh index plot in Figure 5.3.10c shows similar positive regions at these locations. Care must be taken when interpreting the Rayleigh index plot as the motion of surface structures is responsible for the fluctuations in the shear layer rather than actual combustion response. A similar pattern of fluctuations is visible on the surface of the jet along the bottom of the image indicating that the surface fluctuations may surround the jet asymmetrically.

1T Mode Excitation

The reconstructed acoustic field from the Test A 1T-mode samples is shown in Figure 5.3.11. the optical data includes the entire window region which is subjected to a transverse acoustic velocity disturbance. The pressure nodal line passes through the center of the window. The nodal line does not show a sharp discontinuity which means that the sensors along the top and bottom wall of the chamber used for the reconstruction were not perfectly out of phase. The local acoustic disturbance acting upon the window region is shown in Figure 5.3.12. Despite the pressure nodal line passing through the window region, the edges of the window are subjected to pressure fluctuations equal to 2.5% of the mean chamber pressure. These amplitudes are comparable to those reached during 1L mode excitation.

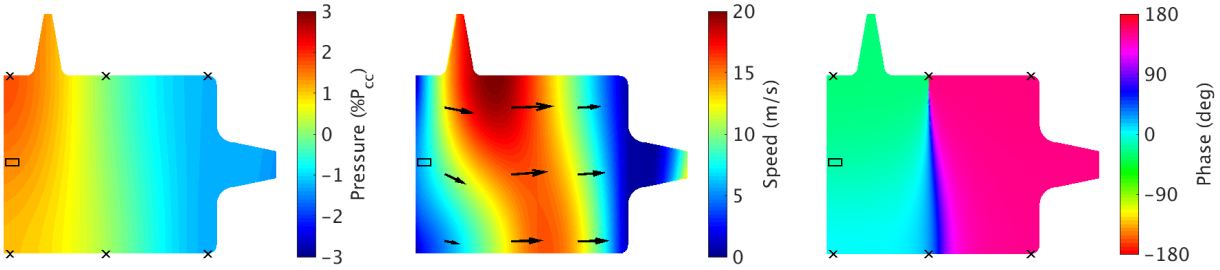

(a) Peak pressure disturbance (b) peak velocity disturbance (c) Relative phase

Figure 5.3.8: Reconstructed acoustic field during Test C 1L-mode sample.

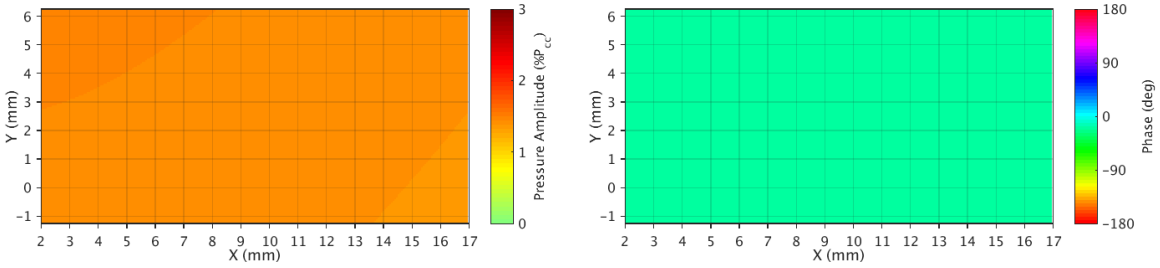

(a) Pressure amplitude (b) Acoustic pressure phase relative to PCCDYN2

Figure 5.3.9: Acoustic pressure field distribution in optical data region during Test C 1L-mode sample.

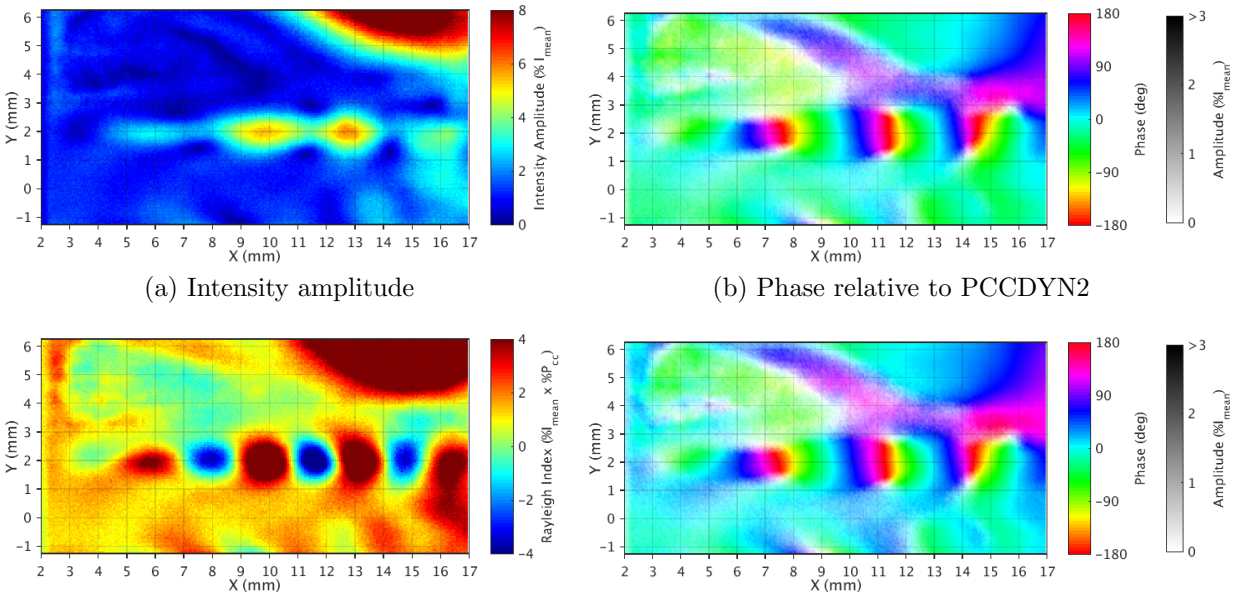

(a) Intensity amplitude (b) Phase relative to PCCDYN2

(c) Rayleigh index (d) Phase relative to local acoustic pressure

Figure 5.3.10: Flame response distribution computed for DMD mode at the excitation frequency for Test C 1L-mode Shadowgraph sample.

Figure 5.3.13 shows the calculated results for the Test A 1T-mode shadowgraph sample. The intensity amplitude of the shadowgraph sample is shown in Figure 5.3.13a and is significantly higher than that for the 1L mode samples, with a peak-to-peak amplitude of over 35% of the mean image intensity. This is a consequence of the motion of light and dark structures in and out of regions in the image resulting in larger peak-to-peak intensity fluctuations.

Figure 5.3.13b shows the phase relative to PCCDYN2. The phase relative to the local acoustic disturbance is shown in figure5.3.13d. As previously discussed in Section 5.2.2, the shadowgraph image captures both the motion of the dark LOx core and the lighter gaseous surrounding flame. As expected, the smaller structures corresponding

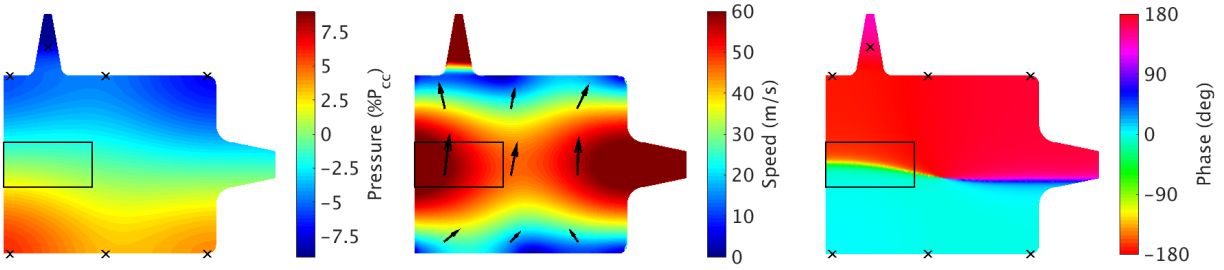

(a) Peak pressure disturbance (b) peak velocity disturbance (c) Relative phase

Figure 5.3.11: Reconstructed acoustic field during Test A 1T-mode sample.

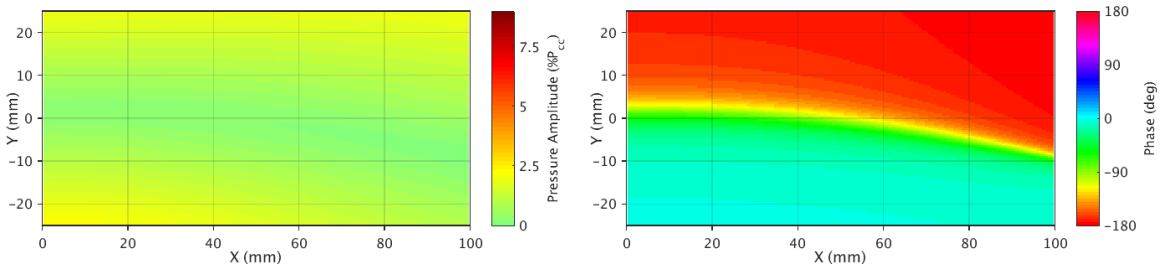

(a) Pressure amplitude (b) Acoustic pressure phase relative to PCCDYN2

Figure 5.3.12: Acoustic pressure field distribution in optical data region during Test A 1T-mode sample.

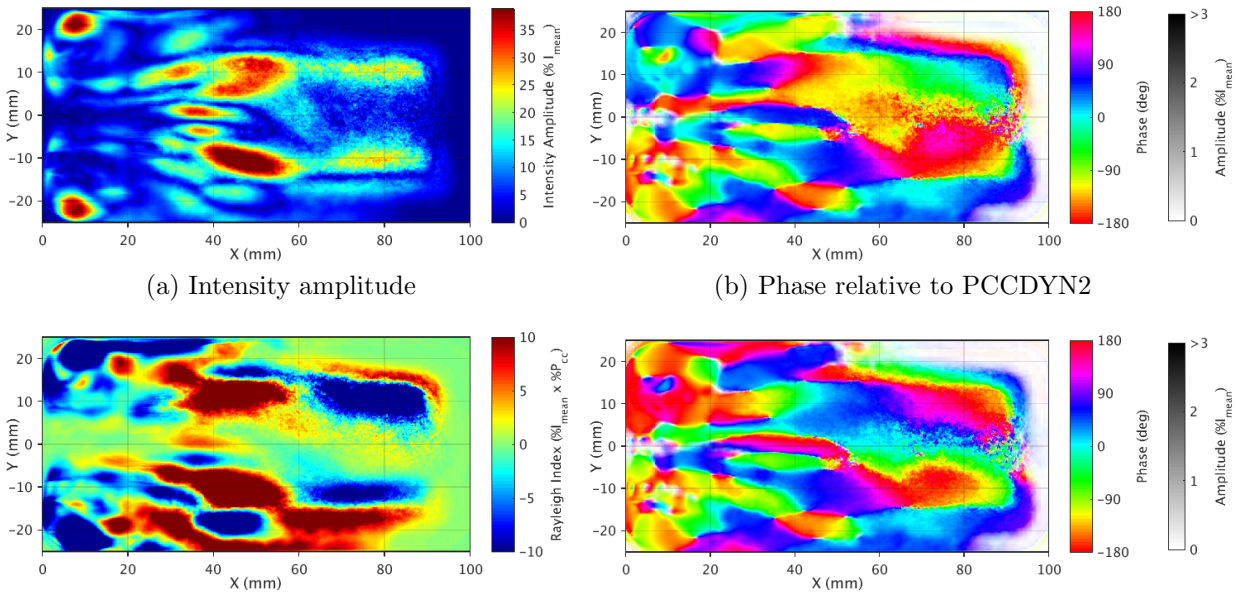

(a) Intensity amplitude (b) Phase relative to PCCDYN2

(c) Rayleigh index (d) Phase relative to local acoustic pressure

Figure 5.3.13: Flame response distribution computed for DMD mode at the excitation frequency for Test A 1T-mode Shadowgraph sample.

to the LOx core fluctuate out of phase with the acoustic disturbance, while the lighter structures corresponding to the surrounding flame are in phase or slightly lag the pressure disturbance. The phase lag relative to the acoustic pressure fluctuations matches the phase lag identified in the previous analysis of the 1L-mode optical data samples.

The Rayleigh index plot in Figure 5.3.13c shows two symmetrical lobes with positive Rayleigh indices between 30 and 60 mm from the injection plane. These lobes represent the transport of the flame enveloping the LOx core of the central injection element. The rayleigh index is negligible along the pressure nodal line. Care must be taken when interpreting the rest of the Rayleigh index distribution as the shadowgraph image is not representative of combustion response.

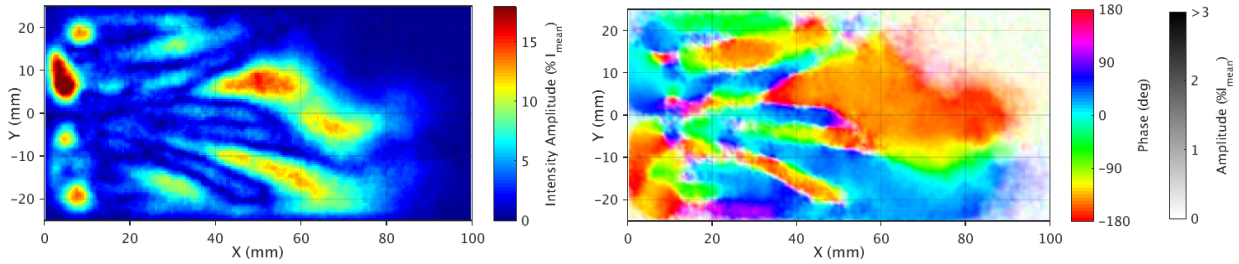

(a) Intensity amplitude (b) Phase relative to PCCDYN2

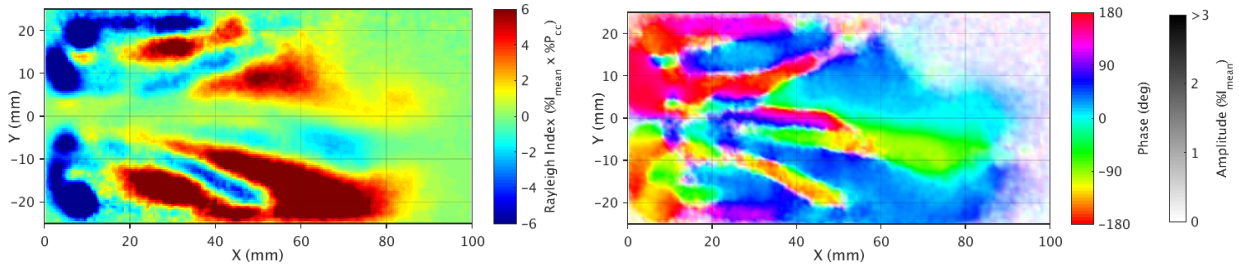

(c) Rayleigh index (d) Phase relative to local acoustic pressure

Figure 5.3.14: Flame response distribution computed for DMD mode at the excitation frequency for Test A 1T-mode OH* sample.

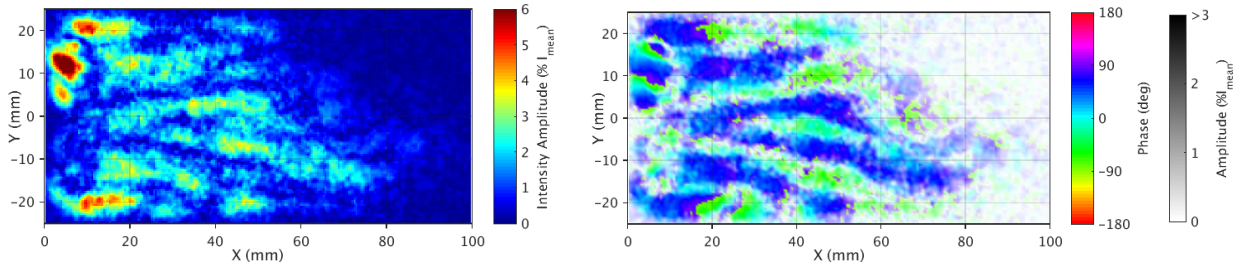

(a) Intensity Amplitude (b) Phase relative to PCCDYN2

Figure 5.3.15: Intensity and phase of DMD mode at the 1T overtone frequency from Test A 1T-mode OH* sample.

Figure 5.3.14 shows the calculated results for the Test A 1T-mode OH* sample. The intensity amplitudes of the OH* sample are lower than the simultaneously captured 1T-mode shadowgraph sample as the flame fills the window region leading to a more uniform intensity in the OH* image. However, the intensity amplitudes of 15% (30 % peak-to-peak fluctuation) are still quite significant. The largest intensity amplitudes occur when the maximum displacement of the flame is reached which shows the highest variation from the mean image used for the DMD calculation.

The horizontal structures in the image represent the transport of the flame by the acoustic velocity. The plot of phase relative to PCCDYN2 is shown in Figure 5.3.14b. The phase relative to the local acoustic disturbance is shown in Figure 5.3.14d. The phase relative to the local acoustic disturbance exhibits an alternating pattern indicating the maximum and minimum displacement of the flame by the acoustic velocity, which occurs at the pressure minimum and maximum during the acoustic cycle.

The computed Rayleigh index for the Test A 1T OH* sample is shown in Figure 5.3.14c. The Rayleigh index calculation shows both positive and negative regions with low values along the pressure nodal line in the center of the window. The regions of maximum displacement appear as four distinct regions with positive Rayleigh indices as the flame is transported by the acoustic velocity into a pressure anti node. The negative regions that appear between positive regions correspond to the lower intensity of the flame when it is displaced across the pressure nodal line.

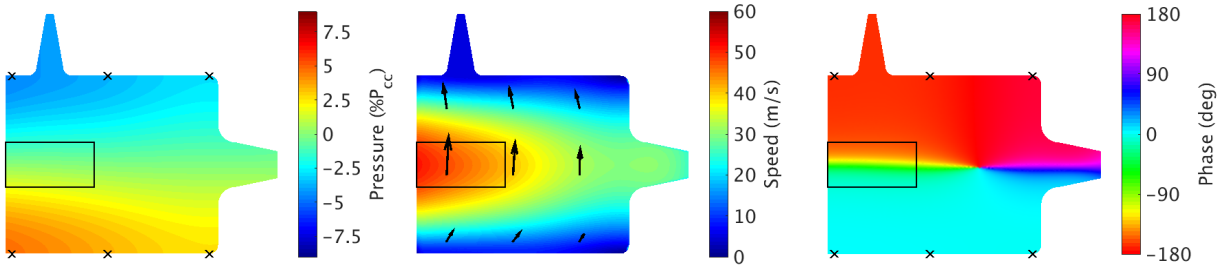

(a) Peak pressure disturbance (b) peak velocity disturbance (c) Relative phase

Figure 5.3.16: Reconstructed acoustic field during Test B 1T-mode sample.

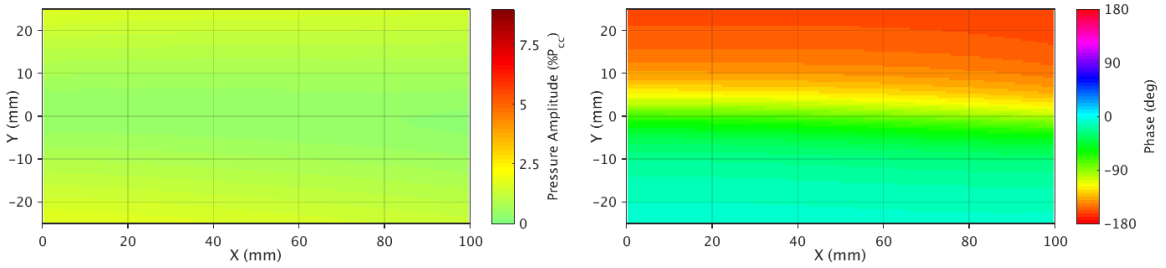

(a) Pressure amplitude (b) Acoustic pressure phase relative to PCCDYN2

Figure 5.3.17: Acoustic pressure field distribution in optical data region during Test B 1T-mode sample.

The regions with negative Rayleigh indices and large intensities near the injection plane are out of phase with the local acoustic pressure disturbance. These fluctuations appear to be the result of shedding and recirculation of the flame near the corners of the window. While these regions have high intensities, the downstream regions corresponding to the motion of the flame are larger resulting in a net positive Rayleigh index over the window region.

The acoustic velocity acts twice across the flame zone per acoustic cycle. Therefore the response of the flame to the acoustic velocity will occur at the overtone of the excitation frequency. Figure 5.3.15 shows the intensity amplitude and phase of the DMD mode at the overtone frequency. The intensity amplitudes are almost half as large as the intensity fluctuations at the excitation frequency shown in Figure 5.3.14a. The regions of high intensity also occur in between the high intensity regions at the excitation frequency. Therefore the overtone mode is capturing the intensity fluctuations as the flame transitions from maximum to minimum vertical displacement.

Figure 5.3.15b shows the phase of the fluctuations at the overtone frequency relative to the PCCDYN2 signal fluctuating at the excitation frequency. As the overtone mode is fluctuating at double the excitation frequency the phase has been scaled to show the relative values from the -90° to +90° interval. The phase plot shows that the peak intensity disturbances occur at phase angles close to ±90° relative to the PCCDYN2 sensor signal. This phase difference indicates that these fluctuations are in phase with the transverse acoustic velocity disturbance. It is not possible to differentiate if these fluctuations are a result of the motion of the flame or a result of increased combustion and heat release. As the fluctuations at the overtone frequency occur twice per acoustic cycle, the overtone fluctuations do not contribute to the Rayleigh index at the excitation frequency.

The reconstructed acoustic field from the Test B 1T samples is shown in Figure 5.3.16. These samples were taken from a period of 1T-mode excitation before the peak response frequency and have a lower acoustic amplitude than the Test A 1T samples. The pressure nodal line passes through the center of the window region. The local acoustic disturbance acting upon the window region is shown in Figure 5.3.17. Like the Test A 1T sample, significant pressure disturbances occur at the upper and lower edges of the window region.

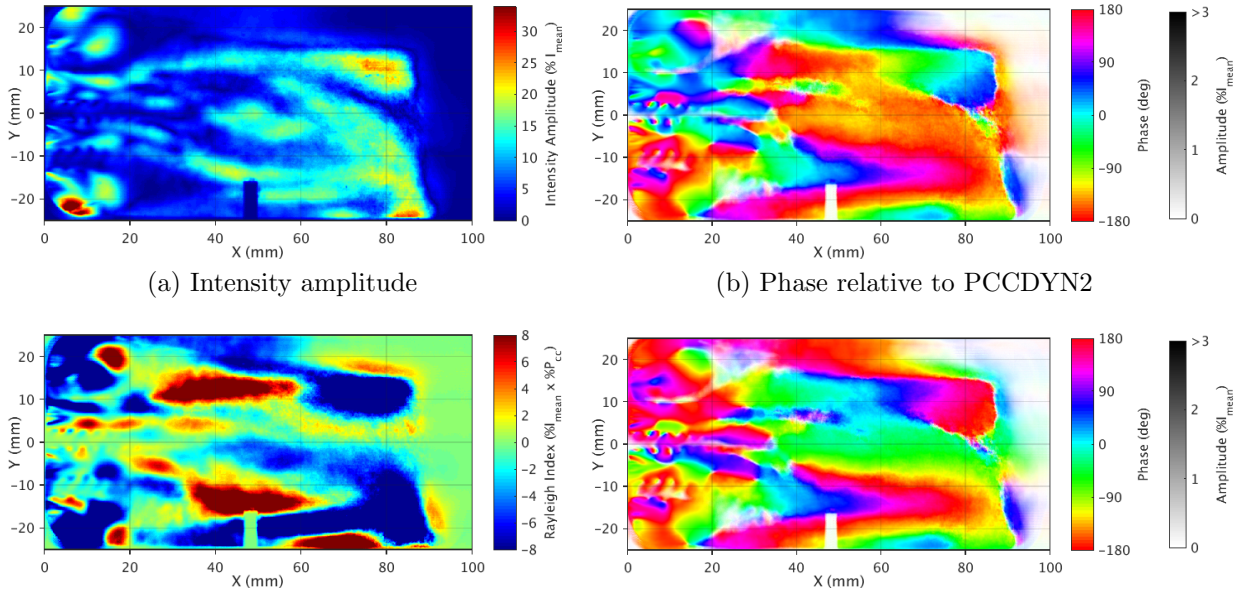

(a) Intensity amplitude

(b) Phase relative to PCCDYN2

(c) Rayleigh index

(d) Phase relative to local acoustic pressure

Figure 5.3.18: Flame response distribution computed for DMD mode at the excitation frequency for Test B 1T-mode shadowgraph sample.

The calculated results for the Test B 1T-mode shadowgraph sample are shown in Figure 5.3.18. The intensity amplitude of the fluctuations at the excitation frequency are considerable and result from the motion of dark and light structures across regions in the image. The fluctuations on the surface of the LOx jet, particularly for the lower coaxial elements, is clearly visible in the intensity distribution.

Figure 5.3.18b shows the phase distribution relative to the PCCDYN2 signal, while Figure 5.3.18d shows the phase relative to the local acoustic disturbance. Some features show a slight symmetry in the phase distribution, such as the fluctuations corresponding to transport of the gaseous medium surrounding the flame. This motion produces two regions between 40 and 70 mm from the injection plane that are mirrored across the pressure nodal line. These regions are in phase with the local acoustic pressure disturbance and produce two regions of positive Rayleigh indices in Figure 5.3.18c.

Other regions surrounding the LOx core from the central injection element are also fluctuating in phase with the local acoustic disturbance producing smaller regions of positive Rayleigh indices. Again, the Rayleigh index is not typically computed from shadowgraph imaging and care must be taken when interpreting the results.

The calculated results for the Test B 1T OH* sample are shown in Figure 5.3.19. The intensity amplitude distribution is dominated by a large structure downstream and two smaller round structures near the injection plane. The large downstream structure is the result of periodic recirculation near the end of the window. The smaller structures near the injection plane correspond to recirculation near the injection plane.

Figures 5.3.19b and 5.3.19d show the phase of the intensity fluctuations relative to the PCCDYN2 signal and the local acoustic disturbance, respectively. The phase distributions show an alternating pattern of in and out of phase fluctuations across the height of the window region. This pattern is similar to those from the Test A 1T mode OH* sample results shown in Figure 5.3.14 which were attributed to the vertical transport of the flame.

Figure 5.3.19c shows the Rayleigh index distribution computed for the Test B 1T-mode OH* sample. The large downstream structures are transported in phase with the local acoustic disturbance resulting in a positive Rayleigh index. Small regions of positive Rayleigh index appear around the LOx core of the central injection element as for the Test B 1T-mode shadowgraph sample.

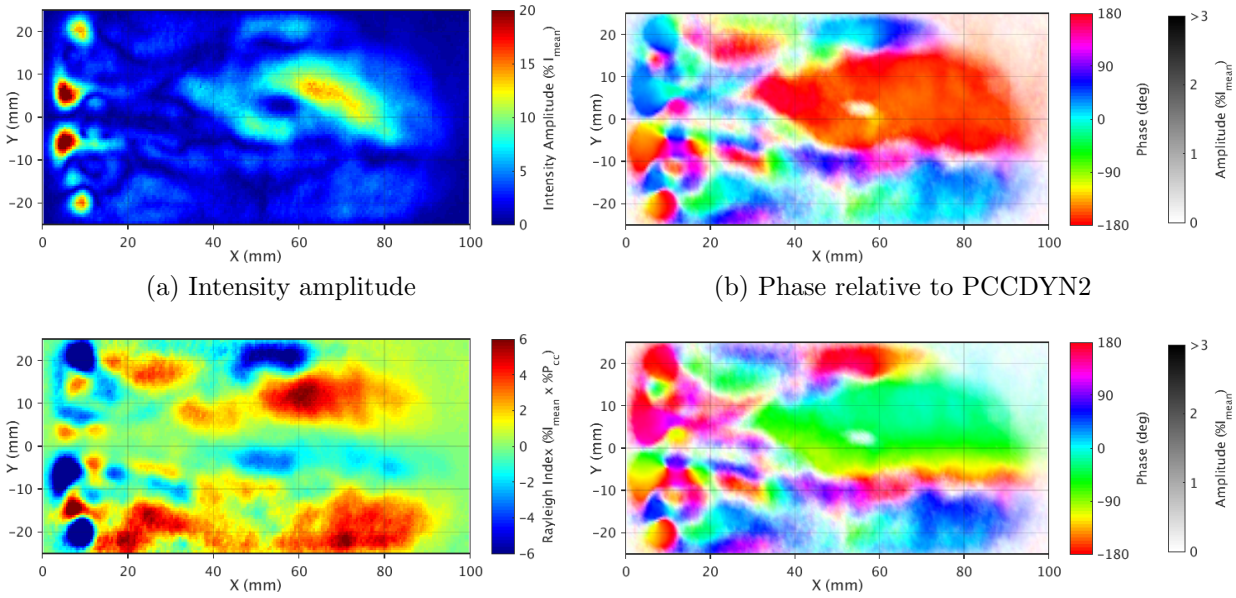

(a) Intensity amplitude (b) Phase relative to PCCDYN2

(c) Rayleigh index (d) Phase relative to local acoustic pressure

Figure 5.3.19: Flame response distribution computed for DMD mode at the excitation frequency for Test B 1T-mode OH* sample.

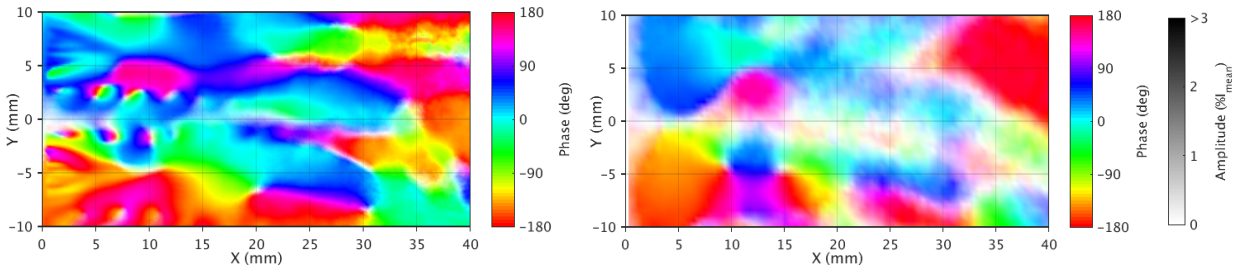

(a) Shadowgraph (b) OH*

Figure 5.3.20: Plot showing DMD mode phase relative to PCCDYN2 signal about central injector for Test B 1T-mode samples.

Characterising the motion of the LOx core and flame from the central injection element are of particular scientific interest. Figure 5.3.20 shows the phase distributions relative to the PCCDYN2 signal of the DMD mode at the excitation frequency in the near injector region from the Test B shadowgraph and OH* 1T-mode samples. The fluctuations in the shear layer of the oxygen stream that can be seen in the shadowgraph phase distribution are not visible in the OH* distribution due to the optical thickness of OH*.

Aside from the fluctuations in the shear layer, a number of similar features can be identified in each of the distributions. The motion of the flame appears as horizontal structures surrounding the LOx core with a similar phase in both the shadowgraph and OH* distributions. Two lobes that are 180° out of phase appear on either side of the LOx core between 5 and 15 mm from the injection plane. These lobes fluctuate in phase with other horizontal structures between 20 and 30 mm downstream. These regions indicate the motion of the lighter, gaseous part of the flame surrounding the liquid core by the acoustic velocity.

The analysis presented here of BKH optical data during 1T mode excitation has provided further insight into the flame response to transverse acoustic excitation. The transport of the flame into the pressure anti-node has been shown to produces a positive Rayleigh index distribution in the window region. The analyis of shadowgraph images has allowed the motion of the LOx core to be distinguished from the motion of the surrounding flame. These results will be further interpreted with additional insight from unsteady

models of BKH injection elements subjected to representative acoustic forcing in Chapter 6.

5.4 Summary

Optical datasets have been analysed to identify and describe the flame response to imposed longitudinal and transverse excitation. The response was first described using DMD analysis to isolate the optical intensity fluctuations at the excitation frequency and its overtones. The flame response to the local acoustic disturbance was then studied using a new analysis method to isolate the mean coherent acoustic and optical intensity fluctuations. This method allowed the phase distribution of the local optical intensity and acoustic fluctuations to be compared. It was used to compute Rayleigh indices and improved upon previous analysis by producing results representative of the mean response at the excitation frequency.

During longitudinal mode excitation the flame is positioned in a pressure antinode. A uniform combustion response to the acoustic pressure fluctuations was observed. Detailed analysis of the phase indicated that the peak optical intensity response lags the peak local pressure disturbance by approximately 45°. As the peak combustion response is understood to occur in phase with the acoustic pressure disturbance, this phase lag suggests that the peak emission occurs when the peak flame temperature is reached with some delay so the emission may be the result of thermal excitation. Despite this phase lag the longitudinal pressure excitation of BKH produces a positive Rayleigh index distribution over the window region.

Analysis of the shadowgraph images focused on the shear layer during 1L-mode excitation identified wave-like surface fluctuations on the surface of the LOx core. These structures are reproduced numerically in Chapter 6, and the numerical results indicate the fluctuations are related to an internal longitudinal acoustic disturbance in the LOx post.

Analysis of BKH optical samples recorded during 1T-mode excitation identified the response of the flame to transverse velocity forcing. The DMD analysis identified horizontal structures that are interpreted as the lighter gaseous part of the flame surrounding the LOx core being vertically transported by the acoustic velocity. The flame response analysis identified the phase of this motion relative to the local acoustic disturbance. This motion is further interpreted as the flapping motion of the flame with the assistance of numerical results presented in Chapter 6. The transport of the flame across the pressure nodal line by the acoustic velocity produced positive Rayleigh index distributions. Alternating ripples on the top and bottom surface of the LOx jet during 1T-mode excitation were also identified. These structures were observed to occur at the same frequency as the imposed acoustic disturbance.

The response of the flame to acoustic excitation, identified in this study, provides further insight into the processes that occur during combustion instabilities. The analysis of the experimental data has identified key features that should be reproduced in numerical models of combustion instability phenomena. The spatial resolution of the intensity, phase, and Rayleigh index distributions will allow further numerical comparisons.

Chapter 6

Excitation Modelling

Numerical modelling of the flame response to acoustic excitation is needed to provide further insight into the mechanisms driving combustion instabilities that is not possible via the limited line-of-sight access to the flame zone available experimentally. Modelling the chamber in its entirety requires confidence that the acoustic excitation and resonant modes can be reproduced numerically. Instead, in this study models of flames from single BKH injection elements were computed and subjected to representative acoustic excitation. This approach reduced the cost and complexity of the model and permitted greater control of the imposed acoustic disturbance acting locally upon the flame.

Similar acoustically forced single injector models have been produced by other research groups to study non-reactive [33, 129, 132] and combusting [42, 65, 110, 128, 134] coaxial injector configurations at supercritical pressures. Aside from identifying key physical phenomena the results of the single injector models are also often used to compute flame transfer functions for use in lower-order modelling approaches. However, due to a lack of available test data it is not always possible to validate the results of the single injector models and the resulting flame transfer functions.

In this study the real-gas modelling approach demonstrated in Chapter 3 is again employed to model the unsteady trans-critical injection and combustion processes. The extension of the steady-state numerical method for unsteady modelling is first described, including a new method developed for imposing acoustic excitation on a sub-domain using the existing capabilities of the chosen CFD tool. Numerical modelling of pressure excitation, representative of BKH 1L-mode excitation, and transverse velocity excitation, representative of BKH 1T-mode excitation, are then presented separately. The numerical results are compared with experimental observations from the analysis of BKH optical data presented in Chapter 5. The numerical results complement the experimental datasets and provide further insight into the response of coaxial elements subjected to high frequency acoustic forcing.

6.1 Numerical Method

The same CFD solver and numerical approach described in Chapter 3 that was applied to the steady-state model of the BKH combustor was employed for the unsteady computations. A steady-state RANS model of a single injection element in a representative sub domain was first computed to produce an initial solution. The single injector model was then continued as an unsteady RANS (URANS) computation. The model is acoustically excited during the unsteady computation by modulating the boundary conditions on the sides of the numerical domain at each physical time step. The URANS model is used to study the mean response of the flame to the imposed acoustic disturbance.

The CFD tool used for this work, the DLR TAU code, has been previously described

in Section 3.1. To perform unsteady computations a Jameson-type dual time stepping scheme with a physical time step size of 5.0×10^{-6} s and 1000 inner iterations per physical time step was used. The ability of the URANS model to capture the propagation of acoustic disturbances at the frequencies of interest was evaluated using a number of simple test cases. Karl and Lüdeke [66] first validated the TAU code for modelling of acoustic damping cavities. Similar acoustic damping cases were used to demonstrate the ability of the solver to accurately capture the propagation of acoustic disturbances at frequencies up to 5 kHz.

During the unsteady computation the boundary conditions of the domain are modified after each physical time step to impose an acoustic disturbance representative of the local acoustic fluctuation acting upon the flame in BKH experiments. The excitation method, numerical domain, boundary conditions, and grid are described in the following sections.

6.1.1 Domain and Boundary Conditions

Two different domains were used to study pressure and velocity excitation of a BKH coaxial injection element. Both domains modelled part of the injector geometry connected to a larger volume representing part of the chamber volume. A 2D axisymmetric domain was used for modelling a BKH injector subjected to acoustic pressure forcing. The axisymmetric domain was chosen as the pressure fluctuations were to be imposed symmetrically about the flame as if it were in a pressure anti-node and velocity node. The axisymmetric disturbance does not disturb the flame from the centerline of the injector and it can therefore be approximated with a 2D axisymmetric domain. The 2D axisymmetric domain is shown in Figure 6.1.1.

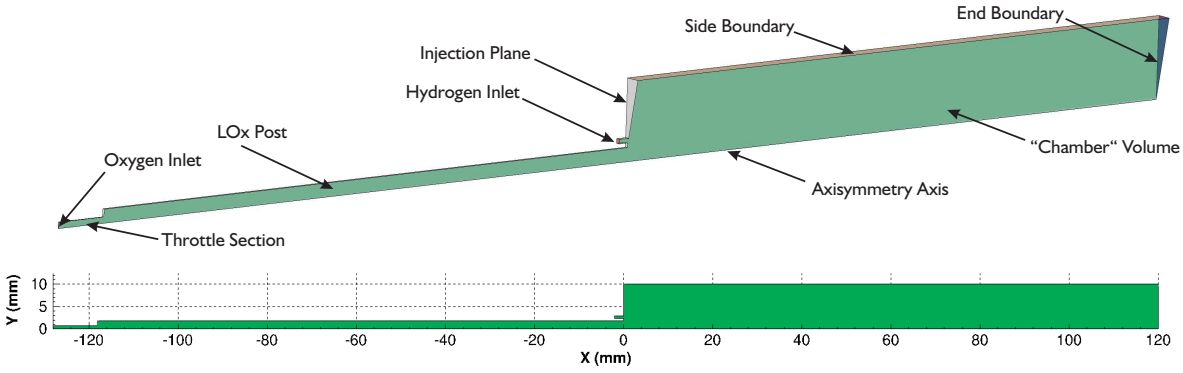

Figure 6.1.1: Domain used for 2D axisymmetric single injector computations.

To investigate LOx post coupling the geometry up to the entrance of the throttle section from the oxygen manifold was included in the 2D axisymmetric domain. The throttle section accelerates the flow from the oxygen manifold and induce a pressure drop to decouple the post and chamber acoustics from the upstream feed system. Gröning et al. [34] studied the naturally excited combustion instability in BKD and identified an internal injector resonance that was coupling with the disturbance in the chamber. The internal injector resonance was also identified in LES of the BKD combustor by Urbano et al. [153].

The last 2 mm of the hydrogen annulus before the injection plane is included in the 2D axisymmetric numerical domain. In the employed modelling approach hydrogen is treated as an ideal gas. The ideal gas assumption leads to an absolute error of more than 3% in the density and specific volume of hydrogen at the BKH injection conditions and becomes more significant at higher pressures and lower temperatures. This error limits the applicability of the modelling approach and it is therefore not employed to model the hydrogen passing through the feed system.

The small volume downstream from the injection plane is chosen to capture the extent of the flame as it propagates into the larger chamber volume. The chamber volume in the 2D axisymmetric model is 120 mm long and has a radius of 10 mm. The length of the domain was chosen to be slightly longer than the 100 mm length accessible via optical access in BKH. The chosen radius of the numerical domain was found to have a significant impact on the resulting flow field. The central coaxial injection element in the BKH combustor is surrounded by four other elements. The distance between the center of the central and outer elements is 15 mm. However the matrix pattern of the injectors means that the central element is not perfectly surrounded. The 10 mm radius was chosen for the current work as it produces a representative flame distribution which contains the flame within the numerical domain during acoustic excitation.

Mass flow rate boundary conditions are specified at the oxygen and hydrogen inlet boundaries. The post walls, post tip, and injection plane are specified as adiabatic viscous walls. An axisymmetry condition is prescribed at the centerline of the axisymmetric domain. To compute an initial steady-state solution the side boundaries of the "chamber" volume is specified as an inviscid wall and a farfield condition is prescribed at the end boundary of the domain. The farfield boundary state is specified by defining the composition, density, velocity, and temperature of a mixture. During the RANS computation the flow across the boundary is determined based on the difference between the internal flow state and the boundary farfield state. The state at the farfield boundary is specified as an equilibrium mixture of combustion products at the desired chamber pressure. This equilibrium mixture is computed using the oxygen and hydrogen flow rates through the injector and is predominantly hydrogen and water. The farfield boundary condition was applied as it allowed a fluid state at a specified pressure to be prescribed along a large portion of the boundary of the numerical domain, allowing the pressure in the domain to be adjusted to match the experimental chamber pressure.

For unsteady computations the side and end boundaries of the chamber domain are specified as near field boundary conditions. The near field boundary condition is modified at each physical time step during the unsteady computation in order to impose the desired acoustic disturbance. The near field boundary condition and excitation method are described in Section 6.1.2.

In order to study the response of a BKH injector subjected to transverse acoustic velocity fluctuations a 3D domain was used which is shown in Figure 6.1.2. The 3D domain was necessary to capture the vertical transport and flattening of the flame by the imposed transverse velocity. In the current work the single injector model is subjected to a one-dimensional transverse disturbance. A symmetry condition is prescribed in the X-Y plane parallel to the imposed disturbance and injection velocity. This symmetry plane allowed the numerical domain to be reduced to include only one half of the injector and flame while still capturing the relevant phenomena.

As the hydrogen and oxygen injectors reside in a pressure node during transverse excitation limited coupling with the injection elements is expected to occur. Therefore the oxygen and hydrogen posts are not included in the 3D numerical domain. Instead only a short section of both the oxygen and hydrogen injectors before the injection plane is included before the injection plane.

Like the 2D axisymmetric model, the downstream volume attached to the injection plane is used to represent a local region of the chamber volume in the 3D numerical domain. The rectangular volume extends 120 mm from the injection plane and is 25 mm wide by 50 mm high. With the symmetry condition the rectangular volume is equivalent to a 50 mm by 50 mm box with the BKH coaxial injection element in the center. The width of the box is comparable to the width of BKH, while the height and length are comparable to the optically accessible region visible through the BKH windows. In BKH

all five co-axial elements and the window cooling injection array are contained within the same volume.

The dimensions of the representative chamber volume were found to significantly affect the flame distribution in the numerical domain. A larger domain allows the hydrogen to avoid the oxygen by circulating further away from the core, a smaller domain forces the oxygen and hydrogen streams to mix. The choice of a rectangular domain also leads to a slight asymmetry of the flame due to minor recirculation in the corner regions during the steady-state computation used to intialise the unsteady calculations. The dimensions of the 3D numerical domain were chosen in order to contain the flame from the single injection element while being sufficiently large that the flame does not intersect the side boundaries during transverse excitation.

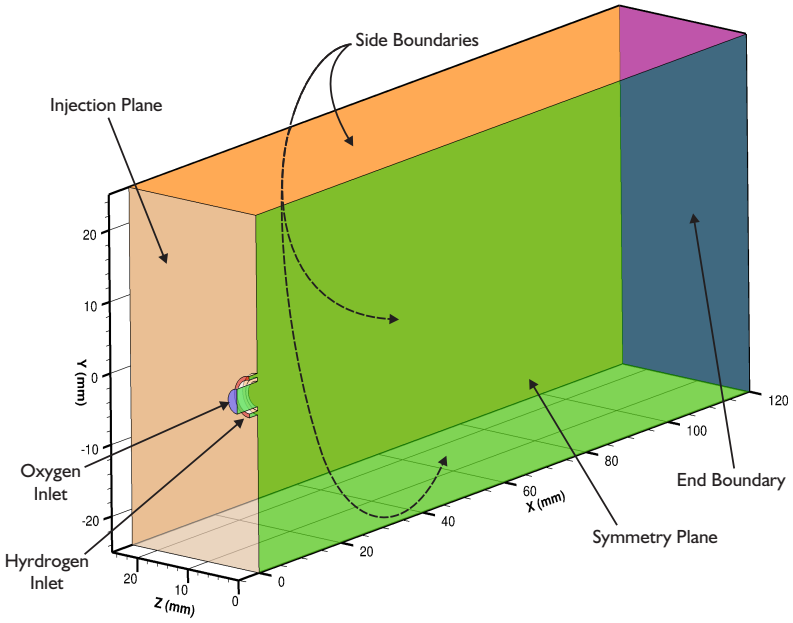

Figure 6.1.2: Domain used for 3D single injector computations.

The inlet boundaries of the oxygen and hydrogen injectors were specified as mass flow boundary conditions. The oxygen post and injection plane boundaries are specified as adiabatic viscous walls. Similar boundary conditions are prescribed to the boundaries of the chamber volume as for the 2D axisymmetric case. To compute a steady-state solution the side boundaries are treated as inviscid walls and a farfield condition is prescribed at the end wall boundary. The farfield condition is specified as an equilibrium mixture of combustion products at the desired chamber pressure. During the unsteady computations with acoustic excitation the side and end boundaries are specified as near field boundaries and modified to impose a transverse acosutic disturbance. The imposed transverse disturance and excitation method are described in Section 6.1.2.

The injection conditions and mass flow rates for both the pressure and velocity excitation cases are specified to match the 60 bar ROF 6 experimental operating point previously defined in Section 3.2.1.

6.1.2 Excitation Method

The single injector models are acoustically excited by modulating the boundary conditions at the sides of the numerical domain to impose the desired disturbance. The disturbance is imposed as a dynamic fluctuation about the steady-state solution:

$$p = \bar{p} + p' \tag{6.1}$$

where $\bar{p}$ is the steady-state pressure distribution and p' is the dynamic acoustic disturbance.

The steady-state solution is computed to determine the initial flow field for the unsteady computations. During the steady-state computation the side boundaries of the "chamber" volume are treated as inviscid walls. The inviscid wall boundary condition ensures there is no mass flow or velocity normal to the side boundaries and that the flame is contained within the numerical domain. A farfield boundary condition is also prescribed to the end boundary of the box, opposite the injection plane, with a defined mixture which is used to control the pressure within the numerical domain. The steady-state solution at the side and end boundary surfaces is stored as the mean solution upon which the dynamic fluctuations are imposed.

To acoustically excite the model a disturbance is imposed at the side and end boundaries which are prescribed as near-field boundaries. The near-field boundary is analogous to the farfield boundary condition where the flux across the boundary is determined based on the difference between the internal flow state and the specified near-field state. The near-field boundary is used to represent an internal fluid boundary rather than a physical wall. The near field boundary is defined by specifying the mixture properties at every point on the boundary surface. This functionality allows a distribution of properties along the boundary surface to be imposed. To impose a disturbance the desired dynamic fluctuation is added to the steady-state solution and imposed at all near-field boundaries. The state of the near-field boundary is updated after each physical time step in the unsteady computation. As the local internal flow field state adapts to the specified near-field distribution the acoustic disturbance is imposed upon the numerical domain.

The steady-state solution at the near field boundaries is modified to match the desired pressure and velocity acoustic disturbances assuming isentropic expansion and compression of the gaseous mixture. The near field condition is prescribed by specifying the mixture composition, temperature, velocity, and density. The gas constant and ratio of specific heats of the mixture at the boundary is known from the initial steady-state solution. As the boundaries are in locations with only warm combustion products, the state of the near field boundaries consists of a mixture of ideal gases. The desired pressure disturbance is first specified. The required density is then determined via the isentropic relation for ideal gases.

$$\frac{p}{\rho^{\gamma}} = \text{Constant} = \frac{\bar{p} + p'}{(\bar{\rho} + \rho')^{\gamma}} \tag{6.2}$$

where $\bar{\rho}$ is the steady-state density of the mixture, ρ' is the resulting density disturbance, and γ is the ratio of specific heats for the mixture.

The temperature of the disturbed near field boundary state is then computed using the ideal gas equation of state. The mixture composition of the steady-state solution is assumed. The steady-state solution mixture at the boundary is predominantly the equilibrium combustion products consisting of approximately 33% Hydrogen and 67% water by mass. In the current work the mass fractions of each species in the mixture is kept constant. In the future this method may be improved by computing the resulting equilibrium mixture as the state of the fluid at the boundary varies during the unsteady computations.

The near-field boundaries were chosen due to the relative ease of implementation with existing numerical tools. However, there are a number of consequences to this approach. In the BKH experiment the primary flame zone is surrounded by secondary hydrogen injection and the bulk chamber ROF is significantly lower than that of the primary injection elements. The flow that is interacting with the central injection element most likely comes from the surrounding coaxial elements. However at high amplitudes the hydrogen rich secondary flow may also mix with the central flame element. The varying mixture of species interacting with the flame is not captured using the near-field boundary excitation method.

The unexcited near-field state imposes the steady-state solution at the boundaries of the domain. As the steady-state solution was computed with inviscid walls, the unexcited near field boundaries produces the same flow field with no flow normal to the side boundaries. As the near field state is modified to acoustically excite the model, the difference in the internal and near field fluid state produces a mass flux across the boundary. The mass entering the domain across the boundary has the specified mixture properties of the near field boundary. Mass exiting the domain may have a different mixture composition and properties based on the local internal fluid state at the boundary.

Therefore a significant limitation of the current approach is that the flow entering the domain during the pressure peak of the acoustic cycle is not the same as the flow leaving the domain during the low pressure part of the acoustic cycle. Flow leaving the numerical domain across the near field boundaries is replaced with a fluid with the steady-state solution mixture composition. The single injector model is therefore more representative of a single isolated element in a chamber full of combustion products. As most of the heat release occurs near the injection plane and the dimensions of the domain have been chosen to ensure the flame does not come into direct contact with the near-field boundaries this limitation does not affect the main results and conclusions of the current work. However the influence of neighbouring jet interaction are also not included in the current model.

The acoustic properties of the employed boundary conditions should also be considered. The mass-flow boundary conditions prescribed at the inlet of the numerical domains are acoustically reflective. This is understood to be not perfectly representative of the physical system in which some acoustic transmission across the boundary would be better represented by an acoustic admittance. However, the high pressure drop between the propellant manifolds and injection plane serves to decouple the system and is therefore reasonably approximated by the mass-flow boundary condition. This boundary condition prescribes a constant propellant flow rate into the numerical domain.

In the current work the near-field boundary conditions were updated after each physical time step of 5×10^{-6} s. This meant that the boundary conditions were updated at least 45 times per acoustic cycle at the highest frequency considered. The near-field boundaries absorb incoming acoustic disturbances with negligible reflection as the flowfield adapts to the near-field state. This time step and update period were found to produce continuous acoustic disturbances at the frequencies of interest as desired. The acoustic condition within the representative chamber volume of the model is therefore completely specified by the disturbance imposed at the near-field boundaries.

Acoustic pressure forcing is used to study the response of the flame to 1L mode excitation of the BKH combustor. A uniform pressure disturbance is imposed across the outer side and end boundaries of the 2D axisymmetric domain at a frequency of 3400 Hz. In the present work four amplitudes of the disturbance were studied. The disturbance is imposed as a harmonic fluctuation at the excitation frequency f with amplitude A.

$$p' = A\,\mathrm{e}^{i2\pi ft} \tag{6.3}$$

Transverse velocity forcing is used to study the response of the flame to 1T-mode excitation of BKH. During 1T-mode excitation the central study element is positioned in a pressure node and velocity antinode. A representative transverse velocity disturbance is imposed on the near field boundaries in an approach similar to that used by Rey et al. [112]. The transverse pressure disturbance is prescribed as a function of the vertical coordinate of the domain, y, the height of the BKH chamber, H=200 mm, and the desired amplitude of the disturbance at the chamber wall, $|p'_{Wall}|$.

$$p' = |p'_{Wall}| sin\left(\frac{y\pi}{H}\right)\mathrm{e}^{i\omega t} \tag{6.4}$$

where t is the time of the unsteady computation and $\omega = 2\pi f$ is the angular excitation frequency.

The transverse velocity disturbance is computed to match the imposed pressure disturbance. Equation 6.4 is substituted into Equation 4.8 to give:

$$\begin{aligned} v' &= \frac{i}{\rho\omega}\nabla\hat{P}\,\mathrm{e}^{i\omega t} \\ &= \frac{i}{\rho\omega}\nabla\left(|p'_{Wall}|sin\left(\frac{y\pi}{H}\right)\right)\mathrm{e}^{i\omega t} \\ v' &= \frac{|p'_{Wall}|}{2\rho f H}cos\left(\frac{y\pi}{H}\right)\mathrm{e}^{i(\omega t+\pi/2)} \end{aligned} \tag{6.5}$$

The mean value of density from the steady-state solution (2.71 kg/m^3) is used for the calculation of the velocity disturbance in the current work.

6.1.3 Mesh

The meshes used for the unsteady computations are shown in Figures 6.1.3 and 6.1.4. Both meshes are unstructured and use a combination of quadrilateral and tetrahedral elements. The quadrilateral elements are used to generate prismatic boundary layers to resolve the flow at viscous wall boundary surfaces. Tetrahedral elements were used for other boundary surfaces representing internal fluid boundaries and to fill the remainder of the numerical domain. The meshes are refined in the shear layer with the size of the mesh elements gradually increasing away from this region.

The 2D axisymmetric mesh used to study pressure excitation is shown in Figure 6.1.3. The 2D axisymmetric computations were relatively inexpensive and a refined mesh with approximately 160,000 nodes was used. The size of mesh elements varied from a minimum size of 0.03 mm in the shear layer, to a maximum element size of 0.5 mm downstream.

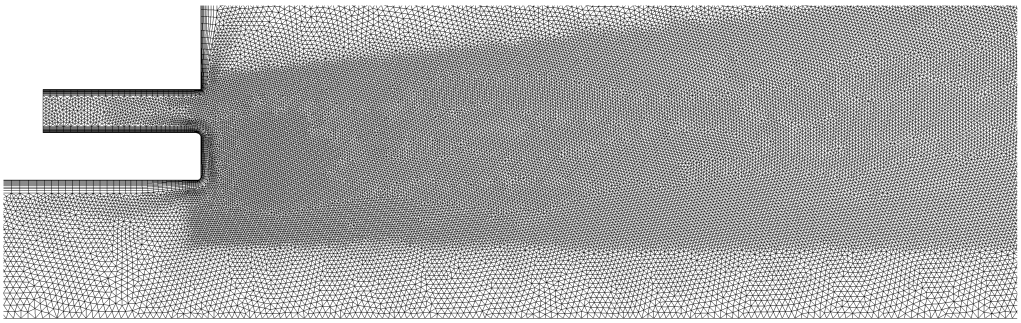

Figure 6.1.3: Near injector region of 2D axisymmetric mesh used for acoustic pressure excitation computations.

The 3D mesh used to study transverse velocity excitation is shown in Figure 6.1.4. The unstructured 3D mesh used approximately 590,000 nodes to fill the half injector domain. The mesh was locally refined in the center of the domain to resolve the shear layer and LOx core. The smallest element size was 0.08 mm in the shear layer at the post tip. A stretching factor of 1.2 was defined to increase the size of the mesh away from the central combustion region with the largest elements having a size of 2 mm at the outer side and end boundaries of the domain.

To reduce the computational cost the 3D mesh is not as refined as the 2D axisymmetric mesh. The 2D axisymmetric mesh therefore had a higher resolution of the shear layer near the injection plane. However, the same flame structure and approximate length, accounting for the difference in the shape of the numerical domain, is produced on both

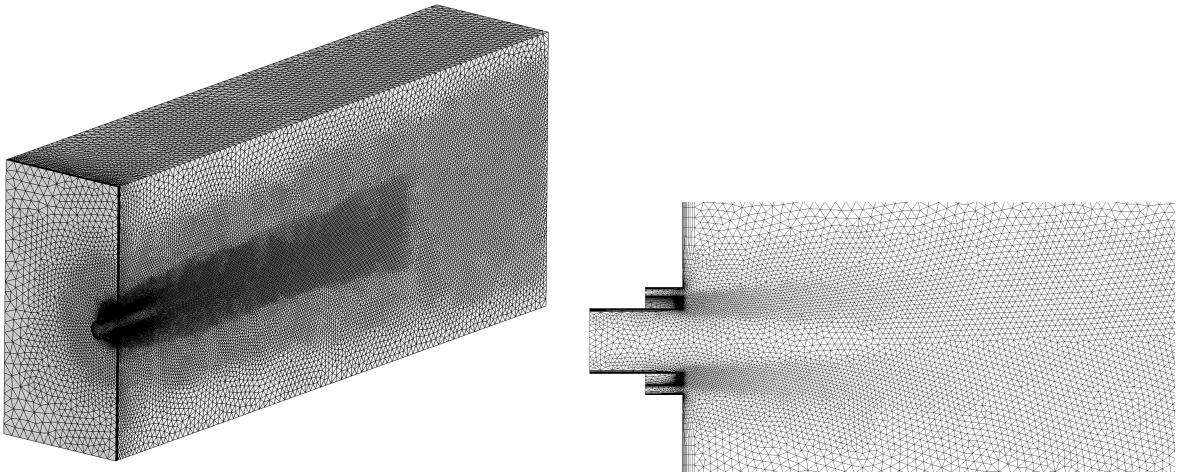

(a) Domain (b) Near injector region

Figure 6.1.4: 3D mesh used for transverse acoustic velocity excitation computations.

meshes. Further mesh refinement did not affect the LOx core length or flame distribution of the steady-state solution. The mesh quality was evaluated and both meshes had maximum aspect-ratio values less than 80. The final mesh of the 3D numerical domain, while coarser than that employed for the 2D axisymmetric domain, was chosen as a compromise in order to produce results in a reasonable period of time.

6.2 Pressure Excitation Results

Pressure excitation of the 2D axisymmetric single injector domain was used to study the response of a BKH injection element to 1L-mode excitation. In the current work a uniform pressure disturbance at the external boundary of the chamber volume in the axisymmetric domain was imposed using the excitation method described in Section 6.1.2. The computation was commenced by imposing the disturbance upon a converged steady-state solution.

In this section the steady-state solution on the 2D axisymmetric domain is first presented. The results with acoustic pressure excitation are then presented and discussed. The excited results are compared with observations from BKH experimental optical data from periods of 1L-mode excitation.

6.2.1 2D Steady-State Results

A steady-state RANS solution was computed on the 2D axisymmetric domain to use as a initial solution for the excited computations. The 2D axisymmetric RANS solution required only approximately 1,700 CPU hours to compute using one 16 core AMD opteron 6274 processor.

The pressure distribution of the steady-state model is shown in Figure 6.2.1. The pressure in the chamber volume is 60.7 bar and is controlled by the pressure specified at the farfield boundary at the end of the domain. A 20 bar pressure drop between the oxygen injection manifold and the chamber occurs over the throttle section of the LOx post. The pressure in the narrower section of the throttle is lower as the flow accelerates before decelerating when entering the larger diameter of the LOx post. The pressure equalizes with the pressure in the chamber volume shortly after the throttle section with only a small pressure gradient along the length of the LOx post.

Figure 6.2.2 shows the property distributions along the axisymmetry axis. As previously noted the pressure decreases in the throttle section of the model as the flow accelerates. It then quickly equalizes along the length of the post. Spurious pressure fluctuations occur

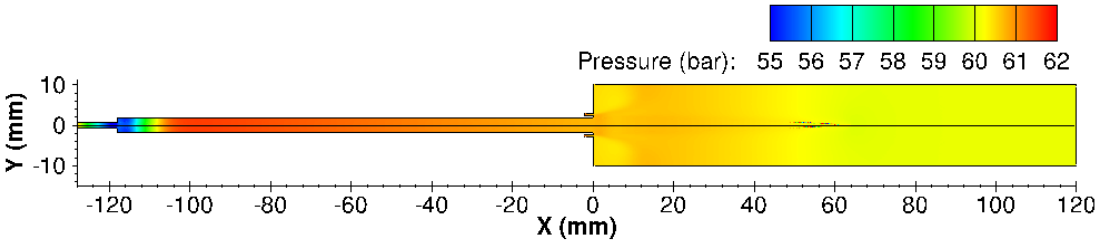

Figure 6.2.1: steady-state pressure distribution computed for 2D axisymmetric single injector model mirrored about axisymmetry axis.

at the exit of the throttle section and at the end of the LOx jet in the chamber volume. The spurious pressure fluctuations are attributed to an issue with the implementation of the real gas model. These fluctuations were not remedied in the current work but could not be shown to significantly impact the results and conclusions made in this thesis.

The dense LOx propagates into the center of the chamber domain and the density begins to gradually decrease from 0 to 60 mm after the injection plane due to heating of the liquid core by combustion processes. The density rapidly decreases at the end of the jet as combustion occurs which is also marked by a steep rise in the temperature.

The axial (X-direction) velocity decreases after the throttle section and remains constant along the length of the post with a final injection velocity at the axisymmetry axis of approximately 17m/s. The velocity in the LOx jet as it propagates into the domain increases slightly along the length of the jet. After combustion the axial velocity increases as the lighter gaseous flow accelerates towards the end of the domain.

Figure 6.2.3 shows the distribution of various properties in the chamber volume of the 2D axisymmetric domain. The density distribution shows the dense oxygen core propagating into the domain with a length of approximately 64 mm. The OH mass fraction distribution indicates the combustion zone between the oxygen and hydrogen streams and surrounds the oxygen core. The temperature distribution shows that a small recirculation zone with relatively cool hydrogen exists at the outer corner of the injection plane. Downstream the temperature is uniform and close to the adiabatic flame temperature for the equilibrium mixture of oxygen-hydrogen combustion products.

The heat release distribution shown in Figure 6.2.3d shows that the majority of the heat release is concentrated in the shear layer near the injection plane. The heat release distribution corresponds closely to the OH distribution shown in Figure 6.2.4b. Downstream the heat release becomes negligible as chemical equilibrium is reached once the oxygen is depleted.

Figure 6.2.4 shows the distributions of OH mass fraction and heat release near the injection plane. The flame is anchored on the outer edge of the oxygen post between the oxygen and hydrogen streams. The regions of maximum heat release occur in the shear layer near the injection plane. The heat release distribution surrounds the peak OH mass fraction distribution. The gap in the middle of the heat release distribution is caused by the dissociation of water at high temperatures which occurs primarily in the hottest region in the center of the flame.

The 2D axisymmetric steady-state single injector results provide insight into how the assumptions in this model affect the flow field. The 2D axisymmetric domain is used to represent the central injector in the BKH experiment and the results can be compared with the steady-state chamber model presented in Chapter 3. The 2D axisymmetric model produces a shorter flame and lower axial velocity than the 3D chamber model. The shorter flame is partially due to the central oxygen stream not being surrounded by other injection elements as in the penta-injector matrix pattern employed in the experiments. The steady-state model results provide a reference for the structure and features of the

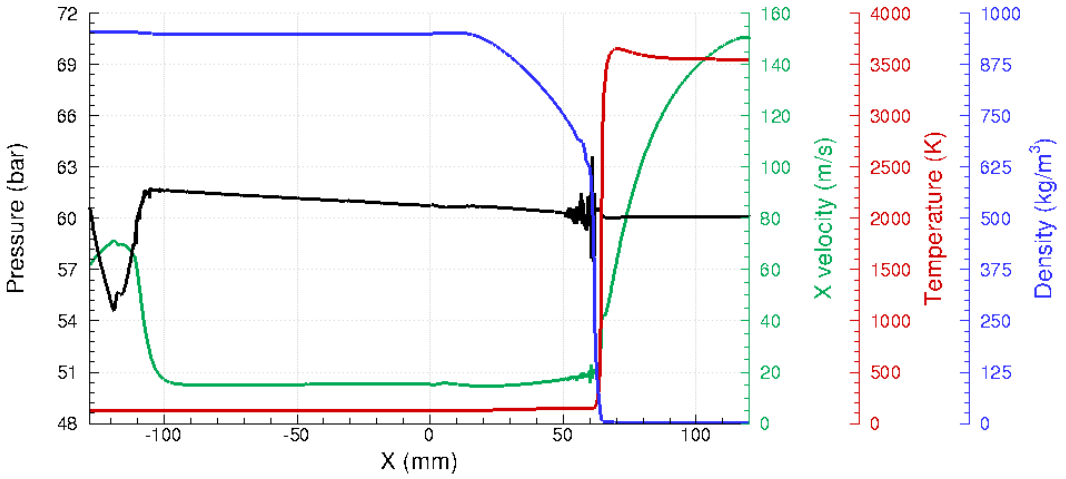

Figure 6.2.2: Distributions along axisymmetry axis of steady-state 2D axisymmetric single injector model.

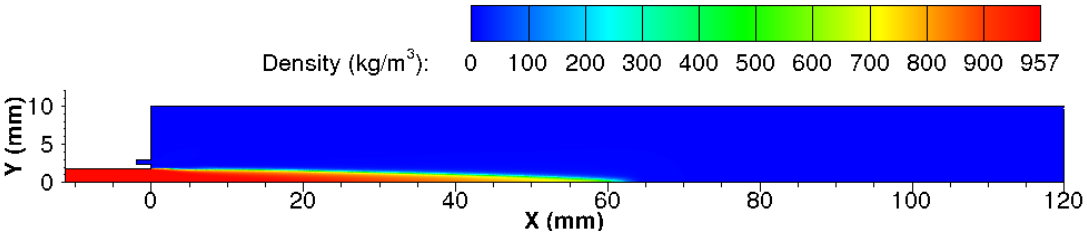

(a) Density distribution

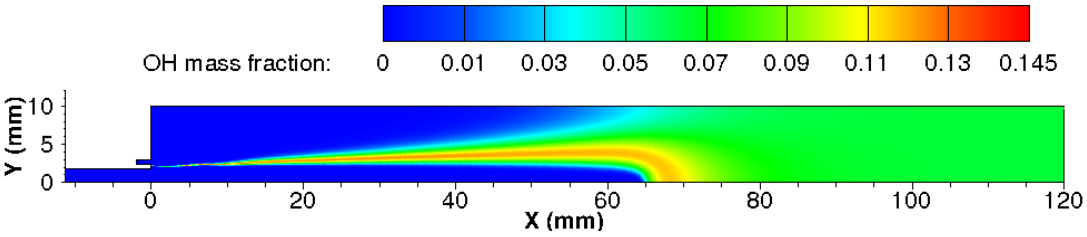

(b) OH distribution

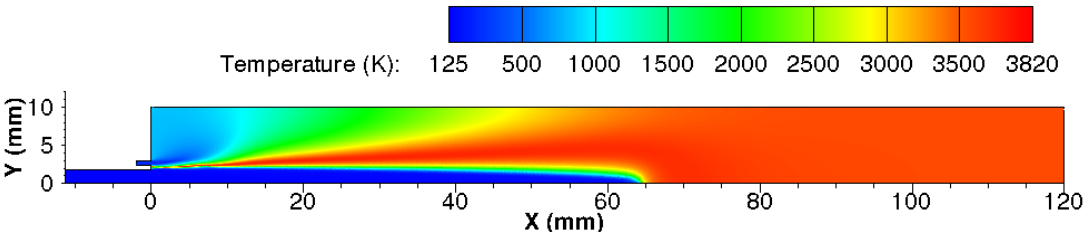

(c) Temperature distribution

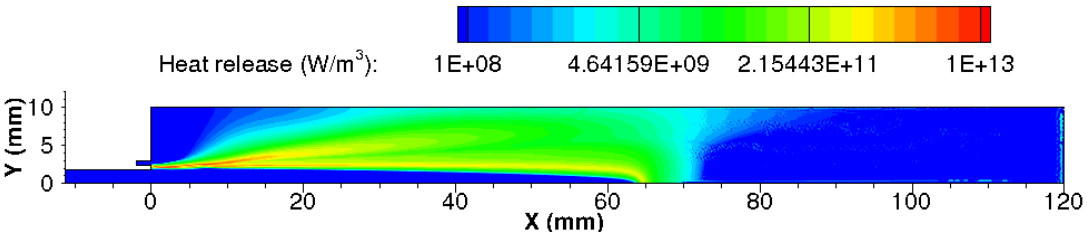

(d) Heat release distribution

Figure 6.2.3: Distributions in chamber volume of steady-state 2D axisymmetric single injector model.

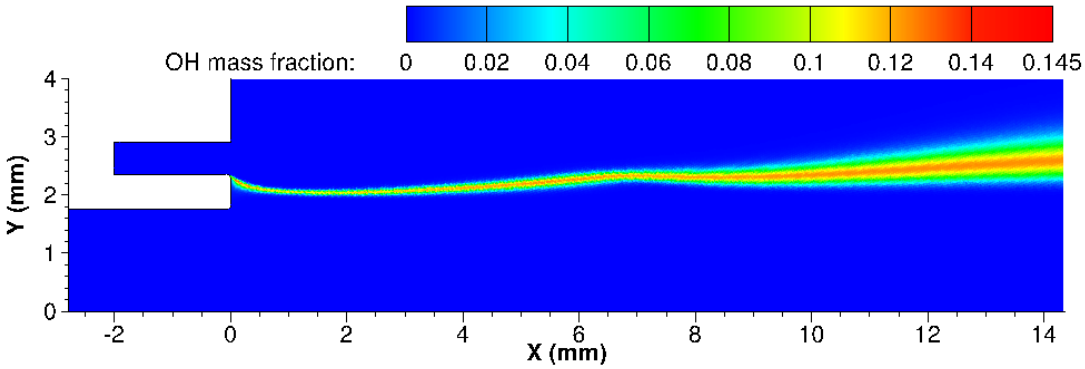

(a) OH distribution

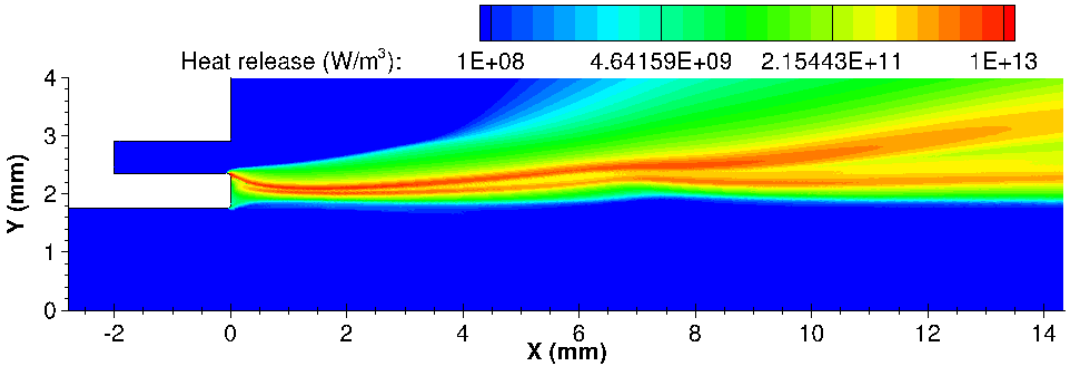

(b) heat release distribution

Figure 6.2.4: OH and heat release distributions near injection plane.

flame without acoustic excitation. Despite the identified differences to the chamber model, the 2D axisymmetric model is used as a qualitative representation of the central BKH injection element and resulting flame.

6.2.2 Excited Results

The steady-state 2D axisymmetric model was subjected to a uniform pressure disturbance during an unsteady computation using the excitation method described in Section 6.1.2. In the current work the response to the uniform pressure excitation at a frequency of 3400 Hz was studied. The 3400 Hz frequency was chosen as it is close to the BKH 1L chamber frequency (3300Hz), and also close to the first longitudinal mode frequency of the oxygen post (3425 Hz). Four levels of acoustic pressure amplitude were investigated corresponding to 2.5, 5, 7.5 and 10% P_{CC} acoustic pressure amplitudes.

Figure 6.2.5 shows the pressure fluctuations from an acoustically forced computation with a pressure amplitude of 3 bar (5 % P_{CC}) in the chamber volume at various points along the axisymmetry axis of the 2D domain. The injection plane is located at an axial coordinate of X=0 mm. Figure 6.2.5a shows that the fluctuations at the injection plane and in the chamber volume (X≥0 mm) have a constant amplitude once excitation has been applied. This shows that the excitation boundary conditions impose a uniform pressure disturbance over the chamber volume at the desired frequency. The pressure fluctuations at the upstream locations in the LOx post (X<0 mm) have a higher amplitude disturbance with significant amplitude variation over the first 0.01 seconds of the unsteady computation. After this period the fluctuations in the oxygen post reach relatively constant amplitudes. The amplitude of the fluctuations in the post are higher than the imposed acoustic disturbance, indicating an internal resonance.

Figure 6.2.5b shows the pressure fluctuations at various axial locations after 0.011s which is sufficiently long that a steady amplitude of the acoustic fluctuations has been

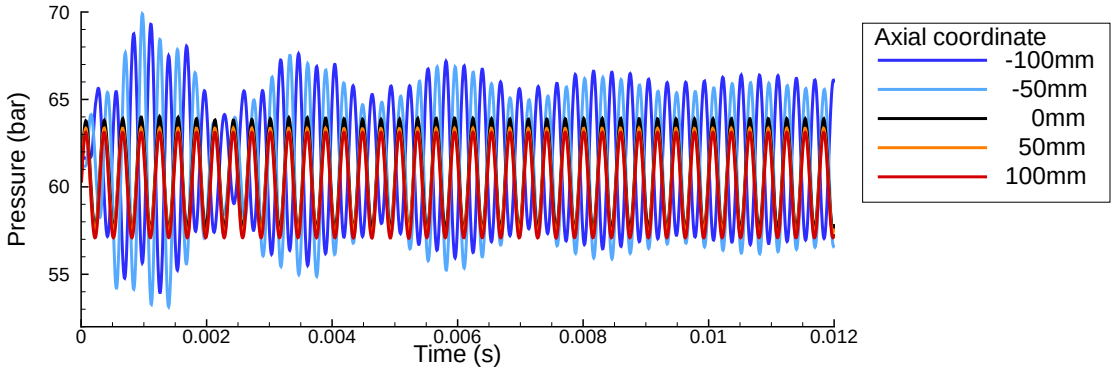

(a) Entire calculation

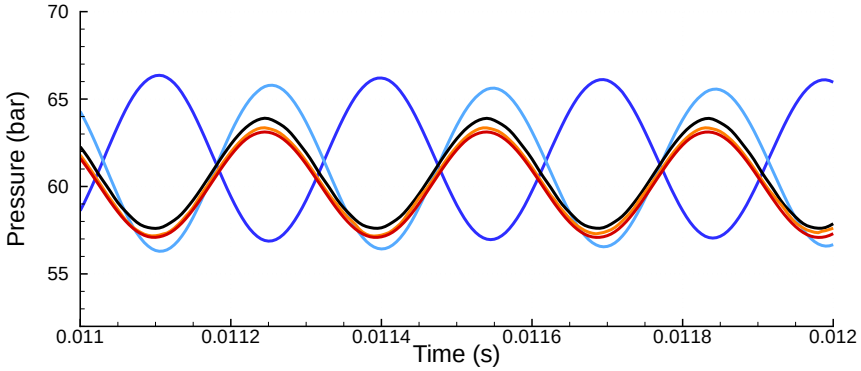

(b) after 0.011s

Figure 6.2.5: Fluctuation of pressure at various locations along axisymmetry axis versus time for 5% P_{CC} pressure amplitude computation.

reached. The pressure fluctuations at the injection plane and in the chamber volume are in phase and have the same amplitude as the imposed disturbance. The upstream fluctuations in the post have higher amplitudes than the fluctuations in the chamber. As the disturbances at -100 and -50 mm are out of phase it is clear that a resonance in the form of a longitudinal mode is being excited in the LOx post.

Figure 6.2.6 shows the axial distributions of properties along the axisymmetry axis from two different periods of the acoustic cycle and are comparable to the steady-state distribution shown in Figure 6.2.2. The pressure in the chamber volume (X>0) is relatively constant and matches the imposed pressure disturbance. The upstream pressure distribution in the LOx post (X<0) shows a longitudinal mode pressure distribution. This distribution has a pressure node at approximately 70 mm before the injection plane and pressure anti-nodes at the oxygen inlet of the oxygen post and 30 mm from the injection plane. The pressure antinode at the inlet is expected as the prescribed mass flow inlet condition reflects the incoming acoustic disturbance. The temperature, axial velocity, and density distributions show that the oxygen core is slightly longer (68 mm) than the steady-state result. Spurious fluctuations in the density distribution along the axisymmetry axis can also be seen in the LOx core (0∼65 mm) after injection.

Figures 6.2.7 and 6.2.8 show the density and OH distributions at different phases of the acoustic cycle from the 5% P_{CC} amplitude computation. The phase is defined so that the peak pressure disturbance in the chamber volume occurs at a phase angle of 0, so that the minimum pressure in the chamber volume occurs at a phase angle of π. This phase definition is consistent with the complex amplitude formulation of the acoustic disturbance employed in Chapters 4 and 5.

The density distributions in Figure 6.2.7 show wave like fluctuations on the surface of the oxygen jet which occur in the shear layer between the oxygen and hydrogen streams. These fluctuations gradually dissipate as they propagate downstream along the surface of the LOx core. The density fluctuations in the shear layer cause only minor fluctuations in

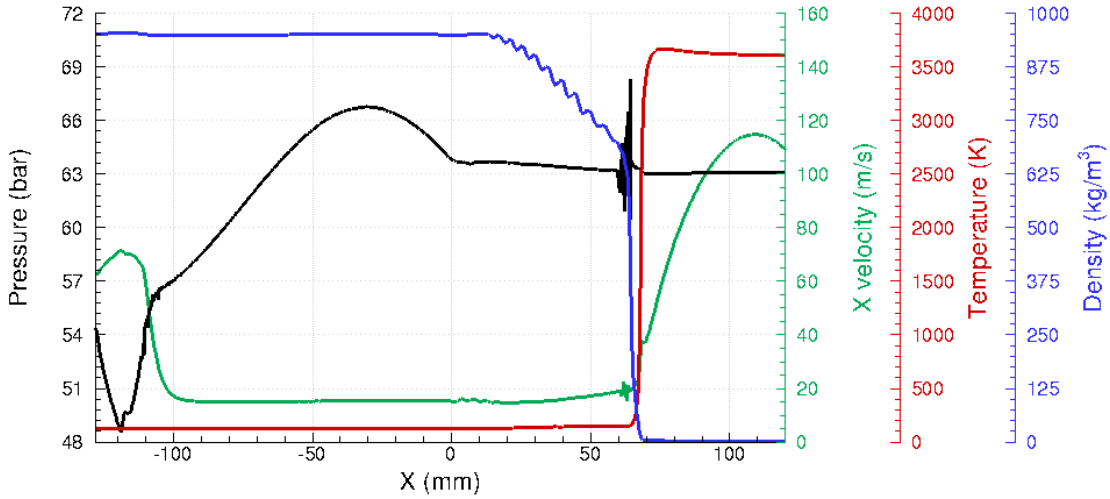

(a) Pressure maximum

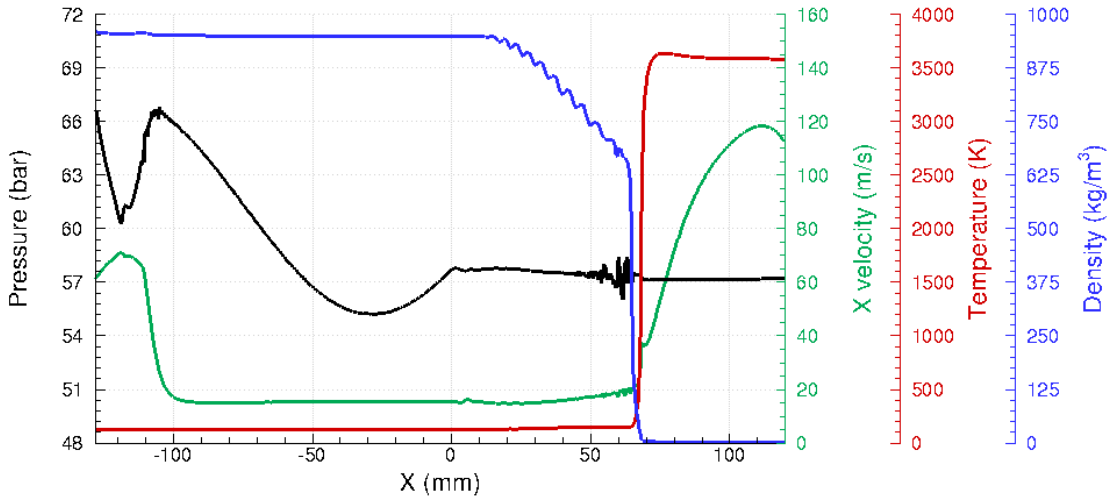

(b) Pressure minimum

Figure 6.2.6: Comparison of axial property distributions along axisymmetry axis at different phases of the acoustic cycle for 5% P_{CC} pressure amplitude computation.

the distribution of other properties. The OH distributions shown in Figure 6.2.8 still closely resemble the steady-state solution with only small fluctuations in the flame distribution observed in the shear layer near the injection plane.

The length of the LOx core is slightly longer than the steady-state solution. The additional length indicates that the excitation method imposes a small flux towards the end of the numerical domain as excitation is imposed. This does not appear to significantly affect the results.

The results of the unsteady computations have been analysed to study the fluctuations in heat release resulting from the imposed acoustic disturbance. The heat release is integrated over the entire domain for each physical time step. As the axisymmetric domain represents only a 1° arc the total integrated result is multiplied by a factor of 360 to represent the total flow through a single injection element. The predicted heat release rate of the single injector model is 1.2 MW. The integrated heat release rate fluctuates at the same frequency as the imposed acoustic disturbance. Like the pressure fluctuations in Figure 6.2.5, after a period of 0.011 s the imposed disturbance produces fluctuations with a relatively constant amplitude throughout the numerical domain.

Figure 6.2.9 compares the pressure, heat release, and injection velocity fluctuations once a steady amplitude has been reached. The heat release fluctuations (red line) lag the

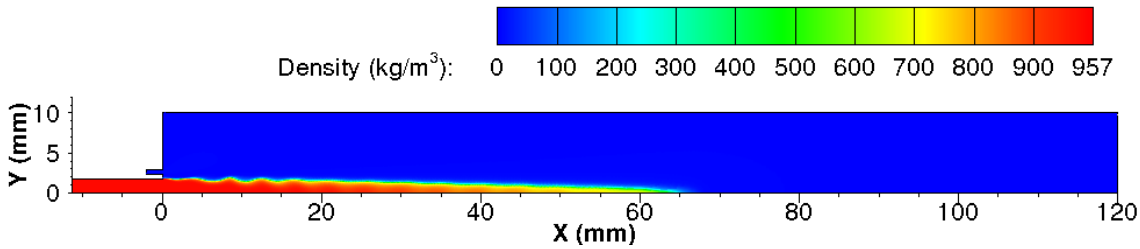

(a) Phase=0

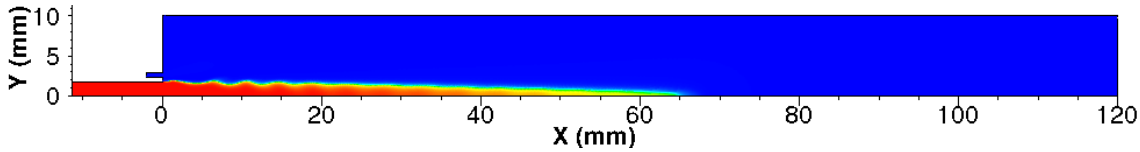

(b) Phase=π

Figure 6.2.7: Density distribution in chamber volume at different phases of the acoustic cycle for 5% P_{CC} pressure amplitude computation.

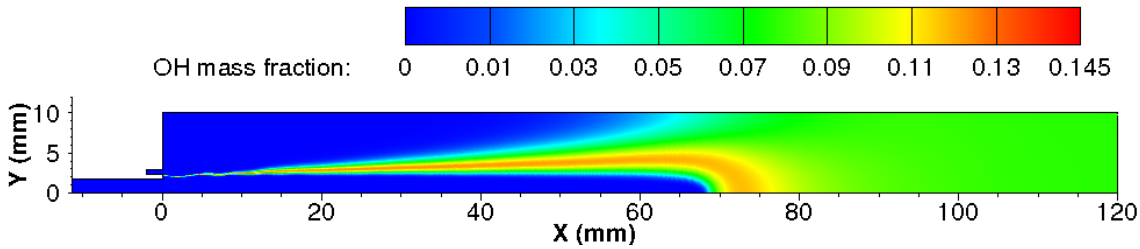

(a) Phase=0

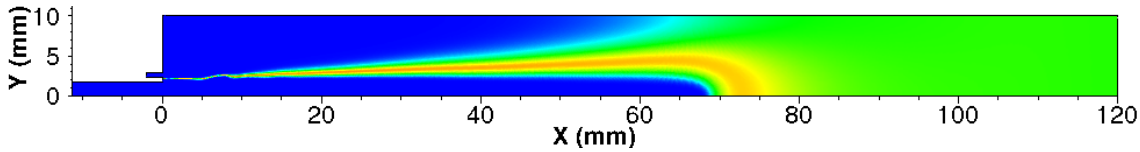

(b) Phase=π

Figure 6.2.8: OH distribution in chamber volume at different phases of the acoustic cycle for 5% P_{CC} pressure amplitude computation.

imposed pressure fluctuations (black line) by approximately one eighth of an acoustic cycle. This phase lag means the heat release fluctuations are almost perfectly out of phase with the fluctutions of the velocity ratio (green line). The velocity ratio is the ratio between the hydrogen (orange line) and oxygen (blue line) injection velocities extracted from the center of the injection element outlet at the injection plane.

The peak hydrogen injection velocity occurs when the local pressure at the injection plane is a minimum and vice versa. Therefore the fluctuations in the hydrogen injection velocity are in phase with the imposed acoustic disturbance. On the other hand the fluctuation in the oxygen injection velocity is not in phase with the hydrogen injection velocity fluctuations or the imposed acoustic disturbance. The phase shift in the response of the oxygen injection velocity is attributed to the internal resonance and admittance of the LOx post. This shift in the phase of the oxygen injection velocity relative to the hydrogen injection velocity is responsible for the fluctuation in the injection velocity ratio. Figure 6.2.9 shows that the velocity ratio fluctuations are in antiphase with the fluctuations of the integrated heat release rate.

Figure 6.2.10 shows the heat release distribution in the numerical domain at different phases of the acoustic cycle. The peak heat release occurs in the shear layer between the coaxial streams and envelopes the dense LOx core. The distributions in Figure 6.2.10

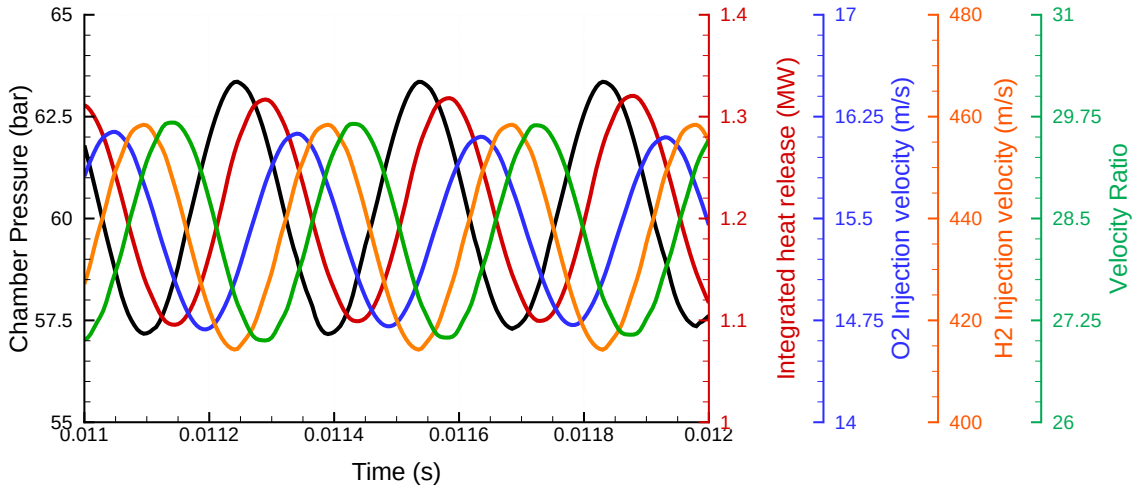

Figure 6.2.9: Comparison of pressure, heat release, and injection velocity fluctuations for 5%P_{CC} pressure amplitude computation.

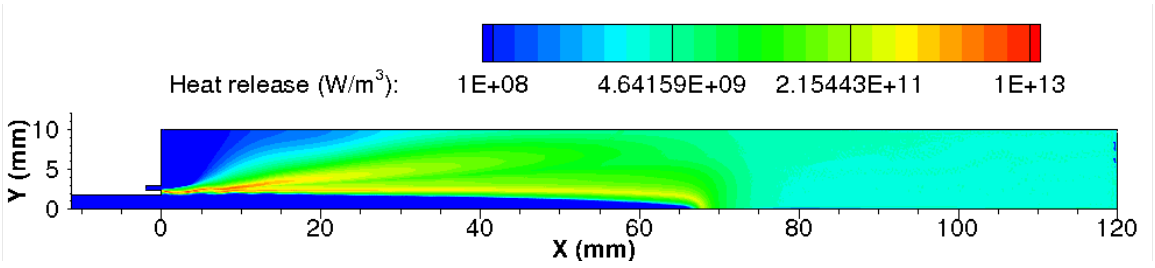

(a) maximum heat release

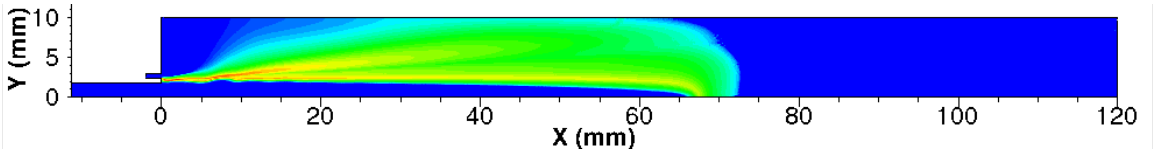

(b) minimum heat release

Figure 6.2.10: Heat release distribution at different phases of the acoustic cycle from the 5% P_{CC} pressure amplitude computation.

show that the heat release is fluctuating downstream. These downstream fluctuations are caused by the changes in the equilibrium mixture as the pressure fluctuates as dictated by the impact of pressure on the finite rate kinetic mechanism. The magnitude of the downstream heat release fluctuation is exaggerated by the logarithmic color scale and is not as significant as the fluctuations near the injection plane.

The heat release fluctuations near the injection plane are shown in more detail in Figure 6.2.11. The maximum heat release occurs in the shear layer that follows the wave like structures on the surface of the LOx core. At the phase of the acoustic cycle with maximum heat release (Figure 6.2.11a) the wave like structures are spaced such that a trough exists directly downstream from the LOx post at $X = 2$ mm. Similarly at the phase of the acoustic cycle with minimum heat release (Figure 6.2.11b) a crest appears in the same position. The heat release distribution also appears generally thicker during the phase of maximum heat release.

The numerical model was excited at the same frequency with four different levels of disturbance amplitudes. The magnitude of the injection velocity ratio fluctuations was found to be proportional to the imposed acoustic disturbance. This in turn meant that the wave like structures produced in the shear layer become more prominent for

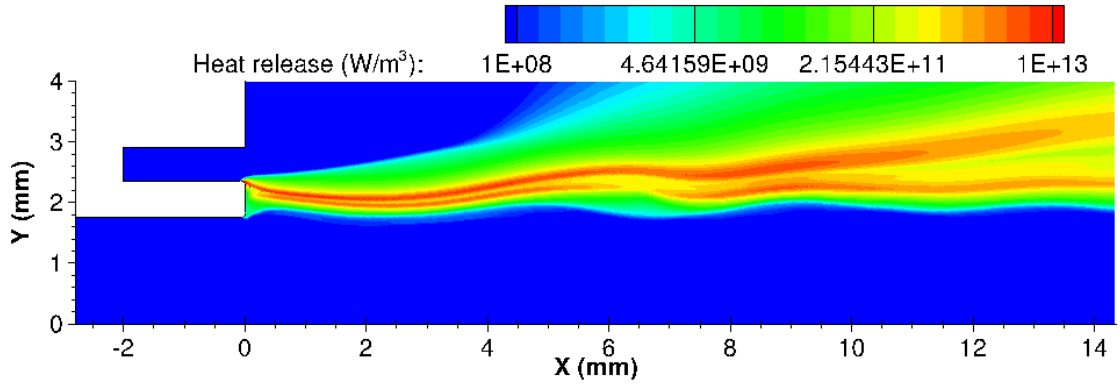

(a) Maximum heat release

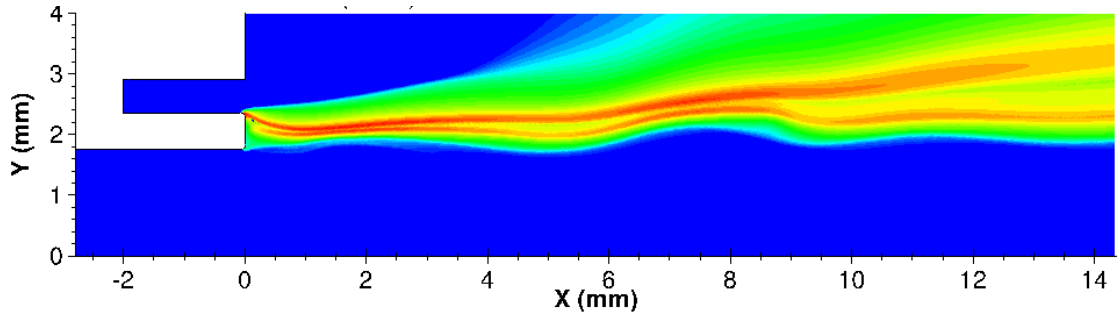

(b) Minimum heat release

Figure 6.2.11: Heat release distributions near the injection plane at different phases of the acoustic cycle from the 5% P_{CC} pressure amplitude computation.

higher amplitude disturbances. Figure 6.2.12 compares the resulting density distributions after a steady amplitude is reached for each imposed acoustic excitation amplitudes investigated numerically. The wave like structures are minor for the lowest amplitude disturbance considered (Figure 6.2.12a). Larger disturbance amplitudes produce larger wave like structures that also propagate further downstream. With a 10% acoustic pressure disturbance amplitude the wave like structures propagatae the entire length of the LOx core and produced periodic shedding at the tip.

The results from the pressure excitation computations with different excitation amplitudes are summarised in Table 6.1. The amplitude of the injection velocity and velocity ratio fluctuations was found to be proportional to the imposed acoustic disturbance. The fluctuations in heat release were found to be approximately double that of the resulting velocity ratio fluctuations.

Table 6.1: Comparison of injection velocity and heat release fluctuations for different amplitudes of acoustic pressure excitation.

Pressure disturbance amplitude (%P_{CC})	Injection velocity amplitude (%*)		Velocity Ratio amplitude (%*)	Heat release amplitude (%*)
	O2	H2		
2.5	2.44	2.54	2.39	4.67
5	4.87	5.01	4.73	9.36
7.5	7.23	7.67	7.12	14.14
10	9.52	10.28	9.52	18.81

* % fluctuation of steady-state solution value.

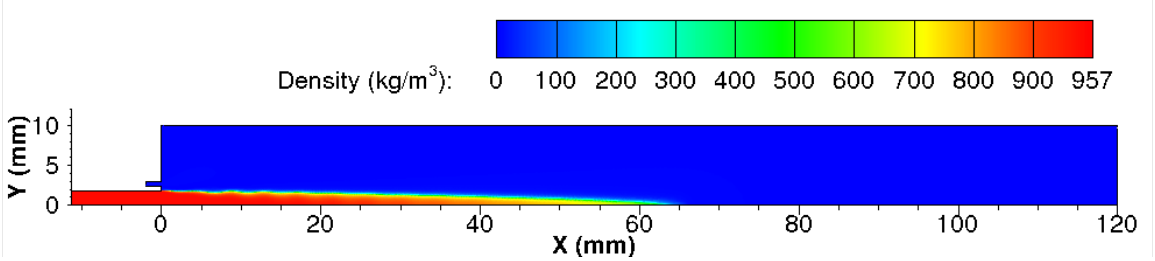

(a) 2.5% P_{CC} amplitude

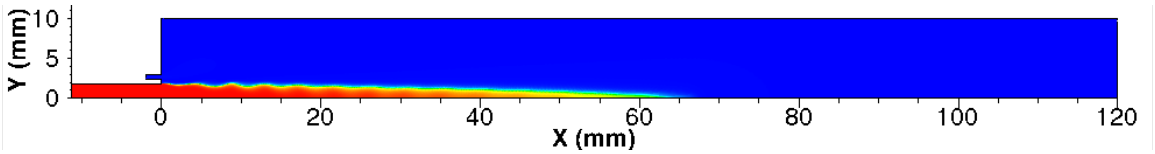

(b) 5% P_{CC} amplitude

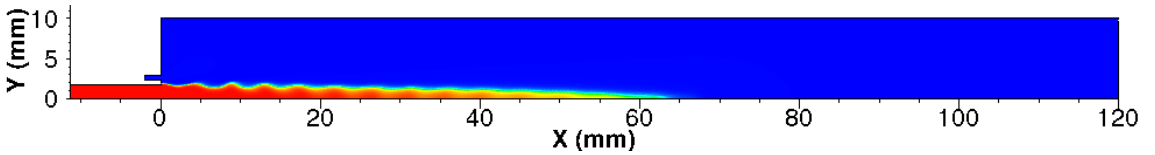

(c) 7.5% P_{CC} amplitude

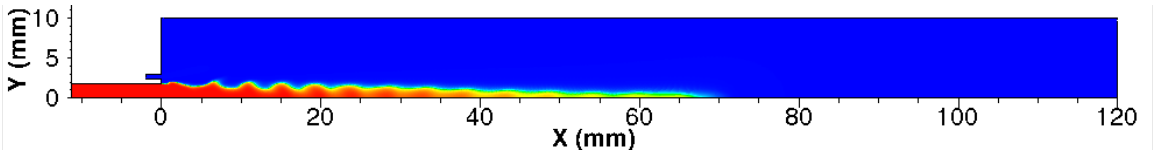

(d) 10% P_{CC} amplitude

Figure 6.2.12: Comparison of density distribution in chamber volume resulting from acoustic pressure excitation with different excitation amplitudes.

6.2.3 Comparison with Experimental Data

The numerical results are compared with BKH optical data samples recorded during 1L-mode excitation and previously analysed in Chapter 5. During 1L-mode excitation the flame fills the window region in BKH and its distribution is not significantly altered by the acoustic disturbance. The DMD analysis of 1L shadowgraph data in Section 5.2.2 identified wave like structures on the surface of the oxygen core. The flame response analysis presented in Section 5.3 identified a 45° phase lag between the local acoustic disturbance and the OH* intensity fluctuations. In this section the results from the pressure excitation computations are post-processed for comparison with the experimental results.

Shadowgraph Imaging

Figure 6.2.13 shows DMD reconstructions of the Test C shadowgraph 1L sample in Table 5.1 at different phases of the acoustic cycle relative to the PCCDYN2 sensor. As previously discussed in Section 5.1 the shadowgraph images capture the surface of the dense oxygen jet which appear white due to combustion light emission. Relatively low amplitudes are reached during 1L mode excitation of BKH and the acoustic disturbance acting upon the flame during the recording is comparable to the 2.5% P_{CC} pressure amplitude computation. Figure 6.2.14 shows plots of the density distribution in the same location from the 2.5% P_{CC} pressure amplitude computation for comparison with the shadowgraph images. The phase of the numerical results is determined based on the phase of the imposed disturbance.

The wave like structures identified on the surface of the LOx core appear in both

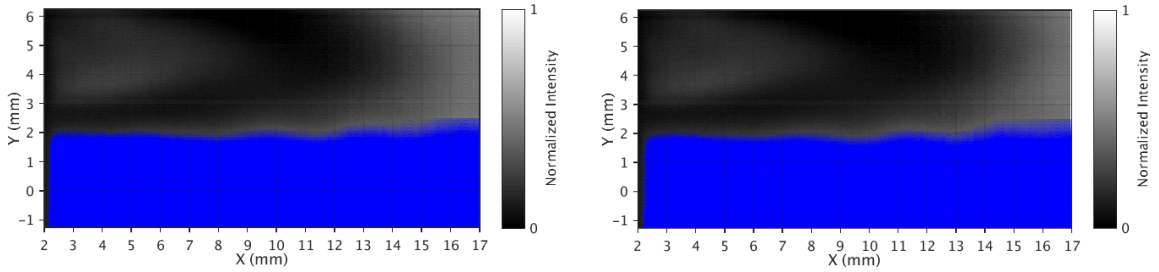

(a) PCCDYN2 Phase = 0 (b) PCCDYN2 Phase = π

Figure 6.2.13: Reconstructed shadowgraph images using DMD modes at excitation and overtone frequency at different phases of the acoustic cycle from Test C shadowgraph 1L sample in Table 5.1. LOx core highlighted in blue.

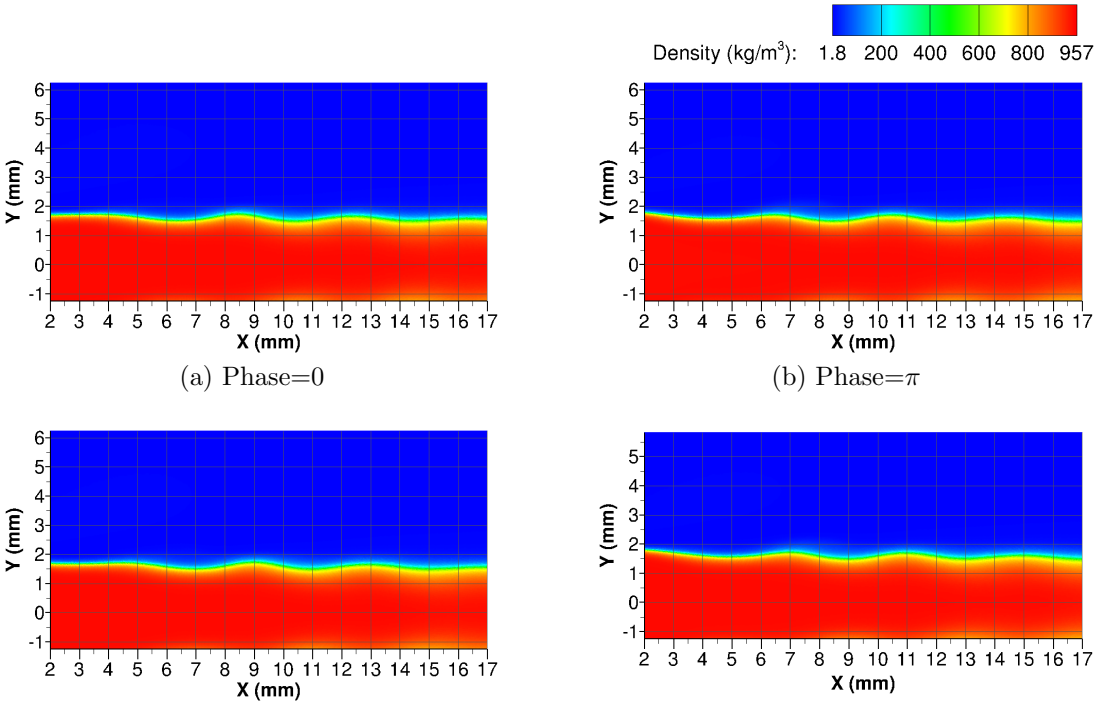

(a) Phase=0 (b) Phase=π

(c) Phase=$\pi/4$ (d) Phase=$5\pi/4$

Figure 6.2.14: Density distribution at same location Test C 1L shadowgraph images at different phases of the acoustic cycle for 1.5 bar pressure amplitude computation.

experimental and numerical results shown in figures 6.2.13 and 6.2.14, respectively. The spacing between the crest and trough of each wave in the numerical results match the spacing of the wave-like structures seen in the experimental images. The axial position of the waves do not coincide at the same phase angles in the experimental and numerical results. The difference in the axial positions may be due to the phase definition, as the acoustic reconstruction results presented in Chapter 4 showed that local acoustic disturbance in the window region led the disturbance at the PCCDYN2 position. Taking this phase difference into account (Figures 6.2.14c & 6.2.14d) the numerical and experimental axial positions of each wave agree well with one another.

OH* imaging

The flame response analysis of the Test A 1L-mode OH* dataset in Section 5.3 identified that the fluctuations in OH* emission occurred within 0∼90° of the peak acoustic pressure disturbance. In addition, the OH* distribution filled the window region and fluctuated uniformly relative to the local acoustic disturbance. As previously discussed in Section 3.3.3, OH* is optically thick and therefore the 2D axisymmetric numerical results cannot

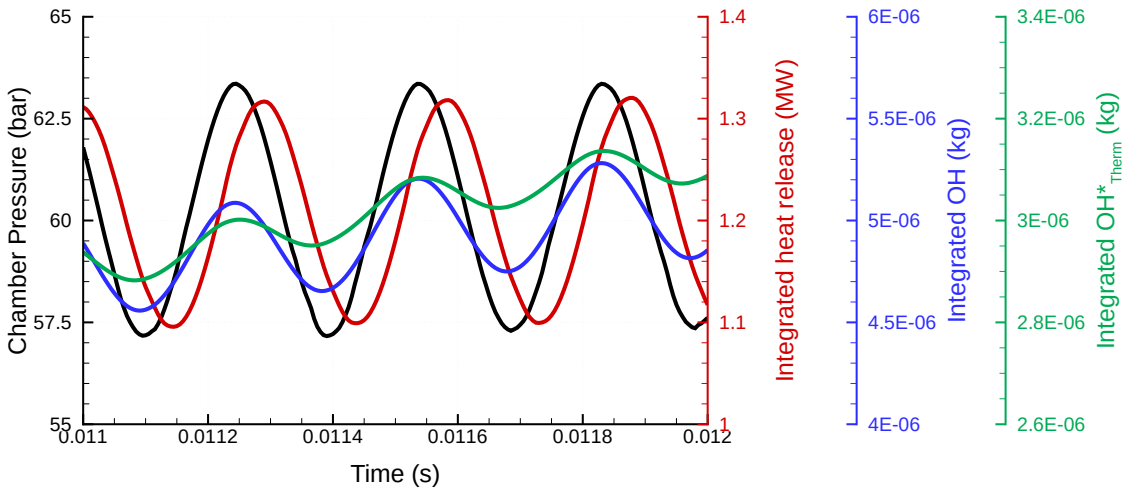

Figure 6.2.15: Comparison of acoustic and volume-integrated values versus time for 5%P_{CC} pressure amplitude computation.

be directly compared with the line-of-sight OH* images. Ray tracing algorithms are needed to post-process the numerical results in order to produce representative line of sight images for comparison.

In this study the integrated mass of OH in the numerical domain is instead considered. The integrated mass of OH is computed by integrating the partial density of OH over the numerical domain. The integrated mass of thermally excited OH* is also computed using the EFRM model suggested by Fiala [23] and described in Section 3.3.3. The concentration of thermally excited OH* is computed using Equation 3.23, converted to a density value by multiplying by the molecular weight, and integrated over the numerical domain. Figure 6.2.15 compares the pressure, integrated heat release, integrated mass of OH, and integrated mass of thermally excited OH* versus time for the 5% P_{CC} amplitude computation.

The total mass of OH and thermally excited OH in the numerical domain exhibit fluctuations at the excitation frequency. Other irregular low frequency fluctuations occur which are attributed to the downstream breakup and shedding of the LOx core. The fluctuations at the excitation frequency of both OH and thermally excited OH are perfectly in phase with the imposed acoustic pressure disturbance. As the kinetic time scales are orders of magnitude smaller than the period of the imposed acoustic disturbance the mixture composition quickly adapts to the imposed acoustic disturbance.

The OH and OH*$_{Therm}$ fluctuations do not occur in phase with the heat release fluctuations which lag the pressure disturbance by a phase of 45°. The experimental results indicated a phase difference between the peak local pressure disturbance and OH* intensity of 0∼90° . While the numerical results agree with the flame response analysis of BKH optical data presented in Chapter 5, it also suggests that additional OH* emission may occur during the period of peak heat release. Further post processing and understanding of OH* emission may be necessary to produce a better comparison. Ray tracing algorithms and full 3D solutions would make the numerical results more readily comparable.

6.2.4 Discussion

The pressure excitation results have provided further insight into the response of a liquid oxygen/gaseous hydrogen coaxial injector to acoustic forcing. Important phenomena, like the internal resonance in the LOx post and the deformation of the oxygen core have been reproduced by the numerical model. The model predicted that the fluctuations in heat

release occur shortly after the peak pressure disturbance and out of phase with velocity ratio fluctuations at the injection plane. The significance and implications of these results are discussed here.

The internal resonance of the LOx post is driven by the acoustic forcing at the chamber and the acoustically reflecting mass flow boundary condition at the inlet of the LOx post. As previously described, this boundary condition is believed to be representative of the physical environment as the pressure drop across the throttle section of the LOx post would produce a similar acoustic response to downstream disturbances. However an assumption of this boundary condition is that the mass flow rate into the numerical domain is constant despite the imposed acoustic disturbance.

The mass-flow boundary condition also prescribes a constant mass flow of fuel through the injector. Due to the high speed and compressibility of the hydrogen gas as it is injected, the fuel flow is expected to respond immediately to the imposed acoustic disturbance. However this means that any internal injector resonance on the fuel side of the injection system is not captured in the current model.

The observation of the similar wave like structures on the surface of the LOx core, resulting from the internal injector resonance both experimentally and numerically, further support the internal injector resonance and results of the numerical model. Similar acoustic coupling between the LOx post and chamber has been identified experimentally by Gröning et al. [34] and reproduced numerically by Urbano et al. [153] who investigated the naturally occurring combustion instability in BKD.

The agreement between the phase of the injection velocity ratio and heat release fluctuations suggest that the fluctuations are related. However it is unreasonable to assume that heat release fluctuations are a direct consequence of the local velocity fluctuations at the injection plane. More likely the fluctuation in velocity ratio leads to similar fluctuations in the shear layer and mixing between the oxygen and hydrogen streams that then propagates downstream. These structures may produce additional fluctuation of the heat release as the surface at which the oxygen and hydrogen streams meet is deformed. The heat release is reduced behind the crests of the wave like structures. The maximum heat release occurs when a trough between wave like structures is positioned immediately after the LOx post tip and the oxygen and hydrogen streams first meet as parallel flows. Similarly, the minimum heat release occurs when a crest is positioned to deflect hydrogen away from the LOx core.

Each unsteady 2D axisymmetric computation required approximately 6000 total CPU hours on one 16 core AMD opteron 6274 processors to compute 1000 time steps, or 17 acoustic cycles. The study of different excitation amplitudes showed that the heat release amplitude increased linearly with the velocity ratio fluctuations. As listed in Table 6.1 the velocity ratio fluctuations were proportional to the imposed pressure disturbance, but the heat release fluctuations were almost twice as large. The linear response and observed gain may be used to design response functions to represent the injector response to acoustic pressure fluctuations in low order modelling approaches.

6.3 Velocity Excitation Results

The single injector model was used to investigate the response of coaxial BKH injection elements to an imposed velocity disturbance representative of the local acoustic disturbance acting upon the flame zone during 1T-mode excitation of BKH. The 3D numerical domain with vertical symmetry normal to the imposed disturbance was used to capture the deformation and flattening of the LOx core and flame as acoustic excitation is imposed. Like the pressure excitation method presented in the previous section, a converged steady-state solution was first computed to produce an initial solution which was then subjected

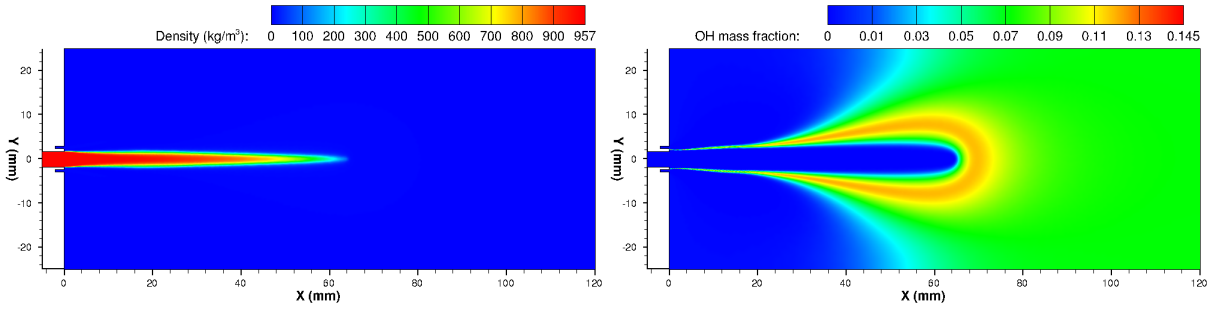

(a) Density distribution (b) OH distribution

Figure 6.3.1: Steady-state solution distributions for the 3D numerical domain.

to acoustic forcing. To impose a transverse velocity disturbance a pressure gradient and acoustic velocity fluctuation is imposed across the numerical domain using the excitation method described in Section 6.1.2.

The steady-state solution on the 3D numerical domain is first presented before the results with transverse acoustic excitation. The transverse velocity is shown to deform the flame and transport the lighter gaseous outer layer of the LOx core. The transverse velocity also accelerates the mixing and breakup of the LOx core causing the flame to retract towards the injection plane. The numerical results are compared with the results from analysis of BKH optical data presented in Chapter 5 of this thesis.

6.3.1 3D Steady-State Results

The steady-state solution results for the 3D numerical domain are very similar to the steady-state solution on the 2D axisymmetric domain. The dense LOx core propagates into the center of the domain and is enveloped by the flame, as indicated by the density and OH mass fraction distributions shown in Figure 6.3.1. The 3D domain required a larger volume to contain the flow than the 2D axisymmetric domain. The larger volume results in larger recirculation zones at the injection plane surrounding the coaxial injection element. The larger volume allows the flow to expand upon entering the volume and does not force the hydrogen and oxygen flows to mix as effectively as the 2D axisymmetric case. The 3D domain therefore produces a flame with a LOx core that is 66 mm long, approximately 6 mm longer than for the 2D axisymmetric domain.

The 3D single injector model produces a steady-state solution with a flame that is shorter than the 3D steady-state chamber computation presented in Chapter 3. Like the steady-state solution for the 2D axisymetric domain, no neighbouring elements exist to contain and accelerate the flow in the single injector model. Neglecting the influence of the neighbouring elements changes the axial velocity and propellant distributions in the single injector model.

Figure 6.3.1 shows that the LOx core and flame are contained completely within the 3D numerical domain. The species distribution at the boundaries of the domain is predominantly hydrogen in the first 50 mm from the injection plane. The mixture composition at the downstream side and end boundaries of the domain is a mixture of equilibrium combustion products. The steady-state solution at the boundary surfaces is used to prescribe the mixture properties at the same boundaries during acoustic excitation. Therefore the mixture composition of the flow entering the numerical domain during acoustic excitation consists of a mixture of equilibrium combustion products intended to imitate a quasi-periodic (mirrored) boundary condition.

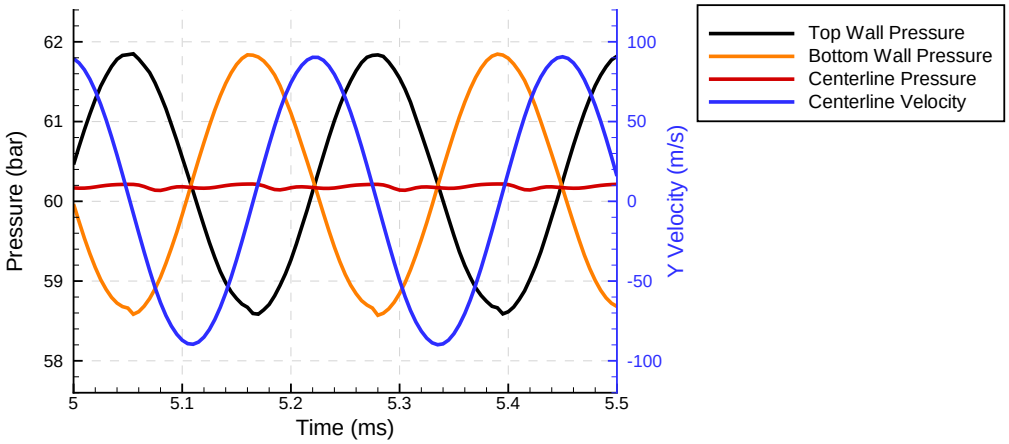

Figure 6.3.2: Resulting disturbance during transverse velocity forcing versus time for 5% P_{CC} amplitude computation.

6.3.2 Excited Results

A transverse velocity disturbance was imposed across the 3D numerical domain to represent the local acoustic disturbance during 1T-mode excitation of BKH. The transverse velocity disturbance was driven by a pressure gradient between the top and bottom boundaries of the domain. In the current study the response of the 3D single injector model to a transverse velocity disturbance fluctuating at a frequency of 4400Hz was computed. The influence of excitation amplitude was investigating by repeating the computation for four different excitation amplitudes. The excitation amplitudes were chosen to match existing experimental datasets and correspond approximately to 1.25, 2.5, 5, and 7.5% P_{CC} amplitude disturbances.

The resulting disturbance across the numerical domain from the imposed acoustic excitation is shown in figures 6.3.2 and 6.3.3. Figure 6.3.2 shows a sample of the resulting pressure and velocity disturbances versus time from different locations in the 3D domain. The pressure at the top and bottom boundaries of the domain fluctuate out of phase with one another to drive the transverse velocity disturbance. Meanwhile, the pressure at the centerline of the domain remains almost constant as desired. The pressure gradient and imposed velocity produces the desired transverse velocity disturbance with the peak transverse velocity amplitude occurring at the centerline of the domain.

Figure 6.3.3 shows the acoustic disturbance at the symmetry plane of the numerical domain at different phases of the acoustic cycle. The acoustic cycle is defined such that $\theta = 0$ corresponds to the peak pressure amplitude at the bottom surface of the domain. This phase definition is consistent with the phase normalisation of the previous acoustic and optical data analysis in Chapters 4 and 5. In the previous analysis the phase was normalised to the phase of the PCCDYN2 sensor signal which is located below the primary flame zone.

The distributions in Figure 6.3.3 shows that the imposed pressure disturbance produces the expected transverse gradient across the numerical domain. Similarly the transverse Y velocity disturbance fluctuates with a $\pi/2$ phase shift relative to the imposed acoustic pressure disturbance. The velocity distributions show that the velocity disturbance is almost uniform downstream. However, the dense LOx core is visible as a stationary structure with little acoustic velocity. The high density of the LOx core causes it to remain almost stationary within the center of domain. Similarly the momentum of the fast moving co-axial hydrogen injection is not overcome by the acoustic velocity. The fluctuations of the acoustic velocity around the LOx core and flame produce a complex velocity disturbance distribution in the near injector region.

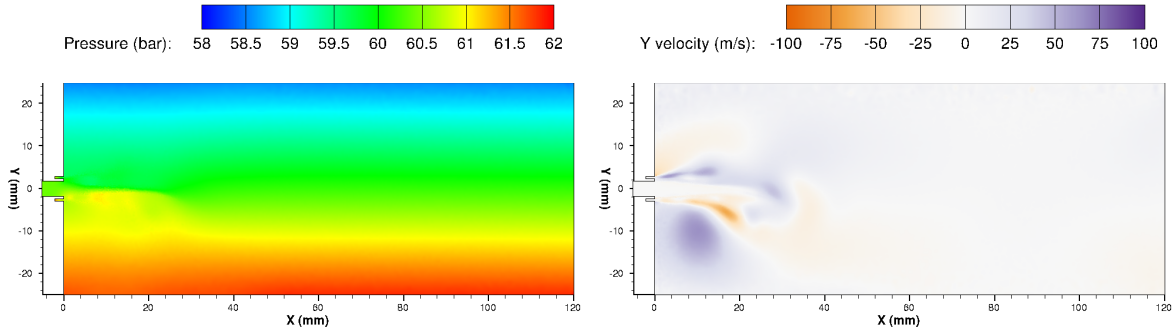

(a) $\theta = 0$

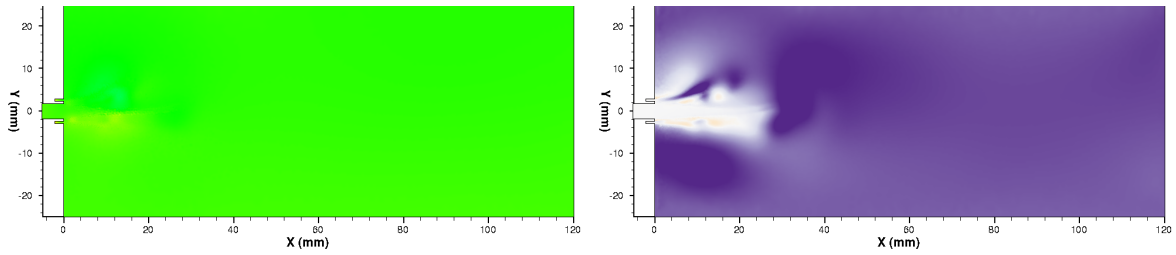

(b) $\theta = \pi/2$

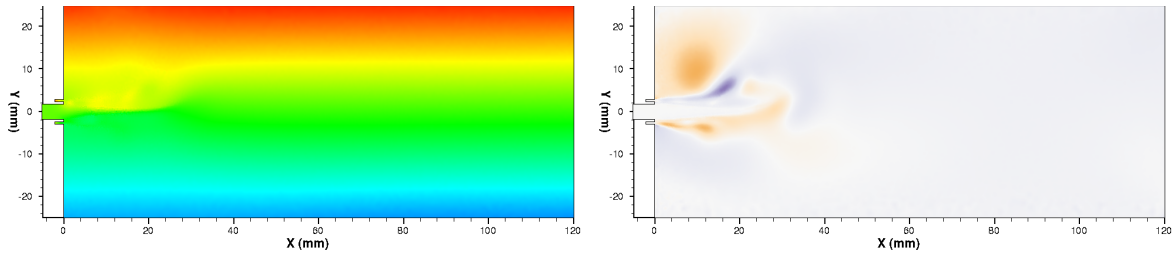

(c) $\theta = \pi$

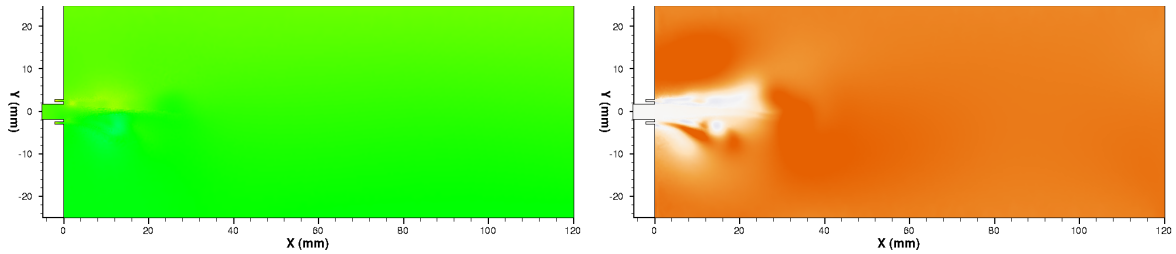

(d) $\theta = 3\pi/2$

Figure 6.3.3: Resulting disturbance distributions during transverse velocity excitation at different acoustic phase angles for 5% P_{CC} amplitude computation.

Figure 6.3.4 shows the deformation of the LOx core as acoustic excitation is imposed. Under the transverse acoustic velocity forcing the LOx core is both transported and deformed by the acoustic velocity. The acoustic velocity fluctuations deform the core and cause it to flatten in the plane normal to the imposed velocity. As the LOx core flattens it is more rapidly consumed by the surrounding hydrogen stream and it retracts towards the injection plane. After multiple acoustic cycles the length of the LOx core stabilizes while still being flattened and transported by the acoustic velocity.

The flame and combustion region envelope the oxygen stream and are similarly deformed by the acoustic disturbance. As the flame follows the retraction of the LOx core the property distribution within the numerical domain is similarly affected. Hardi [49] and Webster [159] previously identified a change in the 1T mode frequency of BKH as acoustic excitation is imposed. Hardi and Webster proposed that the change of acoustic properties as the flame retracts towards the injection plane was responsible for the ob-

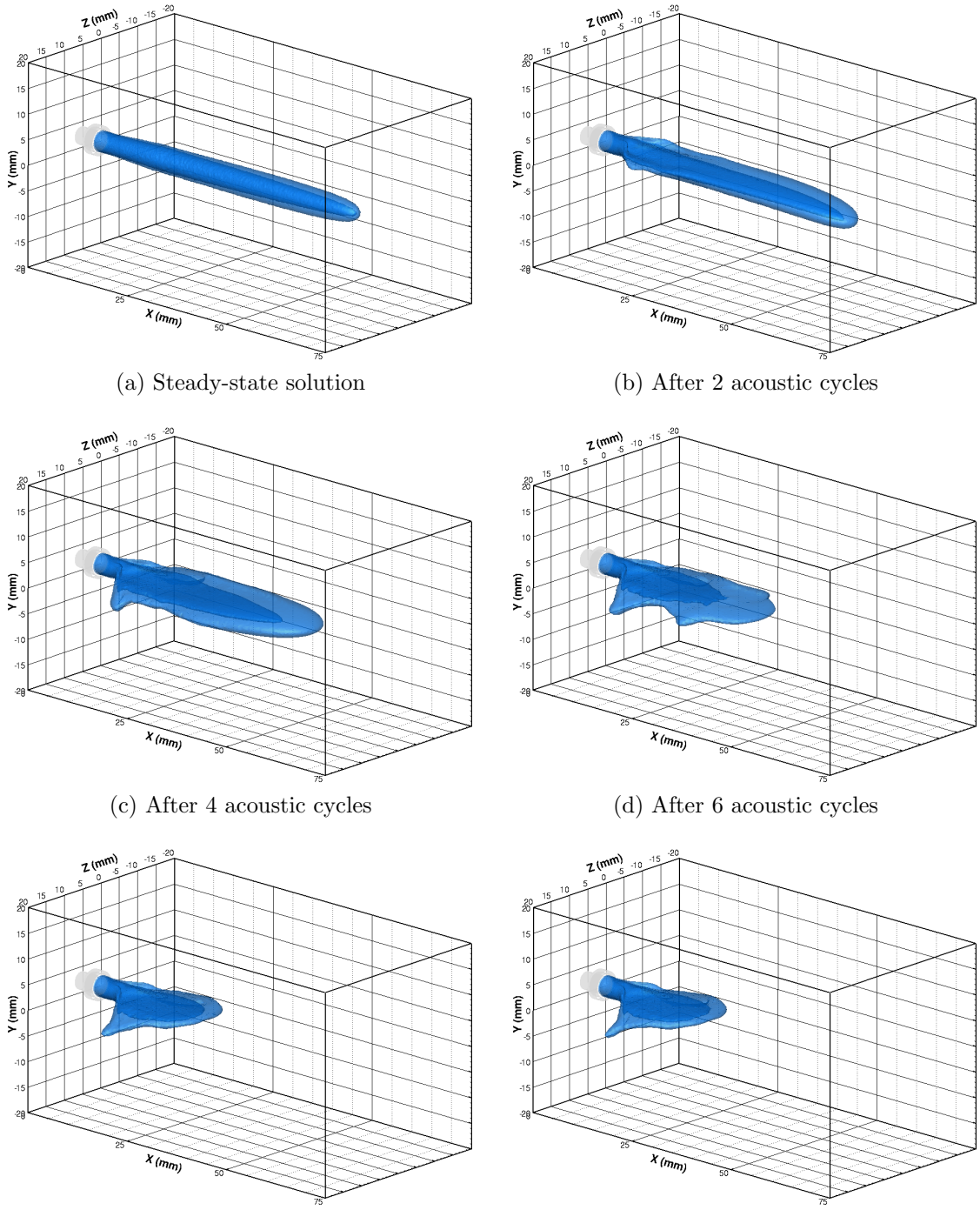

(a) Steady-state solution

(b) After 2 acoustic cycles

(c) After 4 acoustic cycles

(d) After 6 acoustic cycles

(e) After 8 acoustic cycles

(f) After 10 acoustic cycles

Figure 6.3.4: Deformation of the LOx core as transverse acoustic excitation is imposed. Oxygen core shown by blue isosurfaces at density values of 10 and 50 kg/m^3.

served increase in 1T-mode frequency. Figure 6.3.5 shows the speed of sound distribution in the centerplane of the 3D single injector numerical domain before and after acoustic excitation is imposed. The LOx core occupies less of the numerical domain and is replaced with hot combustion products.

The mean volumetric speed of sound over the numerical domain was computed for the steady-state solution and once the core had fully retracted in the excited results. For the 5% P_{CC} amplitude computation the mean volumetric speed of sound once the LOx core had fully retracted was 2.7% less than the steady-state solution. The decrease is due to the mixture of combustion products having a lower speed of sound than the pure hydrogen environment that exists near the injection plane in the steady-state solution.

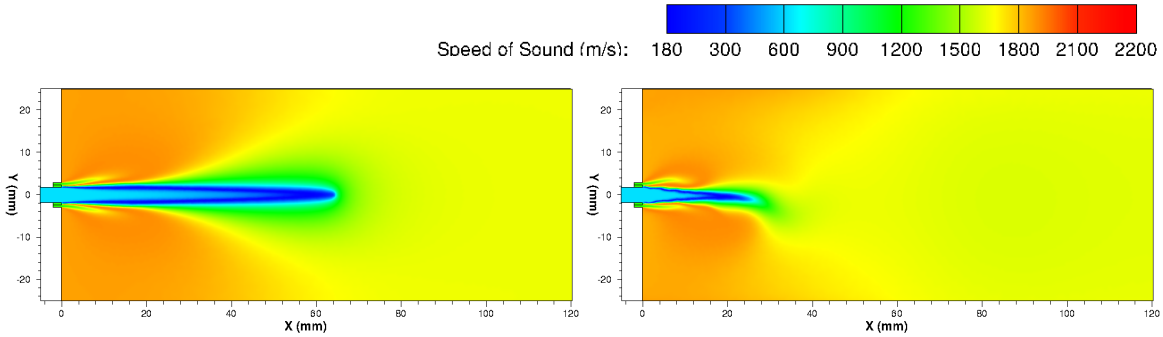

(a) Steady-state solution (b) 5% P_{CC} amplitude transverse disturbance

Figure 6.3.5: Speed of sound distributions with and without acoustic excitation at the centerplane of the 3D single injector model.

A lower speed of sound would produce a lower resonant mode frequency. This does not agree with the experimentally observed increase in the 1T mode frequency during transverse mode excitation. The transport of warm secondary hydrogen into the combustion zone may increase the mean volumetric speed of sound as it has a higher speed of sound than the mixture of combustion products. The single injector model does not include this effect due to the excitation boundary conditions that assume a mixture of combustion products used in the current work.

The jet is also being periodically transported in the transverse direction by the acoustic velocity fluctuations. As the oxygen jet flattens the lighter outer part of the jet is more readily transported than the denser liquid core leading to a flapping motion of the flattened oxygen stream. Figure 6.3.6 shows the motion of the oxygen core over a single period of acoustic excitation. The results in Figure 6.3.6 are from a period of the unsteady computation after 15 acoustic cycles when the flame has already retracted and fluctuates with a relatively constant length.

In addition to the flattening and flapping motion of the downstream LOx core the acoustic velocity fluctuations deform the cylindrically-shaped LOx core near the injection plane. These structures are visible in the density isosurface plots in Figure 6.3.6 between 5 and 10 mm from the injection plane and are observed to propagate downstream. The outer part of the LOx core is deflected to one side by the acoustic velocity as seen in Figure 6.3.6. This motion precedes the flapping motion of the flattened outer portion of the LOx core downstream. The disturbance then propagates along the leading edge of the flattened LOx core.

Figure 6.3.7 shows the distributions of density, OH mass fraction, and heat release in the centerplane of the 3D numerical domain parallel to the imposed transverse acoustic disturbance at different phases of the acoustic cycle. The density distributions show evidence of wave-like structures propagating along the surface of the dense LOx core. The lighter downstream part of the LOx core is observed to deflect as it is transported by the acoustic velocity.

The OH mass fraction and heat release distributions envelope and follow the deflection of the LOx core. At phase angles of $\pi/2$ and $3\pi/2$ a disturbance is seen on the surface of the flame approximately 10 mm from the injection plane in the OH mass fraction distribution. The disturbance occurs on one side of the flame in the direction of the imposed acoustic velocity. This disturbance is a result of the lighter edges of the LOx core being deflected by the acoustic velocity to one side of the flame.

This is visualised in Figure 6.3.8, which shows slices of oxygen and hydrogen mass fraction distributions across the 3D numerical domain at different distances from the injection plane. At a distance of 5 mm from the injection plane the LOx core is mostly cylindrical. Some transport of the outer edges of the cylindrical oxygen core by the acoustic

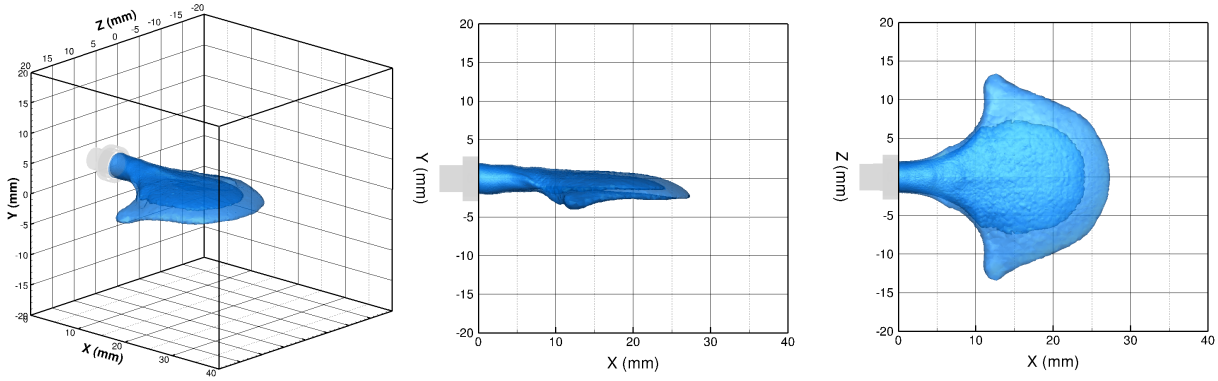

(a) θ =0

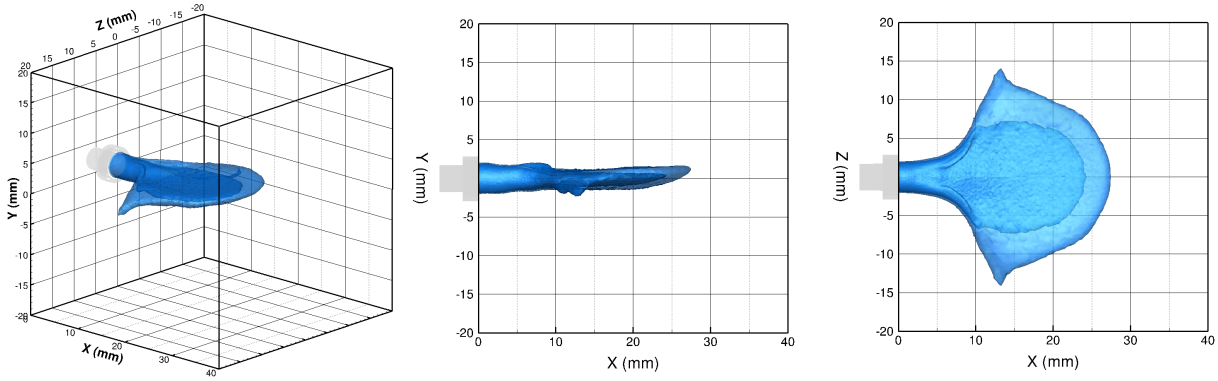

(b) θ =$\pi/2$

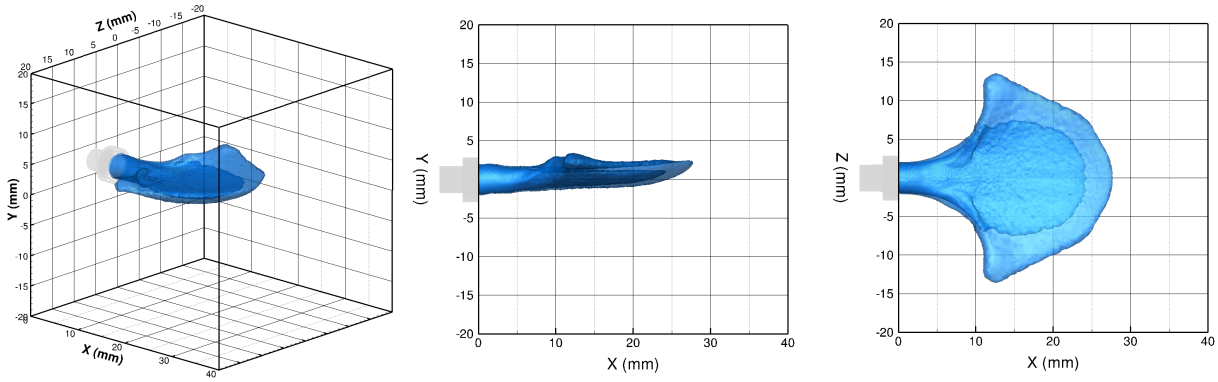

(c) θ =π

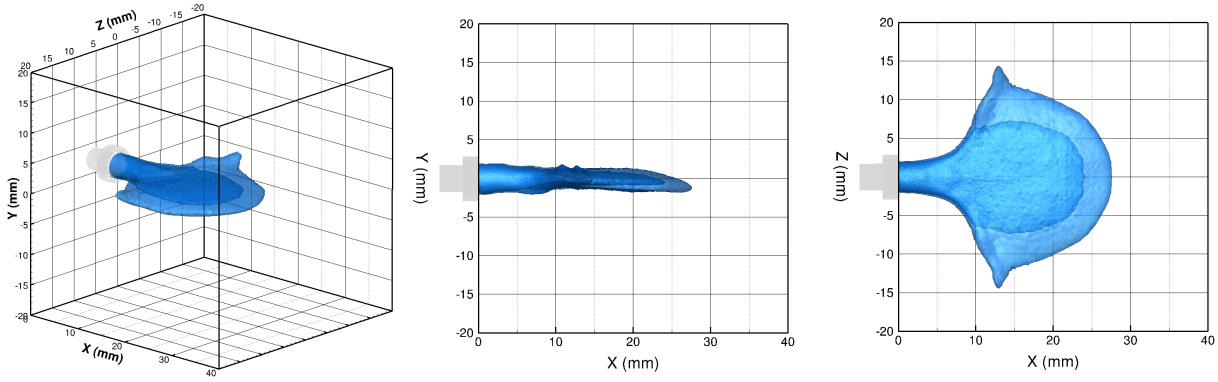

(d) θ =$3\pi/2$

Figure 6.3.6: Motion of the fully retracted oxygen core at different phases of the acoustic cycle. Oxygen core shown by blue isosurfaces at density values of 10 and 50 kg/m^3. Left: isometric view, Middle: side view, Right: overhead view.

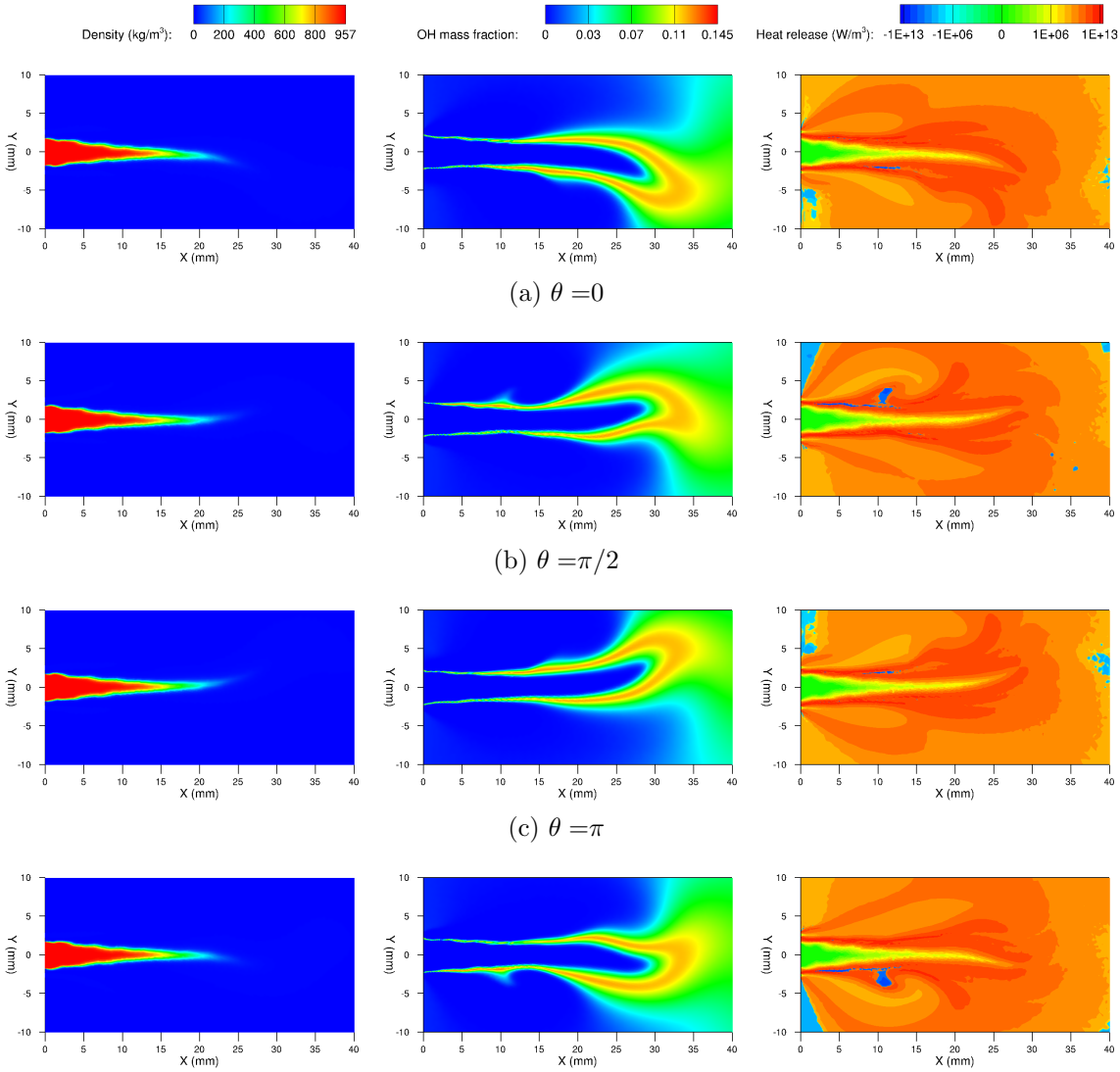

(a) $\theta = 0$

(b) $\theta = \pi/2$

(c) $\theta = \pi$

(d) $\theta = 3\pi/2$

Figure 6.3.7: Property distributions at the symmetry plane of the single injector model at different phases of the acoustic cycle once the core has fully retracted. Left: density, Middle: OH mass fraction, Right: heat release.

velocity is visible. At a distance of 7.5 mm from the injection plane the lighter outer parts of the core are seen to be deflected and wrap around the dense cylindrical section of the core. This motion appears to precede the acoustic velocity disturbance. Further downstream at a distance of 10 mm from the injection plane the flame has been noticeably flattened and stretched normal to the imposed velocity disturbance. A pocket of hydrogen exists and is consumed as the acoustic velocity deflects the core to fold in one direction, and then the other. At 15 mm from the injection plane (Figure 6.3.8: right) the LOx core has flattened into a sheet that flexes about the central axis over each acoustic cycle.

As the oxygen is deflected into the surrounding high velocity hydrogen stream rapid combustion occurs leading to high heat release. The heat release distributions shown in Figure 6.3.7 display regions with negative values between 5 and 15 mm from the injection plane. The negative heat release occurs as the local flame temperature increases and endothermic reactions such as water dissociation take place. This location of high heat release and flame temperature is in the same axial position as the identified rolling-up motion along the edges of the flattened LOx core.

The flattening and deformation of the oxygen core under transverse acoustic forcing has been observed and described previously by a number of researchers. Hakim et al. [42]

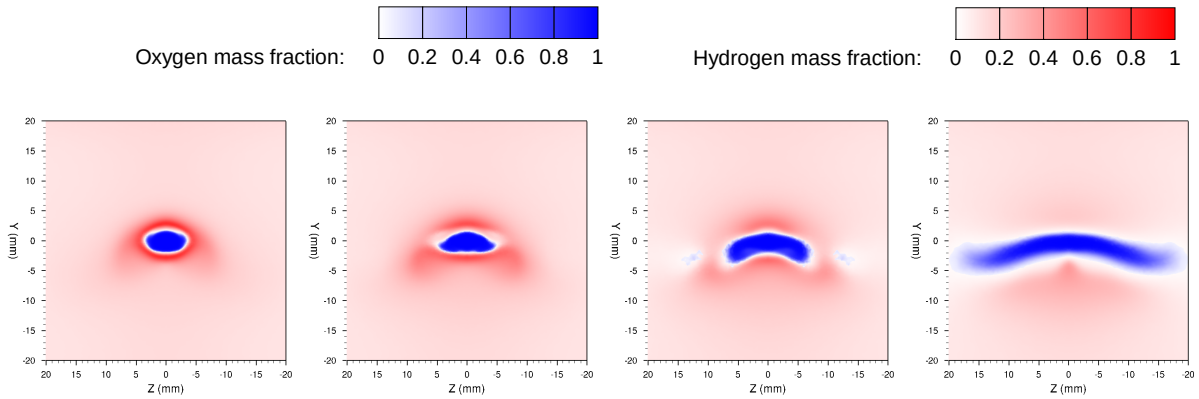

(a) $\theta = 0$

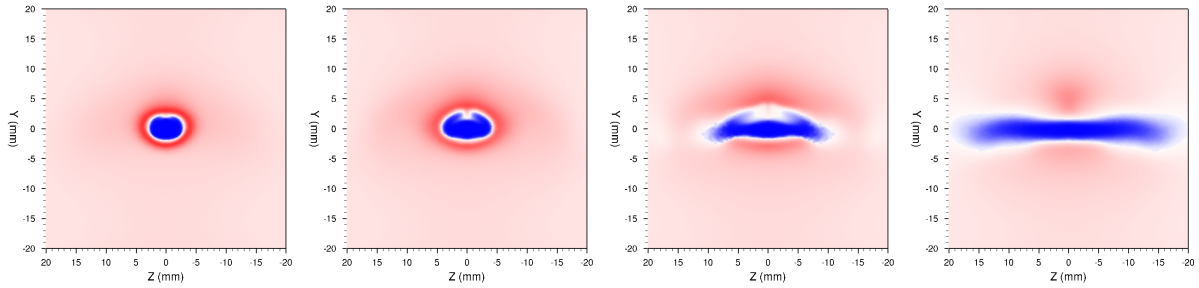

(b) $\theta = \pi/2$

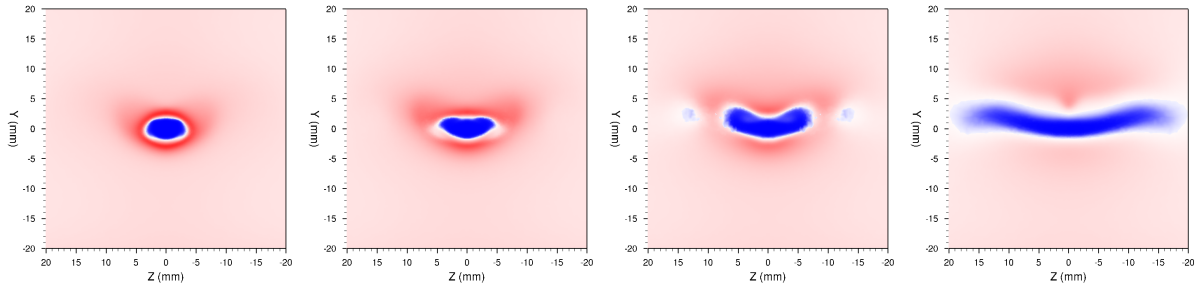

(c) $\theta = \pi$

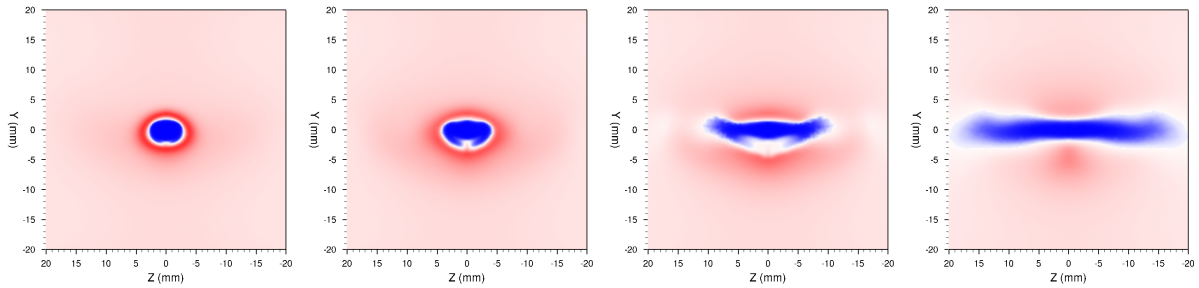

(d) $\theta = 3\pi/2$

Figure 6.3.8: Slices showing oxygen and hydrogen mass fraction distributions at different distances from the injection plane and phases of the acoustic cycle once the core has fully retracted. Left: 5 mm, Middle left: 7.5 mm, Middle right: 10 mm, Right: 15 mm.

describe the flattening of a supercritical jet under transverse acoustic forcing using the unsteady Bernoulli theorem. Hakim et al. explain that the acoustic velocity acting about the jet produces low pressure regions on either side of the LOx core as the lighter gases move past the dense cylindrical jet at the center of the stream. These low pressure regions cause the jet to expand and flatten in the plane of the velocity antinode. Hakim et al. [42] post processed LES results of a single injector model subjected to transverse instabilities and identified regions at the outer edge of the dense oxygen stream with low pressure.

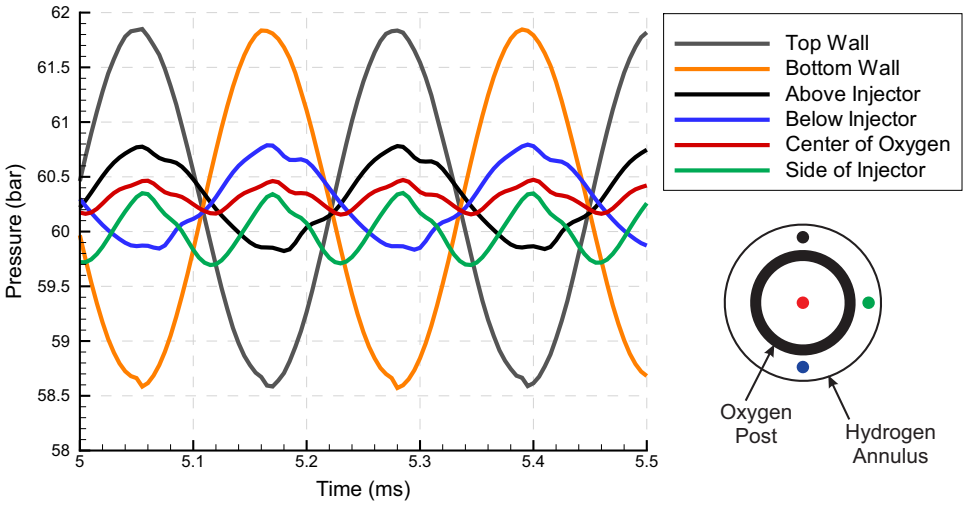

Figure 6.3.9: Pressure fluctuations from multiple locations around the injector at the injection plane.

Similar observations of low pressures at the outer edges of the oxygen jet were observed in the single injector model results computed in this work. Figure 6.3.9 shows the pressure fluctuations versus time from various locations at the injection plane in the numerical domain. The pressure above and below the injector fluctuates in phase with the disturbance imposed at the top and bottom walls of the numerical domain. The pressure at the center and sides of oxygen stream fluctuate at twice the excitation frequency. During periods of peak acoustic velocity the pressure above, below, and in the center of the oxygen stream are approximately the same while the pressure to the side of the LOx core is lower. The pressure difference between the center and side of the oxygen stream positions indicates a pressure drop that would drive the flattening of the LOx core in the plane normal to the imposed disturbance as described by Hakim et al [42].

The single injector model was computed for four different excitation amplitudes. The degree of flattening and retraction of the oxygen stream was found to change with increasing excitation amplitude. At low amplitudes the flow field was undisturbed and resembled the unexcited steady-state distribution. At higher amplitudes the degree of LOx core flattening and the retraction of the flame towards the injection plane increases. The flattening of the LOx core included an increase in the spreading angle of the LOx core in the plane normal to the imposed disturbance. The retraction of the flame towards the injection plane was driven by faster breakup and consumption of the LOx core as the surface area of the core increases and the fuel rich gases surrounding the core are more rapidly transported into the flame.

After subjecting the single injector models to continuous acoustic forcing with constant excitation amplitudes the length of oxygen stream and flame was found to stabilise for each case. The stabilized length of the LOx core was found to exponentially decay with increasing excitation amplitudes. This result matches experimental observations and are further discussed in Section 6.3.3.

The heat release rate is integrated over the single injector domain and, due to the symmetry condition employed in the 3D numerical domain, doubled to represent the heat release rate of a full single injection element. The fluctuation of the integrated heat release as acoustic excitation is imposed for four disturbance amplitudes is shown in Figure 6.3.10. The heat release fluctuation results are summarised in Table 6.1.

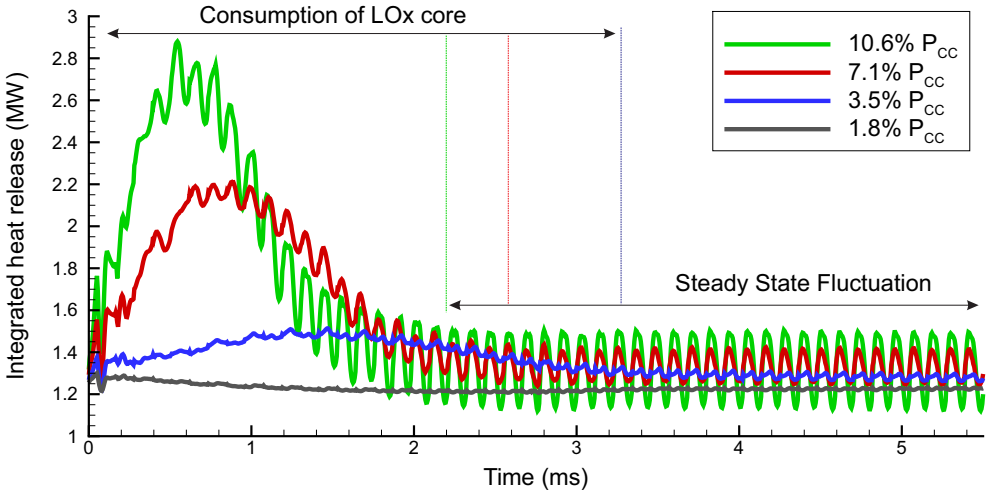

Figure 6.3.10: Evolution of the integrated heat release rate computed for different disturbance amplitudes as transverse acoustic excitation is imposed and the LOx core is consumed.

Table 6.1: Comparison of heat release fluctuations for different amplitudes of transverse acoustic excitation.

Pressure disturbance amplitude ($\%P_{CC}$)	Velocity disturbance amplitude (m/s)	Heat release disturbance (%*)	
		Peak during core breakup	Amplitude once retracted
1.8	22.0	2.8	0.9
3.5	44.1	19.6	3.3
7.1	88.1	74.7	7.1
10.6	132.2	127.5	15.2

* % fluctuation of steady-state solution value.

In Table 6.1 two values describing the amplitudes of the heat release disturbance fluctuations are stated. The first value describes the peak heat release attained during the initial rise as acoustic excitation is imposed and the LOx core that initially propagates 65 mm into the domain is consumed as shown in Figure 6.3.10. The heat release rate initially increases dramatically as additional mixing and transport of fuel species by the acoustic velocity consumes the established LOx core and it retracts towards the injection plane.

The magnitude of the initial rise in heat release is proportional to the imposed disturbance. Lower amplitude acoustic disturbances do not affect the length of the LOx core and the associated rise in heat release is less significant or negligible. Larger amplitude disturbances reduce the length of the LOx core by over 50% and the heat release rate rises significantly as the core is consumed. Higher acoustic amplitudes were also found to consume the LOx core more rapidly.

The second value in Table 6.1 describes the amplitude of the heat release fluctuation after length of the LOx core has stabilized and a steady-state fluctuation is reached under continuous acoustic forcing. The heat release rate fluctuates at double the frequency of the imposed acoustic disturbance. The amplitude of the heat release fluctuation once the core has retracted and a steady-state fluctuation has been reached also increases with larger acoustic disturbance amplitudes.

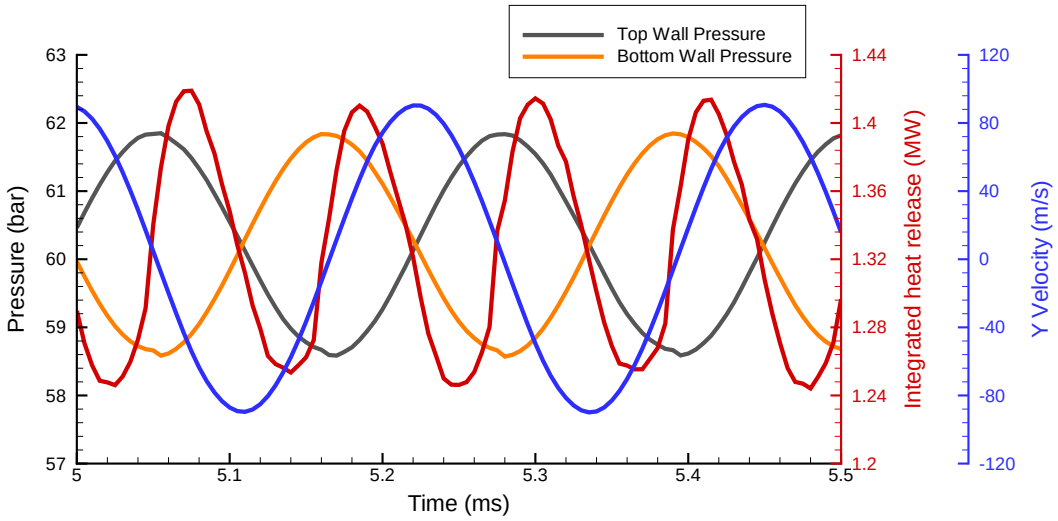

Figure 6.3.11: Pressure, velocity, and integrated heat release fluctuations versus time after the steady oscillations are achieved for the 7.1% P_{CC} amplitude computation.

The fluctuation of the integrated heat release is compared with the imposed acoustic disturbance in Figure 6.3.11. The integrated heat release fluctuates twice per acoustic cycle and the peak heat release occurs approximately 45° after the pressure peak on either the top and bottom sides of the numerical domain. This matches the phase relationship between heat release and pressure fluctuations identified while analysing the pressure excitation of the 2D axisymmetric domain in Section 6.2. It suggests that a similar response to acoustic pressure fluctuations may be occurring on either side of the flame.

6.3.3 Comparison with Experimental Data

The numerical results are compared with optical data from BKH experiments during 1T mode excitation. The length of the LOx core is compared against previous BKH experimental results from Hardi et al. [44, 49]. The results of the unsteady computations are also compared with the previous DMD and flame response analysis presented in Chapter 5. Features identified in the previous DMD and flame response analysis are investigated using the unsteady numerical results.

Previous analysis by Hardi et al. [44, 49] compared the length of the central LOx core in BKH with the amplitude of the transverse mode. Hardi et al. found that the length of the LOx core decayed exponentially as the transverse acoustic amplitude increased. A similar trend has been recovered in the single injector model results. Figure 6.3.12 shows the experimental measurements of the intact core length from Hardi et al. [44] with the numerical results from the single injector model computed with four different excitation amplitudes in the current work.

Hardi et al. suggest a fit of exponential decay to the experimental data, but also note that the fit should be adjusted at low amplitudes where the flame length is expected to match the finite length of the undisturbed flame. The numerical results in Figure 6.3.12 are shown as isosurfaces at density values of 10 and 100 kg/m^3. The isosurfaces show the difference in the length of the core if a different density cut-off value is defined. The results show that as long as a consistent density value is chosen the trend of exponential decay will be recovered in the numerical results.

Quantitative comparison of the experimental and numerical results is difficult as the density gradients associated with the identified features in shadowgraph images used to determine the length of the LOx core are unknown. The experimental results from Hardi et al. [44] are generated by identifying the end of the LOx core of the central injection element

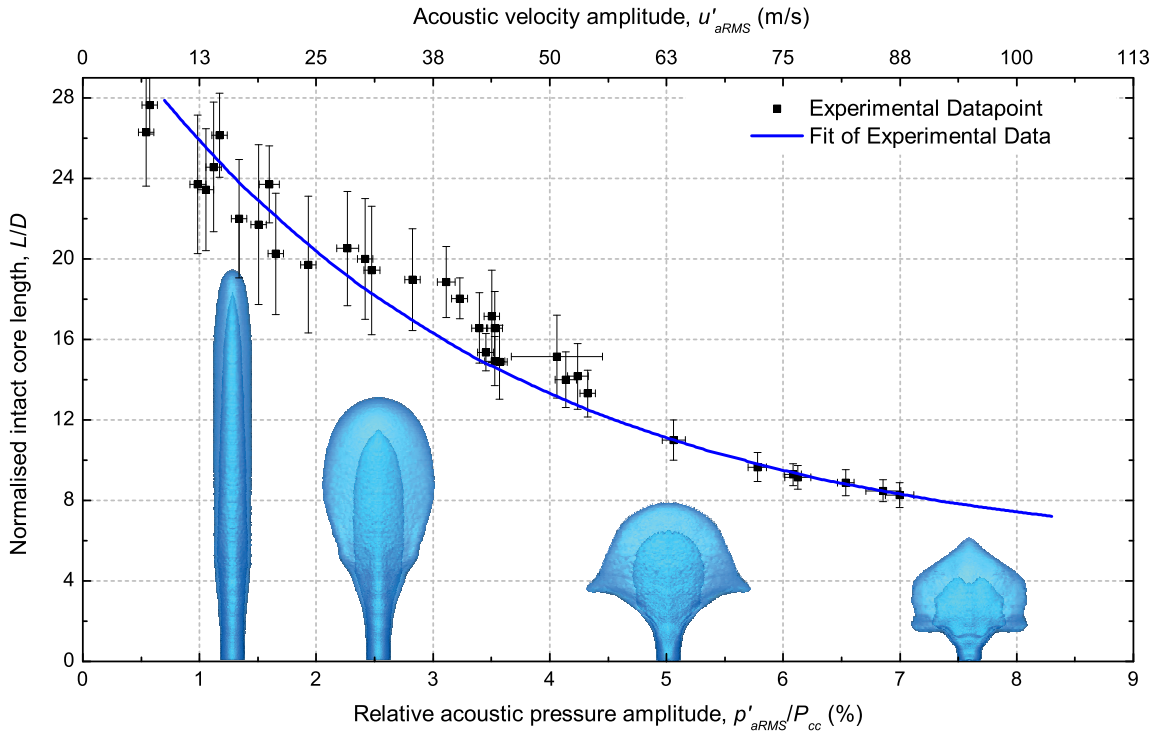

Figure 6.3.12: Experimental and numerical results showing LOx core length versus transverse mode amplitude. Experimental data from Hardi et al. [44]. Density isosurfaces shown at density values of 10 and 100 kg/m^3.

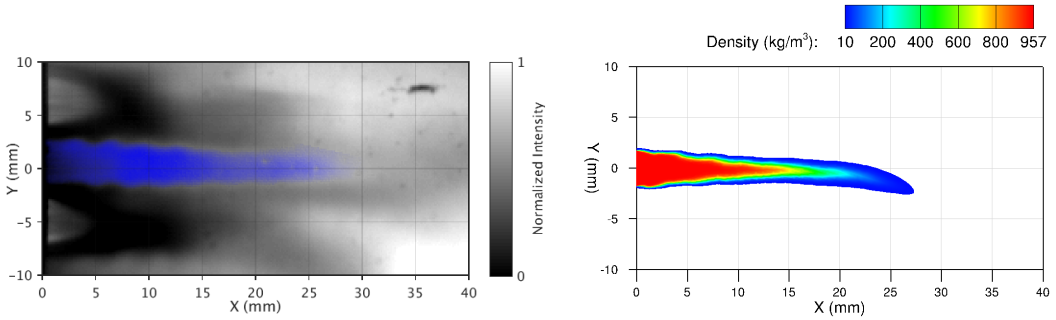

(a) DMD reconstruction (b) CFD result

Figure 6.3.13: Comparison of LOx core surface fluctuations. LOx core highlighted in blue in the DMD reconstruction image. CFD density distribution from computation with 7.1% P_{CC} amplitude. Density shown with a cut-off value of 10 kg/m^3.

in shadowgraph images. This can be affected by the camera settings and back-lighting source used and is therefore not directly related to a specific density value.

The main observations made from the DMD and flame response analysis of BKH optical data during transverse excitation were the identification of ripples on the surface of the LOx jet in shadowgraph images, and the vertical transport of the flame surrounding the dense LOx core. Figure 6.3.13 compares a reconstructed shadowgraph image using the DMD modes at the excitation frequency, originally shown in Figure 5.2.7, with the density distribution in the same region at the same phase of the acoustic cycle from the single injector model results. Both plots in Figure 6.3.13 show wave-like structures alternating between the top and bottom surfaces of the LOx core. The crest and trough of each wave are similarly spaced along the length of the LOx core and become less pronounced downstream.

The surface ripples are caused by the lighter outer part of the dense core being transported by the acoustic velocity to one side of the LOx core upon entering the chamber. The dense fluid does not instantly break up and instead propagates along the

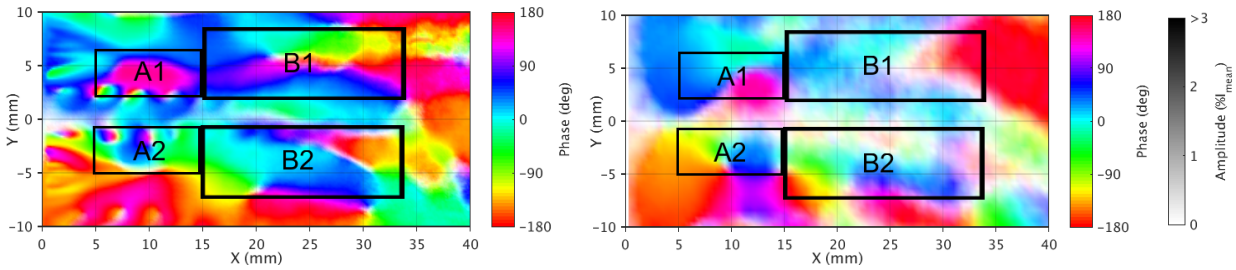

(a) Shadowgraph (b) OH*

Figure 6.3.14: Plot showing DMD mode phase relative to PCCDYN2 signal about central injector for Test B 1T mode samples with labelled areas of interest.

surface of the LOx core. The surface ripples become less pronounced downstream as the LOx core is heated by the flame producing a less distinct boundary in the URANS and reconstructed DMD results.

Areas of interest are superimposed to the phase distribution results from the flame response analysis of the Test B 1T-mode samples in Table 5.1 in the near injector region(Figure 5.3.20) in Figure 6.3.14. The phase in Figure 6.3.14 is defined relative to the PCCDYN2 sensor, which is analogous to the phase convention defined in this section for transverse excitation based on the disturbance at the bottom wall of the numerical domain. The phase value represents the phase at which the peak intensity of the fluctuation at the excitation frequency is observed. The wave-like structures on the surface of the LOx jet are recognizable in the phase distribution of the shadowgraph image (Figure 6.3.14a). Other features of interest are the fluctuations of the lighter gaseous flame about the LOx core by the acoustic velocity. The regions corresponding to this motion have been labelled in Figure 6.3.14.

The regions marked A1, A2, B1 and B2 in Figure 6.3.14 are the locations where the lighter gaseous flame is observed to move around the dense liquid core in the shadowgaph images. The “A” regions are above (A1) and below (A2) the LOx core between 5 and 15 mm from the injection plane. In these regions a circular feature with constant phase is seen in both the shadowgraph and OH* images with phase angles of approximately 135° in A1 and 45° in A2. The phase in the A2 regions also has secondary round features with phase values of approximately -45°. This feature indicating motion at different phases of the acoustic cycle corresponds to the rolling up motion identified from the distributions shown in Figure 6.3.8.

The regions marked B correspond to the downstream motion of the gaseous flame about the flattened LOx core. The maximum displacement of the lighter part of the flame is seen as bands at phase angles of 0° and 180° in the shadowgraph image. From this the mean displacement of the flame is observed to be ±5 mm about the central axis. The structure of the flame at the phase angles of interest is further investigated using the 3D numerical results as shown in Figures 6.3.15 and 6.3.16.

Figures 6.3.15 and 6.3.16 show density and OH mass fraction isosurfaces indicating the position of the LOx core and flame at various phase angles once steady-state oscillation has been reached. The sequences of images show the vertical transport of the flame towards the top of the numerical domain by the transverse acoustic velocity. The minimum and maximum pressure disturbance at the top of the numerical domain occurs at a phase angles of $\theta = 0$ and 180°, respectively.

Starting at a phase angle of 0° (Figures 6.3.15a and 6.3.16a) the flame has reached its maximum vertical displacement towards the bottom of the numerical domain from the previous acoustic cycle. The density isosurfaces in Figure 6.3.15a show the flattened LOx core deflected towards the bottom of the chamber. However, the isometric OH mass

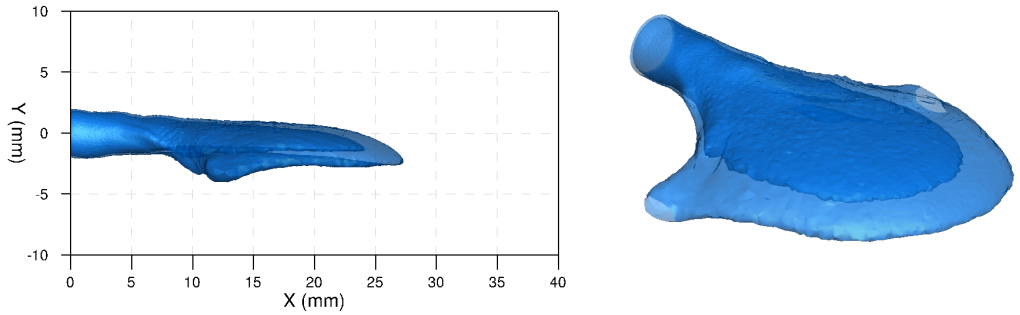

(a) $\theta = 0°$

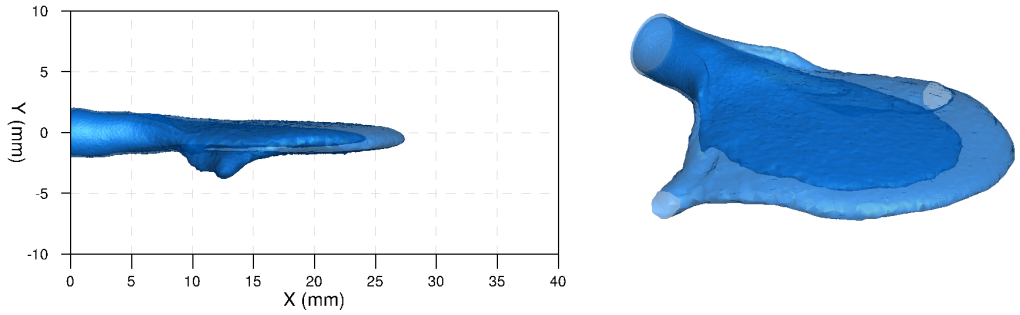

(b) $\theta = 45°$

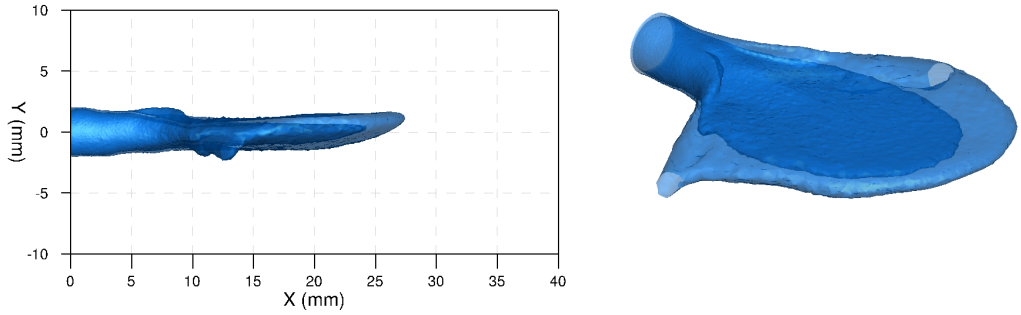

(c) $\theta = 90°$

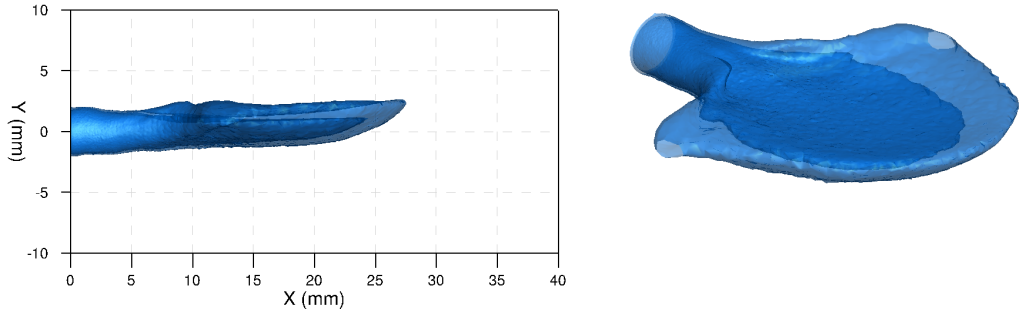

(d) $\theta = 135°$

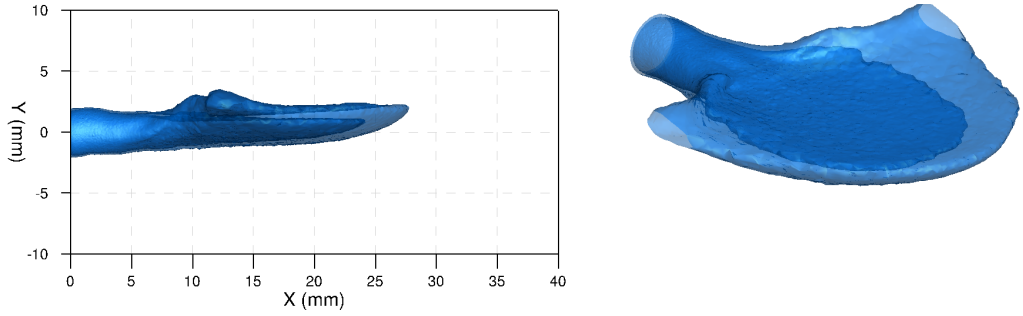

(e) $\theta = 180°$

Figure 6.3.15: Side and isometric view of density isosurfaces at different phase angles. Isosurfaces shown at density values of 10 and 50 kg/m^3.

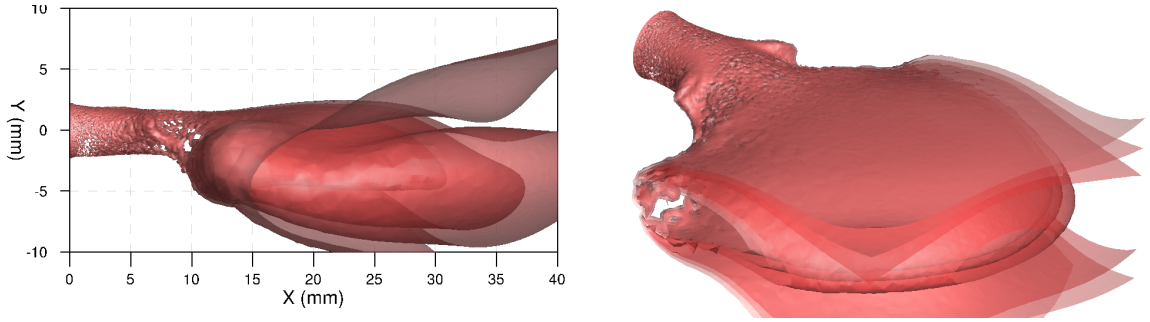

(a) $\theta = 0°$

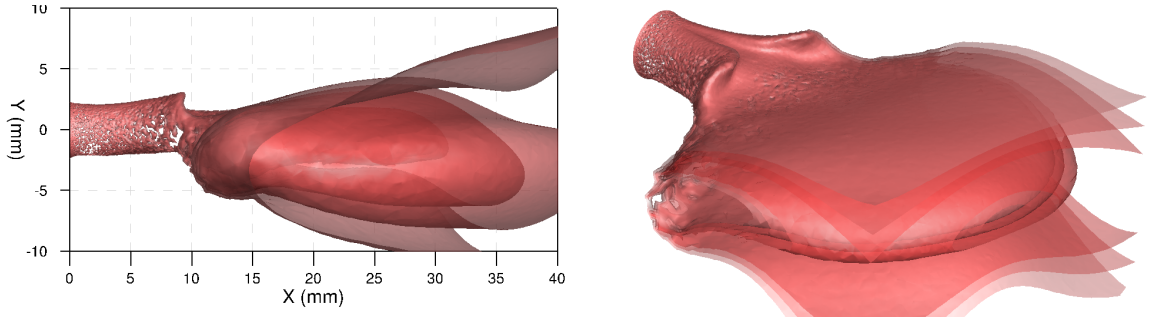

(b) $\theta = 45°$

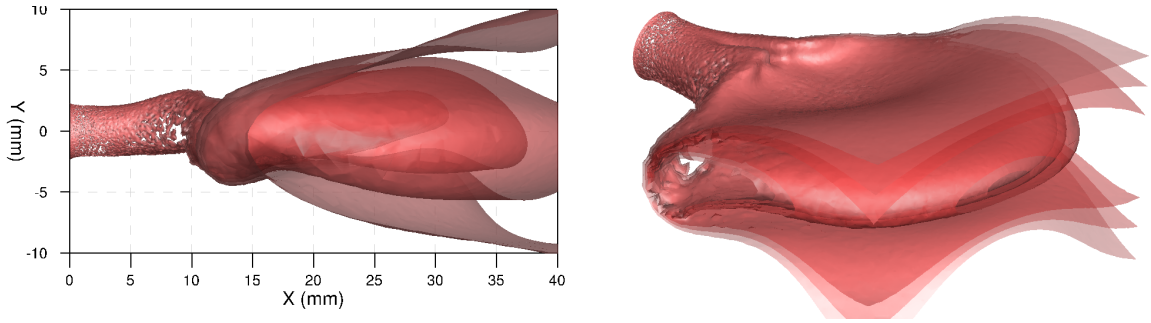

(c) $\theta = 90°$

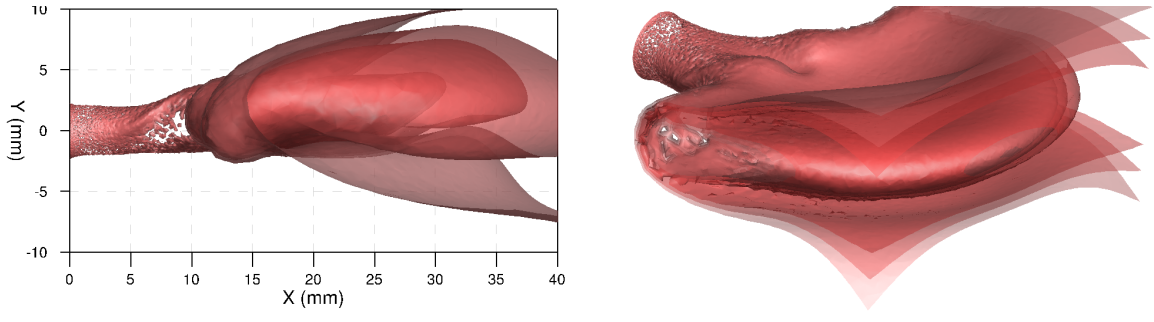

(d) $\theta = 135°$

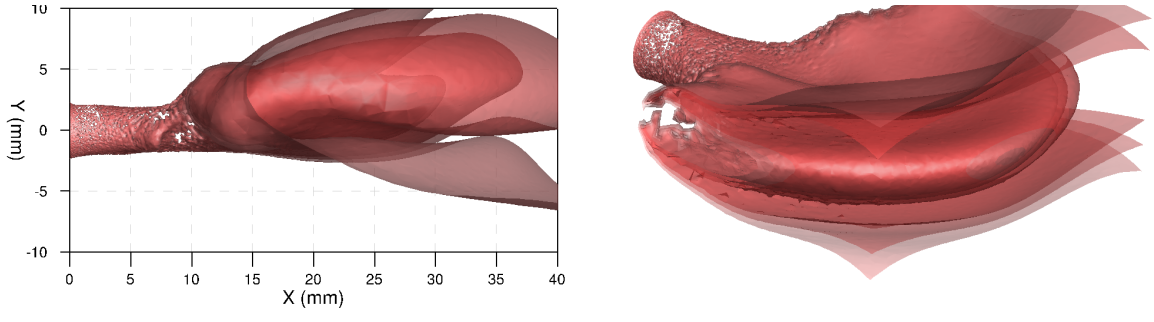

(e) $\theta = 180°$

Figure 6.3.16: Side and isometric view of OH mass fraction isosurfaces at different phase angles. Isosurfaces shown at OH mass fraction values of 0.06, 0.08, and 0.1.

fraction isosurfaces, in Figure 6.3.16a(right), show structures protruding from either side of the LOx core at approximately 7.5 mm from the injection plane. These structures follow the deformation of the lighter gaseous oxygen around the dense core.

At a phase angle of 45° (Figures 6.3.15b & 6.3.16b) part of the less dense LOx has begun to roll around the cylindrical core near the injection plane and the leading edge of the flattened core. However the side view of OH mass fraction distribution, in Figure 6.3.16b(left), shows a distinct peak on the top side of the OH mass fraction distribution at 7.5 mm from the injection plane. This peak corresponds to the lighter gases rolling-up around the cylindrical LOx core as the acoustic velocity begins to act upon them. The peak occurs at the same coordinates as the region marked "A1" in Figure 6.3.14.

As the phase angle increases the dense LOx core follows the motion of the lighter surrounding gases and the leading edge of the flattened core begins to roll-up. At a phase angle of 90° (Figures 6.3.15c and 6.3.16c) the downstream part of the flame has been vertically transported back to the vertical centerline of the numerical domain. The rolling-up motion about the cylindrical core creates a "valley" along the top side of the flame and LOx core.

At a phase angle of 135° (Figures 6.3.15d and 6.3.16d) the rolling up motion begins to propagate outwards from the center along the leading edges of the flattened LOx core and flame surface. This motion continues at a phase angle of 180° causing the leading outer edges of the flame and LOx core to deflect further than some downstream sections.

The result at $\theta = 180°$, shown in Figures 6.3.15e & 6.3.16e, is vertically mirrored to the result at a phase angle of 0°. A similar structure on the outer part of the cylindrical LOx core near the injection plane can be seen to begin moving into the region marked "A2" in Figure 6.3.14 during the opposite half of the acoustic cycle.

The motion in the "B" regions corresponding to the motion in phase with the acoustic disturbance of the flattened flame and LOx core. This motion can be seen from the sequence of images in Figures 6.3.15 and 6.3.16. The identified fluctuations in the "A" regions occur at phase angles of 45 and 135° that both precede and lag the local acoustic pressure disturbance. These fluctuations may still be related to the identified motion 7.5 mm from the injection plane. However it is unclear when the peak emission in the region may occur. It may be produced by the rolling-up motion propagating along the leading edge of the LOx core, or when the flame rolls upon itself above or below the flattened core. Further post-processing is needed to determine the emission from the numerical results quantitatively for comparison with the line-of-sight experimental data.

6.3.4 Discussion

The unsteady single injector model has been successfully applied to study the response of the flame from a co-axial injection element to transverse acoustic excitation. This work served as a demonstration of the employed 3D URANS approach for studying combustion instability phenomena. The model reproduced key phenomena previously observed both experimentally and by other groups using advanced numerical tools.

The URANS approach permitted coarser grids and larger time steps than those needed for higher order modelling approaches. Each unsteady computation required only approximately 35,200 total CPU hours on two 16 core AMD opteron 6274 processors to compute 1000 time steps, or 22 acoustic cycles. Therefore the resources required to produce the results presented in this work were significantly less than similar studies using LES which required millions of CPU hours to compute[41]. While the reduced computational cost is advantageous, the employed modelling approach relies upon a number of assumptions and simplifications that may limit its broader applicability.

The model results reproduced the flattening and retraction of the flame observed experimentally during transverse mode excitation. These features were resolved by the

URANS approach as they are consistently repeatable motions of the mean flame and LOx core position under continuous acoustic forcing.

The numerical results appear to consistently under-predict the length of the LOx core. This is attributed primarily to the assumptions of the single injector model and how it differs from the experimental configuration. First, the single injector model does not include the neighbouring elements which help to contain and accelerate the flow of the central injection element. The steady-state chamber model results presented in Chapter 3 show a longer core than on the single injector model domain. More representative excitation boundary conditions or multi-element models may improve the agreement between numerical and experimental results. The response of the propellant feed system, either by modelling the injection elements in detail or by designing appropriate acoustic boundary conditions, should also be considered in future work. Despite this, the modelling approach employed in this work reproduced key experimental observations and demonstrated the ability to predict the change in the shape of the LOx core, length of the flame, and distribution of acoustic properties. These results are important for acoustic and other low order combustion instability modelling methods.

How the LOx core breaks up in the oxygen-hydrogen diffusion flames studied in the current work is strongly dependant on how the thermal conductivity of the flow is modelled. As previously described in Section 3.1.5, the influence of turbulence on the thermal conductivity of the fluid is modelled by the addition of a turbulent contribution to the thermal conductivity of the mixture. The magnitude of the contribution is dependent on the Prandtl number ratio specified as a parameter of the model.

Variation of the Prandtl number ratio was observed to significantly affect the break up of the LOx core. High turbulent thermal conductivity causes the density of the LOx core to decrease more rapidly upon entering the chamber. The less dense oxygen stream is then more readily transported and deformed by the acoustic velocity. A lower turbulent contribution to the thermal conductivity causes the dense part of the LOx core to propagate further. As the denser stream is deformed its momentum and inertia causes surface structures to become more pronounced and remain intact over greater distances. The parameters chosen in the current work reproduced both features and are believed to be well adjusted to modelling the O2/H2 flames considered. Research that investigates and characterises the thermal conductivity of oxygen in the presence of turbulence and large temperature gradients, either experimentally or from high fidelity simulations, would allow further justification for the chosen model parameters.

The model predicted a large increase in the heat release rate as excitation is imposed and the established LOx core in the numerical domain is consumed. The consumption of the LOx core would depend on the mixture being transported to the flame by the acoustic velocity. In the BKH experiments this mixture is likely unburnt hydrogen due to the large amount of secondary hydrogen injection surrounding the primary combustion zone. Rocket engine combustion chambers typically operate fuel rich and may also include secondary cooling flows or ROF tapering to reduce wall heat fluxes. Therefore similar pockets or regions of unevenly distributed propellants could exist in full scale systems.

The predicted temporary increase of the heat release rate is non-linear with respect to the amplitude of the imposed acoustic disturbance. Such a response may contribute to spontaneously occuring natural instability phenomena. The potential additional heat release would depend on the steady-state mass of oxygen contained in the established flame and LOx core, and how much of the core is consumed, and over what time scale. A limiting case would be when all of the oxygen in the chamber has been consumed and the flame retracts completely to the injection plane.

The unsteady response and breakup of the LOx core as acoustic excitation is imposed would depend upon the turbulent break up of the established core. The employed URANS

approach models would need to be validated extensively before it could be applied to investigate this phenomena. Therefore further investigation of the initial non-linear response of the flame is recommended to be investigated with higher fidelity modelling techniques.

The heat release fluctuation once the core had fully retracted as acoustic excitation was continually imposed was analysed using the single injector model results. This fluctuation is related to the mean response of the flame under continuous acoustic forcing and is therefore captured by the employed URANS modelling approach. The heat release was observed to fluctuate at twice the frequency of the imposed acoustic disturbance and to lag the local pressure fluctuation as the flame is transported by the acoustic velocity. The heat release distribution follows the transport of the LOx core and flame across the pressure nodal line with the peak pressure disturbance. As the peak heat release occurs in phase with the local pressure disturbance it satisfies the Rayleigh criterion. The amplitude of the resulting heat release fluctuations were found to be non-linear as the amplitude of the imposed acoustic disturbance increased.

The acoustic velocity transports the lighter edges of the cylindrical LOx core near the injection plane. The displaced side edges of the LOx core are further deformed as the flow travels downstream. This produced a flapping like motion of the flattened LOx core. The peak heat release fluctuation occurs as the outer edges of the LOx core reach their maximum vertical displacement and the acoustic velocity begins to transport a fuel-rich mixture towards the top of the flame from the boundaries of the domain.

The predicted flapping motion was related to features identified in the previous analysis of BKH optical data presented in Chapter 5. The motion of the flattened LOx core and flame was reproduced in the numerical results. Additional motion corresponding to lighter gaseous parts of the oxygen core rolling-up around the dense LOx core was also identified and related to fluctuations seen in the experimental optical data. This motion appears to be related to the pressure gradient from the transverse acoustic disturbance acting upon fresh propellants entering the chamber. The pressure gradient accelerates the fresh propellant that does not have existing momentum from previous acoustic cycles. Further research must be done to confirm this theory. The influence of the internal acoustics of the LOx post should also be investigated. The numerical results now allow further interpretation of the optical data from the experiment and additional insight into the flame response that was not possible with the limited 2D line-of-sight images.

The DMD and flame response analysis of BKH optical data presented in Chapter 5 identified the mean response of the flame and key features that have been reproduced qualitatively in the numerical results. Further quantitative comparison of the numerical and experimental data is challenging due to the difficulty of producing quantitatively comparable results from the unsteady numerical datasets representative of the 2D line-of-sight experimental optical data. While ray tracing algorithms and other post-processing methods are needed to produce better results from the numerical data, further research on combustion light emission is also necessary to understand what is being captured in the experimental optical data.

This work has identified the capabilities and limitations of the current modelling approach. By understanding its applicability the level of modelling needed to study specific combustion instability phenomena is now better understood. The URANS model reproduced the flattening, retraction, and transverse displacement of the flame observed experimentally and predicted by other higher-order modelling approaches such as LES modelling by Hakim et al. [42]. The results were also used to identify other fluctuations about the cylindrical core, demonstrating its ability to provide further insight into experimental observations.

The model may continue to be applied to study other experimental test cases and operating points. The single injector models could be used to characterise and compare

the response of different injector designs and operating conditions to acoustic forcing. With further validation the results could be used to compute response and flame transfer functions for use in low order models. Many of the discrepancies between the experimental and numerical results stem from uncertainty on the impact of the assumptions of the single injector domain. This could be answered by computing an unsteady model of the full BKH chamber. This was outside the scope of the current work but may be addressed as part of ongoing research. Full chamber computations would require significantly more computational resources and introduce further challenges regarding how to represent the excitation of the chamber by the secondary nozzle and siren wheel acoustic excitation system.

6.4 Summary

The flame response of BKH coaxial injection elements to representative longitudinal and transverse acoustic forcing has been investigated numerically. The modelling approach first applied in this work was demonstrated to produce results of scientific interest in a reasonable time frame and without large-scale computational resources. The model was employed to investigate the flame response to different amplitudes of acoustic excitation.

Longitudinal mode acoustic excitation was modelled by imposing a uniform pressure disturbance, representative of the local acoustic disturbance during BKH 1L-mode excitation, upon a 2D axisymmetric model of a single BKH injection element. The pressure disturbance caused wave-like fluctuations on the surface of the oxygen core and heat release fluctuations that lag the phase of the imposed pressure disturbance by approximately 45°. Both of these features agree with experimental observations of LOx core deformation and OH* intensity fluctuations during longitudinal mode excitation.

Post-processing of the pressure excitation results identified an internal acoustic response in the LOx post. The internal acoustics of the LOx post caused a phase shift in the fluctuation of the oxygen injection velocity relative to the imposed acoustic fluctuations downstream. This phase shift produced fluctuations in the relative velocity of the oxygen and hydrogen streams. The resulting fluctuations in the velocity ratio at the injection plane were perfectly out of phase with the heat release fluctuations. LOx post acoustic coupling has been previously identified experimentally as a potential driving mechanism. The modelling approach employed here may be used to study it further in the future.

The model predicted that the amplitude of the heat release fluctuations increases linearly with respect to the amplitude of the imposed uniform acoustic pressure disturbance. The predicted peak heat release occurred in phase with the peak OH* emission observed experimentally, rather than the peak OH mass fraction.

The response of a single BKH injection element to a transverse velocity disturbance was modelled using a 3D numerical domain with horizontal symmetry. A transverse velocity disturbance and pressure gradient was imposed to produce a disturbance representative of the transverse velocity and pressure fluctuations that act upon the flame during BKH 1T-mode excitation.

The model reproduced experimental observations from BKH 1T-mode excitation, such as the deformation as the flame retracts towards the injection plane once excitation is imposed, and the periodic vertical displacement with continuous acoustic forcing. The trend of exponential decay of the length of the LOx core with increasing acoustic amplitudes was also reproduced. The model also exhibited features identified in the DMD analysis of BKH optical data presented in Chapter 5. Evidence of the alternating wave-like structures on the top and bottom surfaces of the LOx core were observed in the predicted density distributions. The motion of lighter combustion gases surrounding the LOx core that are more-readily displaced was also captured numerically.

The results with transverse excitation were used to describe the flapping motion of the flame under continuous acoustic forcing. The gaseous outer part of the LOx core was more readily transported by the acoustic velocity resulting in a flapping motion of the flattened flame surface. The deformation of the lighter gaseous oxygen surrounding the cylindrical LOx core near the injection plane produce local out-of-phase flapping motion, supported by experimental DMD analysis, that has been identified here for the first time.

The model predicted a large increase in the heat release rate as the LOx core is initially consumed. With continuous acoustic forcing the length of the LOx core stabilizes and the heat release fluctuates with a constant amplitude. The peak heat release was predicted to occur shortly after the peak local pressure disturbance. As the flame is transported across the nodal line this produces a positive coupling between acoustic and combustion processes and agrees with previous experimental observations and theoretical models.

Chapter 7

Conclusions and Future Work

Understanding the flame response to acoustic disturbances is important for the prediction and treatment of combustion instabilities in liquid rocket engines. The BKH experiments are used to study the response of an array of coaxially injected oxygen-hydrogen flames to acoustic disturbances, representative of high frequency combustion instabilities. In this thesis complementary experimental data analysis and numerical modelling of BKH is employed in order to identify and predict the flame response to longitudinal and transverse acoustic excitation.

The experimental data is analysed to isolate the resulting acoustic field and flame response at the imposed excitation frequency. The results of this analysis are used to demonstrate the capability of the employed modelling approaches to reproduce key combustion instability phenomena. The numerical results were in turn used to provide further insight into the conditions in BKH, to further interpret the experimental data, and to further our current understanding of the flame response.

To investigate and characterise the BKH flowfield the first steady-state CFD model of BKH was computed. The model was computed using an in-house CFD tool developed by the DLR with a real-gas modelling capability. The model results were post-processed and compared with available line-of-sight experimental images. The model was found to capture the propagation of the dense LOx cores into the chamber volume. The steady-state results allowed further insight into the flowfield than was possible with the experimental data. The results showed the deflection of the outer injection elements in the BKH penta-injector matrix configuration towards the centerplane of the chamber by the window cooling flow which was not previously understood. The steady-state model demonstrated the capability of the employed CFD approach for modelling trans-critical injection and combustion of oxygen-hydrogen propellants at supercritical pressures.

In order to determine the local acoustic disturbance acting upon the flame during BKH experiments, a new method for reconstructing the acoustic field from dynamic pressure sensor data was developed. The new complex acoustic reconstruction method involves isolating the amplitude and phase of the acoustic disturbance at the frequency of interest. The acoustic field is then reconstructed using a complex acoustic amplitude formulation and knowledge of the spatial distribution of dynamic pressure sensor data. The complex acoustic reconstruction results were used to characterise the evolution of the acoustic field and the local acoustic disturbance with varying excitation frequency. The rotation of the orientation of the acoustic distribution as the excitation frequency transitions between the 1L- and 1T-mode resonant frequencies was identified from the results. This new method is generally applicable to experiments and hardware with a sufficiently high spatial sensor resolution to characterise the acoustic modes of interest. The amplitude and phase results produced as part of the reconstruction process are also useful for validation of acoustic models.

An acoustic model was also developed to address the challenge of predicting the local acoustic disturbance without the availability of experimental data and in a time scale suitable for industrial application. A low-order acoustic model, with a realistic acoustic property distribution provided from the steady-state chamber model, predicted the acoustic disturbance at resonant and non-resonant frequencies. The predicted resonant mode frequencies and distributions, and the predicted evolution of the acoustic field with varying excitation frequency, matched BKH experimental results. The model also predicted the local variation in the acoustic disturbances about the primary flame zone due to the 3-dimensional acoustic property distribution.

DMD analyses was applied to BKH optical data in order to isolate the response of the flame to the imposed acoustic disturbance. Analysis of shadowgraph imaging samples identified wave-like fluctuations on the surfaces of the LOx core during 1L- and 1T-mode excitation. The motion of the lighter gaseous flame surrounding the LOx core was also identified from the images. A new method for comparing the local acoustic disturbance with the observed intensity fluctuations was developed using the properties of the multi-variable DMD algorithm and the new complex acoustic field reconstruction method. This approach allowed the phase between the local acoustic and optical intensity fluctuations to be determined in a quantitative manner representative of the mean fluctuation. The peak intensity fluctuations were found to lag the local acoustic pressure disturbance by approximately 45° during 1L- and 1T-mode excitation. The features and motion identified using this flame response analysis method are of particular interest for use in quantitative validation of combustion instability models.

Finally, the response of BKH coaxial injection elements to acoustic excitation was investigated numerically using single injector models subjected to a representative acoustic forcing. A method was developed for imposing a desired acoustic disturbance to excite the unsteady model by modifying the boundary conditions after each physical time step. This approach was used to investigate the response to 1L- and 1T-mode excitation for multiple acoustic disturbance amplitudes.

The results of the single injector models were compared against available experimental optical data. The models reproduced key observations such as the wave-like structures produced on the surface of the LOx core and the deformation of the LOx core and flame during transverse velocity excitation. The experimentally observed trend of further retraction of the LOx core as the amplitude of the transverse velocity disturbance increases was also recovered. The agreement between experimental and numerical results indicated that the employed modelling approach captured the key phenomena observed experimentally.

Further analysis of the single injector model results was used to characterise the flame response and provide further insight than what is possible from the BKH line-of-sight experimental data. An internal acoustic resonance in the LOx post was identified during longitudinal pressure excitation. The internal acoustics of the LOx post shifted the phase of the velocity fluctuation of the oxygen stream at the injection plane. This phase shift caused a fluctuation in the velocity ratio between the fuel and oxidiser streams which was in antiphase with the predicted heat release fluctuations. The single injector model was used to investigate the response at higher longitudinal pressure excitation amplitudes than those obtained experimentally. The model predicted that the wave-like structures on the surface of the LOx core became more pronounced as the amplitude of the disturbance increases, and that the amplitude of the heat release fluctuations were also proportional to the amplitude of the imposed acoustic pressure disturbance.

When the single injector model is subjected to a transverse acoustic velocity disturbance, representative of a 1T-mode disturbance, the LOx core is flattened and consumed as fresh fuel-rich gases are transported into the flame. As the LOx core and flame retract towards the injection plane a non-linear rise of the heat release rate is predicted. It is proposed

that this large non-linear increase in the heat release rate as the established LOx core is consumed may contribute to spontaneous combustion instability phenomena.

Under continuous acoustic forcing the length of the retracted LOx core and flame stabilises and the flame exhibits a flapping motion as it is vertically displaced by the acoustic velocity. The heat release rate fluctuations of the fully retracted flame were predicted to occur at twice the excitation frequency and lag the peak local acoustic pressure disturbance by approximately 45°. The amplitude of the heat release fluctuations were predicted to increase non-linearly as the amplitude of the disturbance increases. The transverse results provided new insight into the degree of horizontal flattening of the LOx core, that was not directly observable from the line-of-sight optical data. The transport of the lighter gases surrounding the cylindrical core by the acoustic velocity was also identified. A rolling-up motion around the initial cylindrical section and leading edge of the flattened LOx core was described and related to previously identified features from the analysis of BKH optical data.

The analyses presented in this thesis have produced new insights and results describing the response of co-axial oxygen-hydrogen flames to acoustic disturbances representative of high-frequency combustion instabilities. The preparation of BKH experimental results for comparison with numerical models has produced new data for numerical validation. Each of the modelling approaches applied in this work were computationally inexpensive compared to other higher-order modelling approaches. By comparing with experimental data, it was shown that the models reproduced the identified experimental observations. The modelling and analysis methods that have been developed in this project will assist future researchers investigating combustion instabilities.

7.1 Future Work

The work undertaken in this project contributes towards an ongoing combustion instability research program. A number of topics were identified over the course of this project which could not be further investigated within the scope of this project. These topics are described in the following paragraphs and may be pursued as part of future work.

Acoustic impedances are required to represent the acoustic response of the injection and nozzle outlet boundary conditions in both CFD and lower-order acoustic models. In the frame of this project real-valued impedances were assumed. Further characterisation of the acoustic boundary conditions of the complicated injection system and nozzles may allow more representative numerical boundary conditions to be defined. The experimental data analysis presented in this thesis, in particular the calculated amplitude and relative phase results shown in Figure 4.1.6, could be used for future validation of acoustic boundary conditions and models.

The limited understanding of the flame emission that is captured in BKH optical imaging datasets meant that only a qualitative comparison between experimental and numerical results was made in this thesis. The qualitative comparison identified features and phenomena that was reproduced numerically. However, before the numerical results can be relied upon to compute desired results, such as flame transfer functions for lower-order modelling approaches, quantitative validation of the predicted flame response is needed. Further interpretation and understanding of the employed imaging methods and results, and comparable post-processing methods for numerical data, are needed before a quantitative comparison can be completed.

The numerical results predicted that the peak heat release occurs at a phase angle of 45° after the peak local pressure disturbance, while the peak OH* concentration occurs in phase with the pressure disturbance. The 45° phase lag matches the lag identified between the local pressure and peak intensity fluctuations from the optical data analysis.

As this phase difference was identified from analysis of OH* intensity and shadowgraph images, it suggests that the observed optical intensity fluctuations may not be associated exclusively with OH* intensity. Further research on the emission of oxygen-hydrogen flames at supercritical pressures is needed to characterise the source of the radiation captured in the BKH optical imaging datasets.

During application of the CFD modelling approach to BKH a number of model parameters were identified that should be investigated further as part of ongoing work. Better justification for the choice of parameter values affecting the breakup of the LOx core and flame structure such as the Prandtl number ratio may improve agreement with experimental observations and increase confidence in the resulting numerical predictions. Validation against cold-flow numerical test cases, such as supercritical nitrogen jet experiments under external acoustic excitation, could be used to validate models and the choice of such parameters. Experiments with higher thermal gradients between the liquid core and surrounding co-flow, representative of a liquid jet surrounded by combustion products, would be more useful for numerical validation.

The single-injector models do not capture the interaction between multiple injection elements that would occur in full scale rocket engine combustion chambers. Multi-element full-chamber BKH simulations could be used to capture this phenomena. The results of these simulations would more closely resemble the experimental configuration and be more directly comparable to BKH optical datasets. Further investigation of injection system coupling involving both the oxygen and hydrogen injectors could also be investigated by including more details of the injection geometry. The unsteady flame response to acoustic disturbances more representative of the experiment may also be investigated by including the influence of the acoustic axial velocity fluctuations during longitudinal mode excitation. The influence of the fuel-rich mixture assumed to enter the domain during the high-pressure part of the acoustic cycle as excitation is imposed on the single injector models should also be investigated.

The results in this thesis have investigated the flame response for a single BKH operating point. The analyses methods developed in this project may be further applied to investigate additional BKH operating points in order to characterise the flame response at different operating points and to different acoustic disturbances. The analyses methods may also be applied to analyse the results and model other combustion instability experiments with the eventual goal of applying similar methods to full-scale rocket combustion chamber systems.

References

[1] D. Banuti, P.C. Ma, J.-P. Hickey, and M. Ihme. Sub- or supercritical? a flamelet analysis for high-pressure rocket propellant injection. In *52nd AIAA/SAE/ASEE Joint Propulsion Conference Salt Lake City, UT*, volume AIAA 2016-4789, 2016.

[2] Daniel Banuti. *Thermodynamic analysis and numerical modeling of supercritical injection*. PhD thesis, University of Stuttgart, 2015.

[3] Daniel T. Banuti and Klaus Hannemann. The absence of a dense potential core in supercritical injection: A thermal break-up mechanism. *Physics of Fluids*, 28(3), 2016.

[4] Daniel T. Banuti, Volker Hannemann, Klaus Hannemann, and Bernhard Weigand. An efficient multi-fluid-mixing model for real gas reacting flows in liquid propellant rocket engines. *Combustion and Flame*, 168:98 – 112, 2016.

[5] D.T. Banuti. Crossing the widom-line - supercritical pseudo-boiling. *Journal of Supercritical Fluids*, 98:12–16, 2015.

[6] J. E. Bardina, P. G. Huang, and T. J. Coakley. Turbulence modeling validation, testing, and development. Technical Report 19970017828, NASA, 1997.

[7] Javier Bartolome Calvo. *Numerical Simulation of Liquid Rocket Engine Cooling Channels*. PhD thesis, Universitat Politecnica de Catalunya, 2010.

[8] Michael J. Bedard, S.V. Sardeshmukh, Tristan L. Fuller, William E. Anderson, and Mitsuaki Tanabe. Chemiluminescence as a diagnostic in studying combustion instability in a practical combustor. In *50th AIAA/ASME/SAE/ASEE Joint Propulsion Conference*, volume AIAA 2014-3660, 2014.

[9] Josette Bellan. Theory, modeling and analysis of turbulent supercritical mixing. *Combustion science and technology*, 178:253–281, 2006.

[10] S. Candel, M. Juniper, G. Singla, P. Scouflaire, and Rolon C. Structure and dynamics of cryogenic flames at supercritical pressures. *Combustion Science and Technology*, 178(01/03/12):161–192, 2006.

[11] N. Chigier and R.D. Reitz. *Recent advances in spray combustion: spray atomization and droplet burning phenomena*, volume 166, chapter Regimes of jet breakup and breakup mechanisms (physical aspects), pages 109–135. AIAA, New York, 1995.

[12] Ting Horng Chung, Mohammad Ajlan, Lloyd L. Lee, and Kenneth E. Starling. Generalized multiparameter correlation for nonpolar and polar fluid transport properties. *Industrial & Engineering Chemistry Research*, 27(4):671–679, 1988.

[13] L. Crocco and S. Cheng. *Theory of Combustion Instability in Liquid Propellant Rocket Motors*. AGARDOGRAPH No. 8. Butterworth Publications Ltd., 1956.

[14] L. Crocco and W.A. Sirignano. *Behavior of Supercritical Nozzles Under Three-Dimensional Oscillatory Conditions*. AGARDOGRAPH 117. Butterworth Publications Ltd., London, England, 1967.

[15] Luigi Crocco. Aspects of combustion stability in liquid propellant rocket motors part i: Fundamentals. low frequency instability with monopropellants. *Journal of the American Rocket Society*, 21:163–178, Nov-Dec 1951.

[16] Fred E.C. Culick and Vigor Yang. Overview of Combustion Instabilites in Liquid-Propellant Rocket Engines. *AIAA: Progress in Astronautics and Aeronautics*, 169:3–38, 1995.

[17] Rainer N. Dahms and Joseph C. Oefelein. Liquid jet breakup regimes at supercritical pressures. *Combustion and Flame*, 162(10):3648 – 3657, 2015.

[18] R.N. Dahms and J.C. Oefelein. On the transition between two-phase and single-phase interface dynamics in multicomponent fluids at supercritical pressures. *Physics of Fluids*, 25(092103-1), 2013.

[19] R.N. Dahms and J.C. Oefelein. Atomization and dense-fluid breakup regimes in liquid rocket engines. *Journal of Propulsion and Power*, DOI: 10.2514/1.B35562, 2015.

[20] Massimiliano DeBenedictis and Gerard Ordonneau. High Frequency Injection Coupled Combustion Instabilities-Study of Combustion Chamber/Feed System Coupling. In *42nd AIAA/ASME/SAE/ASEE Joint Propulsion Conference & Exhibit*, Sacramento, California, 6-9 July 2006.

[21] Q. Douasbin, S. Gröning, L. Urbano, A. Selle, J.S. Hardi, W. Armbruster, and M. Oschwald. Joint experimental, LES and helmholtz analysis of self-excited combustion instabilities in a hydrogen-oxygen rocket combustor. In *Thermoacoustic Instabilities in Gas turbines and Rocket Engnines: Industry meets Academia*, number GTRE-027, Munich, May 30 - June 2 2016.

[22] Arnold Eucken. Über das Wärmeleitvermögen, die spezifische Wärme und die innere Reibung der Gase. *Physik. Zeits.*, 14(324), 1913.

[23] T. Fiala. *Radiation from High Pressure Hydrogen-Oxygen Flames and its Use in Assessing Rocket Combustion Instability*. PhD thesis, TU München, 2015.

[24] T. Fiala and T. Sattelmayer. Assessment of existing and new modeling strategies for the simulation of OH* radiation in high-temperature flames. *CEAS Space Journal*, 8:47–58, 2016.

[25] Gary A. Flandro, Sean R. Fischbach, and Joseph Majdalani. Nonlinear rocket motor stability prediction: Limit amplitude, triggering, and mean pressure shift. *Physics of Fluids*, 19(9), 2007.

[26] Gary A. Flandro, Joseph Majdalani, and Joseph D. Sims. On nonlinear combustion instability in liquid propellant rocket engines. In *40th AIAA/ASME/SAE/ASEE Joint Propulsion Conference and Exhibit*, number AIAA 2004-3516, Fort Lauderdale, Florida, 11-14 July 2004.

[27] M.L. Frezzotti, F. Nasuti, C. Huang, C.L. Merkle, and W.E. Anderson. Parametric analysis of response function in modeling combustion instability by a quasi-1d solver. In *6th EUCASS, Krakow*, 2015.

[28] R. L. Gaffney, J. A. White, S. S. Girirnaji, and J. P. Drummond. Modeling turbulent/chemistry interactions using assumed pdf methods. In *AIAA/SAE/ASME/ASEE Joint Propulsion Conference and Exhibit*, Nashville, TN, July 6-8 1992.

[29] Romain Garby. *Simulations of flame stabilization and stability in high-pressure propulsion systems.* PhD thesis, Institut de Mécanique des Fluides de Toulouse - IMFT (Toulouse, France), 2013.

[30] A. G. Gaydon. *The Spectroscopy of Flames - Second Edition.* Chapman & Hall LTD, 1974.

[31] T. Gerhold, O. Friedrich, J. Evans, and M. Galle. Calculation of Complex Three-Dimensional Configurations Employing the DLR-TAU-Code. *AIAA paper 97-0167*, 1997.

[32] Peter Gerlinger, Helge Mbus, and Dieter Brggemann. An implicit multigrid method for turbulent combustion. *Journal of Computational Physics*, 167(2):247 – 276, 2001.

[33] M. Gonzalez-Flesca, T. Schmitt, S. Ducruix, and S. Candel. Large eddy simulations of a transcritical round jet submitted to transverse acoustic modulation. *Physics of Fluids*, 28(5), 2016.

[34] S. Gröning, J.S. Hardi, D. Suslov, and M. Oschwald. Injector-driven combustion instabilities in a hydrogen/oxygen rocket combustor. *Journal of Propulsion and Power*, 32(3):560–573, 2016.

[35] S. Gröning, M. Oschwald, and T. Sattelmayer. Selbst erregte tangentiale Moden in einer Raketenbrennkammer unter repräsentativen Bedingungen. In *61. Deutscher Luft- und Raumfahrtkongress*, Berlin, 2012. Deutsche Gesellschaft für Luft- und Raumfahrt (DGLR).

[36] S. Gröning, M. Oschwald, and T. Sattelmayer. Einfluss einer Kavität auf das Druckfeld der ersten Tangentialen Mode einer Raketenbrennkammer unter repräsentativen Bedingungen. In *Deutscher Luft- und Raumfahrtkongress (DLRK)*, 2013.

[37] S. Gröning, D. Suslov, M. Oschwald, and T. Sattelmayer. Stability behaviour of a cylindrical rocket engine combustion chamber operated with liquid hydrogen and liquid oxygen. In *5th EUCASS, Munich*, 2013.

[38] Stefan Gröning, Justin Hardi, Dmitry Suslov, and Michael Oschwald. Influence of hydrogen temperature on the stability of a rocket engine combustor operated with hydrogen and oxygen. *CEAS Space Journal*, 9:59–76, 2017.

[39] R.N. Gupta, J.M. Yos, R.A. Thompson, and K.P. Lee. A review of reaction rates and thermodynamic and transport properties for an 11-species air model for chemical and thermal nonequilibrium calculations to 30000 K. Technical Report No. 1232, NASA Reference Publication, 1990.

[40] E.J. Gutmark and Chih-Ming Ho. Preferred modes and the spreading rates of jets. *Physics of Fluids*, 26:2932–2938, 1983.

[41] L. Hakim, A. Ruiz, T. Schmitt, M. Boileau, G. Staffelbach, S. Ducruix, B. Cuenot, and S. Candel. Large eddy simulations of multiple transcritical coaxial flames submitted to a high-frequency transverse acoustic modulation. *Proceedings of the Combustion Institute*, 35(2):1461–1468, 2015.

[42] L. Hakim, T. Schmitt, S. Ducruix, and S. Candel. Dynamics of a transcritical coaxial flame under a high-frequency transverse acoustic forcing: Influence of the modulation frequency on the flame response. *Combustion and Flame*, 162:3482–3502, 2015.

[43] V. Hannemann. Numerische simulation von stoß- stoß- wechselwirkungen unter berücksichtigung von chemischen und thermischen nichtgleichgewichtseffekten. Technical Report FB 97-07, DLR, 1997.

[44] J. Hardi, H.C. Gomez Martinez, and M. Oschwald. LOx jet atomization under transverse acoustic oscillations. *Journal of Propulsion and Power*, 30(2):337–349, 2014.

[45] J. Hardi, M. Oschwald, and B. Dally. Flame response to acoustic excitation in a rectangular rocket combustor with LOx/H2 propellants. *CEAS Space Journal*, 2:41–49, 2011.

[46] J. S. Hardi and M. Oschwald. Cryogenic oxygen jet response to transverse acoustic excitation with the first transverse and the first combined longitudinal-transverse modes. In *EUCASS Proceedings Series: Advances in AeroSpace Sciences*, volume 8, pages 75–94, 2016.

[47] J.S. Hardi, W.Z. Hallum, C. Huang, and W.E. Anderson. Development of validation approaches for numerical simulation of combustion instability using flame imaging. *50th AIAA/ASME/SAE/ASEE Joint Propulsion Conference*, AIAA 2014-3775, 2014.

[48] J.S. Hardi, W.Z. Hallum, C. Huang, and W.E. Anderson. Approaches for comparing numerical simulation of combustion instability and flame imaging. *Journal of Propulsion and Power*, 32:279–294, 2016.

[49] Justin S. Hardi. *Experimental Investigation of High Frequency Combustion Instability in Cryogenic Oxygen-Hydrogen Rocket Engines.* PhD thesis, The University of Adelaide, 2012.

[50] Justin S. Hardi, Scott K. Beinke, Michael Oschwald, and Bassam B. Dally. Coupling of cryogenic oxygen-hydrogen flames to longitudinal and transverse acoustic instabilities. *Journal of Propulsion and Power*, 30:991–1004, 2014.

[51] Justin S Hardi, Michael Oschwald, and Bassam Dally. Acoustic characterisation of a rectangular rocket combustor with liquid oxygen and hydrogen propellants. *Proceedings of the Institution of Mechanical Engineers, Part G: Journal of Aerospace Engineering*, 227(3):436–446, 2013.

[52] D.T. Harrje and F.H. Reardon, editors. *Liquid propellant rocket combustion instability.* National Aeronautics and Space Administration, Washington, DC, 1972.

[53] Matthew E. Harvazinski, William E. Anderson, and Charles L. Merkle. Combustion Instability Diagnostics Using the Rayleigh Index. In *47th AIAA/ASME/SAE/ASEE Joint Propulsion Conference & Exhibit*, San Diego, California, 31 July - 3 August 2011.

[54] Matthew E. Harvazinski, William E. Anderson, and Charles L. Merkle. Analysis of self-excited combustion instabilities using two- and three-dimensional simulations. *Journal of Propulsion and Power*, 29(2):396–409, 2013.

[55] Matthew E. Harvazinski, Cheng Huang, Venkateswaran Sankaran, Thomas W. Feldman, William E. Anderson, Charles L. Merkle, and Douglas G. Talley. Coupling between hydrodynamics, acoustics, and heat release in a self-excited unstable combustor. *Physics of Fluids*, 27(4), 2015.

[56] Marcus F. Heidman and Paul R. Wieber. Analysis of Frequency Response Characteristics of Propellant Vaporization. Technical Note D-3749, NASA, 1966. NASA Lewis Research Center Colorado.

[57] J.O. Hirschfelder. Generalization of the Eucken Approximation for the Heat Conductivity of Polyatoomic or Chemically Reacting Gas Mixtures. In *Conference on Thermodynamics and Transport Properties of Fluids*. the International Union of Pure and Applied Chemistry and the Institute of Mechanical Engineers, 1012 July 1957.

[58] Cheng Huang, William E. Anderson, Matthew E. Harvazinski, and Venkateswaran Sankaran. Analysis of self-excited combustion instabilities using decomposition techniques. *AIAA Journal*, 54:9:2791–2807, 2016.

[59] Andreas Huber. *Impact of fuel supply impedance and fuel staging on gas turbine combustion stability*. PhD thesis, Lehrstuhl für Thermodynamik, TU München, Garching, 2009.

[60] John J. Hutt and Marvin Rocker. *Liquid Rocket Engine Combustion Instability*, volume 169, chapter High Frequency Injection-Coupled Combustion Instabilites, pages 345–357. American Institute of Aeronautics and Astronautics, 1995.

[61] B. Ivancic and W. Mayer. Time- and length scales of combustion in liquid rocket thrust chambers. *Journal of Propulsion and Power*, 2:247–253, 2002.

[62] B. Ivancic, H. Riedmann, M. Frey, O. Knab, S. Karl, and K. Hannemann. Investigation of different modeling approaches for computational fluid dynamics simulation of high-pressure rocket combustors. *Progress in Propulsion Physics*, 8:95–116, 2016.

[63] Casimir J. Jachimowski. An analytical study of the hydrogen-air reaction mechanism with application to scramjet combustion. Technical Paper 2791, NASA, Langley Research Center Hampton, Virginia, 1988.

[64] Eric J. Jacob. *A Study of Nonlinear Combustion Instability*. PhD thesis, University of Tennessee Space Institute, 2009.

[65] R. Kaess, S. Koeglmeier, R. Behr, J.-P. Rocchi, C. Cruz, and O. Knab. Liquid propellant rocket combustion stability rating evaluation using single flame calculations for combustion dyamics. In *Thermoacoustic Instabilities in Gas turbines and Rocket Engnines: Industry meets Academia*, number GTRE-054, Munich, May 30 - June 2 2016.

[66] S. Karl and H. Luedeke. Application of the DLR TAU Code to Predict acoustic damping rates in generic combustion chamber configurations. Technical Report DLR IB 224 2012 A67, DLR Institute of Aerodynamics and Flow Technology, 2008.

[67] Sebastian Karl. *Numerical Investigation of a Generic Scramjet Configuration*. PhD thesis, Technische Universität Dresden, 2011.

[68] A. Kaufmann, F. Nicoud, and T. Poinsot. Flow forcing techniques for numerical simulation of combustion instabilities. *Combustion and Flame*, 131:371385, 2002.

[69] Bernhard Knapp, Zoltan Farago, and Michael Oschwald. Interaction of LOX/GH2 Spray-Combustion with Acoustics. In *45th AIAA ASME*, 2007.

[70] Bernhard Knapp and Michael Oschwald. High Speed Visualization of Flame Response in a LOX/H2 Combustion Chamber During External Excitation. In *12th International Symposium on Flow Visualisation September 10-14 German Aerospace Center (DLR), Göttingen, Germany*. German Aerospace Center (DLR), 10-14 September 2006.

[71] Kan Kobayashi, Yu Daimon, Nobuyuki Iizuka, Hiroshi Tamura, Tohru Mitani, and Takuo Onodera. Studies on Combustion Instability for Liquid Propellant Rocket Engines. In *47th AIAA/ASME/SAE/ASEE Joint Propulsion Conference & Exhibit*, San Diego, California, 31 July - 3 August 2011.

[72] G. Lacaze and J.C. Oefelein. A non-premixed combustion model based on flame structure analysis at supercritical pressures. *Combustion and Flame*, 159:2087–2103, 2012.

[73] R. Lecourt and R. Foucaud. Experiments on stability of liquid propellant rocket motors. In *AIAA/SAE/ASME/ASEE 23rd Joint Propulsion Conference*, San Diego California, 29 June - 2 July 1987.

[74] E.W. Lemmon and R.T. Jacobsen. Viscosity and thermal conductivity equations for nitrogen, oxygen, argon, and air. *International Journal of Thermophysics*, 25(1):21–69, 2004.

[75] M. Lempke, P. Gerlinger, and M. Aigner. Assumed pdf modeling in rocket combustor simulations. *Progress in Propulsion Physics*, 4:569–582, 2013.

[76] Markus Lempke, Peter Gerlinger, Manfred Aigner, and Michael Rachner. Steady and Unsteady RANS Simulations of Cryogenic Rocket Combustors. In *49th AIAA Aerospace Sciences Meeting including the New Horizons Forum and Aerospace Exposition*, Orlando, Florida, 4-7 January 2011.

[77] A. Mack and V. Hannemann. Validation of the unstructured DLR TAU-code for hypersonic flows. In *Proceedings of the 32nd AIAA Fluid Dynamics Conference and Exhibit*, number AIAA-2002-3111, St. Louis, Missouri, 2002.

[78] F. E. Marble and S. M. Candel. Acoustic Disturbance from Gas Non-uniformities Convected through a Nozzle. *Journal of Sound and Vibration*, 55(2):225–243, 1977.

[79] S. Matsuyama, D. Hori, T. Shimizu, S. Tachibana, S. Yoshida, and Y. Mizobuchi. Large-eddy simulation of high-frequency combustion instability in a single-element atmospheric combustor. *Journal of Propulsion and Power*, 32:628–645, 2016.

[80] W. Mayer and H. Tamura. Propellant Injection in a Liquid Oxygen/Gaseous Hydrogen Rocket Engine. *Journal of Propulsion and Power*, 12(6):1137–1147, 1996.

[81] W. Mayer, J. Telaar, R. Branam, G. Schneider, and J. Hussong. Raman measurements of cryogenic injection at supercritical pressure. *Heat and Mass Transfer*, 39:709–719, 2003.

[82] W.O.H. Mayer and J. Smith. Fundamentals of supercritical mixing and combustion of cryogenic propellants. *Progress in Astronautics and Aeronautics*, 200:339–367, 2004.

[83] Y. Mery, L. Hakim, P. Scouflaire, L. Vingert, S. Ducruix, and S. Candel. Experimental study of the combustion-acoustics coupling in liquid rocket engine high-frequency instabilities. In *Space Propulsion Conference*, Bordeaux, France, 7-10 May 2012.

[84] Yoann Mery, Sebastien Ducruix, Philippe Scouflaire, and Sebastien Candel. Injection coupling with high amplitude transverse modes: Experimentation and simulation. *Comptes Rendus Mcanique*, 337(6):426 – 437, 2009.

[85] Yoann Mery, Layal Hakim, Philippe Scouflaire, Lucien Vingert, Sebastien Ducruix, and Sebastien Candel. Experimental investigation of cryogenic flame dynamics under transverse acoustic modulations. *Comptes Rendus Mcanique*, 341(1):100 – 109, 2013.

[86] C.J. Morgan, K.J. Shipley, and W.E. Anderson. Comparative evaluation between experiment and simulation for a transverse instability. *Journal of Propulsion and Power*, 31(6):1696–1706, 2015.

[87] J.A. Newman and T.A. Brzustowski. Behavior of a liquid jet near the thermodynamic critical region. *AIAA Journal*, 9(8):15951602, 1971.

[88] Franck Nicoud, Laurent Benoit, Claude Sensiau, and Thierry Poinsot. Acoustic modes in combustors with complex impedances and multidimensional active flames. *AIAA Journal*, 45(2):426–441, 2007.

[89] Y. Nunome, M. Takahashi, A. Kumakawa, K. Miyazaki S. Yoshida, and T. Onga. High-frequency Flame Oscillation Observed at a Coaxial LOX/LH2 Injector Element. In *44th AIAA/ASME/SAE/ASEE Joint Propulsion Conference & Exhibit*, Hartford, CT, 21 - 23 July 2008.

[90] Yoshio Nunome, Takuo Onodera, Masaki Sasaki, Takeo Tomita, Kan Kobayashi, and Yu Daimon. Combustion Instability Phenomena Observed During Cryogenic Hydrogen Injection Temperature Ramping Tests for Single Coaxial Injector Elements. In *47th AIAA/ASME/SAE/ASEE Joint Propulsion Conference & Exhibit*, San Diego, California, 31 July - 03 August 2011.

[91] J.C. Oefelein and V. Yang. Comprehensive review of liquid-propellant combustion instabilties in f-1 engines. *Journal of Propulsion and Power*, 9(5):657–677, 1993.

[92] J.C. Oefelein and V. Yang. Modeling high-pressure mixing and combustion processes in liquid rocket engines. *Journal of Propulsion and Power*, 14(5):843–857, 1998.

[93] Joseph C. Oefelein. Thermophysical Characteristics of Shear-coaxial LO_x-H_2 Flames at Supercritical Pressure. *Proceedings of the Combustion Institute*, 30:2929–2937, 2005.

[94] Joseph C. Oefelein. Mixing and Combustion of Cryogenic Oxygen-Hydrogen Shear-Coaxial Jet Flames at Supercritical Pressure. *Combustion Science and technology*, 178:229–252, 2006.

[95] M. Oschwald, Z. Farago, G. Searby, and F. Cheuret. Resonance frequencies and damping of a combustor acoustically coupled to an absorber. *Journal of Propulsion and Power*, 24:524–533, May-June 2008.

[96] M. Oschwald and B. Knapp. *EUCASS Advances in Aerospace Sciences*, chapter Investigation of combustion chamber acoustics and its interaction with LOX/H2 spray flames, pages 243–262. Torus Press & EDP Sciences, 2009.

[97] M. Oschwald and A. Schik. Supercritical nitrogen free jet investigated by spontaneous raman scattering. *Experiments in Fluids*, 27:497–506, 1999.

[98] M. Oschwald, J.J. Smith, R. Branam, J. Hussong, A. Schik, B. Chehroudi, and D. Talley. Injection of fluids into supercritical environments. *Combustion Science and Technology*, 178:49–100, 2006.

[99] D.-Y. Peng and D.P. Robinson. A new two-constant equation of state. *Industrial & Engineering Chemistry Fundamentals*, 15(1):5964, 1976.

[100] A. Pfennig. *Thermodynamik der Gemische.* Springer, 1st edition, 2003.

[101] J. Pieringer and T. Sattelmayer. Numerical Evaluation of the Impact of the Rocket Nozzle on the Evolution of Combustion Instabilities. In *2nd European Conference for Aerospace Sciences (EUCASS)*, Brussels, Belgium, 1-6 July 2007.

[102] T. J. Poinsot and S. K. Lele. Boundary conditions for direct simulations of compressible viscous flows. *Jounral of Computational Physics*, 101:104–129, 1992.

[103] Brian R. Pomeroy, Colling Morgan, and William E. Anderson. Response of a Gas-Centered Swirl Coaxial Injector to Transverse Instabilities. In *47th AIAA/ASME/SAE/ASEE Joint Propulsion Conference & Exhibit 31 July - 03 August 2011, San Diego, California*, 2011.

[104] Brian R. Pomeroy, Nicholas Nugent, and William E. Anderson. Measuring Transverse Combustion Stability at Full Scale Frequencies in a Subscale Combustor. In *46th AIAA/ASME/SAE/ASEE Joint Propulsion Conference & Exhibit*, Nashville, TV, 25-28 July 2010.

[105] J.E. Portillo, J.C. Sisco, Y. Yu, W.E. Anderson, and V. Sankaran. Application of a generalized instability model to a longitudinal mode combustion instability. In *43rd AIAA/ASME/SAE/ASEE Joint Propulsion Conference and Exhibit*, 2007.

[106] Richard J. Priem. Guidlelines for combustion stability specifications and verficiation procedures for liquid propellant rocket engines. Technical Report CPIA Publication 655, Chemical propulsion Information Agency, 1997.

[107] A.A. Putnam and W.R. Dennis. A study of burner oscillations of the organ-pipe type. *Transact. of the ASME*, 76(1), 1953.

[108] Abbott A. Putnam. *Combustion-driven oscillations in industry.* American Elsevier Publishing Company Inc., New York, 1971.

[109] Abbott A. Putnam and William Dennis. Organ-pipe osciallations in a flame-filled tube. *Symposium (International) on Combustion*, 4, issue 1(1):566–575, 1953.

[110] T. Ramcke, M. Schmid, and T. Sattelmayer. Response characterization of LOX-GH2 flame to forced acoustic pressure fuctuations. In *5th EUCASS, Munich*, 2013.

[111] B.J.W.S. Rayleigh. *The Theory of Sound.* Dover Publications, Constable & CO LTD, fisrt edition, 1878.

[112] C. Rey, S. Ducruix, and S. Candel. A method for the transverse modulation of reactive flows with application to combustion instability. *Combustion Theory and Modelling*, 9:5–22, February 2005.

[113] C. Rey, S. Ducruix, P. Scouflaire, and S. Candel. Experimental Analysis of High Frequency Combustion Instabilities Associated with Collective Interactions. In *Proceedings of PSFVIP-4*. Ecole Centrale Paris and C.N.R.S, 2003.

[114] Cedric Rey, Sebastien Ducruix, Franck Richecoeur, Phillippe Scouflaire, Lucien Vingert, and Sebastian Candel. High Frequency Combustion Instabilies Associated with Collective Interactions in Liquid Propulsion. In *40th AIAA/ASME/SAE/ASEE Joint Propulsiton Conference and Exhibit*, Fort Lauderdale, Florida, 11-14 July 2004.

[115] Guillaume Ribert, Nan Zong, Vigor Yang, Laetitia Pons, Nasser Darabiha, and Sebastien Candel. Counterflow diffusion flames of general fluids: Oxygen/hydrogen mixtures. *Combustion and Flame*, 154(3):319 – 330, 2008.

[116] F. Richecoeur, S. Ducruix, P. Scouflaire, and S. Candel. Experimental Investigation of High-Frequency Combustion Instabilities in Liquid Rocket Engine. *Acta Astronautica*, 62:18–27, 2008.

[117] F. Richecoeur, L. Hakim, A. Renaud, and L. Zimmer. DMD algorithms for experimental data processing in combustion. In *Proceeding of the 2012 Summer Program, Center for Turbulence Research, Stanford University*, pages 459–468, 2012.

[118] Franck Richecoeur, Sebastien Ducruix, Phillippe Scouflaire, and Sebastian Candel. Effect of Temperature Fluctuations on High Frequency Acoustic Coupling. *Proceedings of the Combustion Institute*, 32:1663–1670, 2009.

[119] Franck Richecoeur, Philippe Scouflaire, Sebastien Ducruix, and Sebastien Candel. High-Frequency Transverse Acoustic Coupling in a Multiple-Injector Cryogenic Combustor. *Journal of Propulsion and Power*, 22(4):790–799, July-August 2006.

[120] Chandler C. Ross and Paul P. Datner. *Selected Combustion Problems, Fundamentals and Aeronautical Applications*, chapter Combustion Instability in Liquid Propellant Rocket Motors - A Survey, pages 352–380. Butterworths Scientific Publications, 1954.

[121] C.-C. Rossow. Extension of a compressible code toward the incompressible limit. *AIAA Journal*, 41(12):2379–2386, 2003.

[122] V.R. Rubinsky. *Liquid Rocket Engine Combustion Instability*, volume 169, chapter Combustion Instability in the RD-0110 Engine, pages 89–112. American Institute of Aeronautics and Astronautics, 1995.

[123] S.V. Sardeshmukh, Michael J. Bedard, Tristan L. Fuller, and William E. Anderson. The Use of OH* and CH* as Heat Release Markers in Combustion Dynamics. In *Thermoacoustic Instabilities in Gas turbines and Rocket Engnines: Industry meets Academia*, number GTRE-026, Munich, May 30 - June 2 2016.

[124] Swanand V. Sardeshmukh, William E. Anderson, Matthew E. Harvazinski, and Venkateswaran Sankaran. Prediction of combustion instability with detailed chemical kinetics. In *53rd AIAA Aerospace Sciences Meeting, AIAA SciTech*, volume 16, 2015.

[125] T. Sattelmayer, R. Kathan, S. Köglmeier, and A. Nicole. Transverse instability damping computations for rocket engines. *Journal of Propulsion and Power*, 31(4):1148–1158, 2015.

[126] T. Sattelmayer, M. Schmid, and M. Schulze. Impact of injector mass flow fluctuations on combustion dynamics in liquid engines. *Journal of Spacecraft and Rockets*, 52(5):1417–1429, 2015.

[127] M. Schmid. *Thermoakustische Kopplungsmechanismen in Flüssigkeitsraketentriebwerken*. PhD thesis, Munich Technical University, 2014.

[128] M. Schmid and T. Sattelmayer. Influence of pressure and velocity perturbations on the heat release fluctuations for coaxial GH2/GO2 injection. In *4th European Conference for Aerospace Sciences (EUCASS)*, Saint Petersburg, July 4 - 8 2011.

[129] M. Schmid and T. Sattelmayer. Interaction of Acoustic Pressure Fluctuations with Supercritical Nitrogen Jets. In *48th AIAA/ASME/SAE/ASEE Joint Propulsion Conference & Exhibit*, Atlanta, Georgia, 30 July - 01 August 2012.

[130] Peter J. Schmid. Dynamic mode decomposition of numerical and experimental data. *Journal of Fluid Mechanics*, 656(doi:10.1017/S0022112010001217):528, 2010.

[131] Peter J. Schmid. Dynamic mode decomposition. 1. October 2013.

[132] T. Schmitt, J. Rodrigues, I.A. Leyva, and S. Candel. Experiments and numerical simulation of mixing under supercritical conditions. *Physics of Fluids*, 24(055104), 2012.

[133] M. Schulze, J. Gikadi, and T. Sattelmayer. Acoustic admittance prediction of two nozzle designs of different length using frequency domain simulation. In *5th EUCASS, Munich*, 2013.

[134] M. Schulze and T. Sattelmayer. Linear stability assessment of a cryogenic rocket engine. In *Thermoacoustic Instabilities in Gas turbines and Rocket Engnines: Industry meets Academia*, number GTRE-055, Munich, May 30 - June 2 2016.

[135] D. Schwamborn, T. Gerhold, and V. Hannemann. *On the Validation of the DLR-TAU Code*, chapter 72, pages 426 – 433. Number ISBN 3-528-03122-0. New Results in Numerical and Experimental Fluid Mechanics, Notes on Numerical Fluid Mechanics, 1999.

[136] Dieter Schwamborn, Thomas Gerhold, and Ralf Heinrich. The DLR TAU-code: Recent Applications in Research and Industry. In P. Wesseling, E. Onate, and J. Périaux, editors, *European Conference on Computational Fluid Dynamics (ECCOMAS CFD)*, TU Delft, The Netherlands, September 5-8 2006.

[137] Laurent Selle, Franck Nicoud, and Thierry Poinsot. Actual impedance of nonreflecting boundary conditions: Implications for computation of resonators. *AIAA Journal*, 42(5):958–964, 2004.

[138] T. Shimizu, D. Hori, S. Yoshida, S. Tachibana, S. Matsuyama, J. Shinjo, Y. Mizobushi, and K. Kobayashi. On acoustic damping of a cylindrical chamber in resonant modes. *Fluid Dynamics Research*, 44(045506):1–20, 2012.

[139] Kevin James Shipley. *Multi-injector Modeling of Transverse Combustion Instability Experiments*. PhD thesis, Purdue University, 2014.

[140] G.G. Simeoni, T. Bryk, F.A. Gorelli, M. Krisch, G. Ruocco, M. Santoro, and T. Scopigno. The widom line as the crossover between liquid-like and gas-like behaviour in supercritical fluids. *Nature Physics*, 6:503–506, 2010.

[141] W. A. Sirignano, J. P. Delplanque, C H. Chiang, and R. Bhatia. *Liquid Rocket Engine Combustion Instability*, volume 169, chapter Liquid-Propellant Droplet Vaporization: A Rate-Controlling Process for Combustion Instability, pages 307–343. American Institute of Aeronautics and Astronautics, 1995.

[142] James C. Sisco, Randolph J. Smith, Vebkateswaran Sankaran, and William E. Anderson. Examination of Mode Shapes in an Unstable Model Rocket Combustor. In *42nd AIAA/ASME/SAE/ASEE Joint Propulsion Conference & Exhibit*. Purdue, 2006.

[143] M. Sliphorst, S. Gröning, and M. Oschwald. Theoretical and experimental identification of acoustic spinning mode in a cylindrical combustor. *Journal of Propulsion and Power*, 27(1):182–189, 2011.

[144] Mark Sliphorst. *High Frequency Combustion Instabilities of LO_x/CH_4 Spray Flames in Rocket Engine Combustion Chambers*. PhD thesis, Technische Universiteit Delft, 2011.

[145] R. Smith, M. Ellis, G. Xia, V. Sankaran, W. Anderson, and C.L. Merkle. Computational Investigation of Acousitcs and Instabilities in a Longitudinal - Mode Rocket Combustor. *AIAA Journal*, 46:2659–2673, 2008.

[146] R. Smith, G. Xia, W. Anderson, and C.L. Merkle. Computational studies of the effect of oxidiser injector length on combustion instability. *Combustion Theory and Modelling*, vol. 16(no. 2), 2012.

[147] G. Soave. Equilibrium constants from a modified redlich-kwong equation of state. *Chemical Engineering Science*, 27:11971203, 1972.

[148] P.R. Spalart and S.R. Allmaras. A one-equation turbulence model for aerodynamic flows. In *30th Aerospace Sciences Meeting and Exhibit, Aerospace Sciences Meetings*, number AIAA-92-0439, Reno,NV,U.S.A., 6-9 January 1992.

[149] S. Srinivasan, R. Ranjan, and S. Menon. Flame dynamics during combustion instability in a high-pressure, shear-coaxial injector combustor. *Flow, Turbulence and Combustion*, 94(1):237–262, 2015.

[150] George P. Sutton. History of Liquid-Propellant Rocket Engines in Russia, Formerly the Soviet Union. *Journal of Propulsion and Power*, 19(6):1008–1037, November-December 2003.

[151] George P. Sutton and Oscar Biblarz. *Rocket Propulsion Elements*. John Wiley & Sons, 2010.

[152] A. Urbano, Q. Douasbin, L. Selle, G. Staffelbach, B. Cuenot, T. Schmitt, S. Ducruix, and S. Candel. Study of flame response to transverse acoustic modes from the LES of a 42-injector rocket engine. *Proceedings of the Combustion Institute*, 36, Issue 2:26332639, 2017.

[153] A. Urbano, L. Selle, G. Staffelbach, B. Cuenot, T. Schmitt, S. Ducruix, and S. Candel. Exploration of combustion instability triggering using large eddy simulation of a multiple injector liquid rocket engine. *Combustion and Flame*, 169:129–140, 2016.

[154] Bram van Leer. Towards the ultimate conservation difference scheme. v. a second-order sequel to godunovs method. *Journal of Computational Physics*, 32(1):101 136, 1979.

[155] B. Vieille, C. Chauveau, and I. Gökalp. Studies on the break-up regimes of LOX-droplets. In *37th AIAA Aerospace Sciences Meeting and Exhibit*, number AIAA 99-0208, Reno, NV, January 11-14 1999.

[156] John P. Wanhainen, Harold C. Parish, and E. William Conrad. Effect of Propellant Injection Velocity on Screech in a 20,000 Pound Hydrogen-Oxygen Rocket Engine. Technical Note TN D-3373, NASA, 1966.

[157] J.P. Wanhainen, C.E. Feiler, and C.J. Morgan. Effect of chamber pressure, flow per element, and contraction ratio on acoustic-mode instability in hydrogen-oxygen rockets. *NASA*, NASA-TN-D-4733:36, 1968.

[158] J.P. Wanhainen and C.J. Morgan. Effect of injection element radial distribution and chamber geometry on acoustic-mode instability in a hydrogen oxygen rocket. *NASA*, NASA-TN-D-5375:45, 1969.

[159] Samuel Charles Leslie Webster. *Analysis of Pressure Dnymaics, Forced Excitation and Damping in a High Pressure LOX/H2 Combustor*. PhD thesis, RWTH Aachen University, 2016. DLR Forschungsbericht 2016-17.

[160] M. Wierman, N. Nugent, and W. Anderson. Combustion response of a LOX/LCH4 element to transverse instabilites. In *47th AIAA/ASME/SAE/ASEE Joint Propulsion Conference & Exhibit*, San Diego, California, 31 July - 3 August 2011.

[161] Matthew Wierman. *Measurement of combustion response to transverse modes at high pressure*. PhD thesis, Purdue University, 2014.

[162] Wierman, M., Pomeroy, B., and Anderson, W. Development of combustion response functions in a subscale high-pressure transverse combustor. In Array, editor, *EUCASS Proceedings Series Advances in AeroSpace Sciences*, volume 8, pages 55–74, 2016.

[163] David C. Wilcox. *Turbulence Modelling for CFD (Third Edition)*. DCW industries, 2006.

[164] C. R. Wilke. A viscosity equation for gas mixtures. *The Journal of Chemical Physics*, 18(4):517–519, 1950.

[165] Anthony Young. *The Saturn V F-1 Engine: Powering Apollo Into History*. Praxis Publishing Ltd., 2009.

[166] B. A. Younglove. Thermophysical properties of fluids. 1. argon, ethylene, parahydrogen, nitrogen, nitrogen trifluoride and oxygen. *Journal of Physical and Chemical Reference Data*, 11:Supplement No. 1, 1982.

[167] Y. C. Yu, J. C. Sisco, V. Sankaran, and W. E. Anderson. Effects of Mean Flow, Entropy Waves, and Boundary Conditions on Longitudinal Combustion Instability. *Combustion Science and technology*, 182:7:739–776, 2010.

[168] Michelle. M Zaller and Mark D. Klem. *Liquid Rocket Engine Combustion Instability,*, chapter 7: Shear Coaxial Injector Spray Characterization, pages 191–213. American Institute of Aeronautics and Astronautics, 1995.

[169] Ben T. Zinn. Pulse Combustion: Recent Applications and Research Issues. In *Twenty-Fourth Symposium on Combustion/The Combustion Institute*, volume 1, pages 1297–1305, 1992.

[170] B.T. Zinn, W.A. Bell, B.R. Daniel, and A.J. Smith Jr. Experimental Determination of Three-Dimensional Liquid Rocket Nozzle Admittances. *AIAA Journal*, 11 No. 3:267–272, 1973.

[171] B.T. Zinn and T.C. Lieuwen. *Combustion Instabilities in Gas Turbine Engines : Operational Experience, Fundamental Mechanisms, and Modeling*, chapter Combustion Instabilities: Basic Concepts, pages 3–29. American Institute of Aeronautics and Astronautics, 2000.

[172] L. Zipperer and F. Herning. Beitrag zur berechnung der zähigkeit technischer gasgemische aus den zähigkeitswerten der einzelbestandteile. *Das Gas- und Wasserfach*, 79: 49, 1936.

[173] Maurice J. Zucrow and Joe D. Hoffman. *Gas Dynamics Volume II, second edition*. Robert E. Krieger Publishing Company, 1985.

Appendix A

Thermodynamic and Chemical Model Constants

A.1 Chemical Kinetics Mechanism

Table A.1: 7 step oxygen-hydrogen scheme published by Gaffney et al. [28].

Reaction number	Reaction	a_r^f[m^3/mol]	b_r^f	c_r^f[K]
1	$H_2 + O_2 \leftrightarrow 2OH$	1.70×10^7	0.0	24157.0
2	$H + O_2 \leftrightarrow OH + O$	1.20×10^{11}	-0.91	8310.5
3	$OH + H_2 \leftrightarrow H_2O + H$	2.20×10^7	0.0	2591.8
4	$O + H_2 \leftrightarrow OH + H$	5.06×10^{-1}	2.67	3165.8
5	$2OH \leftrightarrow H_2O + O$	6.30×10^6	0.0	548.6
Reaction number	Reaction	a_r^f[m^6/mol^2]	b_r^f	c_r^f[K]
6	$H + OH + M \leftrightarrow H_2O + M$	2.21×10^{11}	-2.0	0
7	$2H + M \leftrightarrow H_2 + M$	7.30×10^6	-1.0	0

The third body efficiencies for reactions 6 and 7 are:

Reaction number	H_2	O_2	H	O	OH	H_2O
6	1	1	1	1	1	6
7	2	1	1	1	1	6

A.2 Modified Benedict-Webb-Rubin Equation

The Modified Benedict-Webb-Rubin Equation of state and its coefficients have been published by Younglove [166]. It can be written [2]:

$$p(\rho, T) = \sum_{n=1}^{9} \rho^n F_{n-1} + e^{-\delta^2} \sum_{n=10}^{15} \rho^{2n-17} F_{n-1}. \tag{A.1}$$

The functions F_n are given in Table A.1. The coefficients of the Modified Benedict-Webb-Rubin equation of state for oxygen are $\gamma = -0.0056$ and the G_i listed in Table A.2.

Table A.1: Functions F_n of the Modified Benedict-Webb-Rubin equation of state.

n	F_n
0	RT
1	$G_1T + G_2T^{0.5} + G_3 + G_4/T + G_5/T^2$
2	$G_6T + G_7 + G_8/T + G_9/T^2$
3	$G_{10}T + G_{11} + G_{12}/T$
4	G_{13}
5	$G_{14}/T + G_{15}/T^2$
6	G_{16}/T
7	$G_{17}T + G_{18}T^2$
8	G_{19}/T^2
9	$G_{20}/T^2 + G_{21}/T^3$
10	$G_{22}/T^2 + G_{23}/T^4$
11	$G_{24}/T^2 + G_{25}/T^3$
12	$G_{26}/T^2 + G_{27}/T^4$
13	$G_{28}/T^2 + G_{29}/T^3$
14	$G_{30}/T^2 + G_{31}/T^3 + G_{32}/T^4$

Table A.2: Coefficients G_i of the Modified Benedict-Webb-Rubin equation of state for oxygen.

i	G_i
1	-4.365859650e-05
2	2.005820677e-02
3	-0.4197909916
4	1.878215317e+01
5	-1.287473398e+03
6	1.556745888e-06
7	1.343639359e-04
8	-0.2228415518
9	4.767792275e+02
10	4.790846641e-08
11	2.462611107e-04
12	-1.921891680e-02
13	-6.978320847e-07
14	-6.214145909e-05
15	-1.860852567e-02
16	2.609791417e-06

i	G_i
17	-2.447611408e-08
18	1.457743352e-05
19	-1.726492873e-07
20	-2.384892520e+02
21	-2.301807796e+04
22	-2.790303526e+00
23	9.400577575e+03
24	-4.169449627e-03
25	0.2008497853
26	-1.256076520e-05
27	-6.406362964e-02
28	-2.475580168e-09
29	1.346309703e-06
30	-1.161502470e-11
31	-1.034699798e-09
32	2.365936964e-08

Appendix B

List of Publications

The following is a list of the publications resulting from the work presented in this thesis.

Journal Articles

[1] Scott Beinke, Daniel Banuti, Justin Hardi, Michael Oschwald, and Bassam Dally. Modelling of a Co-axial LOx/GH2 Injection Element Under High Frequency Acoustic Disturbances. In *Progress in Propulsion Physics*, 2016. (In Press).

[2] Justin S. Hardi, Scott K. Beinke, Michael Oschwald, and Bassam B. Dally. Coupling of cryogenic oxygen-hydrogen flames to longitudinal and transverse acoustic instabilities. *Journal of Propulsion and Power*, 30:991–1004, 2014.

Conference Articles

[1] S. Beinke, D. Banuti, J. Hardi, M. Oschwald, and B. Dally. Modelling of a Coaxial LOx/GH2 Injection Element Under High Frequency Acoustic Disturbances. In *6th European Conference for Aeronautics and Space Sciences (EUCASS)*, Krakow, Poland, 29 June - 3 July 2015.

[2] S. Beinke, J. Hardi, M. Oschwald, and B. Dally. Modelling acoustic excitation of high frquency combustion instability experiments. In *5th European conference for Aerospace Sciences (EUCASS), Munich*, 2013.

[3] S. Beinke, J. Hardi, M. Oschwald, and B. Dally. Modelling an acoustically perturbed rocket engine combustion chamber with cryogenic propellant injection. In *19th Australasian Fluid Mechanics Conference*, 2014.

[4] Scott Beinke, Bassam Dally, and Michael Oschwald. Modelling Acoustic Excitation for the Simulation of Combustion Instability Experiments. In *18th Australasian Fluid Mechanics Conference*, 2012.

[5] Justin S. Hardi, Scott K Beinke, Michael Oschwald, and Bassam B. Dally. Coupling behaviour of LOx/H2 flames to longitudinal and transverse acoustic instabilities. In *48th AIAA/ASME/SAE/ASEE Joint Propulsion Conference & Exhibit*, Atlanta, Georgia, 29 July - 1 August 2012.

[6] M. Wierman, S. Beinke, W. Anderson, M. Oschwald, M. Schulze, M. Zahn, and T. Sattelmayer. Investigation of Modeling and Post-Processing Methods for Combustion Instability Experiments. In *Proceedings of the 2nd Sonderforschungsbereich/Transregio 40 Summer Program*, Technische Universität München, 15 July - 9 August 2013.